Relationships between structures and performance of SOFC anodes

Klemensø, Trine

Publication date:
2006

Document Version
Publisher's PDF, also known as Version of record

Relationships between structures and performance of SOFC anodes

Trine Klemensø
Ph.D. thesis
September 2005

Technical University of Denmark
Topsøe Fuel Cell A/S
Risø National Laboratory

Trine Klemensø
Relationships between structures and performance of SOFC anodes

Ph.D. thesis, September 2005
Technical University of Denmark, Topsøe Fuel Cell A/S, Haldor Topsøe A/S, Risø National Laboratory, and the Danish Industrial PhD programme

Contents

Preface

This thesis is a result of a Ph.D. project carried out under the Danish Industrial PhD Programme. The participating parties were Haldor Topsøe A/S, Topsøe Fuel Cell A/S, the Technical University of Denmark (DTU), and Risø National Laboratory.

All parties involved are greatly acknowledged for financial support, and for providing facilities. I thank Haldor Topsøe A/S for the necessary persistence in the implementation of the project, and the interest in me as a candidate.

I would like to thank my supervisors Jørgen Gutzon Larsen (Topsøe Fuel Cell A/S), Torben Jacobsen (DTU) and especially Mogens Mogensen (Risø National Laboratory) for guidance, inspiration and discussions.

I am very grateful to the SOFC-group at Risø, and the R&D groups at Haldor Topsøe A/S and Topsøe Fuel Cell A/S, who formed a solid and competent base for the project. Bent F. Sørensen (Risø National Laboratory) is thanked for "mechanical support". Karin Vels Hansen (Risø National Laboratory) is thanked for proof reading.

Thanks to colleagues, friends and family who shared the joy and troubles, and tolerated and encouraged on the way.

Trine Klemensø
Roskilde, September 2005

Dansk resumé

Den nuværende teknologiske nikkel-YSZ-cermet i den anode-supporterede fastoxid brændselscelle (SOFC) degraderer under redox-cykling. Degraderingen er et kritisk punkt i forbindelse med kommercialisering af teknologien.

Undersøgelser af nikkel-YSZ-cermets med variabel sammensætning og mikrostruktur blev udført under redox-cykling for at opnå indsigt i degraderingsmekanismen og for at identificere parametre og karakteriseringsteknikker til udvikling af cermet-strukturen. Undersøgelserne omfattede direkte iagttagelser af mikrostrukturen (optisk mikroskopi, SEM, ESEM, billedanalyse), bulk-målinger (porøsitet, dilatometri, mekaniske egenskaber), målinger af de elektriske egenskaber (ledningsevne, impedans spektroskopi), målinger af redox kinetikken (TGA, synkrotron), og anvendelse af simple modeller af det lagdelte system.

En mikrostrukturel model af redox-mekanismen er beskrevet. Degraderingen under redox-cykling blev tilskrevet en dynamisk omfordeling af Ni/NiO-fasen under reducerende forhold og i forbindelse med re-oxidationen. Omfordelingen medfører brud i YSZ-matricen og efterfølgende bulk-udvidelse af cermet-strukturen ved oxidation. Bulk-udvidelsen vil resultere i brud i elektrolytten.
Omfordelingen af den reducerede nikkel foregår som partikel-afrunding og nikkel-sintring. Sintringsgraden afhænger af temperatur, den keramiske komponents sammensætning, og sandsynligvis af de lokale porøsitetsforhold. Omfordelingen af NiO-fasen under oxidation afhænger af kinetikken og den lokale porøsitet. Ved høje temperaturer involverer NiO-væksten opsplitning af partiklerne. Ved lavere temperatur sker væksten i form af en ekstern oxid-skal.

Den mekaniske styrke af den keramiske cermet-komponent fremstod som en teknologisk potentiel parameter til forbedring af redox-stabiliteten. Dog vil betydelig forstærkning af strukturen være påkrævet. En forstærkning, der vil resultere i en halvering af bulk-ekspansionen under re-oxidation, blev estimeret nødvendig.

Modificering af cermet-sammensætningen med additiver fremstod som en lovende mulighed for forbedring af redox-stabiliteten. Betydelig forstærkning, samt reduktion af Ni-sintringen, syntes opnåelig gennem anvendelse af additiver. Yderligere eksperimentelle undersøgelser kræves for at afdække det fulde potentiale. Det fremtidige udviklingsarbejde vil være empirisk baseret, eller omfatte detaljerede beskrivelser af sammenhængene mellem mikrostrukturelle parametre og bulk-egenskaberne.

Abstract

The nickel-YSZ cermet of the state-of-the-art anode-supported solid oxide fuel cell (SOFC) degrades upon redox cycling. The degradation is a critical issue for the commercialization of the technology.

Nickel-YSZ cermets with variable composition and microstructure were examined during redox cycling to obtain knowledge of the degradation mechanism, and to identify parameters and characterization tools to improve the cermet. The investigation techniques included direct observations of the microstructure (light microscopy, scanning electron microscopy, environmental scanning electron microscopy, image analysis), bulk measurements (porosity, dilatometry, mechanical properties), measurements of the electrical performance (direct current conductivity, impedance spectroscopy), measurements of the redox kinetics (thermo gravimetric analysis, synchrotron), and application of simple models of the layered system.

A model of the redox mechanism on the microstructural level was described. The degradation related to redox cycling was ascribed to a dynamic reorganization of the Ni/NiO phase, when in the reduced state and upon re-oxidation. The redistribution generated fractures in the YSZ matrix, and bulk expansion of the cermet structure upon oxidation. The bulk expansion promoted cracking of the electrolyte.
The redistribution of the reduced nickel phase was observed to occur as rounding of the particles, and nickel sintering. The degree of sintering depended on the temperature, the composition of the ceramic component, and possibly on the local porosity. The redistribution of the NiO phase upon oxidation was seen to depend on the kinetics and the local porosity. At higher temperatures the oxide growth involved fragmentation of the particles. At lower temperatures the growth occurred in the form of an external oxide peel.

The mechanical strength of the ceramic component was indicated as a technological potential parameter for improving the redox stability. However, considerable strengthening was indicated to be required. Strengthening that will result in a reduction of the bulk expansion upon re-oxidation with a factor of two was estimated.

Modification of the cermet composition with additives was indicated as a possibility for improving the redox stability. Significant strengthening and reduction of the nickel sintering were indicated achievable with additives. However, further experimental work will be required to discover the full potential of the application of additives. The future work will be empirically based, or include detailed descriptions of the relationships between microstructural parameters and the cermet bulk properties.

1 Introduction

The energy market is an issue of great future and political importance. The conventional technology is based on combustion of fossil fuels. However, limited fossil resources and the associated emission of large amounts of pollutants (CO_2, NO_x, SO_2), makes it insufficient and inappropriate for the future.
Fuel cells are a possible energy technology for the future. In fuel cells, the chemical energy of the fuel is converted into usable form by electrochemical combustion. Less CO_2 per kWh is released, the emission of NO_x and SO_2 is nearly eliminated, and the efficiency is for some types of fuel cells higher than for conventional combustion. Fuel cells can work as electrolyzers, producing storage fuel from excess renewable energy (e.g. sources like hydroelectricity, geothermal, biomass, solar and wind power). In addition, fuel cells are modular in design. This facilitates adjusted energy production, an arbitrary decentralization of the power grid, and improved security of supply. In an energy system based on, or changing into, renewable energy sources, fuel cells may become a key technology. Unless otherwise stated, the reference of this chapter is Minh and Takahashi [1].

1.1 Fuel cells

1.1.1 Principle of operation

Fuel cells produce electrical energy by electrochemical combustion of gaseous fuels. The reactions take place at two porous, electronic conducting electrodes that are separated by an ionic conducting electrolyte. The cell reactions generate a potential difference between the electrodes, and a DC current through the external circuit. The operating principle is illustrated in Figure 1.1.

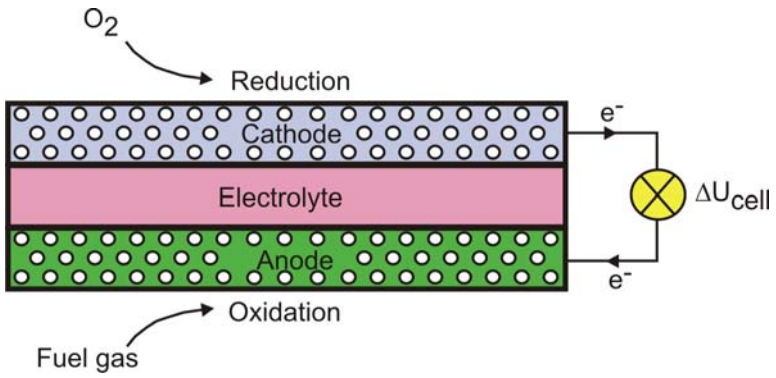

Figure 1.1. Sketch of the operating principle of a fuel cell.

The cell potential difference (ΔU_{cell}) is defined by the electromotive force (EMF), the voltage loss due to leaks (ΔU_{leak}), and the operation of the cell ($\Delta U_{current}$) (cf. Equation 1.1). The EMF is the theoretical potential difference at open circuit conditions, i.e. when the current density (i) is zero. The EMF is determined by the Nernst equation (cf. Equation 1.2). ΔU^{o}_{cell} is the potential under standard conditions, R is the gas constant, T is the temperature, n is the number of electrons involved, F is Faraday's constant, and Q is the reaction quotient.
Gas leakages and imperfect ionic conduction in the electrolyte result in a voltage loss. The difference between EMF and ΔU_{leak} is the actual measured potential at open circuit conditions, and is referred to as the open circuit voltage (OCV).
A potential drop is associated with the operation of the fuel cell, and related to the current density. The drop results from ohmic resistance (R_{ohmic}) in the electrodes, electrolyte and

contacts, and from polarization resistance (η) due to restrictions on the reaction rates. The relationship is shown in Equation 1.3.

Eq. 1.1 $$\Delta U_{cell} = EMF - \Delta U_{leak} - \Delta U_{current}$$

Eq. 1.2 $$EMF = \Delta U^{o}_{cell} - \frac{R \cdot T}{n \cdot F} \cdot \ln Q$$

Eq. 1.3 $$\Delta U_{current} = i \cdot R_{ohmic} + \eta(i)$$

The cell potential will depend on the cell materials, current density, and type, composition and partial pressure of the gasses applied. At OCV a typical cell generates about 1 volt. By connecting cells in series, called stacking, an arbitrary voltage can be build.

1.1.2 Performance

The performance of a cell or a stack can be stated in a number of ways. The power density (watts per cm^2 of cell) is a way of measuring the performance. However, the power output is very dependent on fuel composition and cell voltage.
If the current density-voltage curve (i,V-curve) is approximately linear, the slope of the curve is a more specific performance measure. The slope is named the area specific resistance (ASR), and defined as shown in Equation 1.4. The unit of the ASR is $\Omega \cdot cm^2$. The ASR is to a large degree only sensitive to the temperature [2].

Eq. 1.4 $$ASR = \frac{EMF - \Delta U_{cell}}{i}$$

The long-term stability of the cells and robustness towards temperature- and redox cycling, are important aspects of the performance as well. The degradation is typically reported as the drop in ASR, cell potential or power density upon time or cycling.

1.1.3 Types of fuel cells

The operational principle of fuel cells has been known for almost two centuries, first described by Sir Humphrey Davies (1802) and Sir William Grove (1839) [3]. Since then, different types have been developed. The five main types are AFC (alkaline), PEMFC (polymer), PAFC (phosphoric acid), MCFC (molten carbonate), and SOFC (solid oxide). Each type is characterized by the electrolyte, which it is named after, temperature range of operation, possible electrical efficiency, and usable fuels.
Previous development focused on the low temperature fuel cells (AFC, PEMFC, PAFC). AFC was used in the space programme of NASA in the 1960'ties, and full-scale test-units of MCFC and PAFC were developed in the start 1990'ties. The present research and development focus world wide on SOFC and PEMFC. SOFC based products have potential for being commercial and on the market within 5-10 years. The prospects of PEMFC are believed to be more long-termed. SOFC aims for applications requiring continuous power/heat production. PEMFCs have potential for propulsion of cars.

1.2 Solid oxide fuel cells

A SOFC is characterized by a solid, dense oxide electrolyte with high oxide ion conductivity. With hydrogen as fuel the electrochemical reactions at the two electrodes are as shown in Equations 1.5 and 1.6.

Eq. 1.5 Anode: $H_2 + O^{2-} \rightarrow H_2O + 2\ e^-$

Eq. 1.6 Cathode: $\frac{1}{2}\ O_2 + 2\ e^- \rightarrow O^{2-}$

The reactions involve exchange of species from the three phases: gas, oxide ion conductor, and electron conductor. Thus, it is understandable that the three phases boundary (TPB) zone is an important parameter on the polarization resistance [4, 5, 6]. The microstructure of the electrodes is therefore as important for the cell performance as the cell design and materials.
For commercialization of the SOFC technology, cost-performance competitive combinations of stack design, cell design, materials, microstructures, and processing methods must be developed.

1.2.1 Designs

Stack design

Various stack- and cell designs have been developed. For stacking, the commercialization efforts are focused on two main designs: tubular and flat plate design. The two types are sketched in Figure 1.2.

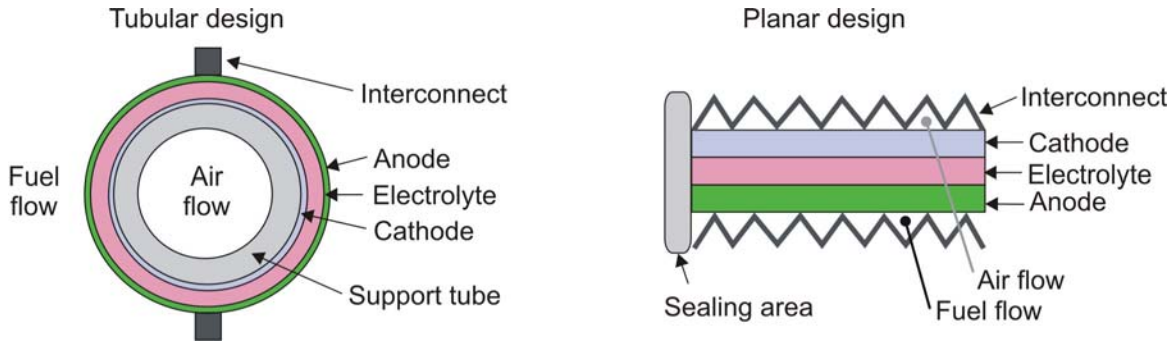

Figure 1.2. Sketch of the two main stack designs: the tubular and planar design.

The advantage of the tubular design is the simple gas manifolds, where sealing is not needed. On the other hand, the flat plate design has the shortest possible current path across the cell, is more compact, and has a simple geometry allowing for use of simple and cheap manufacturing techniques. The drawbacks of the planar design are the need for sealing, and the low mechanical robustness.

Cell design

For the planar stack design, three cell designs exist: electrolyte-, anode-, and metal-supported. The designs are named after the structurally supporting member of the cell as illustrated in Figure 1.3. The three designs are also called respectively the first, second and third generation cell.
The first developed design was the electrolyte-supported. The design demanded operation temperatures around 1000°C for obtaining a reasonably low ohmic resistance of the electrolyte, and for a reasonable performance of the electrodes. However, lower operational temperatures

allow for use of cheaper materials, to for instance interconnect and manifolds, and were therefore desirable.

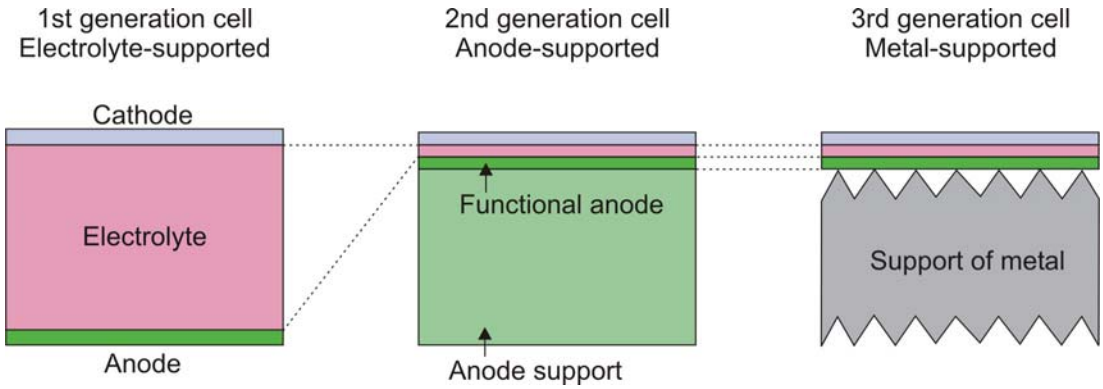

Figure 1.3. Sketch of the three planar cell designs.

This led to the development of the second generation, anode-supported cell. In this design the electrolyte is thin, and the anode is divided into two parts: the electrochemical active part (the functional anode), and the anode support (cf. Figure 1.3). With the anode-supported design, the electrodes have been improved to work at temperatures around 800°C. The anode-supported design is at present the most prevalent, but suffers from too high degradation of the materials, lack of redox stability, and insufficient cost-performance relations.
To meet these demands, a third generation metal-supported cell design is under development. The design is meant to work at temperatures around 600°C, where the degradation mechanisms are further restrained. The cheap materials, potential redox stability, and improved mechanical properties make the design a feasible candidate for commercial mass production [7].

1.2.2 Materials

The choices of materials for each component are restricted by the performance properties, the working conditions, the other materials in the stack, and the processing route. The material needs to be physically and chemically stable at the operation temperature, and in the atmospheres experienced under operation and fabrication. Morphologic changes, chemical interaction, and mismatch in thermal expansion coefficient (TEC) will influence, and can be detrimental for the material properties and cell performance.

Anode

The state-of-the-art anode is a porous cermet of nickel and yttria stabilized zirconia (YSZ). The ceramic component is 8 mol% YSZ (8YSZ) in the functional anode, and 3 mol% YSZ (3YSZ) in the anode support. The pores allow for gas diffusion, and the Ni phase provides electronic percolation paths and catalytic properties. The YSZ phase implies a matching TEC with the ceramic electrolyte and cathode. In addition, the application of 3YSZ in the support is believed to enhance the mechanical strength, and by applying the superior oxide ion conductor 8YSZ in the functional anode, the area of the active TPB zone is increased.
A problem with the use of Ni as anode material is that the cermet is not redox stable. Reductions and re-oxidations involve large volume changes of the nickel phase. The volume changes are reflected in the bulk cermet structure as well [8, 9]. This presents a need for an anode gas protection system, both when running in fuel cell and electrolyzer mode. In most cases this is not economically feasible.
Another problem with the use of nickel is the sintering of the metal [10, 11]. The performance of the material degrades as the sintering reduces the number of percolation paths and the TPB zone.

To minimize or avoid the problems with nickel, and improve the performance of the anode, a number of alternative materials have been tested as electrodes. The main groups are nickel alloys, or mixed conductors of the types flourite, rutile, tungsten bronze, pyrochlore, and perovskite [12, 13]. However so far, the tested materials generally display performances far below the conventional Ni-anode, or have other disadvantages such as low electronic conductivity or phase instability.

Electrolyte

The electrolyte needs to be dense, and to posses high oxide ion conductivity. The classical material is dense sintered 8YSZ. At this yttria content, the maximum conductivity in the ZrO_2-Y_2O_3 system is found.
To accommodate better cell performance, and permit lower operation temperatures, materials with higher oxide ion conductivity are investigated. Another motive for search of alternative materials is the degradation in conductivity of 8YSZ when operated. The degradation is associated with phase transformation, and increased grain boundary resistance, possibly related to impurity segregation. The materials under investigation include ZrO_2 with various dopants, and doped CeO_2 [1, 6].

Cathode

Porous Sr-doped lanthanum manganite (LSM) is the present choice for the cathode material. The material has a high electrocatalytic activity for reduction of oxygen, sufficient electronic conductivity, can be TEC matched with YSZ, and is stable in the oxidizing atmosphere at high temperatures prevailing in the cathode. However, the LSM/YSZ interface is not chemically stable at high temperatures, where phases with low conductivity will form. The present research on cathodes is focused on improving the performance by modifications of the LSM structure, and by investigating alternative perovskite materials.

Interconnect

Metallic interconnects are generally used. The interconnect experiences dual atmosphere (cf. Figure 1.2), and needs to be gas tight, and to have a high electronic conductivity. To minimize corrosion and associated degradation in conductivity, the corrosion behavior of various metals and metal coatings are investigated. At present, ferritic iron chromium alloys are the preferred materials.

Sealing

For sealing, an electrically insulating material with stability in the dual atmospheres, and towards all other components is needed (cf. Figure 1.2). Wetting and TEC match to the other stack components, as well as a degree of deformability, is crucial for obtaining tight seals. Traditional sealing materials are glass-based, covering either glass or glass ceramics. Publications on the compositions are limited. Research on compositions providing better gas tightness towards the present stack materials is an ongoing issue for improving the performance of the planar stack design [14].

1.2.3 Processing

The performance of a component is as critically dependent on the microstructure, as on the material itself. The microstructure in turn depends on the fabrication process, and treatment and characteristics of the starting powders. The range of process techniques, and process routes is restricted by the demand for low cost, a minimum of unit operations and scale-up capability.
Cheap and simple wet ceramic shaping techniques are feasible for the planar cell design. The mechanically supporting member of the cell is typically made by tape casting. The thin films can

be applied by various techniques e.g. spray painting, screen-printing, vapor deposition, impregnation, and spin coating. Sintering is done by co-sintering and separate sintering of the components. However, tailoring of the microstructure by adjusting the processing route is complex, as the number of parameters is excessive and interrelated. The influences on the microstructure and their complex interactions are sketched in Figure 1.4.

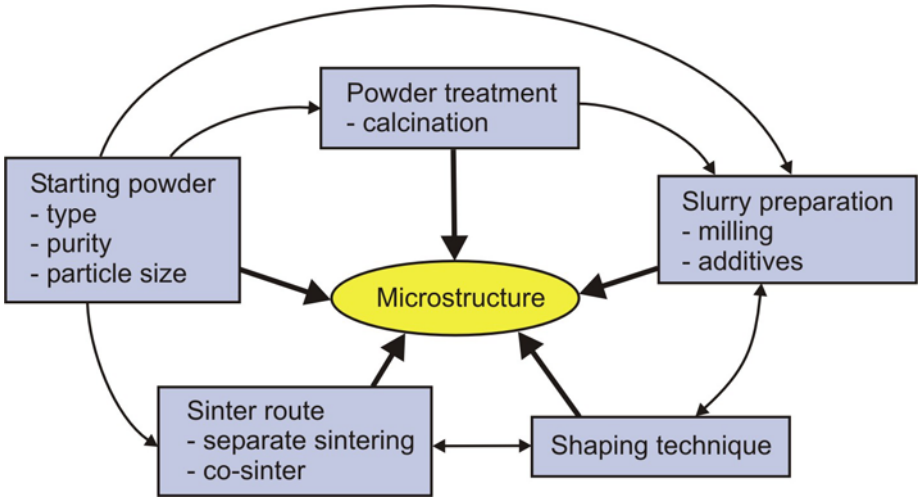

Figure 1.4. Illustration of the process parameters influencing on the microstructure.

1.2.4 Commercialization

The research and development issues before commercialization of the SOFC technology include scale-up of processes and production, improvement of reproducibility of the components, and improvement of the energy-economy. The issue of reducing the system price is related to reduction of the components costs, as well as improving the performance, lifetime and robustness of the components. Globally, hundreds of companies do active research in the fuel cell technologies, and about one third of them concentrate on SOFC [15].
SOFC-based systems are possible in a wide range of applications. Different market segments, and the estimated market prospects are illustrated in Figure 1.5. Some of the first commercial products are expected to be combined heat-power systems (CHP) for residential or commercial use, and auxiliary power units (APU) for transports. Larger scale products are believed potential, but with a longer time frame.

Market	Short-term		Mid-term	Long-term
Product scale	Small 1-50 kW		Medium 50 kW - 1 MW	Large 1-30 MW
Product	 Residential combined heat-power (CHP)	 Auxiliary power units for transports (APU)	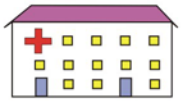 Commercial combined heat-power (CHP)	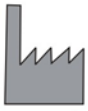 Power plants

Figure 1.5. Potential market segments for the SOFC technology.

1.2.5 Redox stability

Failure in fuel supply or shutdown of the system is critical for stacks based on non-redox stable anodes. During such incidents the anode risks exposure to an oxidizing atmosphere at high temperatures due to diffusion of air from the surroundings, backflow or leak currents.
The requirements to redox stability depend on the product. A stationary CHP system is expected to endure about a 100 cycles in the stack lifetime, corresponding to a maximum of 20 cycles per year [16]. For mobile applications, fuel gas interruptions are expected more frequently, and requirements are on the scale of several thousands redox cycles during a lifetime [7].
To avoid this, an anode gas protection system, including an inert purge gas, is a possibility. However, a safety system of this type is believed only economic feasible in large systems and niche products. Protection systems are not believed to be an option in commercial small to medium scale systems below about 100 kW [12].
To improve redox stability, alternative anode materials with reduced or no Ni-content are being investigated (cf. Section 1.2.2). Other attempts involve avoidance of introduction of air by valves [17], cell designs that are not anode supported [7, 8, 18], or modification of the anode microstructure [8, 19, 20].

1.3 Objective and layout of the thesis

Improvement of the anode performance, including durability and robustness, is an important step in the commercialization of the SOFC technology. The performance of the nickel-YSZ cermet is closely related to the cermet microstructure. The aim of this thesis is to contribute to the understanding of the structure-performance relationship in the anode with emphasis on the redox performance. Cermet structures and their redox behavior are characterized and quantified, and from this key structural parameters on the redox behavior, and development tools are identified. The knowledge is applied to improve the cermet redox performance.

The studies included preparation of different nickel-YSZ cermets, characterization of bulk properties (porosity, dilatometry), microstructure (light microscopy, scanning electron microscopy, environmental scanning electron microscopy, image analyses), kinetics (thermo gravimetric analysis, synchrotron), electrical performance (DC conductivity, impedance spectroscopy), and mechanical properties (strength test). The investigated cermets differed in chemical composition, shape, and microstructure. Several samples of each type (so called sibling samples) were prepared. The different characterization techniques were applied to different, but nominally identical samples from the sibling batch.

The different methods applied are described in separate chapters. Chapter 2 deals with bulk properties, Chapter 3 deals with microstructure, Chapter 4 deals with kinetics, Chapter 5 deals with electrical properties, and the Chapters 6-8 are related to strength measurements. Chapter 6 describes a method for tensile strength test. Chapter 7 is about the cermet strengths, and Chapter 8 describes layer models of the cell, where the strength of the anode cermet is a parameter. Chapter 9 deals with cermet compositions modified by additives.
The samples from a sibling batch are believed to be nominally identical. Thus, when different samples from the same sibling batch are used for the different techniques, the same common sibling name is used in the different chapters.
For each chapter a separate experimental section, and discussion and conclusions are given. The overall discussion, conclusions, and outlook are contained in Chapter 10, 11, and 12, respectively.

2 Bulk properties of nickel-YSZ cermets*

2.1 Introduction

Redox stability of the anode in small- and medium- scale solid oxide fuel cells (SOFC) is considered to be important for commercial and safety reasons [19, 21, 22]. The technological aim has been reported to be 5-20 cycles per year during the lifetime of the cell [16, 19]. The commercial lifetime of 5 years thus corresponds to a total of 25-100 cycles.
However, in the state-of-the-art and prevalent nickel-yttria stabilized zirconia (YSZ) anode-supported design, oxidation of the anode is known to be detrimental to the cell performance [8, 19, 23]. The degradation upon redox cycling is believed related to bulk expansion of the anode, causing formation of cracks in the electrolyte. For some reason, the anode does not revert to the pre-reduced volume upon re-oxidation, but will instead expand. The size of the bulk expansion is known dependent on microstructural factors such as particle sizes [19]. However, the mechanism behind the process has not previously been investigated [8, 9, 19].
In this chapter the redox behavior of nickel-YSZ cermets with variable porosity and strength was examined. The investigations included dilatometry and microstructural examinations. From the observations, a model of the redox mechanism occurring in the anodes was proposed.

2.2 Experimental

2.2.1 Sample preparation

Samples with variation in porosity and strength were obtained by applying different ceramic components into the cermets, and by using different sample shaping techniques. The samples were prepared from NiO powder (99 % from Alfa Aesar), alumina (Catapal® from Sasol) and either 3 or 8 mol% yttria stabilized zirconia powder (TZ-3YB or TZ-8Y from Tosoh Co.). The solid material contents in the oxidized and reduced state of the three investigated compositions are shown in Table 2.1.

Table 2.1. The compositions of the investigated materials.

Material	Component	Oxidized state		Reduced state	
		Wt %	Vol %	Wt %	Vol %
I	NiO / Ni	56.8	54.4	51.0	41.3
	8YSZ	43.2	45.6	48.9	58.8
	Sum	100.0	100.0	99.9	100.1
II	NiO / Ni	55.7	52.9	49.7	43.2
	3YSZ	43.7	46.1	49.6	55.7
	Al_2O_3	0.6	1.0	0.7	1.1
	Sum	100.0	100.0	100.0	100.0
III	NiO / Ni	56.0	50.9	50.0	41.2
	3YSZ	35.2	35.5	40.0	42.6
	Al_2O_3	8.8	13.5	10.0	16.2
	Sum	100.0	99.9	100.0	100.0

The content of nickel was approximately the same in all three compositions. The ceramic component applied was either calcined 8 mol% yttria stabilized zirconia (8YSZ), calcined 3 mol% yttria stabilized zirconia (3YSZ), calcined 3YSZ containing 20 wt% alumina, or uncalcined 3YSZ. The as-delivered raw YSZ powder was calcined as described elsewhere [24,

* This chapter is to be published with minor revisions as T. Klemensø, C. Chung, P.H. Larsen, M. Mogensen, The mechanism behind redox instability of anodes in high-temperature solid oxide fuel cells, Journal of the Electrochemical Society, 152, 11 (2005).

25]. 3YSZ is expected to have improved mechanical properties compared to 8YSZ up to relatively high temperatures [26, 27]. Addition of alumina to YSZ is reported to increased the strength [27, 28], and pre-calcination of the YSZ powder is on empirically grounds believed to improve sintering, and thereby potentially to be improve the strength [24].

The powders were prepared into slurries, and thin foils were subsequently made using tape casting technique. Three sample geometries were made from the green tapes. (1) "Rolled samples" were made from rolling green tape into cylinders. The green rolls were fixed with Pt wire. After sintering the cylindrical samples were approximately 20 mm in length and 5 mm in diameter. (2) "Layered samples" were made from stacking pieces of green tape. Each layer was wetted with ethanol to assist adhesion. After sintering, the layered samples were cut down to a size of 18 mm x 4 mm x 4 mm. (3) Some of the green tapes were heat treated to produce powder, and the resulting powder was pressed. Pressed bar shaped samples of dimensions ca. 50 mm × 5 mm × 5 mm were made using uniaxial pressing followed by isostatic pressing at 80 MPa. After sintering, the bars were cut down into lengths of 20 mm.
The samples were sintered at 1300°C. Successive reductions and up to four redox cycles were performed during dilatometer measurements at temperatures of 700°C, 850°C and 1000°C. In addition, a sample was subjected to temperature cycling in-between gas shifts. Table 2.2 shows a list of the tested samples. The sample name indicates the composition of the ceramic component, sample shape, and test conditions. Samples containing the ceramic components 8YSZ, 3YSZ, 3YSZ + 20 wt% Al_2O_3, and uncalcined 3YSZ are in the sample names abbreviated to respectively 8Y, 3Y, 3YA, and Raw3Y. Tests with identical samples composition, shape, and test conditions are differentiated by the added serial letter in the last part of the sample name.

Table 2.2. List of samples. The first part of the sample name indicates the composition of the ceramic component. Raw 3YSZ means uncalcined powder. 20 wt% Al_2O_3 refers to the weight percent of the ceramic phase. The last parts of the sample name refer to sample shape and temperature at which redox cycling was carried out. TC means temperature cycled. Samples of identical composition, shape, and test conditions are differentiated by a serial letter in the last part of the sample name.

Sample name	Ceramic composition	Shape	Temperature	Thermal treatment
8Y-bar-1000-a	8YSZ	Bar	1000°C	Isothermal
8Y-bar-1000-b	8YSZ	Bar	1000°C	Isothermal
8Y-bar-1000-c	8YSZ	Bar	1000°C	Isothermal
3Y-bar-1000	3YSZ	Bar	1000°C	Isothermal
8Y-roll-1000	8YSZ	Roll	1000°C	Isothermal
8Y-roll-700	8YSZ	Roll	700°C	Isothermal
8Y-bar-1000-TC	8YSZ	Bar	1000°C	1000°C-100°C in-between gas shifts
3Y-roll-850	3YSZ	Roll	850°C	Isothermal
Raw3Y-roll-850	Raw 3YSZ	Roll	850°C	Isothermal
3Y-layer-850	3YSZ	Layered	850°C	Isothermal
3YA-layer-850	3YSZ + 20 wt% Al_2O_3	Layered	850°C	Isothermal

2.2.2 Experimental procedure

Measurements were performed with a Netzsch Dil 402E dilatometer and a Setaram DHT 2050 differential dilatometer. In the Netzsch instrument the samples were loaded horizontally and fixed with a spring load. Baselines were achieved using polycrystalline alpha-alumina. In the Setaram instrument, the samples were loaded vertically, and baselines were measured simultaneously using alpha-alumina. The data for the two instruments are considered to be consistent when baseline correction is performed. For both instruments, the uncertainty is stated to be 1 μm, corresponding to an uncertainty of 0.01% on the relative expansions of the ca. 20 mm long samples.

The samples were heated to 700°C, 850°C, or 1000°C at 2°C/min in air, and allowed to equilibrate. For redox cycling 9 vol% H_2/N_2 was used as the reducing gas and air as the oxidizing medium. The sample chamber was flushed with N_2 in-between atmosphere changes. Temperature cycling from 1000°C to 100°C and back to 1000°C was performed with heating/cooling rates of 2°C/min.
The microstructure of the samples was investigated by scanning electron microscopy (SEM). A Fei Quanta 600 equipped with an EDAX® thin window detector and EDAX® Genesis software was used.
The porosity of the samples was quantified by mercury porosimetry, Archimedes' method, and by weighing and geometrical gauging. An Autopore IV 9500 V1.05 instrument from Micromeritics Instrument Corporation was used as mercury porosimeter.
With the Archimedes' method, the open porosity (ε_{arch}) is calculated as shown in Equation 2.1 [29]. As the water density can be assumed to be constant, ratios between masses of water correspond to ratios between volumes. Thus, the open porosity equals the ratio between the mass of the water in the pores (m_{pores}) and the mass of the displaced water and the water in the pores ($m_{displaced} + m_{pores}$). The sample weight in the dry state is denoted m_{dry}, the sample weight suspended in water is $m_{suspended}$, and m_{wet} is the sample weight after removal from the water. The suspended weight was taken after the sample had been immersed for 3 hours in boiling water, and cooled in the water for 36 hours. Immediately upon removal from the water, the sample was wiped with a wet cloth, and m_{wet} was measured.

Eq. 2.1
$$\varepsilon_{arch} = \frac{m_{pores}}{m_{displaced} + m_{pores}} = \frac{m_{wet} - m_{dry}}{m_{wet} - m_{suspended}}$$

The samples were weighed with a Mettler AE 163, and the dimensions measured with a Vernier gauge, and a Mitutoyo 7002 dial thickness gauge. For straight-sided shaped specimen of known composition, the geometrical porosity (ε_{geom}) is calculated as shown in Equation 2.2. V_{geom} is the geometrically measured volume, V_{solid} is the volume of solids calculated from the sample weight (m), and the weight fractions (x_i), and densities (ρ_i) of the consisting components (i).

Eq. 2.2
$$\varepsilon_{geom} = \frac{V_{geom} - V_{solid}}{V_{geom}} = \frac{V_{geom} - \sum_{1}^{i}\left(\frac{m \cdot x_i}{\rho_i}\right)}{V_{geom}}$$

2.3 Results

2.3.1 Dilatometry

The measured dilatometry profiles of two of the samples (8Y-bar-1000-a and 3Y-bar-1000) are illustrated in Figure 2.1. Periods of oxidizing and reducing atmospheres are marked "Air" and "H_2", respectively. The flushes with N_2 in-between atmosphere changes were short (15 minutes), and are not indicated in Figure 2.1. When flushing times were as short as this, no changes in sample length were observed during flushing.
The two samples were seen to expand similarly upon heating, and to stabilize when the test temperature (1000°C) was attained. During the first period with reducing atmosphere, no change in length was recorded (cf. Figure 2.1). This was a common feature observed in most of the samples.
Successive oxidizing atmospheres were accompanied by relatively rapid expansions, and upon subsequent reductions shrinkage was seen. Complete reduction or oxidation was observed to

occur within 2 and 3 hours of exposure to reducing/oxidizing atmosphere, respectively. However, in some cases during later reduction steps, stabilization was not obtained after 2 hours in reducing atmosphere (not clearly seen in Figure 2.1). Samples displaying this behavior were generally characterized by severe macro cracking. In such cases, the shrinkage values obtained after 2 hours of reduction were used for data comparison.
As an exception, the alumina-rich sample displayed shrinkage even during the first reduction, and full stabilization was not achieved after up to 48 hours of exposure to reducing atmosphere. In this case, both shrinkage after 2 hours reduction and the maximum measured shrinkage value are reported.

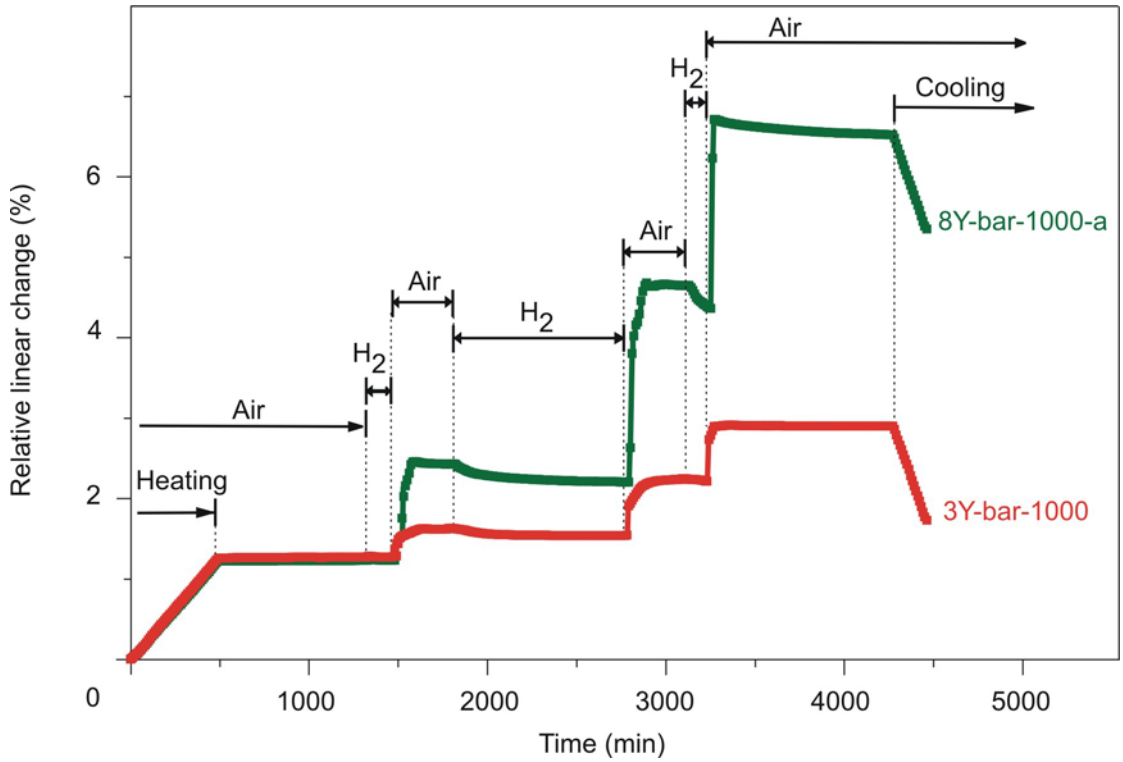

Figure 2.1. Dilatometry profiles of the samples 8Y-bar-1000-a (green) and 3Y-bar-1000 (red) during changing reducing atmosphere (marked "H_2") and oxidizing atmosphere (marked "Air").

Reproducibility

To investigate the variation of identically prepared samples, three samples of the type 8Y-bar-1000 were tested under identical conditions. The measured relative linear changes associated with each redox step for the samples 8Y-bar-1000-a, 8Y-bar-1000-b, and 8Y-bar-1000-c are listed in Table 2.3.

Table 2.3. Relative linear changes of identical prepared and tested samples (8Y-bar-1000-a, 8Y-bar-1000-b, 8Y-bar-1000-c) upon successive redox steps. Data on the sample 8Y-bar-1000-TC subjected to combined temperature and redox cycling is included. Uncertainty on the data is ± 0.01%. Absence of measurement is marked with (-).

Redox step	Relative linear change [%]			
	8Y-bar-1000-a	8Y-bar-1000-b	8Y-bar-1000-c	8Y-bar-1000-TC
1st red	0.00	-0.10	-0.07	-0.01
1st ox	1.19	1.21	1.25	3.09
2nd red	-0.22	-0.10	-0.10	-0.17
2nd ox	2.44	-	1.21	5.55

The samples 8Y-bar-1000-b and 8Y-bar-1000-c displayed significant shrinkage upon the first reduction. This was unusual behavior, and not observed in any other tested nickel-YSZ cermets (also cf. the following sections). Opposed to the other measurements, the large shrinkages upon

the first reduction were obtained after longer time of exposure to reducing conditions, 23-30 hours compared to 2 hours, and the shrinkages were observed to occur gradually over the period of time.
The first re-oxidation was associated with expansions in the range of 1.2% in all samples. The relative expansions differed by less than 5%. However, during the second cycle, the relative expansion upon re-oxidation differed by a factor of two between 8Y-bar-1000-a and 8Y-bar-1000-c.

Shape

Three different sample geometries were tested. The measured dimensional changes associated with each redox step are listed in Table 2.4. Samples containing 3YSZ as the ceramic component (i.e. 3Y-roll-850 and 3Y-layer-850) were tested at 850°C and can be compared. Samples containing 8YSZ (i.e. 8Y-roll-1000 and 8Y-bar-1000-a) were tested at 1000°C, and are comparable.

Table 2.4. Relative linear changes of samples with different shapes upon successive redox step. Uncertainty on the data is ± 0.01%. Asterisk (*) indicates shrinkage values after 2 h reduction, where stabilization was not achieved. Absence of measurements is marked with (-).

Redox step	Relative linear change [%]			
	3Y-roll-850	3Y-layer-850	8Y-roll-1000	8Y-bar-1000-a
1st red	0.00	0.00	0.00	0.00
1st ox	0.90	0.46	4.95	1.19
2nd red	-0.23	-0.18	-0.78	-0.22
2nd ox	1.43	1.17	6.46	2.44
3rd red	-0.26	-	-0.96*	-0.24*
3rd ox	1.96	-	2.14	2.13

For both test compositions and temperatures, higher dimensional changes were observed for the rolled sample compared to respectively the layered and the bar shaped sample. The trend was particularly obvious during the first two cycles, and more pronounced in the high-temperature, 8Y composition samples, where a roll and a bar shaped sample were compared.
Enhanced dimensional changes were observed during the second cycle in all samples. For layered and bar shaped samples, the expansion doubled upon the second oxidation. Upon the third oxidation further increase in expansion was seen in the sample 3Y-roll-850, whereas the materials containing 8YSZ as ceramic component showed reduced expansion.

Composition of the ceramic component

The effect of the strength of the ceramic component was indirectly studied by investigating the effect of yttria content, alumina addition and calcination of the ceramic powder. The dimensional changes of the sample associated with each redox step are listed in Table 2.5. As shape and temperature of the experiments vary, the data were only directly comparable two by two.
The alumina-rich sample (3YA-layer-850) stabilized exceptionally slowly upon reduction. Shrinkage values after the standard 2 hours of reduction, as well the maximum measured shrinkage (recorded after up to 48 hours exposure to reducing atmosphere) are shown in the last two columns of Table 2.5 for this case.
No dimensional changes were generally observed during the first reducing period, except for the alumina-rich sample (3YA-layer-850), where a maximum of up to 0.40% shrinkage was measured (cf. Table 2.5).
Upon the first oxidation, expansion occurred in all samples. However, lower expansions were recorded for 3Y samples than 8Y samples (compare 3Y-bar-1000 and 8Y-bar-1000-a), and for samples with calcined powder than those with raw powder (compare 3Y-roll-850 and Raw3Y-roll-850) (cf. Table 2.5).
Addition of 20 wt% alumina to the ceramic phase appeared to enhance the expansion that was almost doubled compared to the equivalent sample without alumina (compare 3YA-layer-850

and 3Y-layer-850). If, however, the shrinkage during the preceding reduction is taken into account, the effect of the first cycle for the alumina-rich sample is 0.44% (= 0.84% - 0.40%). This net effect (i.e. n'th expansion - n'th maximum shrinkage) is similar to the sample without alumina, with a net effect of the first cycle of 0.46% (cf. Table 2.5).
In agreement with the observation in the previous section, the expansion was greater for the rolled sample (3Y-roll-850), than for the layered and bar shaped samples of the same composition (3Y-layer-850 and 3Y-bar-1000) (cf. Table 2.5).

Table 2.5. Relative linear changes of samples with different ceramic component upon successive redox steps. Uncertainty on the data is ± 0.01%. Asterisk (*) indicates shrinkage values after 2 h reduction, where stabilization was not achieved. For the sample 3YA-layer-850 a second sub-column is shown. In the sub-column to the right, the values of the maximum measured shrinkage (after 28-48 h of reduction) are shown. Absence of measurements is marked with (-).

Redox	Relative linear change [%]						
step	8Y-bar-1000-a	3Y-bar-1000	3Y-roll-850	raw3Y-roll-850	3Y-layer-850	3YA-layer-850	
1st red	0.00	0.00	0.00	0.00	0.00	-0.08*	-0.40
1st ox	1.19	0.35	0.90	1.22	0.46	0.84	0.84
2nd red	-0.22	-0.08	-0.23	-0.23	-0.18	-0.08*	-0.42
2nd ox	2.44	0.70	1.43	1.83	1.17	0.80	0.80
3rd red	-0.24*	-0.01	-0.26	-	-	-	-
3rd ox	2.13	0.67	1.96	-	-	-	-
4th red	-	-	-0.53	-	-	-	-
4th ox	-	-	1.81	-	-	-	-

Shrinkage occurred in all samples during the second reduction. The maximum recorded shrinkage of the alumina-rich sample was in the same order during both the first and second reduction, and the value was at least twice the magnitude of that of other samples.
With the alumina-rich sample as an exception, the trends from the first oxidation were continued upon the second oxidation with enhanced effect. The relative expansions upon the second oxidation have increased, and as before lower expansions were measured on bars with 3Y than 8Y, and on samples prepared from pre-calcined powders.
Unlike the other samples, the alumina-rich sample displayed slightly reduced expansion upon the second oxidation. When considering the net effect of the second cycle, much less change was observed for the alumina-rich sample (0.80% - 0.42% = 0.38%) opposed to the corresponding sample without alumina (1.17% - 0.18% = 0.99%).
Bar shaped samples were subjected to a third cycle. During the third reduction, significant shrinkage was only observed in 8Y-bar-1000-a. Upon the third re-oxidation, the expansion of 8Y-bar-1000-a was reduced, and for 3Y-bar-1000 the expansion was in the same range as during the second oxidation.

Temperature

Two identical prepared samples of the type 8Y-roll were subjected to redox cycling at respectively 700°C and 1000°C. The relative linear changes observed upon each redox step are compared in Table 2.6.

Table 2.6. Relative linear changes of identical prepared samples of the type 8Y-roll upon redox cycling at 700°C and 1000°C, respectively. Uncertainty on the data is ± 0.01%. Absence of measurement is marked with (-).

Redox step	Relative linear change [%]	
	8Y-roll-700	8Y-roll-1000
1st red	-0.01	0.00
1st ox	0.99	4.95
2nd red	-0.19	-0.78
2nd ox	-	6.46

The dimensional changes were more severe for the high-temperature sample. Even if the preparation method was assumed to result in variations of the expansions of up to 100%, the expansion was much worse at the higher temperature (cf. Table 2.6).

Temperature cycling

The effect of temperature cycling was investigated by subjecting a sample to 1000°C-100°C temperature cycles in-between atmosphere changes. The dilatometry and temperature profiles of the sample 8Y-bar-1000-TC are shown in Figure 2.2.

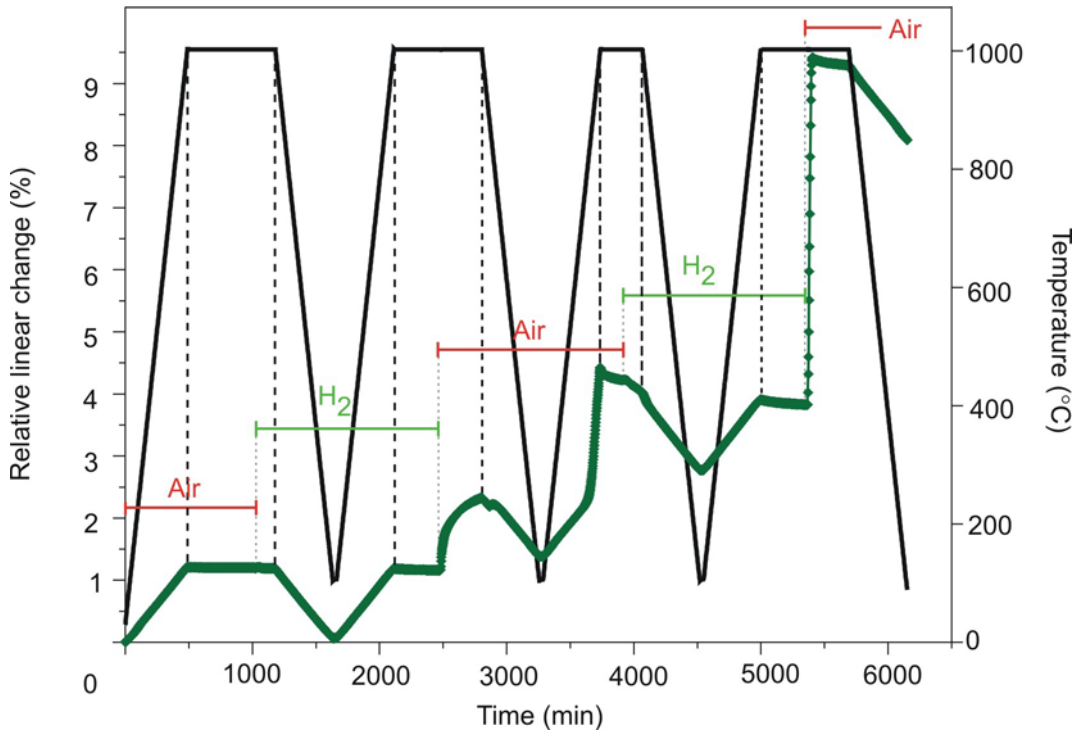

Figure 2.2. Dilatometry profile (dark green) of the sample 8Y-bar-1000-TC during combined temperature cycles (black), and changing atmospheres (reducing periods marked "H_2" and oxidizing marked "Air").

Upon the first re-oxidation, stabilization appeared not to be achieved before the following temperature cycle was finished. During re-heating an enhanced expansion was seen, that ended after 1000°C was reached again (cf. Figure 2.2).
The linear dimensional changes upon the single redox steps for the temperature cycled sample (8Y-bar-1000-TC) were included in Table 2.3. The table contained information on similar, but not temperature cycled samples. The sample 8Y-bar-1000-a was a "twin" to 8Y-bar-1000-TC, i.e. they originated from the same pressed sample. When comparing the two twin samples temperature cycling seems to have a detrimental effect on the dimensional changes associated with oxidations. The expansions were more than a factor of two higher for the sample subjected to temperature cycling.

The calculated thermal expansion coefficient (TEC) of the different states is listed in Table 2.7. When possible, the average of the heating and cooling ramp was applied for the calculations. TEC data from literature of the individual phases are included in the table.
The measured TEC values were within the range of the values reported in the literature [30, 31, 32]. From the measurements it was indicated that reduction has little influence on the TEC. Similar values were seen for the as-sintered and the first reduced state, and for the second reduced and second oxidized state (cf. Table 2.7).

However, when the values before and after redox cycling were compared (i.e. when the as-sintered was compared to the second oxidized state, and the first reduced state compared to the second reduced state), the TEC appeared to have increased upon redox cycling.

Table 2.7. Measured TEC values of the sample 8Y-bar-1000-TC, and TEC values of the individual phases reported in the literature [33].

Material	State	Temperature range [°C]	TEC [10^{-6} K^{-1}]
8Y-bar	As-sintered	30-1000	12.4
8Y-bar	2nd oxidized	100-1000	13.2
8Y-bar	1st reduced	100-1000	12.5
8Y-bar	2nd reduced	100-1000	13.3
8YSZ	-	50-1000	10.3
NiO	-	50-1000	14.1
Ni	-	50-1000	16.9

2.3.2 Macro- and microstructural observations

From SEM images it was qualitatively verified that the applied shaping techniques resulted in different as-sintered porosities. Examples of SEM micrographs of polished as-sintered samples of bar shape, layer, and roll are shown in Figure 2.3. The micrographs are backscatter electron images (BSE). Pores appear black. The lighter phase is YSZ, and the darker phase is NiO.

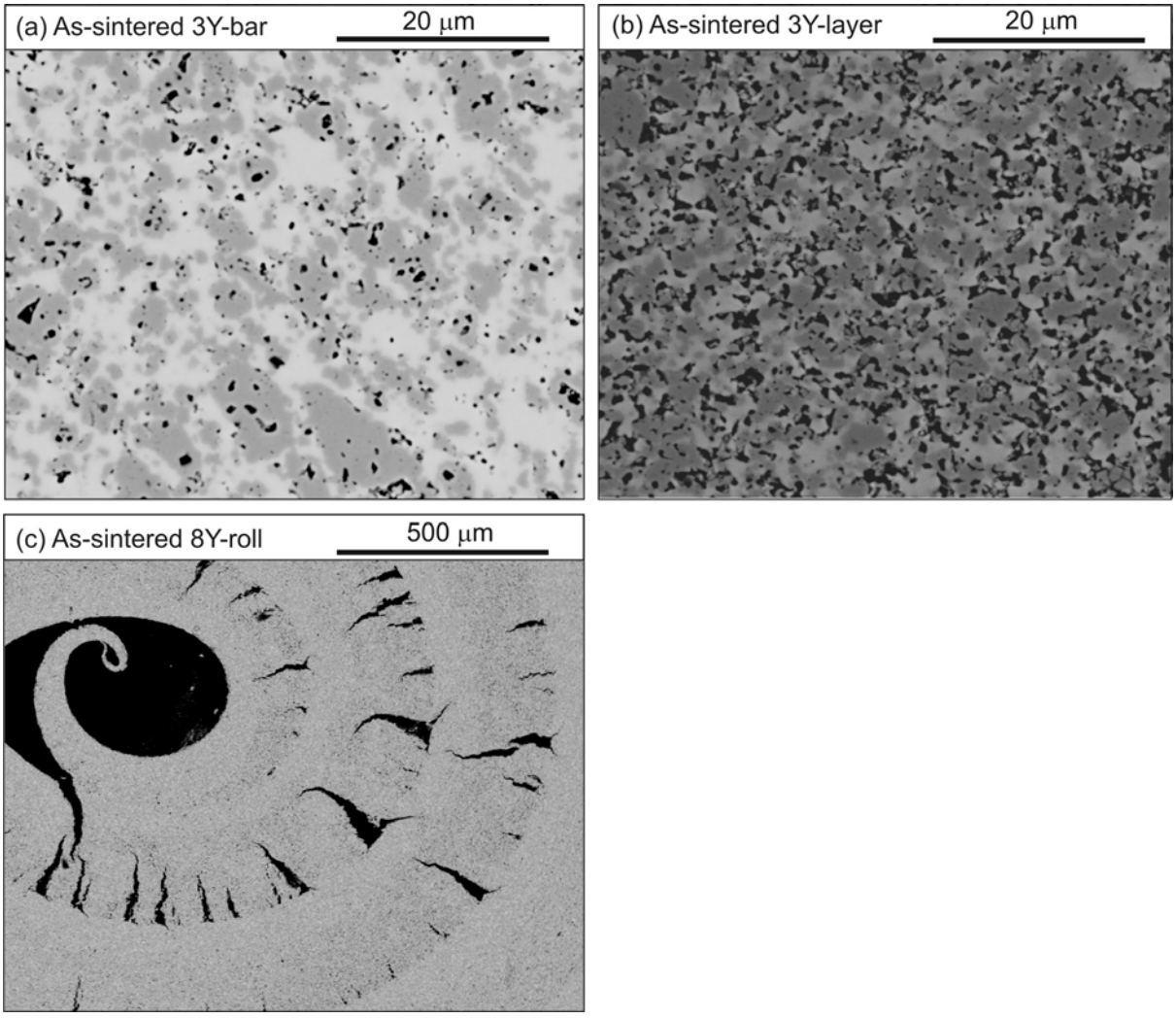

Figure 2.3. SEM-BSE micrographs of polished as-sintered samples. (a) 3Y-bar. (b) 3Y-layer. (c) 8Y-roll.

The bars were observed to be less porous than the layered samples (cf. Figures 2.3a and b). The layered samples were again less porous than the rolls, despite both sample types originated from the same green tape cast material. The roll shaped samples appeared to become damaged during preparation. Relatively big micro cracks were seen associated with the surface under tension upon rolling (cf. Figure 2.3c). The damage introduced during preparation was believed to account for enhanced porosity of the rolls.

The porosity of the samples, as quantified by weighing and geometric gauging (ε_{geom}), Archimedes' method (ε_{arch}), and mercury porosimetry (ε_{Hg}), are listed in Table 2.8.

Table 2.8. Porosity of the samples in the as-sintered, reduced, and re-oxidized state. The porosities have been estimated by weighing and geometric gauging (ε_{geom}), by Archimedes' method (ε_{arch}), and by mercury porosimetry (ε_{Hg}). Absence of measurement is marked with (-).

State	Method	Porosity [%]						
		8Y-bar	8Y-layer	3Y-bar	3Y-layer	3Y-roll	3YA-layer	3YA-roll
As-sintered	ε_{geom}	1.5±2.3	12.3±6.0	7.5±1.0	17.0±4.2	-	-	-
	ε_{arch}	0.5±1.0	4.4±1.0	5.9±1.0	14.9±1.0	-	-	-
	ε_{Hg}	-	-	-	17.1±1.0	15.0±1.0	13.7±1.0	17.9±1.0
Reduced	ε_{geom}	23.8±1.5	28.3±1.3	27.8±0.8	35.5±1.2	-	-	-
	ε_{arch}	17.1±1.0	27.3±1.0	25.6±1.0	33.0±1.0	-	-	-
	ε_{Hg}	18.0±1.0	-	23.9±1.0	-	-	-	-
Re-oxidized	ε_{geom}	12.7±0.7	-	18.0±0.9	28.6±3.3	-	-	-
	ε_{arch}	3.7±1.0	19.9±1.0	11.8±1.0	12.4±1.0	-	-	-
	ε_{Hg}	-	10.1±1.0	-	-	-	-	-

The microscopic visible lower porosity of the as-sintered bars compared to layers was confirmed. However, the as-sintered rolls did generally not display higher porosity than the layers (cf. Table 2.8), as was observed in the micrographs.
For porosity information on the rolls, mercury porosimetry was only applied. The method is known to be more appropriate for detection of small to intermediate sized pores. Porosities above ca. 100 μm are difficult to detect, like for instance the defects introduced upon rolling. Thus, the similarity in the measured as-sintered porosity between rolled and layered samples is ascribed to the test method.
The porosity increased significantly upon reduction for all samples and methods. When re-oxidized, the porosity was reduced again. However, the porosity did not reduce to the as-sintered state porosity (cf. Table 2.8).

Redox cycles were observed to give rise to macroscopic visible cracks. Figure 2.4 illustrates samples subjected to three redox cycles. The macro cracks observed in 3Y-bar-1000 were few and shallow (cf. Figure 2.4a). In contrast, severe cracking were seen in the 8Y-bars and rolled samples (cf. Figure 2.4b, 2.4c), and delamination was seen in the layered samples (cf. Figure 2.4d).

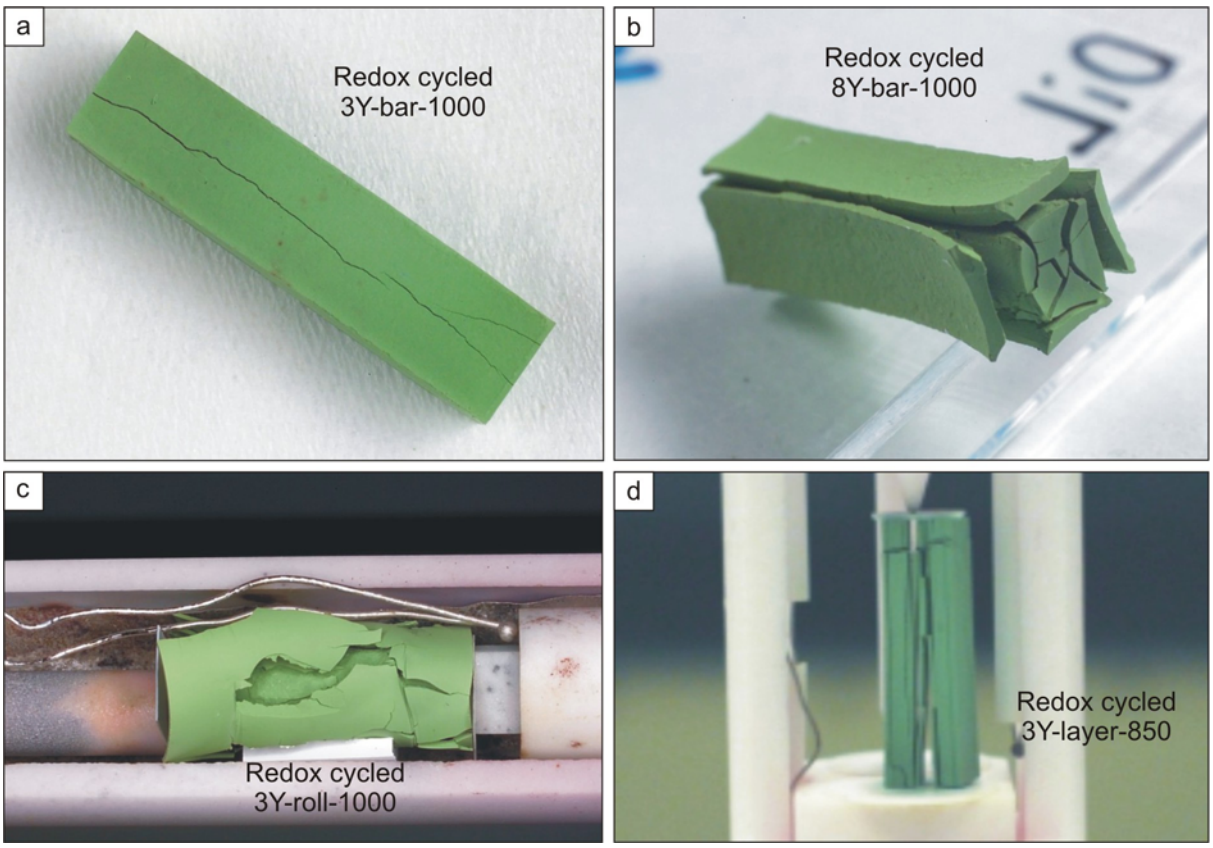

Figure 2.4. Samples subjected to three redox cycles. (a) 3Y-bar-1000. (b) 8Y-bar-1000. (c) 8Y-roll-1000. (d) 3Y-layer-850.

The microstructural effects of redox cycling were investigated with SEM. As examples, SEM backscatter images of the sample 8Y-bar-1000 in the as-sintered and redox cycled states are shown in Figure 2.5. The YSZ appeared as the lighter phase, NiO as the darker phase, and pores appeared as black.
Increased porosity with the number of redox cycles was generally observed. This was consistent with the porosity measurements (cf. Table 2.8). From the images, it was also evident that the YSZ phase appeared less coherent upon redox cycling. Actual micro cracks were rarely seen, although a few was identified, and are indicated by arrows in Figure 2.5c. The failures in the re-oxidized states appeared predominantly open and wide.

The phases present in the alumina-rich sample (3YA-layer) were investigated by XRD. In the as-sintered state, traces of the spinel phase ($NiAl_2O_4$) were evident, as reported in the literature [34]. SEM investigations also indicated the presence of a fine-grained Ni-Al-phase (not shown here) in the samples [35]. Upon reduction of the sample, it was not possible to detect any alumina phases by XRD, however from thermodynamics it is believed that the spinel will reduce into Ni and Al_2O_3.
The apparent disappearance of Al phases in the diffractogram upon reduction may be explained by the lower atomic number of aluminum compared to nickel and zirconium, and the small grain sizes. The strongest peak from the observed Al containing phase was only 5% compared to the strongest peak of the other phases.

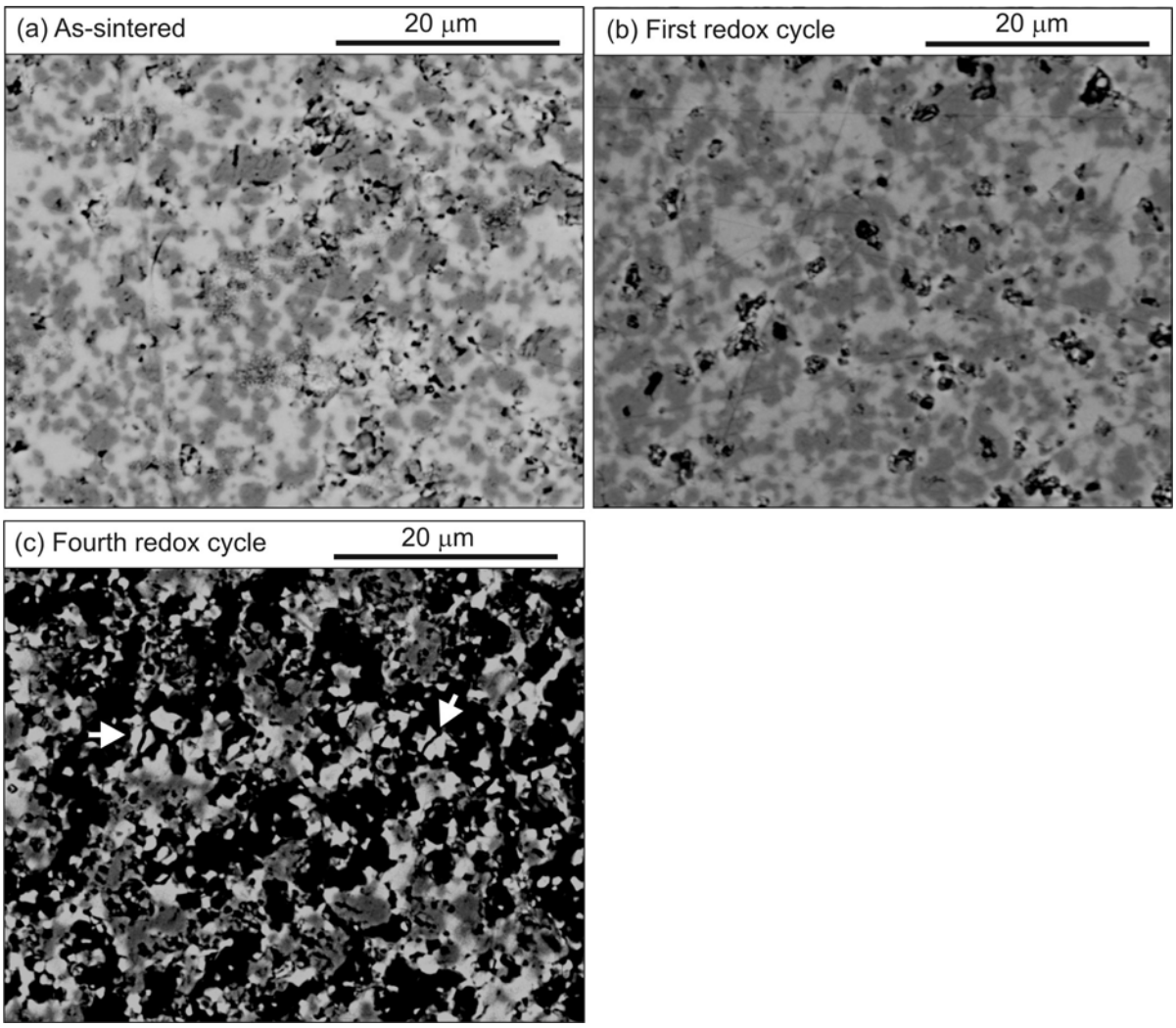

Figure 2.5. SEM-BSE micrographs of the sample 8Y-bar-1000 in the as-sintered and redox cycled states. (a) Sintered. (b) After the first redox cycle. (c) After the fourth redox cycle. The white arrows point to well-defined micro cracks.

2.4 Discussion

Based on the experimental observations, a model illustrating the redox processes has been developed. The model is shown in Figure 2.6. The processes are illustrated for the 2-dimensional structure shown in Figure 2.6a consisting of uni-sized particles.
Figure 2.6a represents the as-sintered structure, and pink circles represent YSZ particles, green circles represent NiO particles, and the interstices are porosity. In accordance with the SEM images of the sintered structures (cf. Figure 2.3), the model cermet in the as-sintered state is relatively dense, and consists of percolating networks of YSZ and NiO.

Upon reduction, the phase change of NiO to Ni occurs and implies a 25% volume reduction of the nickel phase [3]. Thus, reduction is bound to introduce decreased nickel particle sizes and reorganization of the phase. The changes in the nickel phase are illustrated in Figure 2.6b. The reduced nickel particles are represented with gray color. However, the YSZ phase is believed unaffected by the first reduction process as illustrated by an unchanged YSZ particle network in Figure 2.6b.
The generally observed lack of dimensional change upon the first reduction (cf. Tables 2.3-2.6), is explained by the stable YSZ network. From the porosity data of the reduced samples (cf. Table

2.8) it is also indicated, that the reduction is accommodated by increased porosity within the structure, and no markedly shrinkage. It was however indicated that the porous network is not insensitive to heat treatment at 1000°C, but appeared subjected to creep (cf. Section 2.3.1).

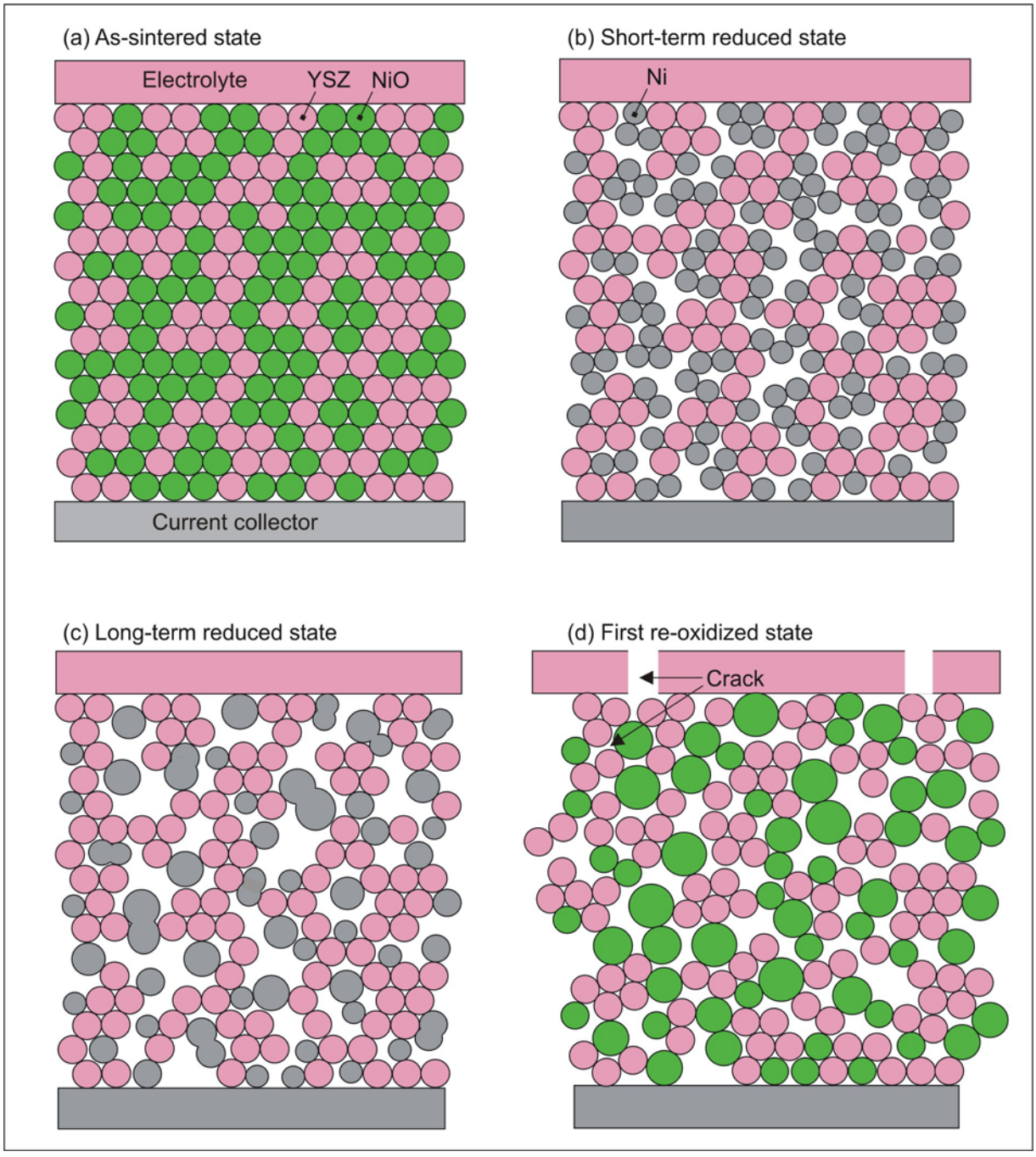

Figure 2.6. Cartoon illustrating the microstructural changes in the nickel-YSZ cermet upon the different redox steps. Pink particles represent YSZ, and green and gray particles represent respectively NiO and Ni. (a) As-sintered state. (b) Short-term reduced state. (c) Long-term reduced state. (d) First re-oxidized state. The two arrows point to a crack in the electrolyte and a failure in the ceramic network in the cermet, respectively.

As an exception, a considerable shrinkage was observed in the alumina-rich sample (3YA-layer-850) upon the first reduction (cf. Table 2.5). The exceptional case may be explained by the presence of the spinel phase ($NiAl_2O_4$) in the as-sintered state (cf. Section 2.3.2). If all of the alumina is assumed to react as seen by Kesler and Landingham [34], 13 wt% of the NiO will be in the form of spinel. If the spinel phase in the as-sintered state of the structure, is a part of the

ceramic network, decomposition of the oxide structure during reduction, can explain the observed shrinkages. The much slower stabilization time observed for nickel reductions of the alumina-rich sample may reflect slower kinetics for the spinel phase (cf. Section 2.3.2).
Reorganization of the Ni network will continue after the initial reduction due to sintering [10, 11, 36, 37, 38, 39, 40, 41, 42]. Sintering is known to intensify with increased porosity and temperature. In Figure 6c, Ni sintering is illustrated by increased particle sizes and coalescence of grains.

When re-oxidized, the nickel phase will expand back to the as-sintered volume (corresponding to a phase volume expansion of 33%). However, the structural changes while in the reduced state, results in a different oxidized volume structure. The changed NiO network is believed to induce local tensile stresses in the YSZ network that in some places causes failure. The local failures in the network then allows for the observed bulk expansion and increased porosity. This again will give rise to cracks in the electrolyte. The processes are illustrated in Figure 2.6d.

The model implies that the damage depends on the ceramic network strength, and the degree of Ni redistribution. Lower bulk expansions upon the first re-oxidation were indeed observed for cermets with improved mechanical properties due to the yttria content or pre-calcination of the powder (cf. Section 2.3.1). Lower bulk expansions upon the first re-oxidation were also seen for samples with lower porosity (cf. Sections 2.3.1 and 2.3.2), and lower bulk expansion was suggested for samples tested at lower temperature (cf. Section 2.3.1).

However, from the reproducibility study on the sample type 8Y-bar-1000 (cf. Section 2.3.1), the dilatometer measurements were seen to be sensitive to minor variations in microstructure. For identically prepared bar shaped samples, a minor variation of 5% upon the first oxidation were seen. During the second oxidation, the variation between samples increased to a factor of 2. The variation is believed to reflect the stochastic nature of the Ni redistribution process, and the fracture mechanism. The increase in variation upon the second oxidation may be explained by the increased porosity.
Thus, the relatively dense bar shapes are predicted to display smaller variations compared to the more porous geometries. Measurements on rolls were used for investigating the effect of test temperature, and pre-calcination of the powder (cf. Section 2.3.1). Considering this, the conclusions regarding these are to be taken tentatively.
Also, the effect of porosity was based on comparisons with rolls, and is to be taken tentatively (cf. Section 2.3.1). In addition, rolls are believed to have reduced strength due to the higher porosity and deformation introduced during the green state shaping. Thus, when comparing rolls with other shapes, the difference in strength becomes a second variable.

If temperature cycling is believed to weaken the ceramic part of the cermet structure, the model predicts enhanced expansion for a temperature cycled sample upon redox cycling. From the change in the TEC values upon redox cycling (cf. Section 2.3.1) it was indicated that the YSZ network was damaged, and the nickel network became increasingly influential due to temperature cycling. In accordance, increased expansion for a temperature cycled sample was observed.

Upon following redox cycles, the steps illustrated in Figure 2.6 are repeated. In accordance with observations, reduction now implies shrinkage in all cases, as the YSZ network is partly disconnected (cf. Section 2.3.1).
The increased porosity created during the first re-oxidation will promote increased Ni reorganization and enhanced bulk expansion. Enhanced dimensional changes upon the second cycle were also observed in most cases (cf. Section 2.3.1). However, considering an uncertainty from sample preparation above 50%, the tendency is only suggested in few cases.

As the structure becomes increasingly porous and fragmented with the number of redox cycles, and Ni sintering diminishes, the microstructural changes are expected to accommodate within the structure, and bulk expansion to decrease. Ignoring the uncertainty from sample preparations, indications of diminished bulk expansion were seen during the third cycle (cf. Table 2.4). From Table 2.4 it was indicated that the effect first appeared in the high-temperature tested samples (8Y-roll-1000 and 8Y-bar-1000-a) that expanded the most during the first and second cycle. In accordance with the model, it is expected that the effect first occurs in the samples with accelerated degradation processes.

The effect of adding alumina to the ceramic phase was ambiguous, and the impact on the strength complex. Due to formation and dissociation of a nickel alumina spinel, large dimensional changes were associated with the single reduction and re-oxidation steps (cf. Table 2.5). Thus, the phase change is expected to reduce the strength of the ceramic network. However, when the net effect of the first cycle was considered, the performance of the alumina-rich sample was not worse. From this it appeared that the spinel related dimensional changes are reversible, and do not promote significant weakening of the structure. In addition, indications of the alumina-rich sample performing better upon the second cycle were seen.

2.5 Conclusions

The redox behavior of nickel-YSZ anode materials with variable sample geometry and ceramic component was examined. From this, the effect of porosity, ceramic strength, temperature, and temperature cycling was investigated. The conclusions are:

- Dilatometry is an appropriate method for investigating the bulk redox behavior. However, for redox cycles following the first cycle, the stochastic nature of nickel redistribution and ceramic failure may introduce large variations in the data.

- Improved mechanical properties of the ceramic cermet component result in less bulk changes upon redox cycling.

- Higher as-sintered cermet porosity resulted in larger bulk changes upon redox cycling. This is a combined effect of the porosity, and the lower strength. The effect of the porosity alone could not be deduced.

- Temperature cycling was indicated to weaken the ceramic structure.

- The temperature at which redox cycling was carried out was indicated to be important. Less damage on the ceramic structure was suggested at lower temperatures.

- The key parameters for achieving redox stable anodes appeared to be the ceramic network strength, and the degree of restriction of the Ni particle relocation and coarsening.

- The redox mechanism is believed to be characterized by nickel redistribution in the reduced state that prevents reversion to the as-sintered structure when re-oxidized. Instead, the redistributed nickel phase promotes damage on the ceramic cermet component, and the electrolyte, upon re-oxidation.

- The damage is believed to increase upon the first successive redox cycles. However, it was suggested to diminish after a number of cycles. Thus, the first redox cycles are believed to be more critical.

Acknowledgement

H. Z. Stummann (Haldor Topsøe A/S) is acknowledged for technical support on the dilatometer. F. W. Poulsen (Risø National Laboratory) is acknowledged for help and discussion of the XRD data. Y. L. Liu (Risø National Laboratory) is acknowledged for the SEM analyses of the alumina-rich sample.

3 Microstructural characteristics of nickel-YSZ cermets

3.1 Introduction

The nickel-YSZ anode performance is known to degrade when subjected to redox cycling [8, 19, 23, 43], and to degrade over time when operated [10, 36, 44, 45]. The degradations are attributed to changes on the microstructural level. However, the changes in the microstructure are to a wide degree only qualitatively described in the literature.
Upon reduction, the wetting properties between nickel and YSZ change significantly. The poor wettability between the metal and the YSZ provides a driving force for nickel redistribution and sintering. However, observation and quantification of the changes have been restricted by difficulties in characterizing the fine and complex cermet structure, and in separating the three phases present (Ni, YSZ, and pores).
When applying light microscopy the high backscattering from the Ni phase prevents separation between pores and YSZ. With scanning electron microscopy (SEM), the similar backscatter coefficients of Ni and YSZ only allow the solids to be distinguished from the pores. In addition, the microscopy based investigations are restricted to polished cross sections to obtain sufficient contrast between the phases. From quantitative stereology extrapolation from two-dimensional data to three-dimensional is known possible, and e.g. equality of volume fraction and area fraction is proved to exist [46]. However, the three-dimensional structure (e.g. grain shapes and network extension) are not seen in polished sections. Thus, in some cases only the porosity [47, 48], or the Ni phase [42] was examined with microscopy, or a combination of light microscopy and SEM was applied to investigate all phases [49, 50].
Simwonis et al. [10] reported of a method where the three phases were separated using light microscopy. The method involved coating of the sample with a thin interference film of Fe_2O_3. However, the coating process has been stated to be difficult to control [51], and the optically based microscopy provides a relatively poor lower grain size resolution of 0.35 μm [10]. Lee et al. [51] have reported of a method based on SEM, followed by image development, where the three phases are separable.
Coarsening of the Ni particles upon ageing under reducing conditions were quantified by Simwonis et al. [10], and Vassen et al. [42]. However, long operation times are believed to be required for measuring the changes in the complex microstructure. After 4000 hours of exposure, an increase in the average Ni diameter from ca. 2 μm to 2.6 μm [10], or from 1 μm to ca. 1.24 μm [42] has been measured. A tendency to more rounded Ni particles, and slightly coarser pores was also observed [10]. The references proposed models for the particle size increase as a function of time. However, the model was either very simple and based on a 2-particle model [42], or requiring material specific experimental data [10].

Re-oxidations are bound to imply nickel particle swelling. This occurs because of the higher volume of the oxide formed compared to the metal (a factor of 1.7), and due to the oxide growth taking place on the external oxide surface, as the nickel oxide layer has prevailing cationic transport properties [52].
When expanding particles come into contact, further growth is stopped, and the surfaces will adapt their shape to each other. However, the interaction of adjacent surfaces is complexly related to the rate of the oxidation process (determined by temperature and partial pressure of oxygen), and the size and shape of the contacting grains [52].
Re-oxidized Ni-YSZ cermets have been examined in SEM, and they displayed a homogeneous increase in the microstructural porosity [9, 53, 54]. Fouquet et al. [8] reported that re-oxidized NiO grains appeared finer and more porous than in the as-sintered state, and that micro cracks

were introduced into the YSZ matrix. Macro cracks visible to the naked eye have also been observed upon re-oxidation [8, 23].

In this chapter the changes in the microstructure of nickel-YSZ cermets upon reduction, ageing, and re-oxidation, was investigated and quantified. The methods used included conventional microscopy (light microscopy and SEM), and in-situ environmental scanning electron microscopy (ESEM). The in-situ examination was done on both polished and fractured surfaces to get an impression of the development in three dimensions. Image analysis software was applied for quantification of the changes. The effect of the sample porosity and the composition of the ceramic component (yttria content), on the changes in the microstructure was examined.

3.2 Experimental

3.2.1 Sample preparation

Samples were prepared from NiO powder (99% from Alfa Aesar), alumina powder (Catapal® from Sasol), and 3 mol% yttria stabilized zirconia (3YSZ) or 8 mol% yttria stabilized zirconia powder (8YSZ) (TZ-3YB or TZ-8Y from Tosoh Co.). Two compositions, with similar NiO contents and variable ceramic components, were prepared. The compositions were denoted 8Y and 3Y, and the solid material contents were respectively 56.8 wt% NiO, 43.2 wt% 8YSZ for 8Y, and 55.7 wt% NiO, 43.7 wt% 3YSZ, 0.6 wt% Al_2O_3 for 3Y.
The powders were processed into slurries that subsequently were tape cast into thin foils. Part of the green foils was heat treated to burn out of the binder, and the resulting powder was pressed (uniaxial followed by isostatic pressing at 80 MPa) into bar shaped samples. The green foils and bars were sintered at 1300°C.
Some of the sintered samples were subsequently completely reduced at 1000°C with 9 vol% H_2 in N_2 for 1 or 96 hours. Some of the samples were further oxidized at 1000°C in air for 1 hour.
Except for the sample investigated in ESEM, all samples were cast into epoxy resin before polishing, and the polished cross-section investigated by microscopy. With ESEM, both a polished and fractured surface was examined.
The samples were named after the oxidation state (s = sintered, r = reduced, ro = re-oxidized), composition (3Y, 8Y), and sample shape (bar, strip). For example a sintered bar of 3Y composition was denoted s-3Y-bar.

3.2.2 Experimental procedure

A Leitz Aristomet optical microscope was applied for examining reduced samples containing metallic nickel. For SEM imaging, a Fei Quanta 600 equipped with EDAX® thin window detector and EDAX Genesis software was used. A thin silver coating (10 nm) was applied to the samples to minimize charging effects.
The ESEM instrument was of the type Philips XL30 ESEM-FEG. Redox cycling was carried out at temperatures up to 800°C, and with total gas pressures around 5-10 mbar. Reductions were done with 9 vol% H_2-Ar, and oxidations with air. N_2 was used as purge gas. Three temperature steps, and two redox cycles were performed. First, the sintered sample was heated in 9 vol% H_2-Ar to 800°C for two hours (the first reduction). After purging the chamber, air was introduced for one hour (first oxidation), and the sample was then cooled in air to room temperature. The sample was once again heated in 9 vol% H_2-Ar to 800°C, this time for four hours (second reduction), and cooled to room temperature, still in 9 vol% H_2-Ar. Finally, the sample was

heated slowly to 800°C in air. The sample was exposed to the air for ca. four hours (second oxidation).
The microstructures were analyzed with the image analysis software Image Pro-Plus 4.0 (Media Cybernetics). For SEM image analyses 10-28 representative images of a sample were analyzed. Each image covered an area of 46 µm x 52 µm. For light microscope image analyses, 15-18 images (each covering 33 µm x 45 µm) of a sample were analyzed. The resolution is lower for light microscopes (ca. 0.2 µm) than for SEM (1-50 nm) [29]. Based on a qualitative estimation of the resolution of the applied light microscope and software, identified particles below 0.45 µm in diameter were manually screened out.
X-ray powder diffraction (XRD) was applied for identification of the phases present in the samples. A Stoe Bragg-Brentano diffractometer with Cu-K_α x-ray as radiation source was used.
For analysis of particle size distribution (PSD) light scattering particle sizing (also known as laser diffraction) was used. A Beckman Coulter LS 13 320 instrument, with a measurement range of 0.04-2000 µm was applied [55].
Sample porosity was quantified by weighing and geometrical gauging. The procedures were as described in Chapter 2, Section 2.2.2.

3.3 Results

3.3.1 Characterization of the samples

Phases

Diffractograms of the solid, as-sintered bars are shown in Figure 3.1.

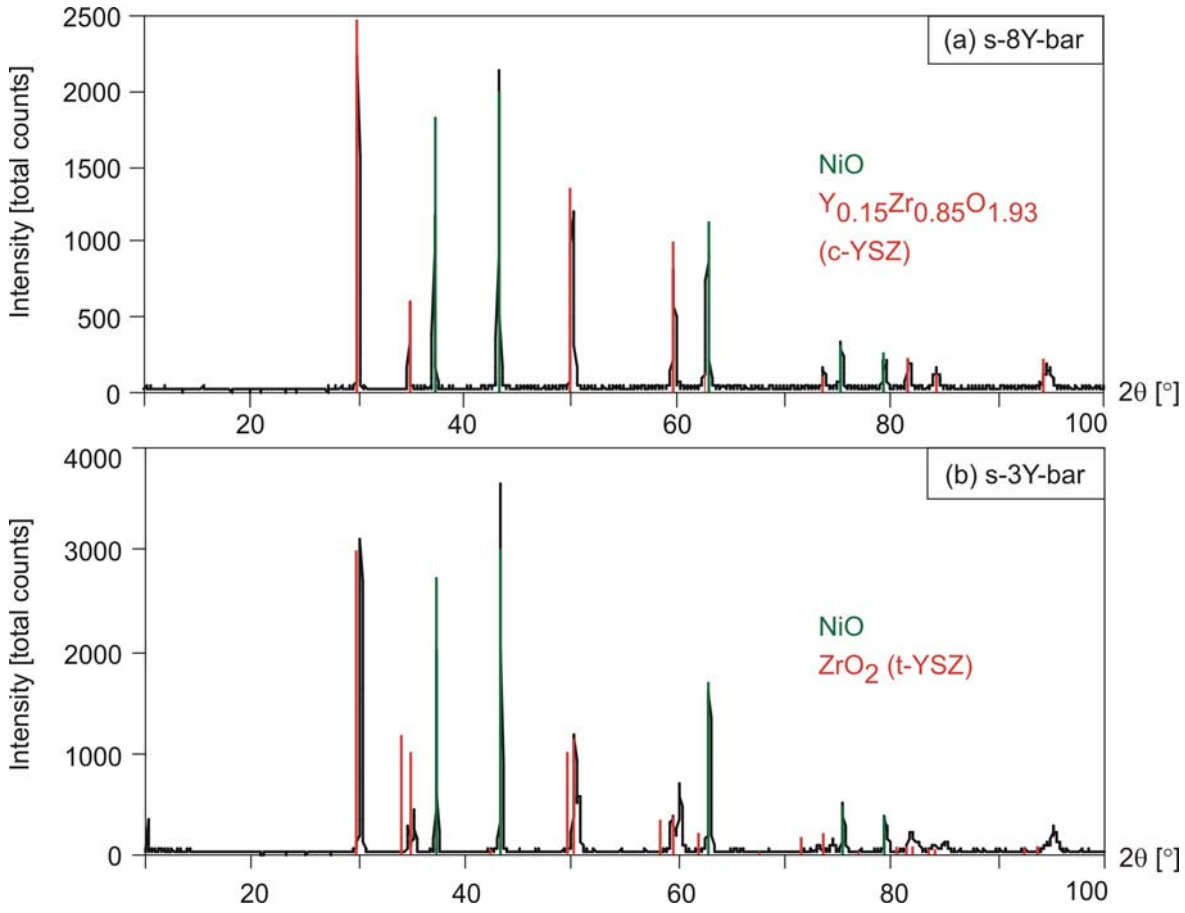

Figure 3.1. X-ray diffractograms of (a) s-8Y-bar, and (b) s-3Y-bar. Peaks corresponding to NiO (green), cubic YSZ (c-YSZ), and tetragonal YSZ (t-YSZ) (red) are indicated.

The analyses were performed on solids in the as-sintered, reduced, and re-oxidized state. Crushing of the sintered samples was observed to affect the zirconia phase.
The phases present in s-8Y-bar (cf. Figure 3.1a) were determined to be NiO and cubic yttria stabilized zirconia (c-YSZ), corresponding to $Y_{0.15}Zr_{0.85}O_{1.93}$ in the software database. The cubic lattice parameter was by Werner refinement determined to 5.1396 ± 0.0005 Å.
The phases present in s-3Y-bar (cf. Figure 3.1b) were determined to be NiO and tetragonal yttria stabilized zirconia (t-YSZ). The software database did not contain t-YSZ. Thus, ZrO_2 that is known to have similar peaks, was used for identification. The peak displacements observed were ascribed to this discrepancy. The tetragonal parameters were by Werner lattice refinement determined to c = 5.1704 ± 0.0007 Å, and a = b = 3.6084 ± 0.0004 Å.
Complete reduction after treatment in reducing atmosphere was confirmed by replacement of the NiO peaks by Ni peaks in the diffractograms. Complete re-oxidation of the nickel was also confirmed by x-ray diffraction for samples subjected to re-oxidization.

Particle size distribution of starting materials

The particle size distribution of the slurries for tape casting, and the powders for pressing was analyzed by light scattering particle sizing. It was possible to analyze the mixtures of NiO and YSZ particles, as the refractive index (RI) of the two phases is similar. For NiO it is 2.1818, and RI for ZrO_2 is in the range 2.19-2.20 [56]. The uncertainty of the instrument was qualitatively observed to be 0.3 μm on the 50% quantile (D_{50}). The D_{50} is the particle diameter under which 50 vol% of the particles are found. The measured D_{50} are shown in Figure 3.2.

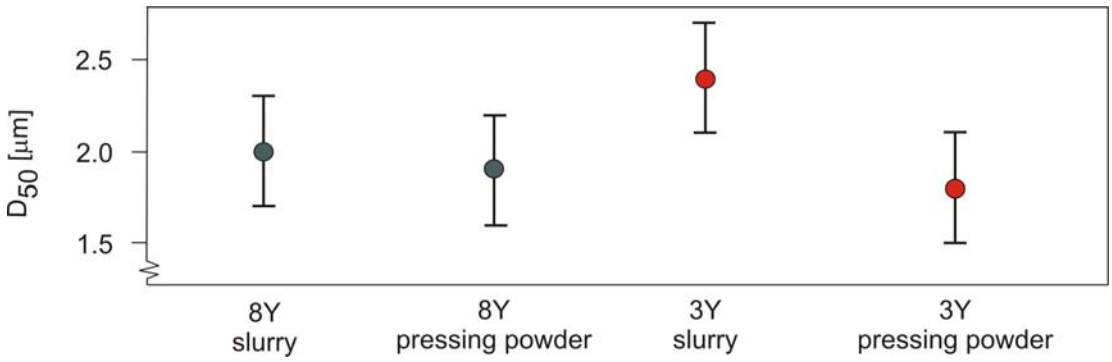

Figure 3.2. D_{50} of the slurries for tape casting, and the powders for pressing. The uncertainty on the measurements is indicated by error bars.

Considering the uncertainty, all samples displayed a D_{50} around 2 μm. In addition, the particle size distributions were uni-modal in all cases. Thus, the starting materials appeared similar, and no significant change in the particle size distribution was observed after processing to pressing powder.

Reproducibility

To estimate the reproducibility of the sample microstructure, several samples of each type were produced. The samples were visually inspected, and the density and porosity calculated based on geometrical gauging and theoretical sample composition. The calculated data on the samples are listed in Table 3.1.
The density of the as-sintered bars was markedly higher than the corresponding strips. This was also reflected in the lower porosity of the bars (cf. Table 3.1).
Upon reduction and re-oxidation, all sample types displayed a similar variation in average density and porosity. As example, the variation is illustrated for 3Y-strip in Figure 3.3.

Table 3.1. Average density and porosity based on geometrical gauging. The standard deviation is included. N denotes the number of samples.

State	Parameter	8Y-bar	8Y-strip	3Y-bar	3Y-strip
As-sintered	N	41	16	39	12
	Density [g/cm^3]	6.3 ± 0.2	5.6 ± 0.4	5.9 ± 0.1	5.3 ± 0.2
	Porosity [%]	1.5 ± 2.3	12.7 ± 6.4	7.5 ± 0.9	14.7 ± 3.3
Reduced	N	10	10	14	15
	Density [g/cm^3]	5.5 ± 0.1	5.2 ± 0.1	5.2 ± 0.1	4.6 ± 0.1
	Porosity [%]	23.8 ± 1.5	28.3 ± 1.3	27.8 ± 0.8	35.5 ± 1.2
Re-oxidized	N	5	-	11	10
	Density [g/cm^3]	5.6 ± 0.1	-	5.2 ± 0.1	4.5 ± 0.2
	Porosity [%]	12.7 ± 0.7	-	18.0 ± 0.9	28.6 ± 3.3

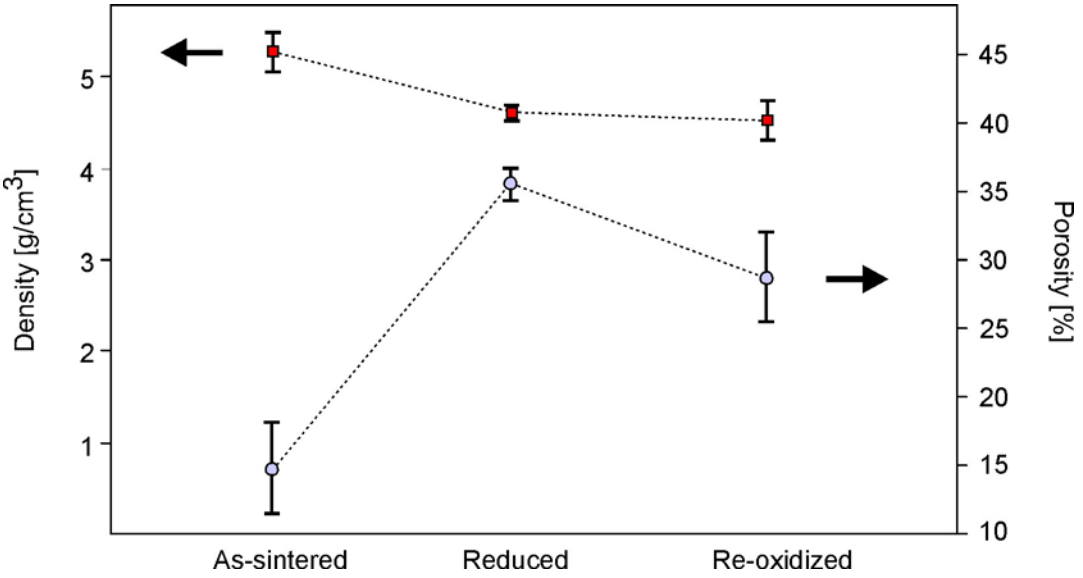

Figure 3.3. Average density (red) and porosity (blue) of samples of the type 3Y-strip in the as-sintered, reduced, and re-oxidized state. Error bars indicate the standard deviations.

Upon reduction, the density decreased, and the porosity increased correspondingly. The re-oxidized states were characterized by densities similar to the reduced states. However, the porosity was reduced, but still above the as-sintered values. This indicated that bulk expansion occurred upon re-oxidation.
The standard deviation on the porosity was observed to be relatively large, irrespective of the oxidation state. In most cases it was above 1% (cf. Table 3.1). Thus, a clear variation between the as-sintered sibling samples (i.e. identically prepared samples) appeared to be present.

The surfaces of the as-sintered samples were smooth. Upon reduction the color of the samples changed from green to dark gray. Other visible changes were not observed.
In some cases, re-oxidation caused fracturing of the bars, or cracking and warping of the strips (cf. Figure 3.4a). Five out of ten ro-8Y-bar fractured, one out of ten ro-3Y-bar fractured, and all of the ro-8Y-strips were visually damaged upon re-oxidation. The same macroscopic failure pattern occurred in the failed bars. The bars were split into a quadruple with pyramidal end-pieces as sketched in Figure 3.4b.

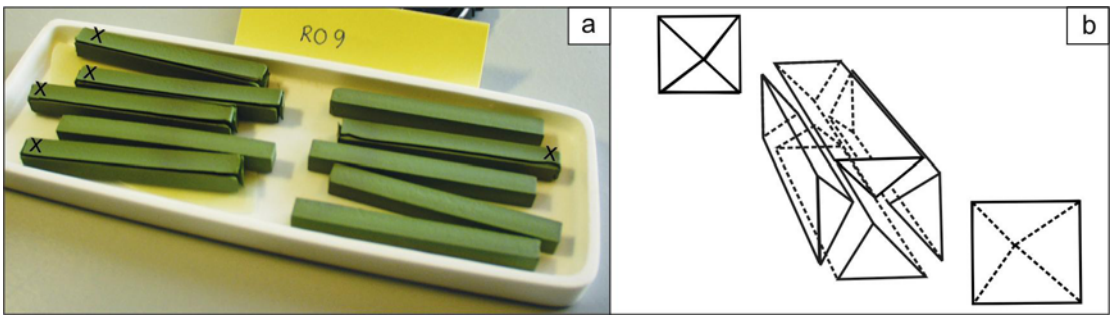

Figure 3.4. (a) Batch of ten ro-8Y-bar samples. Five of the samples were fractured, and are marked with a cross. (b) Sketch of the failure pattern observed in the fractured bar shaped samples.

3.3.2 Light microscopy

Samples subjected to reducing conditions for respectively 1 hour and 96 hours were examined with light microscope. Representative examples of micrographs of r-3Y-bar aged for 1 and 96 hours are shown in Figure 3.5.

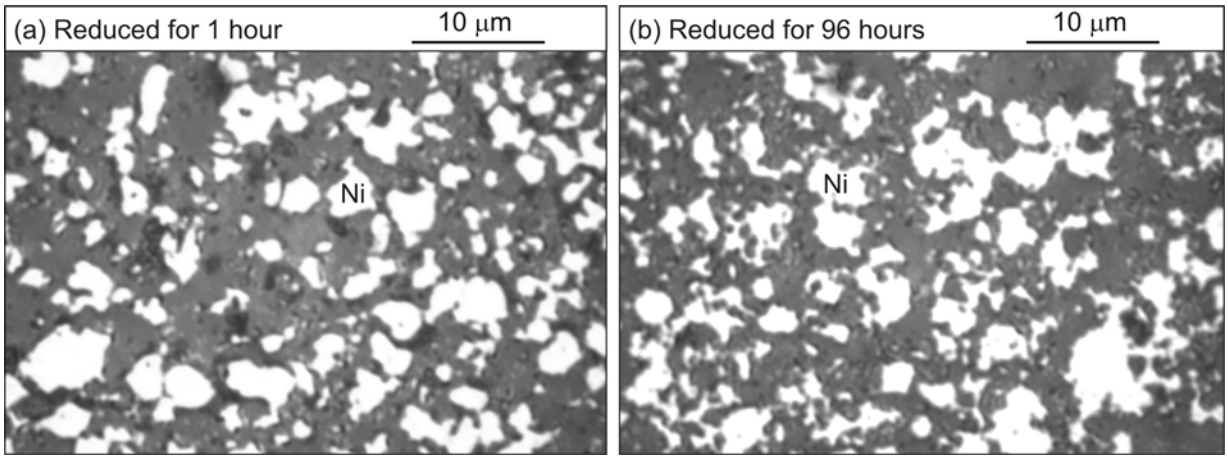

Figure 3.5. Micrographs of r-3Y-bar. (a) Aged for 1 hour. (b) Aged for 96 hours.

Metallic nickel was clearly distinguishable as the bright phase. However, no qualitative difference appeared associated with the ageing.
The micrographs of the structures were subjected to image analysis. The microstructures were characterized by grain diameter, area, and roundness of the Ni particles, as defined by the functions of the software. The grain diameter is defined as the average length of the diameters measured at 2 degrees intervals and passing through the centroid of the particle. The area is the area within the outline of an identified particle. The roundness is a measure of the shape deviation from a circle, and is calculated from the ratio between the particle perimeter and particle area. The roundness of a circle is equal to 1.
Between 1435-2530 Ni grains were identified and analyzed for each structure. The average grain diameter, area, and roundness are illustrated in Figure 3.6 for the four sample types. The standard deviations based are indicated by error bars. The specific data values are listed in Appendix B, Table B1.
The samples r-8Y-bar and r-8Y-strip display a tendency to reduced Ni grain diameter and area upon ageing. Otherwise, the ageing did not seem to have a significant effect on the analyzed parameters.

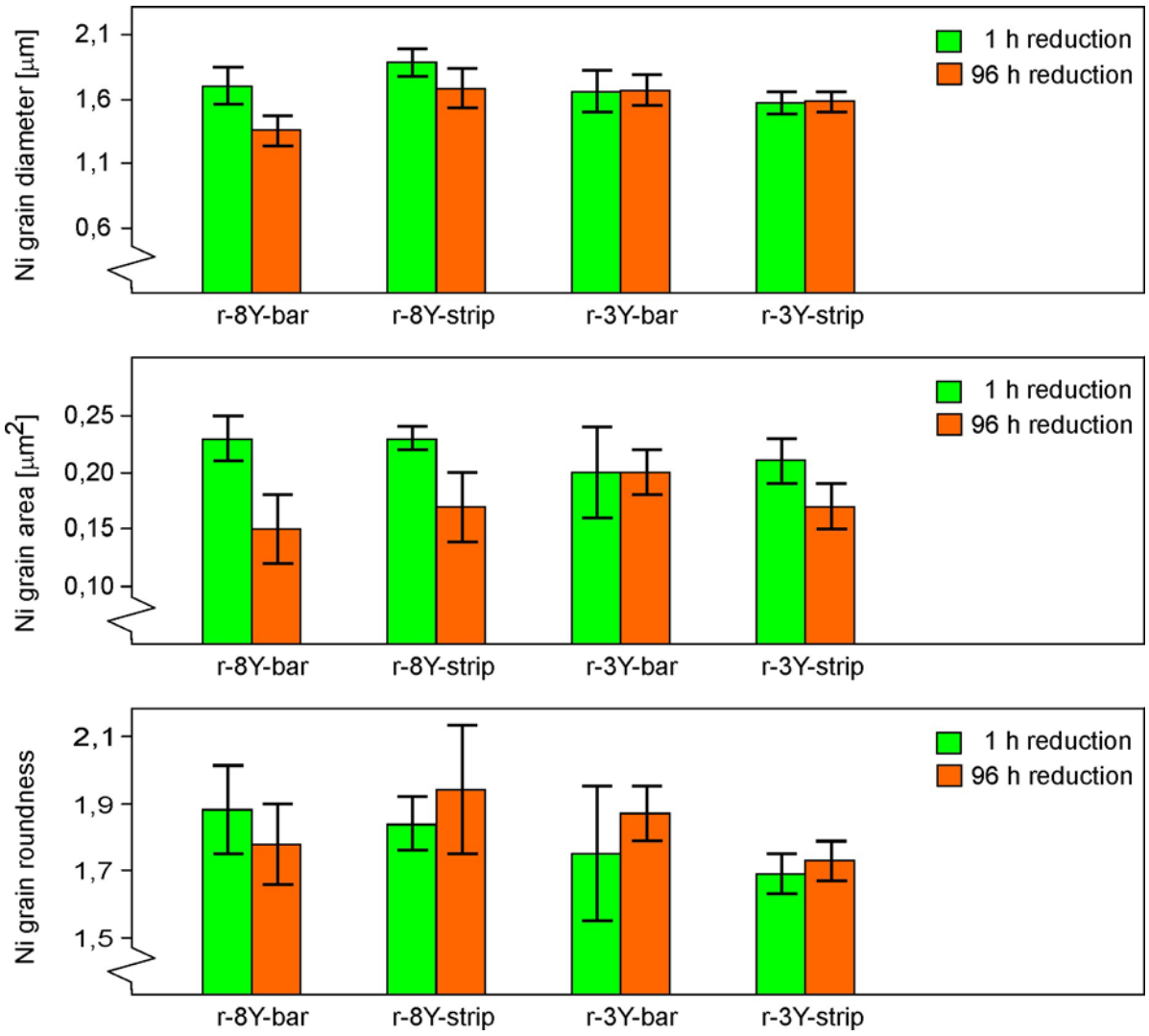

Figure 3.6. Average Ni grain diameter, area, and roundness after respectively 1 hour (green) and 96 hours (red) of reducing conditions, based on image analysis of light microscopy micrographs. Error bars indicate the standard deviations.

3.3.3 Scanning electron microscopy (SEM)

The as-sintered, reduced, and re-oxidized samples were examined with SEM. In the oxidized state, the three phases were separable. YSZ appeared as the brighter phase, NiO as the darker phase, and pores appeared black. In the reduced state it was only possible to distinguish between porosity (black) and solid phase (bright). Examples of SEM-BSE micrographs (backscatter electron images) of a polished 3Y-bar sample in the as-sintered and reduced state, and after being re-oxidized for one and four times, are shown in Figure 3.7.

The as-sintered microstructure of the bars was observed to be relatively dense, and the NiO particles appeared embedded in a matrix of YSZ (cf. Figure 3.7a). Similar microstructures were seen in strips, except for the structures being more porous. A gradation in porosity through the layer thickness of the strips, related to the casting process, was also observed.

The porosity of the samples increased visibly upon reduction (cf. Figure 3.7b). For the strips, the increase depressed the originally as-sintered porosity gradation. However, a porosity gradation developed in the denser bars. Higher porosities occurred along the rim of edge (< 200 µm) compared to the bulk. The micrograph in Figure 3.7b was from the edge of the sample.

The re-oxidized microstructures were seen to differ significantly from the as-sintered state. The structures were now more porous, and with coarser pores (cf. Figure 4.7c). Upon successive

redox cycles the development continued, resulting in coherent pore formations, and less coherent YSZ network (cf. Figure 4.7d). The porosity gradation introduced into the bars during reduction, initially remained in the re-oxidized states, but was depressed with the number of cycles as the structures became increasingly porous. No difference in microstructure was visible between samples with macro cracks, and samples that appeared intact upon re-oxidation.

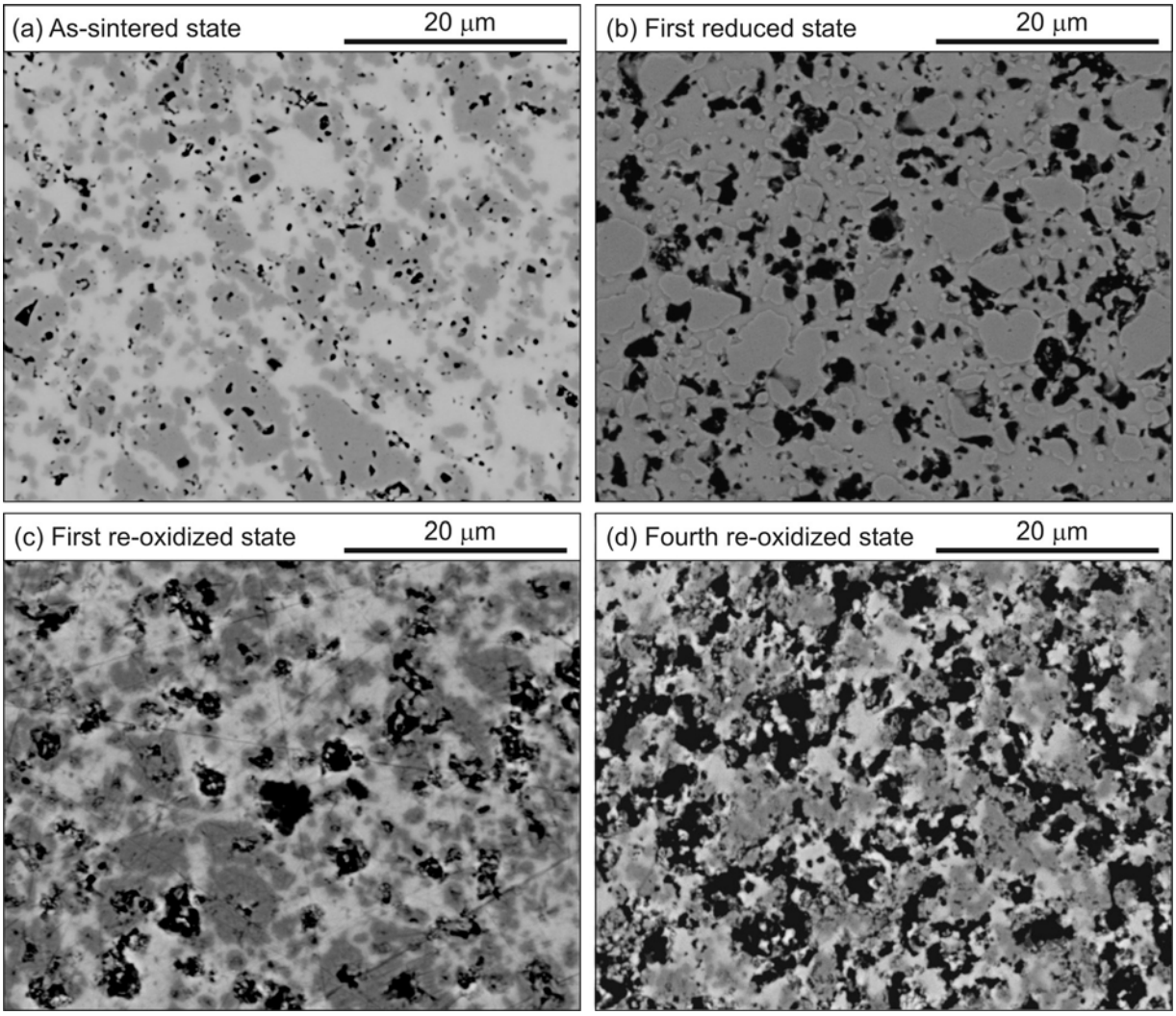

Figure 3.7. SEM-BSE micrographs of a polished 3Y-bar. The micrographs are from the edge of the sample. (a) As-sintered state. (b) First reduced state. (c) First re-oxidized state. (d) Fourth re-oxidized state.

The contrast between the phases was too low for particle characterization by applying image analysis. Removal of the noise demanded extensive manual sorting. However, image analyses were considered reasonable for analysis of the phase fractions that are less sensitive to noise on the pixel level.

Image analyses of the phase fractions as observed in SEM micrographs, resulted in large data variations. As an example, the range in the phase fractions for the three phases (pores, NiO, YSZ), for the sample 3Y-strip in different states is illustrated in Figure 3.8. Data on all the samples are listed in Appendix B, Table B2.

The large variations observed, emphasized the importance of covering a large sample area when applying image analysis. However, despite the scattering in the data, the data on the porosity supported the visually observed trends. Generally, the measured porosity increased upon reduction, and re-oxidations were seen to promote increased porosity compared to the as-sintered state.

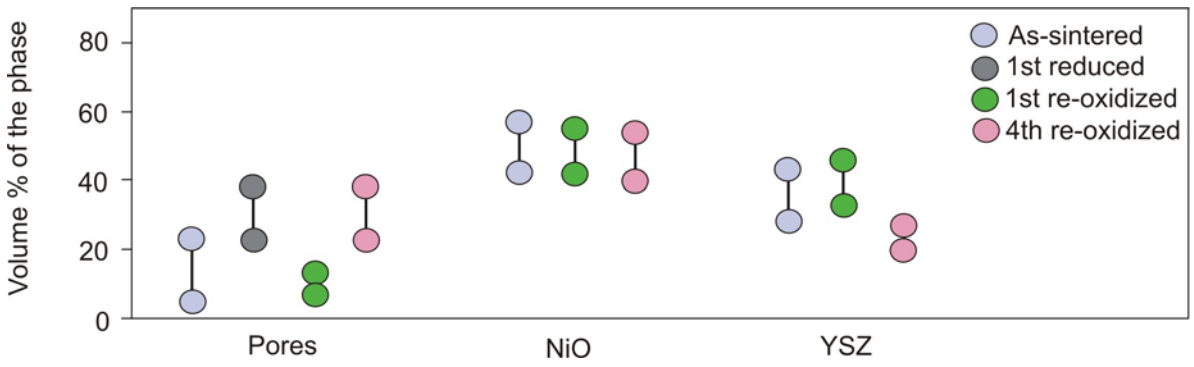

Figure 3.8. The range in phase fractions as observed with SEM-BSE micrographs and image analyses. The analyses was based on 3Y-strip samples in the as-sintered, first reduced, first re-oxidized, and fourth re-oxidized state.

3.3.4 Environmental scanning electron microscopy (ESEM)

By applying ESEM it was possible to follow individual particles in-situ during redox cycling. The imaging was done with a GSE (gaseous secondary electron) detector. Figure 3.9 illustrates the same sample area of a polished 3Y-bar, while being subjected to the first redox step. During the redox cycling, the nickel grains changed in size and shape, and were seperable from the YSZ, which appeared unaffected. The phases were further verified with the SEM EDX (energy dispersive x-ray) detector. Three nickel particles are singled out, and indicated A, B, and C in the figure.

In the as-sintered state, the individual nickel grains were difficult to discern (cf. Figure 3.9a). However, when the first reduction was started, the outline of the grains appeared within minutes, as the nickel particles shrunk in size. The nickel grains reduced further in size and became increasingly rounded as the reducing conditions proceeded. The rounding were evidently faster for smaller grains (cf. Figure 3.9b).

When re-oxidized for the first time (at 800°C), the nickel particles increased in size, but did not revert to the as-sintered shape (cf. Figure 3.9c). Instead the particles were observed to fragment into 2-4 grains, and to grow out of the polished plane. Close-up of some of the growing structures are shown in Figures 3.5d and e. The out-of-plane growth is observed as the brighter parts of the particles.

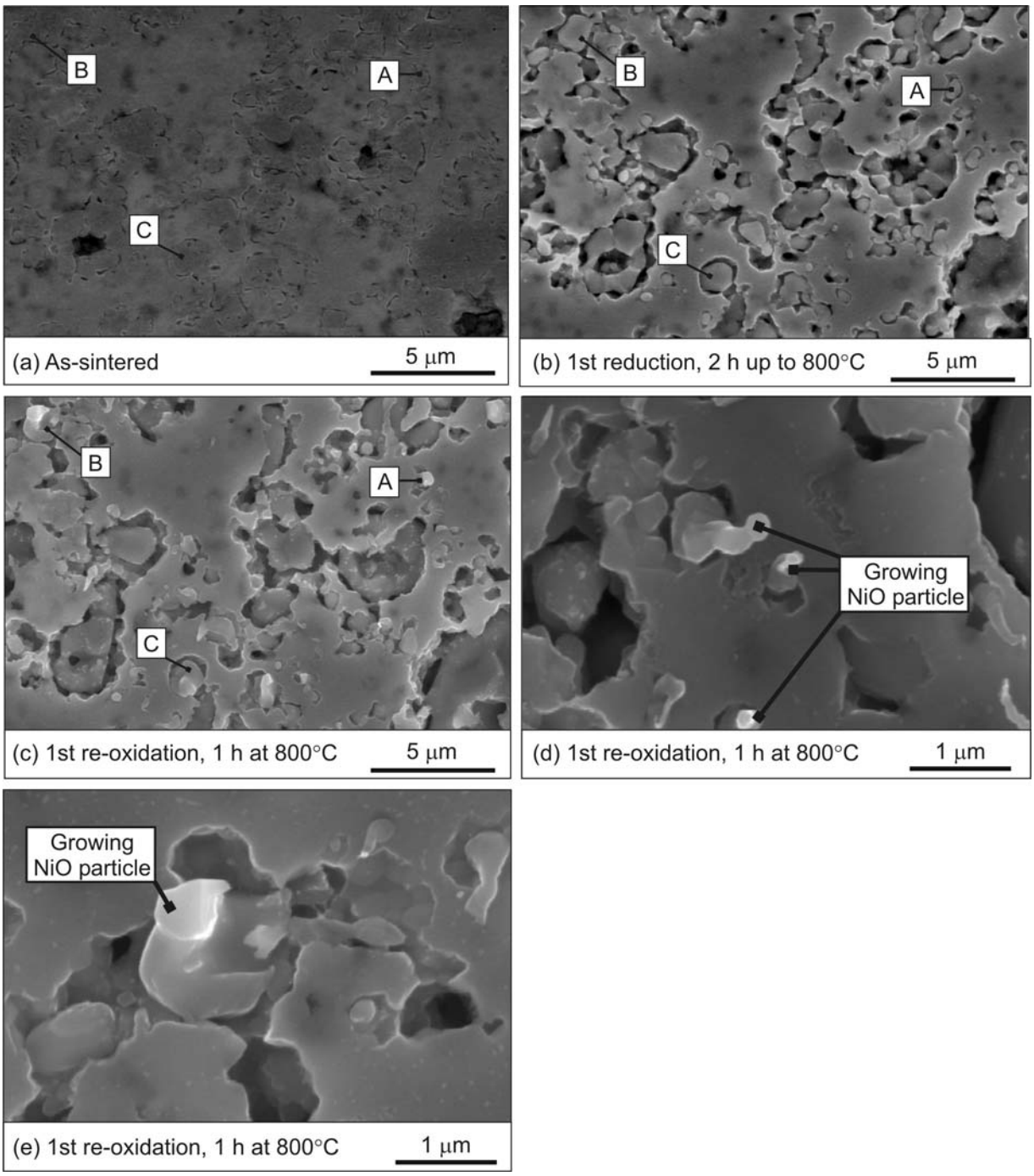

Figure 3.9. ESEM micrographs of a polished 3Y-bar during the first redox cycle. The images a, b, and c are of the same area. Three Ni particles are indicated as A, B, and C. (a) As-sintered. (b) Reduced for 2 h during heating to 800°C. (c) Re-oxidized for 1 h at 800°C. (d, e) Close-up of growing nickel particles after 1 h re-oxidation at 800°C.

ESEM micrographs of the second redox cycle are illustrated in Figure 3.10. The images are from the same sample area as shown in Figure 3.9.

Upon the second reduction, the fragmented oxidized nickel particles re-grouped into single particles that decreased in size (compare Figures 3.9c and 3.10a). After exposure to reducing conditions for 2 hours, the nickel grains were further rounded compared to 2 hours within the first reduction. The rounded shape appeared particular evident at fracture surfaces (cf. Figure 3.10b).

In contrast to the first re-oxidation that was carried out at 800°C, the second oxidation was done while heating from room temperature to 800°C. The slower oxidation promoted a different oxide

growth. The nickel particles grew, but were not fragmented, and maintained the roundness from the reduced state (cf. Figure 3.10c). The uniform growth was in close-up observed as a granulated oxide peel that developed around the grains (cf. Figures 3.10d and e).

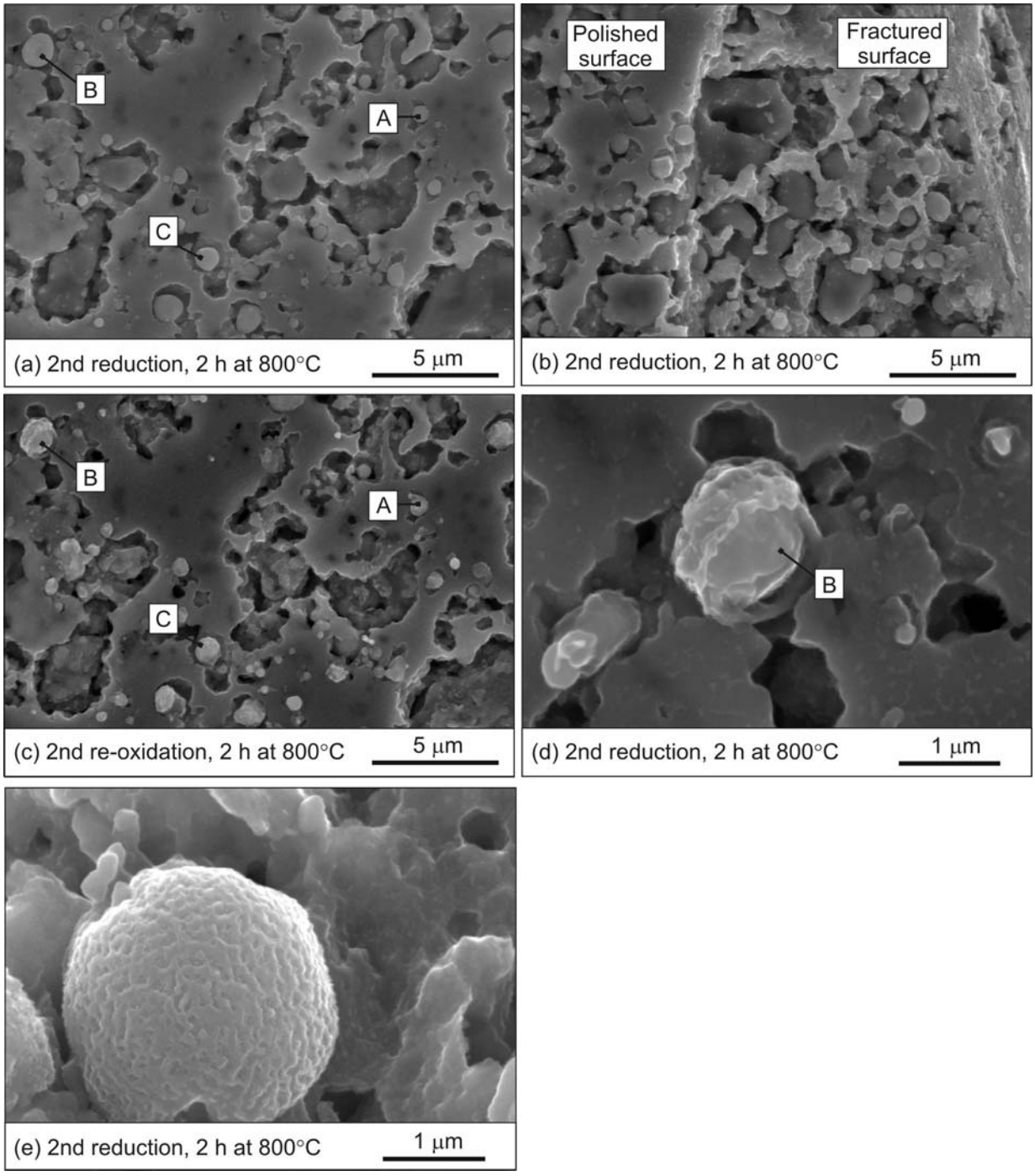

Figure 3.10. ESEM micrographs from the second redox cycle. The images a and c show the same area as Figure 3.5a-c, and the three Ni particles A, B, and C are indicated. (a) Reduced for 2 h at 800°C. (b) Polished and fractured surface after 2 h of reduction at 800°C. (c) Re-oxidized for 2 h at 800°C. (d, e) Close-up of growing nickel particles after 2 h re-oxidation at 800°C.

The changes experienced by the nickel particles were quantified by image analyses. The marked particles A, B, C were subjected to analysis, and characterized by the longest in-plane linear dimension, particle cross-section area, and roundness. The development in the three parameters upon the redox cycling is illustrated in Figure 3.11. The measurement data are shown in Appendix B, Table B3.

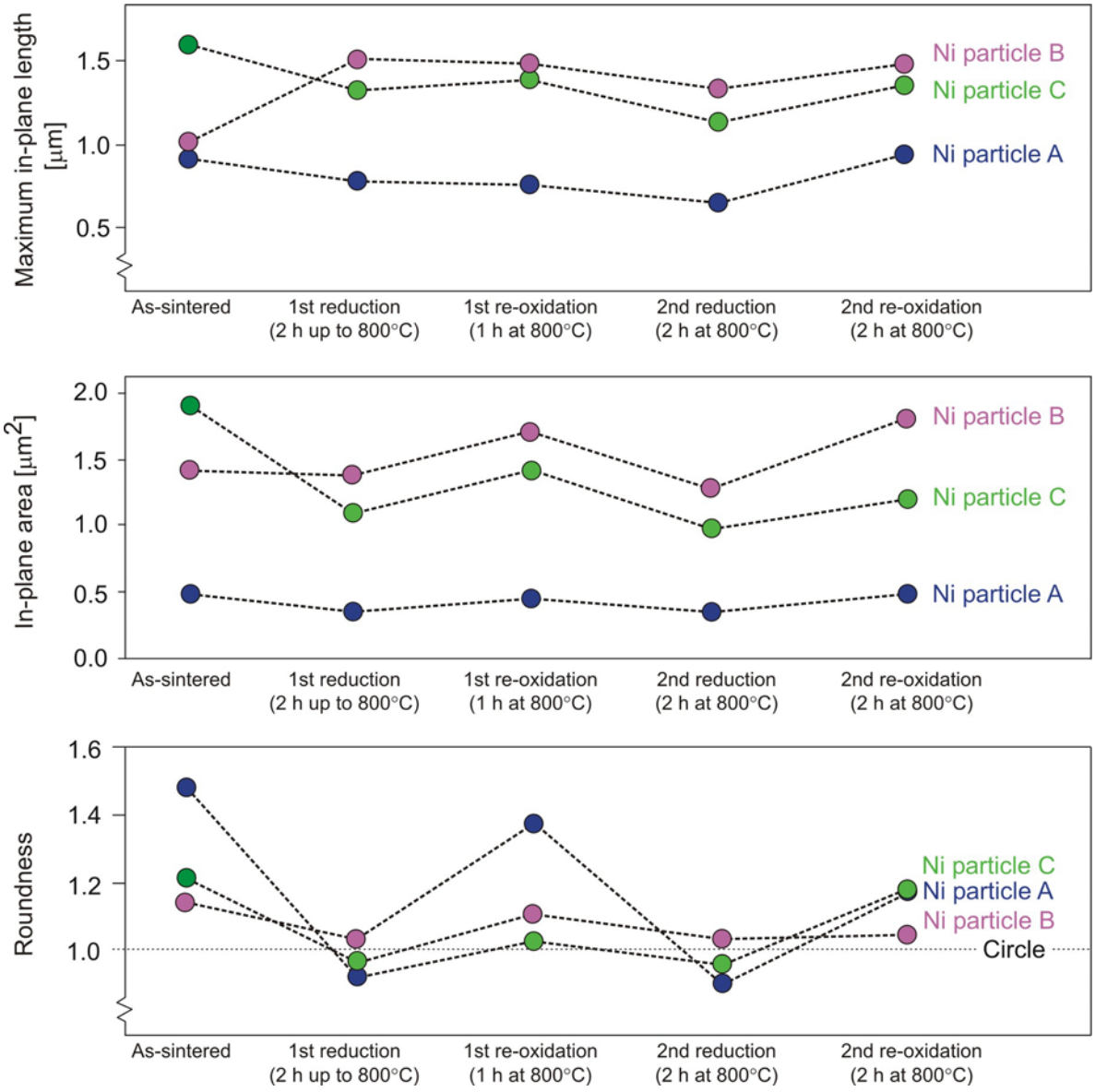

Figure 3.11. The change in maximum in-plane length, area, and roundness of the three nickel particles A, B, and C during two redox cycles. The symbol sizes correspond to the estimated uncertainty on the measurement.

Upon the reductions, the maximum in-plane length was generally observed to decrease, the in-plane area decreased, and the roundness increased (cf. Figure 3.11). This corresponded well with the visual observations.

When comparing the two reduced states, a weak tendency to a smaller in-plane length in the second reduced state was seen. The visual observation of increased roundness in the second reduced state was not reflected in the roundness parameter (cf. Figure 3.11).

When comparing the three oxidized states, the development was ambiguous. The length and area parameters after the two redox cycles were observed to be unchanged, and to have increased and decreased for A, B, and C, respectively. The particles A and B were seen to become increasingly rounded with redox cycling. For C, an improvement in roundness was only observed during the first cycle (cf. Figure 3.11).

3.4 Discussion

The particle size distributions of the starting materials appeared similar (cf. Section 3.3.1). However, shaping and sintering introduced differences in porosity and porosity distributions between the sample types. Strips were visibly more porous than bars, and displayed graded porosity. A large variation in porosity between identically prepared samples was also observed (cf. Section 3.3.1). However, the variation was not evident with microscopy.

Upon full reduction, an increase in porosity was observed both in SEM, and indicated by image analysis (cf. Section 3.3.3).
In the bars, an outer rim with higher porosity was observed to have formed after 96 hours of reduction. The rim indicated migration of the nickel phase associated with the progression of the reaction front. However, any migration of the nickel phase was not evident with the light microscopy observations, or quantifiable with image analyses of similar treated samples (cf. Section 3.3.2).
ESEM observations showed that redistribution of the nickel did occur on the particle scale. Rounding of the nickel grains was observed to start almost simultaneously with the reduction, and to proceed faster in smaller grains (cf. Section 3.3.4).
From image analyses of the ESEM micrographs, rounding of the grains were indicated upon reduction, and after to redox cycles. However, only three grains were analyzed. Both the image analyses based on ESEM and SEM showed that significant variation occurred on the micro-scale, and that representative measure of changes requires a large amount of analyses.

In accordance with literature (cf. Section 3.1), complete re-oxidation resulted in an enhanced porosity. The increase was evident with SEM examinations, and indicated by image analyses (cf. Section 3.3.3).
ESEM examinations showed that considerable changes occurred in the nickel phase as well. The changes appeared to be dependent on the temperature, corresponding to the reaction rate. When the reaction proceeded fast (when carried out at 800°C), the nickel grains divided into 2-4 grains upon re-oxidation, and the growth took place into voids. For slower reaction rates, a peel of protective nickel oxide developed around the nickel particles. In both cases, the growth of the nickel phase was observed not to influence the YSZ phase that appeared microstructurally stable through all steps (cf. Section 3.3.4).
The different oxide growths were observed in two successive re-oxidation steps. The number of the redox cycle may be a parameter on the growth pattern. However, the reaction kinetics is believed to be the dominant influence.
On the macro-scale, re-oxidation caused fractures in some of the bars. The fracture pattern of the failed bars was similar in these cases (cf. Section 3.3.1). This indicated that the variations in microstructures were not reflected on the bulk-scale.

The microstructural observations were consistent with the model of the redox mechanism proposed in Chapter 2. Redistribution of the nickel phase in the reduced state was visibly verified. Damage on the YSZ network was observed after re-oxidation, however not in-situ. The in-situ observations were done on polished sections. Thus, sufficient void existed around the growing particles, into which the growth did indeed occur. The growth into voids is believed to prevent damage to occur in the in-situ tested sample.
In addition to the model proposed in Chapter 2, the changed NiO network upon re-oxidation was observed to be influenced by the oxide growth that could involve uniform growth of the reduced particles, or split-up of the grains. The growth pattern depended on the temperature. This was in consistence with the temperature dependence on the redox behavior indicated in Chapter 2.
No significant difference in the microstructural development was observed between samples of different porosity (i.e. bars versus strips), or between samples with different ceramic component

(i.e. 3Y or 8Y composition). However, it was indicated that 3Y is stronger than 8Y as assumed (cf. Chapter 2), since a lower fraction of 3Y-bars failed macroscopically upon re-oxidation.

3.5 Conclusions

The anode cermet microstructure was investigated during the different steps in redox cycling. The conclusions are:

- The as-sintered porosity and porosity distribution were observed to be quantitatively and qualitatively sensitive to processing. Variations between methods, and variation between identically prepared samples (sibling samples) were observed. The microstructural variation between siblings was indicated not to be reflected in the bulk redox cracking behavior.

- Reduction was seen to be associated with increased porosity, and redistribution of the nickel phase. The processes were observed in-situ as shrinkage and rounding of the nickel particles. The rounding occurred faster in smaller grains.

- The short-term nickel sintering (< 96 hours) was not quantifiable with light microscopy and image analysis.

- Compared to the as-sintered state, re-oxidation was qualitatively seen to be associated with increased porosity, coarser and more coherent pore structures, and less coherent YSZ network. The porosity was quantified to be at least doubled upon the first re-oxidation.

- Re-oxidations were also observed to be associated with a redistribution of the NiO phase. The redistribution was indicated to be dependent on the oxidation kinetics. For faster oxidations, the Ni/NiO particles divided into 2-4 particles, which grew into voids. For slower oxidations, a peel of oxide grew around the nickel particles.

- An effect of the sample porosity on the microstructural changes was not observed.

- An effect of the strength of the ceramic component on the redox behavior was indicated. The stronger samples displayed statistically fewer macro cracks upon re-oxidation.

- The microstructural observations were in consistency with the model of the redox mechanism proposed in Chapter 2. The presence of redistribution of the NiO phase upon re-oxidation at higher temperature constituted an additional detail to the model.

- ESEM appeared to be a valuable technique for qualitative observations of the microstructure. However, in combination with image analyses, the method was not appropriate for attaining statistical quantitative information on the structures.

- Quantitative microstructural data may be achieved of the structures when in the oxidized state, by combined SEM and image analysis. However, extensive work is required for statistical values.

Acknowledgement

C. C. Appel and S. Ullmann (Haldor Topsøe A/S) are acknowledged for help with the ESEM experiments. B. Davidsen (Haldor Topsøe A/S) is acknowledged for technical support on the SEM experiments.

4 Redox kinetics of nickel-YSZ cermets

4.1 Introduction

The state-of-the-art nickel-YSZ cermet anode degrades upon redox cycling. The degradation is ascribed to microstructural changes associated with the reduction and re-oxidation process [8, 19, 23, 43] and cf. Chapter 2. Based on Chapter 3, the microstructural changes are believed to be dependent on the temperature at which the redox cycling is carried out. Different oxide growth was observed when the oxidation was done at 800°C, and when the oxidation occurred while heating from room temperature to 800°C. In the last case, the nickel oxidation is believed to initiate around 300°C, and to proceed very slowly until 550°C [57].
The temperature of the redox cycling has been indicated to influence on the bulk redox behavior. Less bulk damage upon re-oxidation was indicated at lower temperatures (550-700°C compared to 800-1000°C) (cf. Chapter 2 and [9]), and lower bulk conductivity of the Ni-YSZ cermets was indicated, when the nickel reduction was carried out at lower temperature [40].
The observed temperature dependence of the microstructural and bulk redox behavior may be reflected in the kinetics. Thus, the redox kinetics of the nickel-YSZ anode is of interest. In addition, the knowledge is of relevance as the kinetics is believed to be a potential parameter in achieving redox stable anodes. By control of the oxidizing kinetics, events of re-oxidizing conditions may become less detrimental [9, 43, 57, 58, 59].
The reduction and re-oxidation mechanisms of nickel-YSZ cermets have previously been investigated. The mechanisms were observed to be influenced by the cermet microstructure [8, 9, 57], and the ceramic component [8, 60, 61]. However, the investigations have been limited to the first redox cycle, and in most cases to non-technological cermet structures.
In this chapter the kinetics of the technologically relevant cermet materials upon successive redox cycles was investigated. Thermo gravimetric analysis (TGA) was applied, and by comparison with simple cermet structures, the effect of the as-sintered sample porosity, the composition of the ceramic component (yttria content), and the temperature was examined. In addition to the investigations of the bulk kinetics, the kinetics was investigated on a more local level based on synchrotron analyses.

4.2 Experimental

4.2.1 Sample preparation

Samples with variable ceramic component and porosity were prepared. Three compositions were made. The NiO (99% NiO powder from Alfa Aesar) content was in all cases 56 wt%. The ceramic component was either 8 mol% yttria stabilized zirconia (8YSZ) (TZ-8Y from Tosoh Co.), 3 mol% yttria stabilized zirconia (3YSZ) (TZ-3YB from Tosoh Co.) with a minor amount (0.6 wt%) of Al_2O_3 (Catapal® from Sasol), or 3 mol% yttria stabilized zirconia with 20 wt% Al_2O_3 added (TZ3Y20AB from Tosoh Co.).
Variable sample porosity was obtained by applying different shaping techniques. From the starting powder materials, three different forms of samples were produced: layer, bar, and powder. The starting powders were processed into slurries that subsequently were tape cast into thin foils. Layer samples were made from pieces of the green foil. A part of the green foil was heat treated to produce powder. Part of the resulting powder was used as powder sample. The other part of the powder was pressed into bar shaped samples. The pressing was done by uniaxial followed by isostatic pressing at 80 MPa. After being shaped, the layer and bar samples were sintered at 1300°C.

The investigated samples and the experimental conditions are summarized in Table 4.1. The sample names refer to the composition of the ceramic component, sample shape, and test temperature. In the sample name, the ceramic components 8YSZ, 3YSZ, and 3YSZ with 20 wt% Al_2O_3 are abbreviated to respectively 8Y, 3Y, and 3YA.

Table 4.1. List of samples and experimental test conditions. The sample name refers to the composition of the ceramic component, sample shape, and test temperature (T_{test}).

Sample name	Ceramic	Shape	Experimental conditions		
			T_{test}	Reducing	Oxidizing
8Y-powder-1000	8YSZ	Powder	1000°C	9%H_2-N_2, 100 mL/min	Air, 100 mL/min
8Y-bar-1000	8YSZ	Bar	1000°C	9%H_2-N_2, 100 mL/min	Air, 100 mL/min
3Y-powder-1000	3YSZ	Powder	1000°C	9%H_2-N_2, 100 mL/min	Air, 100 mL/min
3Y-layer-1000	3YSZ	Layer	1000°C	9%H_2-N_2, 100 mL/min	Air, 100 mL/min
3Y-bar-1000	3YSZ	Bar	1000°C	9%H_2-N_2, 100 mL/min	Air, 100 mL/min
3Y-layer-850	3YSZ	Layer	850°C	4%H_2-3%H_2O-Ar, 175 mL/min	Air, 100 mL/min
3YA-layer-850	3YSZ + 20 wt% Al_2O_3	Layer	850°C	4%H_2-3%H_2O-Ar, 175 mL/min	Air, 100 mL/min

4.2.2 Experimental procedure

A Seiko TG/DTA 320 U instrument was used for the thermo gravimetric analysis. The precision of the instrument was ± 1 μg. Correction for buoyancy between the reference and the samples was made, by applying a correction volume of alumina to the reference.
The samples were heated in air at 2°C/min to either 1000°C or 850°C. When the temperature was attained, two or three redox cycles were carried out under isothermal conditions. Air was used as oxidizing medium, and either 9 vol% H_2-N_2 or 4 vol% H_2-3 vol%H_2O-Ar was used as reducing medium. The airflow was 100 mL/min, and the flow of the two reducing gasses was respectively 100 mL/min or 175 mL/min. The difference in buoyancy between the applied gasses was observed to be insignificant.
An Autopore IV 9500 V1.05 instrument from Micromeritics Instrument Corporation was used for porosity measurements.
Synchrotron analyses were performed at beamline ID15 at the European Synchrotron Radiation Facility (ESRF). An x-ray beam with a wavelength of 0.173 angstrom was applied. The analyzed sample volume was below 62,000 μm^3. The depth resolution was ca. 70 μm. The samples were heated to ca. 850°C, and subjected to two redox cycles. 4 vol% H_2-3 vol% H_2O-He was used as reducing gas, and air as oxidizing medium. The experiments were carried out by a group from Risø National Laboratory. Further details can be seen in [62].

4.3 Results

4.3.1 Porosity

The porosity of the differently shaped samples, and samples of different compositions were measured in the as-sintered state. The porosity measurements were either based on geometrical gauging and weighing, or done by mercury porosimetry. The powder samples were assumed loosely packed in the sample container. Thus, the porosity was assumed to be 48%. The data are summarized in Table 4.2. An estimated uncertainty on the porosity is included in the table.
The layer samples displayed a porosity around 15%. This was much lower than the assumed porosity of the powder samples. The porosity of the bars was even lower, and at least a factor of two below the layer samples.

Table 4.2. Porosity of the samples before measurement. The porosity was either based on geometrical gauging, mercury porosimetry, or was estimated.

Sample name	State	Method	Porosity [%]
8Y-powder-1000	Powder	Estimated	48 ± 10
8Y-bar-1000	As-sintered	Geometrical gauging	2.93 ± 0.06
3Y-powder-1000	Powder	Estimated	48 ± 10
3Y-layer-1000	As-sintered	Geometrical gauging	14.51 ± 0.29
3Y-bar-1000	As-sintered	Geometrical gauging	7.01 ± 0.14
3Y-layer-850	As-sintered	Geometrical gauging	15.54 ± 0.31
3YA-layer-850	As-sintered	Mercury porosimetry	13.7 ± 1.0

4.3.2 Time for complete reduction and re-oxidation

Theoretical reaction time

The time for complete reduction or re-oxidation of the nickel phase to occur, will depend on the transport and reaction mechanisms. However, experimental conditions like the amount of nickel, gas flow, and gas composition may contribute with restrictions as well.

The minimum required time for complete reduction or re-oxidation, based on the experimental conditions is denoted the theoretical reaction time (t_{theory}). If it is assumed that all of the reducing or oxidizing gas reacts with the nickel, the theoretical reaction time can be approximated from the ideal gas law (cf. Equation 4.1), the flow rate, and the gas composition (cf. Equation 4.2). n_{gas} is the required mol of the reducing or oxidizing gas component, and is calculated from the amount of nickel in the sample. R is the gas constant, T is the temperature in Kelvin, p is the pressure, and f is the volume percent of the reducing or oxidizing component in the gas mixture.

Eq. 4.1 $$V_{gas} = \frac{n_{gas} \cdot R \cdot T}{p}$$

Eq. 4.2 $$t_{theory} = \frac{V_{gas}}{f \cdot \text{flow rate}}$$

The theoretical reaction times for complete reduction ($t_{theory,red}$) or oxidation ($t_{theory,ox}$) of the tested samples are listed in Table 4.3. The expected mass change associated with the reactions is included.

Table 4.3. Theoretical reaction times for complete reduction ($t_{theory,red}$) and complete re-oxidation ($t_{theory,ox}$) of the tested samples.

Sample name	Mass change [mg]	$t_{theory,red}$ [min]	$t_{theory,ox}$ [min]
8Y-powder-1000	15.55	2.42	0.52
8Y-bar-1000	18.99	2.95	0.63
3Y-powder-1000	9.97	1.55	0.33
3Y-layer-1000	12.71	1.98	0.42
3Y-bar-1000	20.58	3.20	0.69
3Y-layer-850	4.94	0.87	0.15
3YA-layer-850	3.80	0.67	0.11

The theoretical reaction times were observed to be in the order of 3 minutes or below (cf. Table 4.3). It was believed that the reactions will not complete within this time scale. Thus, the applied amount of sample, flow rates, and gas composition were not expected to limit the reaction rates.

The mass change was in all cases orders of magnitude above the resolution of the instrument (± 1 μg) (cf. Table 4.3). Thus, this will not be a source of error.

Measured reaction time

The thermo gravimetric profile, and the simultaneously measured profile of the oxygen partial pressure (pO_2), is illustrated in Figure 4.1a for the sample 8Y-bar-1000. The period around the first redox cycle is shown enlarged in Figure 4.1b. Complete reaction was believed accomplished, when the weight became stable following a shift in atmosphere. Shifts in atmosphere are marked by arrows, and "H_2" for reducing conditions, and "Air" for oxidizing.

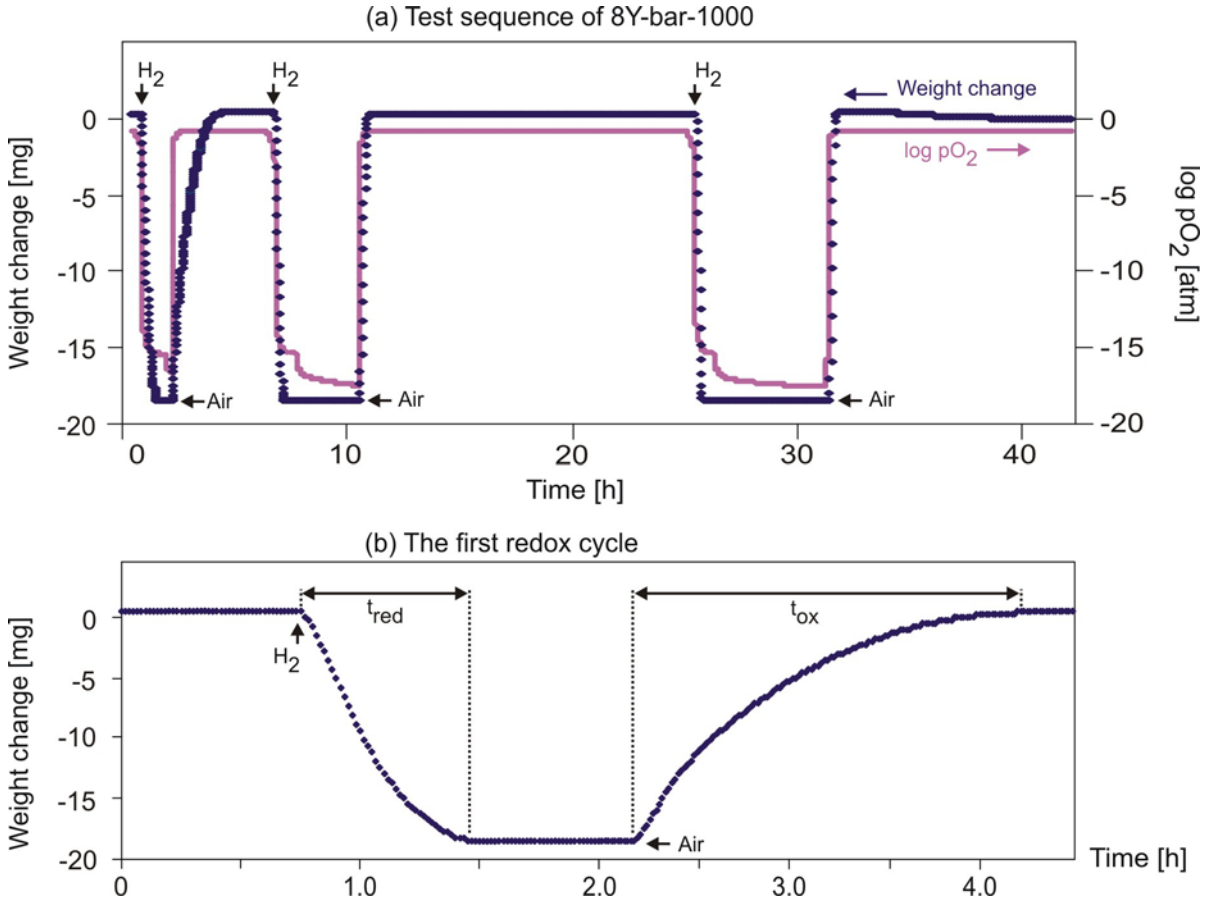

Figure 4.1. Thermo gravimetric and pO_2 profiles of the sample 8Y-bar-1000. (a) The test sequence. Shifts in atmosphere are marked by arrows, and "H_2" and "Air" for respectively reducing and oxidizing conditions. The size of the measurement points comprises the uncertainty on the measurement. (b) Focus on the period around the first redox cycle. The times for complete reduction (t_{red}) and re-oxidation (t_{ox}) are indicated.

The time for complete reaction was determined from the differentiated thermo gravimetric curve. When the slope between succeeding measurement points (i.e. Δweight [mg]/Δtime [h]) was calculated, natural fluctuations of 0.05 mg/h was observed. The time for reaction was then taken as the period in which the slope was steeper than 0.05 mg/h.
Thermogravimetry measurements were done every minute. However, due to the natural fluctuations, the uncertainty on the time for complete reaction was estimated to be ± 2 minutes.

Similar profiles were obtained for all the tested samples. The course of the pO_2 illustrated in Figure 4.1a was generally observed. The pO_2 became quickly stable upon shifts to the oxidizing air (around $10^{-0.7}$ atm). However, upon shifts to reducing atmosphere, the pO_2 decreased in two characteristic steps. After 15 minutes of reducing conditions, the pO_2 had decreased and leveled to ca. $10^{-15.5}$ atm. The pO_2 then dropped further, and continued with a steady decrease. The two pO_2 levels upon reduction is believed to reflect the formation of free water when NiO is reduced, and the slow loss of adsorbed water in the system.

4.3.3 Progress of the reactions

Reduction

The progress of the reductions for the three types of samples: bar, layer, and powder with the composition 3Y that were tested at 1000°C, are shown in Figure 4.2. The progress is illustrated for respectively the first, second, and third reduction, and is shown as the normalized mass change as a function of an arbitrary running time. The minor deviations from 100% normalized mass change, are ascribed to deviations from the theoretical synthesized nickel content. For the corresponding samples of the composition 8Y similar reduction courses were observed.

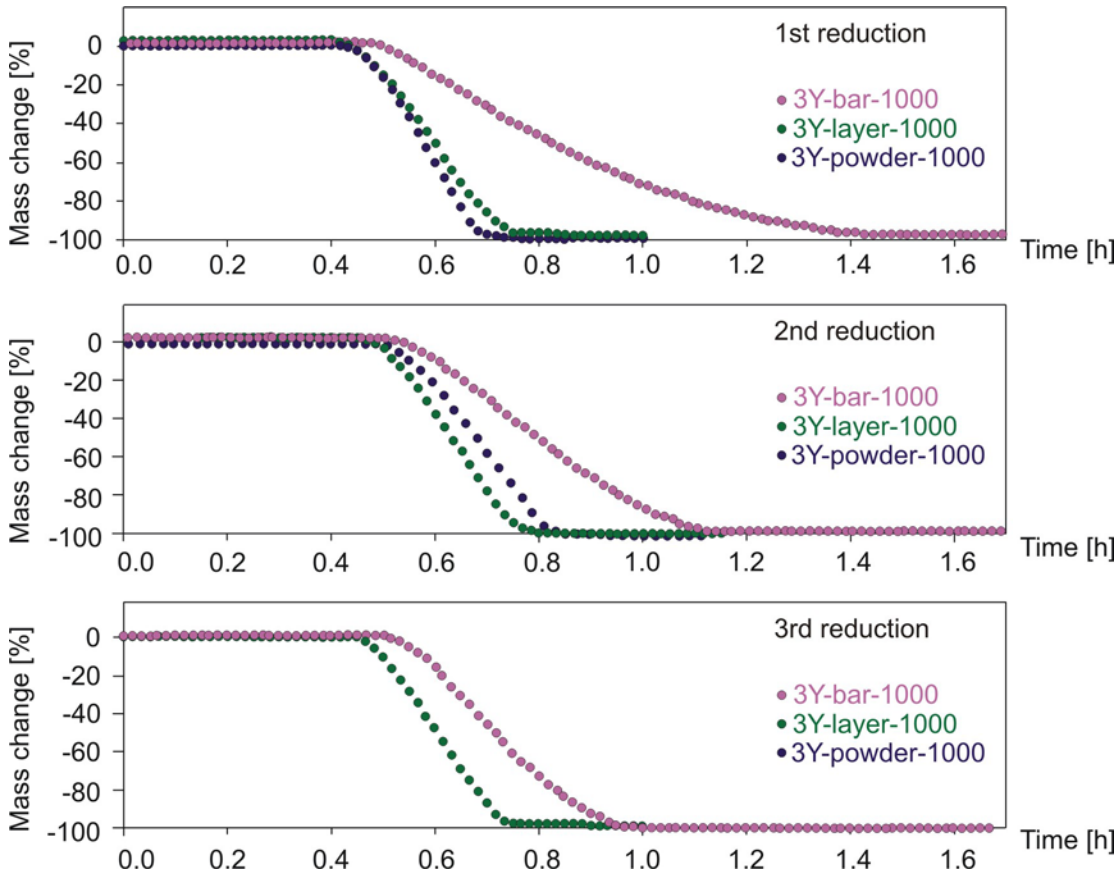

Figure 4.2. Progress of the reductions for the three types of samples: bar, layer, and powder with the composition 3Y that were tested at 1000°C. The progress is illustrated for respectively the first, second, and third reduction, and shows the normalized mass change as a function of an arbitrary running time.

For all three reductions, the reduction of the powder (3Y-powder-1000) and layer (3Y-layer-1000) samples progressed approximately linearly. In contrast, complete reduction was approached asymptotically for the bar sample (3Y-bar-1000). This was particular evident during the first reduction. Upon the second and third reduction, the reduction of the bar approached a more linear trend.

Figure 4.3 shows the time for complete reduction as a function of the start porosity. The position of the bar, layer, and powder samples on the porosity axis is indicated in the figure. Samples of composition 8Y are represented with diamond symbols, and circles represent the 3Y composition. The three orders of reduction are symbolized by different colors. The size of the measurement point comprises the uncertainty on the measurement. The uncertainty on the porosity is not indicated. The measured values can be seen in Appendix C, Table C1.

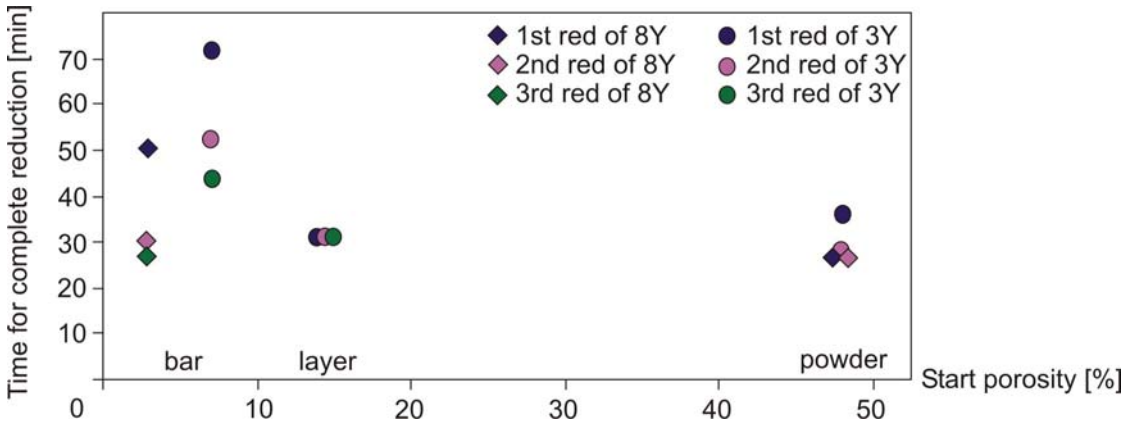

Figure 4.3. Time for complete reduction at 1000°C as a function of the start porosity of the sample. The position of the bar, layer, and powder samples on the porosity axis is indicated. Samples of composition 8Y and 3Y are represented by diamonds and circles, respectively. The three orders of reduction are symbolized by different colors. The size of the measurement point comprises the uncertainty on the measurement. The uncertainty on the porosity is not indicated.

For the samples with a porosity higher than ca. 15% (i.e. layer and powder samples), the time for complete reduction was ca. 30 minutes, irrespective of the order of reduction (cf. Figure 4.3). On the other hand, the low-porosity bar samples displayed a strong dependence on the order of reduction. For the first reduction (blue symbols in Figure 4.3), complete reduction of the bars was much slower (50 ± 2 or 72 ± 2 min). However, upon the subsequent reductions, the time for complete reduction of the bars decreased, and approached the reduction times for powder and layer samples. The advance was more pronounced for the bars of 8Y composition.

Re-oxidation

The progress of the re-oxidations for the three types of samples: bar, layer, and powder with the composition 3Y that were tested at 1000°C, are shown in Figure 4.4. The progress is illustrated for respectively the first and second re-oxidation, and shown as the normalized mass change as a function of an arbitrary running time. For the corresponding samples of the composition 8Y similar reduction courses were observed.

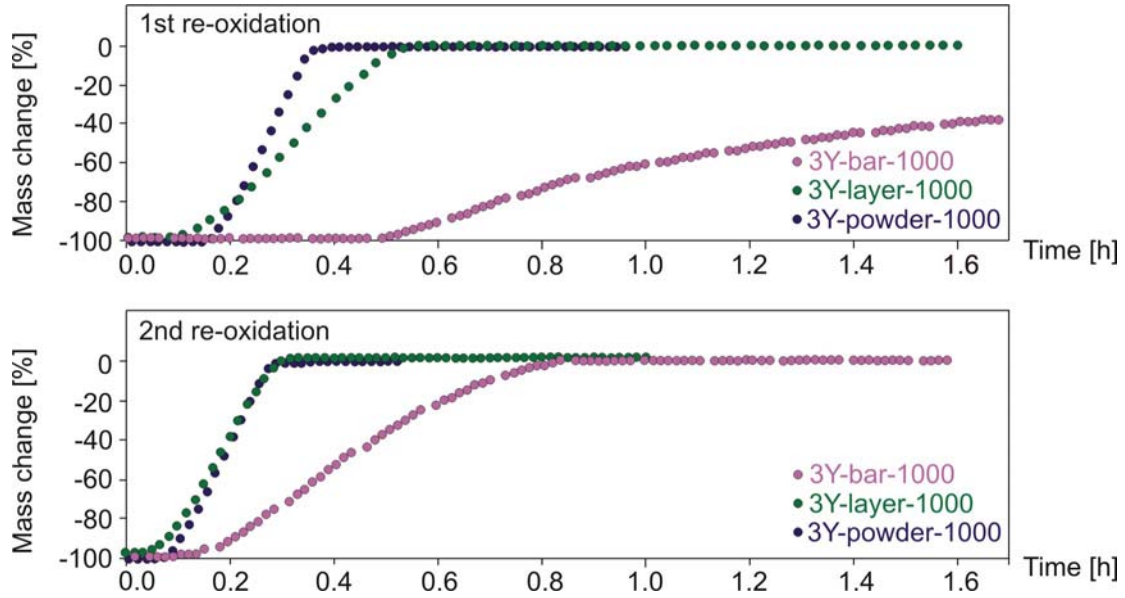

Figure 4.4. Progress of the re-oxidations for the three types of samples: bar, layer, and powder with the composition 3Y that were tested at 1000°C. The progress is illustrated for respectively the first and second oxidation, and shows the normalized mass change as a function of an arbitrary running time.

The progression of the re-oxidation appeared similar to the case of reduction. For the powder (3Y-powder-1000) and layer (3Y-layer-1000) samples, the re-oxidation proceeded approximately linearly. The bar sample approached complete re-oxidation asymptotically. For the first re-oxidation of the bar, complete oxidation was approached very slowly, and the complete reaction is not illustrated in Figure 4.4. Upon the second oxidation the bar oxidized markedly faster, and the progression approached a linear trend.

The time for complete re-oxidation as a function of the start porosity of the sample is shown in Figure 4.5. The position of the bar, layer, and powder samples on the porosity axis is indicated in the figure. Samples of composition 8Y are represented by diamond symbols, and circles represent the 3Y composition. The three orders of reduction are symbolized by different colors. The size of the measurement point comprises the uncertainty on the measurement. The uncertainty on the porosity is not indicated. The measured values can be seen in Appendix C, Table C2.

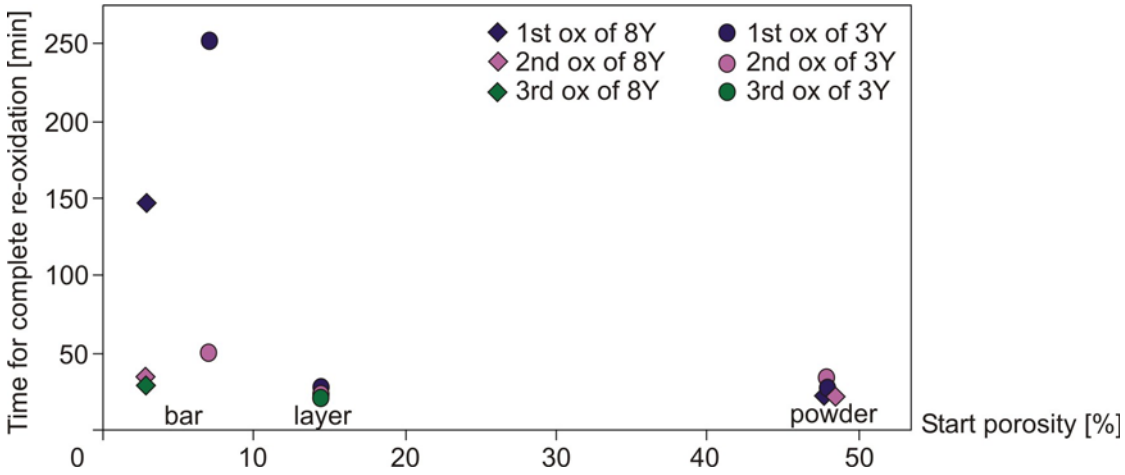

Figure 4.5. Time for complete oxidation at 1000°C as a function of the start porosity of the sample. The position of the bar, layer, and powder samples on the porosity axis is indicated. Samples of composition 8Y and 3Y are represented by diamonds and circles respectively. The three orders of reduction are symbolized by different colors. The size of the measurement point comprises the uncertainty on the measurement. The uncertainty on the porosity is not indicated.

By analogy with the reduction process, the samples with a porosity higher than ca. 15% (i.e. layer and powder samples) displayed similar time for complete re-oxidation, irrespective of the order of re-oxidation (cf. Figure 4.5). The time was approximately 25 min. This was slightly faster than the corresponding reduction process of 30 min duration.
The re-oxidation of the low-porosity bars displayed a strong dependence on the order of re-oxidation. The dependence was much more pronounced than for the reduction processes. The first re-oxidation (blue symbols in Figure 4.5) was complete after 5-10 times the oxidation time for layer and powder samples (147 ± 2 or 252 ± 2 min compared to 25 min). However, upon for the second re-oxidation, the re-oxidation time of the bars approached the powder and layer. The advance was more pronounced for the bars of 8Y composition.

4.3.4 Composition of the ceramic component

An effect of the yttria content of the zirconia phase on the redox kinetics was examined by comparing samples of the compositions 3Y and 8Y (i.e. containing either 3 mol% or 8 mol% yttria) that were otherwise corresponding.

From Figure 4.3 the reduction kinetics of powders and bars with respectively 3Y and 8Y composition can be compared. For the powders, the first reduction was observed to be faster for the 8Y powder than the 3Y powder. Upon the second reduction, no significant difference was seen. The 3Y and 8Y bar samples were compared in spite of the 3Y bar being slightly more porous from the start. However, despite of this, for all three orders of reduction complete reduction was achieved faster in the 8Y bar compared to the 3Y bar.
From Figure 4.5 the re-oxidation kinetics of the samples was compared. When comparing the powders, the oxidations proceeded slightly faster in the powder of 3Y composition compared to 8Y. For the bars, the oxidations were seen to be almost twice as fast in the 8Y compared to 3Y.

The effect of 20 wt% alumina added to the ceramic phase was investigated by comparison of the samples 3Y-layer-850 and 3YA-layer-850 (cf. Table 4.1). The complete reaction times measured for the two compositions are shown in Table 4.4.

Table 4.4. Measured times for complete reduction and re-oxidation for the samples 3Y-layer-850 and 3YA-layer-850.

Sample	1st reduction [min]	1st re-oxidation [min]	2nd reduction [min]	2nd re-oxidation [min]
3Y-layer-850	26 ± 2	25 ± 2	22 ± 2	27 ± 2
3YA-layer-850	34 ± 2	23 ± 2	20 ± 2	53 ± 2

The reaction times for the sample 3Y-layer-850 were seen not to vary significantly between the successive redox steps. For the alumina-rich sample, significant differences were seen. The first reduction was slightly slower than for 3Y-layer-850. However, the second reduction of the alumina-rich sample proceeded faster, and no significant difference to 3Y-layer-850 appeared.
The first oxidation time was similar for the two samples. Upon the second re-oxidation, the oxidation of the alumina-rich sample proceeded twice as slow.

4.3.5 Temperature

Identical layer samples of the composition 3Y were tested at 850°C and 1000°C. The times for complete reaction during the first and second redox steps are shown in Table 4.5.

Table 4.5. Complete reaction times for 3Y-layer samples tested at 850°C and 1000°C.

Sample	1st reduction [min]	1st re-oxidation [min]	2nd reduction [min]	2nd re-oxidation [min]
3Y-layer-850	26 ± 2	25 ± 2	22 ± 2	27 ± 2
3Y-layer-1000	31 ± 2	27 ± 2	31 ± 2	23 ± 2

The differences between the two temperatures were seen to be minor. Slightly slower times for complete reduction were observed for the test at 1000°C. For the re-oxidation processes, no significant difference was seen between 850°C and 1000°C.

4.3.6 Synchrotron data

The kinetics of the nickel phase transformations upon reduction and re-oxidation was investigated in-situ by synchrotron analysis [62]. The measured progression of the first reduction and re-oxidation for a sample of the type 3Y-layer is shown in Figure 4.6. The figure illustrates the volume fraction of Ni (red) and NiO (green) as a function of the time exposed to the reducing or oxidizing gas.

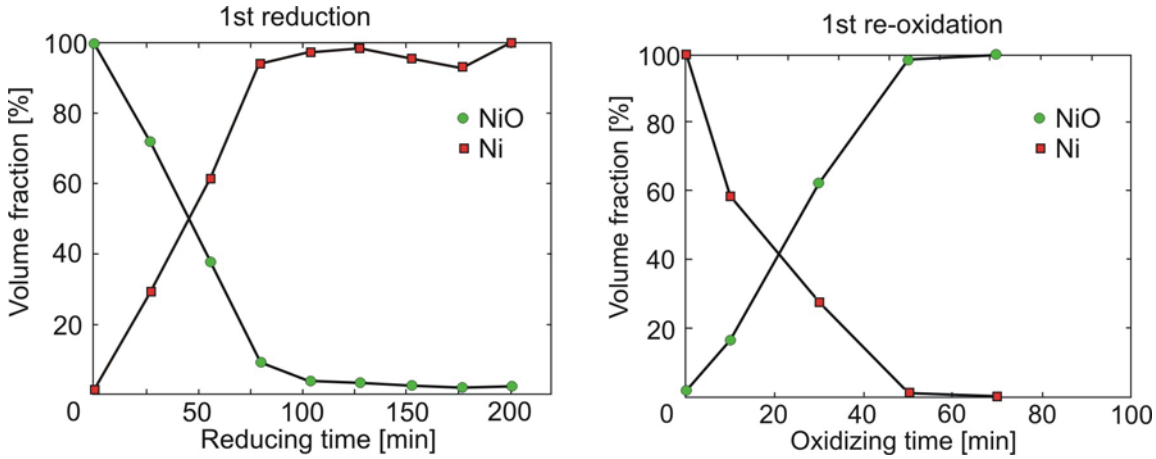

Figure 4.6. Progression of the first reduction and re-oxidation of a 3Y-layer sample, shown as the volume fraction of Ni (red) and NiO (green) as a function of time exposed to the reducing or oxidizing gas [62].

The volume fraction of Ni and NiO was at any time observed to sum to 100% (cf. Figure 4.6). Complete transformation to Ni and NiO was observed upon reduction and re-oxidation, respectively, within the uncertainty of the data. This indicated that the synchrotron analyses provided a viable method for study of the in-situ kinetics. The measured times for complete reaction are listed in Table 4.6. For comparison, the corresponding data from the TGA analysis on an identical sample, tested under similar conditions were included in the table.

Table 4.6. Time for complete reduction or re-oxidation of the sample 3Y-layer-850 as measured with synchrotron and TGA. The uncertainty on the synchrotron measurements was reported to be 5%.

Method	1st reduction [min]	1st re-oxidation [min]	2nd reduction [min]	2nd re-oxidation [min]
Synchrotron	92 ± 5	42 ± 2	78 ± 4	50 ± 3
TGA	26 ± 2	25 ± 2	22 ± 2	27 ± 2

For all redox steps, the time for complete reduction or re-oxidation was observed to be at least twice as slow, when measured with synchrotron compared to TGA. Also in contrast to the TGA data, the synchrotron measurements displayed a large difference between reductions and re-oxidations. The first as well as the second reduction proceeded significantly slower than the two re-oxidations.

The nickel phase transformations were also investigated as a function of sample depth. It was indicated that the kinetics was slightly faster near the surface exposed to the reducing or oxidizing gas. The trend was more pronounced during first cycle compared to second cycle [62].

4.4 Discussion

4.4.1 Progression of the reactions

Linear progression of the reduction was observed for samples with start porosity above 15%, and for samples with lower start porosity, after they were subjected to redox cycling. Upon the first reduction, the samples with lower start porosity displayed asymptotic trends.
The linear behavior of the nickel reduction is in agreement with the literature [57, 48, 53]. Further, two rate-determining steps for the reduction have been identified. The initial rate is believed determined by chemisorption of H_2 on the NiO particle surfaces, and the second by the inward progression of the Ni nucleation front. Both steps are related to the interface.

Linear progression was also observed when re-oxidizing samples with start porosity above 15%, and for samples with lower start porosity, after they were subjected to redox cycling. The low-porosity samples displayed asymptotic trends upon the first re-oxidations.
The observed linear behavior of the nickel re-oxidation is not consistent with the literature. Nickel oxidation has commonly been described as semi-parabolic or logarithmic [9, 57]. The oxidation is governed by Ni diffusion through the growing oxide layer. Since cationic transport prevails in the oxidized NiO surface, the NiO growth will occur on the external oxide surface [9, 52, 53, 57]. Short-circuiting diffusion mechanisms, as for instance outward Ni diffusion along grain boundaries or dislocations, inward diffusion of O_2 along grain boundaries, and gaseous transport of O_2 through micro fissures, may be active as well [57].

The porosity of the anode materials is known to increase upon redox cycling (cf. Chapter 2 and [9]). The transition from asymptotic to linear reaction trend of the samples with low start porosity (below 7%) indicates that gas diffusion limitations occur during the initial reactions.
Thus, for the low-porosity samples, gas diffusion limitation is believed to prevent interface controlled (linear) reduction kinetics. For the oxidations, gas diffusion and not bulk diffusion mechanisms is responsible for the asymptotic trend of the low-porosity samples.
The linear progression of the oxidations when sufficient porosity exists, suggests that the surface oxidation reaction is the restriction, and not the bulk Ni diffusion. This may be explained by the microstructure. For a fine grained nickel structure, the Ni bulk diffusion will be of less importance, as the diffusion distance will be short. The presence of a more fine grained structure for the investigated samples, was further indicated by the time for complete re-oxidation. Compared to the oxidations in the literature, where parabolic or logarithmic trends were observed [9, 57], much shorter times for complete oxidations were observed in this study (25 minutes compared to above 200 minutes).

4.4.2 Time for complete reaction

For samples where gas diffusion was believed not to be an issue, the time for complete reduction was ca. 30 min, and 25 min for oxidations. The synchrotron measurements indicated a vague progression front from the gas flow direction.
Much slower redox kinetics was observed for samples with low start porosity due to gas diffusion limitations. When redox cycled, the porosity increased, and the gas diffusion limitation disappeared. The kinetics then approached that of 25-30 minutes. However, the advancement occurred faster for samples of composition 8Y compared to 3Y (cf. Sections 4.3.3 and 4.3.4). This corresponds to faster disintegration of the 8Y structure, which is in accordance with the model of the redox mechanism proposed in Chapter 2.

The composition of the cermet influenced on the redox kinetics. Faster reactions were generally observed for the samples containing 8YSZ compared to 3YSZ. The influence of the yttria content was evident for the low-porosity samples (bars), and less pronounced for the porous powders (cf. Section 4.3.4). The dependence on the porosity indicated that the mechanism separating the two compositions at low porosity is related to the grain boundaries.
Addition of alumina to the ceramic component had a complex effect on the kinetics. Only some of the redox steps appeared to be affected. Slower reactions were observed for the first reduction and the second re-oxidation (cf. Section 4.3.4). The samples with alumina are believed to contain the $NiAl_2O_4$ spinel phase (cf. Chapter 2). The complex kinetics pattern is believed related to the dissociation (reduction), and regeneration (oxidation) of the spinel phase.

No difference in reaction times was observed when the redox cycling was carried out at respectively 850°C and 1000°C. The oxide growth was previously observed to be dependent on the temperature (cf. Chapter 3). This was not reflected in the kinetics. However, the investigated temperature range was limited compared to the previous growth studies, where the oxidation was done at 300-800°C.
The Ni network formed upon reduction was indicated dependent on the temperature of reduction, for temperatures between 650-1000°C [40]. This was also not reflected in the kinetics.

Compared to TGA, the synchrotron measurements resulted in much slower reaction times, and significant difference between the times for reduction and re-oxidation.
The long reaction times could be explained by the presence of a slower reacting particle core, which was only detectable with the synchrotron. However, the synchrotron measurements did not provide kinetics on the individual grains, and the achieved kinetics curves were linear. Even though the synchrotron did not provide resolution to the grain level, a small sample volume (ca. 40 μm x 40 μm x 40 μm) was analyzed compared to the bulk. Thus, the analyzed volume may be unrepresentative of the bulk. If, for instance the volume investigated was dominated by coarser nickel grains compared to the bulk, longer reaction times would be expected.
The experimental synchrotron set-up may provide another explanation for the slow reaction times. The sample chamber was relatively big compared to the sample [62]. Thus, only a fraction of the reducing or oxidizing gas may interact with the sample, and the amount of H_2 or O_2 may have been a limitation on the reactions. Limitations in the reacting gasses will also explain the significant slower reductions compared to oxidations observed with synchrotron, as the H_2 concentration in the reducing gas is much lower than the O_2 concentration in air.

4.5 Conclusions

The redox kinetics of nickel-YSZ anode materials was studied, and the effect of the initial sample porosity, composition of the ceramic component, and temperature was investigated. The conclusions are:

- Gas diffusion limits the initial redox reactions in low-porosity cermets (< 7% as-sintered porosity). With approximately doubled sample porosity (> 15%), gas diffusion limitations were not observed.

- By tape casting, sufficient porosity is produced to avoid gas diffusion limitations on the redox reactions.

- For porous samples, both reduction and re-oxidation were observed to proceed linearly with time. The deviation from the parabolic or logarithmic oxidation trend, generally proposed in the literature, is ascribed to the fine particle sizes of the cermet.

- The linear trends indicated that the redox reactions were interface controlled.

- Complete reduction and re-oxidation occurred within 30 and 25 minutes, respectively. No effect of lowering the temperature from 1000°C to 850°C was observed.

- The ceramic component influenced on the redox kinetics. The reactions proceeded faster for cermets containing 8YSZ compared to 3YSZ. The effect was indicated to be related to the grain boundaries of the ceramic phase. The effect of adding alumina was ambiguous.

- Redox cycling was observed to give rise to mechanical disintegration of the samples. Faster disintegration was observed for samples containing a mechanically weaker ceramic component. The observations were consistent with the model of the redox mechanism proposed in Chapter 2.

- Comparison of the bulk kinetics with synchrotron data, displayed reaction times differing by at least a factor of two. This indicated that the volume being investigated with the synchrotron was not representative of the bulk, or that the experimental set-up was not optimized for examination of the kinetics.

Acknowledgement

B. H. Simonsen (Risø National Laboratory) is acknowledged for technical support on the experiments with the samples 3Y-layer-850 and 3YA-layer-850. A. Hagen (Risø National Laboratory), R. V. Martins (Risø National Laboratory and GKSS), H. F. Poulsen (Risø National Laboratory), V. Honkimäki (European Synchrotron Radiation Facility), T. Buslaps (European Synchrotron Radiation Facility), and R. Feidenshans'l (Risø National Laboratory) are acknowledged for the synchrotron experiments and associated data treatment.

5 Electrical performance of nickel-YSZ cermets

5.1 Introduction

The performance of the anode in a solid oxide fuel cell (SOFC) depends on the kinetics of the electrode reactions, the anode conductivity, and the anode contact to the adjacent layers. Thus, when developing new anode structures and materials, the electrical and electrochemical performance are key parameters.
The conductivity of the anode cermets has been examined by DC (direct current) measurements, and appeared to be an evident monitor for changes in the microstructure [7, 22, 36, 40, 41, 63]. The reaction kinetics has been studied by electrochemical impedance spectroscopy (EIS). Ideally, a whole cell is tested, and the anode contribution to the electrochemical resistance derived from the full spectrum. This is a difficult way since several processes contribute to the total cell resistance [64]. Alternatively, symmetrical anode cells, i.e. cells with identical electrode material on both sides of the electrolyte, have been studied. Primdahl [3] and Chung [65] studied symmetrical cells made by spraying anode slurries onto the sides of a thick, tape cast electrolyte foil. However, the anodes manufactured this way are not believed to represent the technological anode-supported electrode, as the electrochemical performance is known to be sensitive to the fabrication procedure.
In this chapter the changes in the cermet microstructure upon redox cycling were characterized with electrical measurements. The conductivity of both the nickel network and the YSZ network was studied, and the changes upon reduction, ageing at high temperature, and re-oxidation were quantified. The effect of the composition of the ceramic component (yttria content), cermet porosity, and temperature of reduction on the conductivity properties was examined. The chapter also presents a method for fabricating symmetrical anode cells based on technologically relevant manufacturing procedures. The cells were studied by EIS, and the effect of oxidation, and the ceramic component (yttria content) was observed.

5.2 Experimental

5.2.1 Sample preparation

Composition

Samples were prepared from NiO powder (99% from Alfa Aesar), alumina powder (Catapal® from Sasol), and 3 mol% yttria stabilized zirconia (3YSZ) or 8 mol% yttria stabilized zirconia powder (8YSZ) (TZ-3YB or TZ-8Y from Tosoh Co.). Two compositions with similar NiO contents, and either 3YSZ or 8YSZ were prepared. The two compositions were denoted 8Y and 3Y, and the solid material contents were respectively 56.8 wt% NiO, 43.2 wt% 8YSZ for 8Y, and 55.7 wt% NiO, 43.7 wt% 3YSZ, 0.6 wt% Al_2O_3 for 3Y.

Samples for DC measurement

The powders were processed into slurries that subsequently were tape cast into thin foils. A part of the green foils was heat treated into powder, and the resulting powder was pressed (uniaxial followed by isostatic pressing at 80 MPa) into bar shaped samples. The green foils and the bars were sintered at 1300°C. After sintering, the bars were mechanically cut down into lengths of 20 mm, and the foils were cut by laser into strips of 9 mm width and 50 mm length.
Some of the sintered samples were subsequently fully reduced at 1000°C with 9 vol% H_2 in N_2 for 96 hours. Some of the samples were further subjected to a redox cycle i.e. oxidized (at 1000°C in air for 1 hour), and re-reduced with the same procedure as the first reduction. Following this, the metallic nickel was removed by acid treatment. A 10 molar hydrochloric acid

(10 M HCl) in combination with periods of heating was applied. The samples were exposed to the acid until constant weight was attained. The exposure time lasted from 138-342 hours.
A list of the samples tested with DC conductivity is shown in Table 5.1. The two types of samples (cermet and porous YSZ without nickel) are differentiated by a prefixed "P" in the sample name. The subsequent parts of the sample names refer to the composition of the ceramic component, and the sample shape. The last part of the sample name refers to the temperature of reduction (T_{red}) for the cermets, and to the pre-treatment of the cermet before nickel removal for the porous YSZ. Tests of identical samples performed under identical conditions are separated by a serial letter added to the last part of the sample name. The temperature range (T_{meas}) at which measurements were carried out is included in Table 5.1.

Table 5.1. List of the samples tested with DC conductivity. The sample name indicates type of sample, composition of the ceramic component, sample shape, temperature of reduction (T_{red}) for cermets, and pre-treatment of the cermet before nickel removal for the porous YSZ. Identical tests are separated by a serial letter added to the last part of the sample name. The temperature range (T_{meas}) at which measurements were carried is shown in the last column.

Sample type	Sample name	Ceramic	Shape	Pre-treatment	T_{red} [°C]	T_{meas} [°C]
Cermet	8Y-bar-1000	8YSZ	Bar	-	1000	1000
	8Y-strip-1000	8YSZ	Strip	-	1000	1000
	3Y-bar-1000-a	3YSZ	Bar	-	1000	1000
	3Y-bar-1000-b	3YSZ	Bar	-	1000	1000
	3Y-bar-1000-c	3YSZ	Bar	-	1000	700-1000
	3Y-bar-800	3YSZ	Bar	-	800	800
	3Y-bar-850	3YSZ	Bar	-	850	850
	3Y-bar-1200	3YSZ	Bar	-	1200	1200
	3Y-strip-1000	3YSZ	Strip	-	1000	1000
Porous YSZ	P-8Y-bar-red	8YSZ	Bar	Reduction + acid	-	500-1000
	P-8Y-bar-ox	8YSZ	Bar	Redox cycle + acid	-	500-1000
	P-3Y-bar-red	3YSZ	Bar	Reduction + acid	-	500-1000
	P-3Y-bar-ox	3YSZ	Bar	Redox cycle + acid	-	500-1000

Samples for EIS measurement

Two-electrode symmetrical cells with identical Ni-YSZ electrodes on each side of the electrolyte were prepared for EIS measurements. The electrodes corresponded to the technological cermet structure. The technological half-cells consist of tape cast 3Y slurry (the anode-support), on the surface of which 8Y slurry is sprayed in a thin layer (the anode), followed by a thinly sprayed electrolyte layer.
Symmetrical samples for test of the technological 8Y structure were produced by sandwiching two half-cells. The samples were denoted "8Y-sym". Symmetrical samples for test of the technological 3Y structure were produced by sandwiching two anode-supports, one with, and one without sprayed electrolyte. The samples were denoted "3Y-sym". The parts were sandwiched and joined in the green state, and subsequently sintered under load (0.3-18 g/cm^2) at 1300°C.

5.2.2 DC measurements

A 4-electrode set-up was applied for DC conductivity measurements. Electrodes of platinum (Pt) wire were mounted onto the strip and bar shaped samples. For measurement on bars, the current electrode wires were wrapped around the sample ends (cf. Figure 5.1). The wires were guided by mechanically cut grooves at the edges of the bar. To ensure contact, Pt paste was applied. Potential probes fixed in the DC set-up were used for the bars. The probes were distanced by ca. 7 mm in the set-up, and were contacted to the center of the bar by a spring load (cf. Figure 5.1).
For measurement on strips, both current and potential probes were applied to the sample (cf. Figure 5.1). For mechanical handling, the samples were placed on top of a ca. 2 mm thick

ceramic plate. The Pt wires were wrapped around the joined sample and support plate, guided by grooves cut mechanically into the support plate. Potential probes were placed symmetrically around the center of the sample spaced 12 mm apart. Current probes were attached at the ends. Pt paste was also applied to ensure contact. The paste was sintered at 1100°C for 1 hour before measurements.

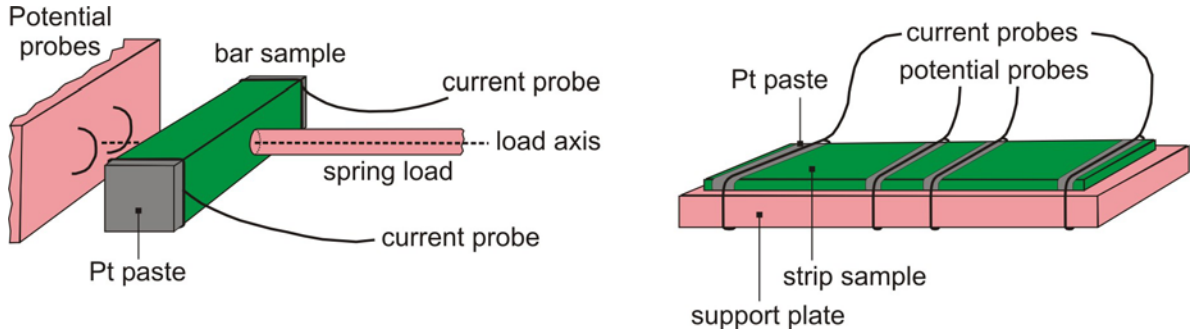

Figure 5.1. The experimental set-up for DC measurements on bar and strip shaped samples.

The samples were heated to the desired temperature (800-1200°C) in air, with a gas flow rate of 100 ml/min (adjusted at 25°C). The cermets were subsequently reduced in a dry 4.5 vol% H_2-N_2 mixture with the same total gas flow. In some cases, the temperature was changed during measurements. For the cermets, redox cycling was carried out by changing the gas flow to air for ca. 24 hours. N_2 was used as flushing gas for ca. 15 min in-between gas-shifts.
The pO_2 and the resistance were logged with 1-15 minutes interval. The resistance was measured using a Keithley 580 micro-ohmmeter. A current pulse defined by the hardware was enforced in both directions, and the potential between the probes measured. The resolution of the instrument in the measurement range of 200 mΩ was 10 μΩ. For reliability reasons, a measurement was rejected if the resistance for opposite current directions differed by more than 5%. Otherwise, the average of the two resistances was used. The average resistance (R_{ave}) was converted to conductivity (σ) as shown in Equation 5.1. The distance between the potential probes is denoted l, and a and b is respectively the sample width, and sample thickness.

Eq. 5.1 $$\sigma = \frac{l}{a \cdot b \cdot R_{ave}}$$

5.2.3 EIS measurements

The electrochemical tests were carried out on symmetrical cells cut into a size of 4 mm x 4 mm, or circular cells with a diameter of ca. 8 mm. To ensure satisfactory current collection, an additional current collect layer of Pt paste was applied to the anodes.
The impedance spectroscopy was carried out around OCV in a one-atmosphere set-up. The set-up could house 4 samples for testing at a time. The samples were heated to 850°C or 1000°C in air, and then reduced and aged in wet H_2 (H_2 + 3 vol% H_2O), or diluted wet H_2 in N_2 (9 vol% H_2 + 3 vol% H_2O + N_2). A total gas flow rate of 100 ml/min (adjusted at 25°C) of dry gas was used. The samples were exposed to reducing gasses for at least 1 hour prior to making measurements. In some cases, the samples were subjected to a period of oxidizing conditions, and then reduced again. The oxidation was obtained by changing the gas flow to air for 24 hours.
4-lead, 2-electrode impedance was measured in the frequency range 50 mHz to 1 MHz with an applied voltage of 25 mV using a Solartron 1260 FRA. The impedance spectra were acquired by the Risø National Laboratory Elchem software, and the spectra were fitted using ZView2 [66].

5.2.4 Other techniques

The microstructure of the samples was investigated with scanning electron microscopy (SEM). A Fei Quanta 600 equipped with an EDAX® thin window detector and EDAX Genesis software was used.
Sample porosity was quantified by mercury porosimetry, or by weighing and geometric gauging. The procedures were as described in Chapter 2, Section 2.2.2.

5.3 Results

5.3.1 Cermet conductivity

The conductivity, and simultaneously measured oxygen partial pressure (pO_2), for the sample 3Y-bar-1000-b as a function of time is shown in Figure 5.2. The profiles were acquired by continuous measurements during successive periods of reducing and oxidizing conditions as reflected by the course of the pO_2 curve.

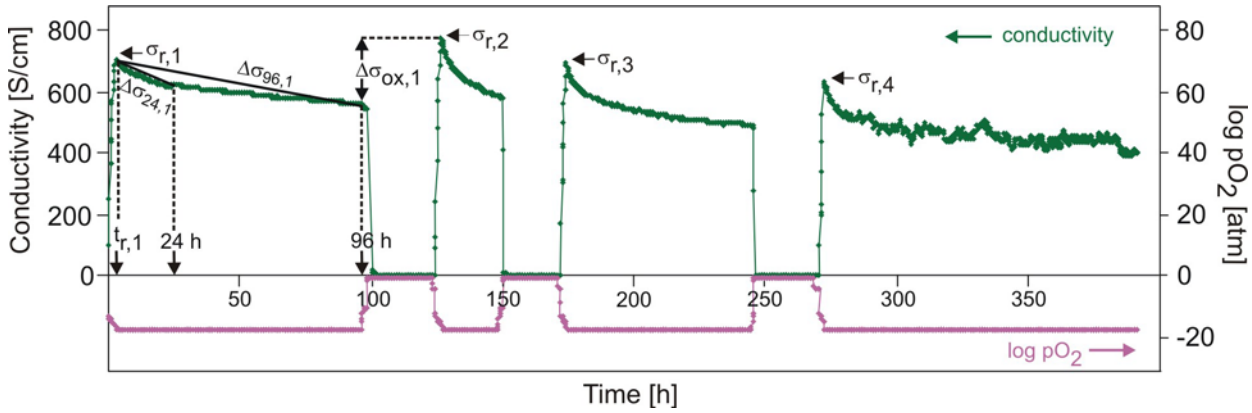

Figure 5.2. Conductivity and pO_2 profiles of the sample 3Y-bar-1000-b. The parameters used to characterize the electrical behavior are illustrated for the first reducing period (indicated with "1" in the subscripts). $\sigma_{r,1}$ and $t_{r,1}$ is respectively the time and conductivity at the initial complete reduction. $\Delta\sigma_{24,1}$ and $\Delta\sigma_{96,1}$ describes the degradation by the slope of the straight line between the initial complete reduction and the measurement points after 24 and 96 hours of reducing conditions. $\Delta\sigma_{ox,1}$ is the relative change in conductivity between before and after the first oxidizing event. For the following reducing periods corresponding parameters were defined.

The electrical behavior was characterized by the parameters: $\sigma_{r,i}$, $t_{r,i}$, $\Delta\sigma_{24,i}$, $\Delta\sigma_{96,i}$, and $\Delta\sigma_{ox,i}$, where i refers to the order of the reducing period. The parameters are illustrated in Figure 5.2 for the first reducing period (i = 1).
For the first reduction, the time was set to zero (t = 0 h) after constant temperature was attained, and when the reducing gas flow was started. The reducing conditions were immediately followed by an increase in conductivity as the reduction progressed into the sample (cf. Figure 5.2). When maximum or constant conductivity was obtained, the sample was assumed completely reduced. The time for complete reduction is denoted $t_{r,1}$, and the conductivity at this point is $\sigma_{r,1}$ (cf. Figure 5.2).
When the samples were held under reducing conditions, the conductivity was generally seen to decrease. The ageing was rapid in the beginning, and diminished with time. Full relaxation was not achieved during the measured periods (cf. Figure 5.2). To quantify the degradation, the slope of the straight line between the initial fully reduced state ($t_{r,1}$,$\sigma_{r,1}$) and the measured points after

respectively 24 and 96 hours of test, ($t_{24,1}$,$\sigma_{24,1}$) and ($t_{96,1}$,$\sigma_{96,1}$), was used. The slopes were denoted $\Delta\sigma_{24,1}$ and $\Delta\sigma_{96,1}$, and calculated as shown in Equations 5.2 and 5.3. The unit is S/cm/h.

Eq. 5.2 $$\Delta\sigma_{24,1} = \frac{\sigma_{24,1} - \sigma_{r,1}}{t_{24,1} - t_{r,1}}$$

Eq. 5.3 $$\Delta\sigma_{96,1} = \frac{\sigma_{96,1} - \sigma_{r,1}}{t_{96,1} - t_{r,1}}$$

The conductivity was observed to differ before and after an oxidizing event (cf. Figure 5.2). The relative change was denoted $\Delta\sigma_{ox,1}$, and calculated as shown in Equation 5.4.

Eq. 5.5 $$\Delta\sigma_{ox,1} = \frac{\sigma_{after,1} - \sigma_{before,1}}{\sigma_{before,1}}$$

Reproducibility

The variation in the electrical properties between identically prepared samples was investigated. The conductivity profiles for three sibling samples of the type 3Y-bar-1000 are shown in Figure 5.3. The conductivity is only illustrated for periods with reducing conditions. Arrows marked with "TC" and "n'th ox" indicates respectively temperature cycle and the n'th oxidizing event. Broken lines indicate periods where the measurements were interrupted by software failures.

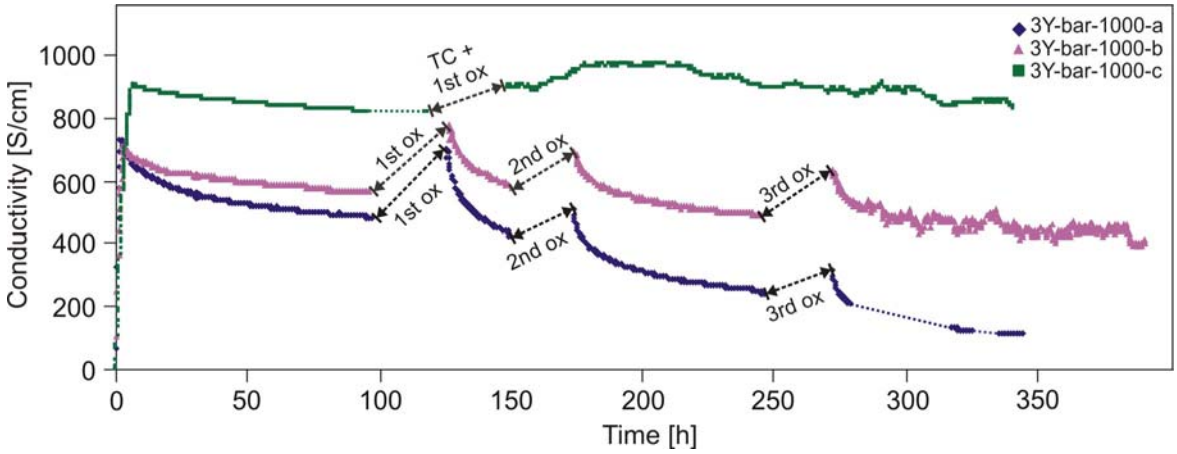

Figure 5.3. Conductivity profiles of three identically prepared samples of the type 3Y-bar-1000. The conductivity is only shown for periods with reducing conditions. Arrows marked with "TC" and "n'th ox" indicates respectively temperature cycle and the n'th oxidizing event. Broken lines indicate absence of measurements due to software interruptions.

The three samples displayed markedly different profiles. Identically prepared samples are generally expected to have similar microstructures. However, on the micro scale slight variations will inevitably be present. These variations appeared to be evident when measuring conductivity. The parameters characterizing the behaviors are listed in Table 5.2.

Measurements were done with at least 15 min interval. Thus, the uncertainty on the time for complete reduction ($t_{r,i}$) was 0.25 h. The uncertainty on the conductivity was estimated to 5%, and the uncertainty on the calculated degradation rates and oxidation effects was assumed to be 1 S/cm/h and 10%, respectively.

For the first reducing period (i = 1), the time for full reduction differed significantly between the three samples. Differences above 4 hours were observed, and the differences appeared to be maintained upon the succeeding reductions (cf. Table 5.2).

The fully reduced conductivity for the first period ($\sigma_{r,1}$) was approximately 700 S/cm for both sample a and b. However, sample c, which also displayed the longest time for fully reduction, showed a significantly higher conductivity in the range of a 100 S/cm (cf. Table 5.2). Upon the third reduction, a similar difference emerged between sample a and b (cf. Table 5.2).

Table 5.2. Electrical characteristics of three identically prepared samples of the type 3Y-bar-1000. The values in the last column marked with asterisk (*) are not directly comparable with the other samples due to different treatment between the first and second reducing period.

i	Parameter	Unit	3Y-bar-1000-a		3Y-bar-1000-b		3Y-bar-1000-c	
1	$t_{r,1}$	h	1.92	± 0.25	2.74	± 0.25	6.63	± 0.25
	$\sigma_{r,1}$	S/cm	731	± 37	706	± 35	905	± 45
	$\Delta\sigma_{24,1}$	S/cm/h	-7	± 1	-4	± 1	-2	± 1
	$\Delta\sigma_{96,1}$	S/cm/h	-3	± 1	-1	± 1	-1	± 1
	$\Delta\sigma_{ox,1}$	%	45	± 10	37	± 10	* 7	± 10
2	$t_{r,2}$	h	1.46	± 0.25	2.44	± 0.25	* 6.96	± 0.25
	$\sigma_{r,2}$	S/cm	699	± 35	776	± 39	* 899	± 45
	$\Delta\sigma_{24,2}$	S/cm/h	-11	± 1	-9	± 1	* 1	± 1
	$\Delta\sigma_{96,2}$	S/cm/h	-		-		* 0	± 1
	$\Delta\sigma_{ox,2}$	%	16	± 10	17	± 10	-	
3	$t_{r,3}$	h	1.50	± 0.25	2.32	± 0.25	-	
	$\sigma_{r,3}$	S/cm	509	± 25	693	± 35	-	
	$\Delta\sigma_{24,3}$	S/cm/h	-8	± 1	-7	± 1	-	
	$\Delta\sigma_{96,3}$	S/cm/h	-		-		-	
	$\Delta\sigma_{ox,3}$	%	24	± 10	31	± 10	-	

When comparing the degradations of the first reducing period, no significant difference was observed between the samples after 96 hours. However, on the short 24 hours scale the sample 3Y-bar-1000-a displayed faster degradation (cf. Table 5.2). Upon the following reducing periods, the short-term degradation increased into similar values for the samples 3Y-bar-1000-a and b (cf. Table 5.2).

The first oxidizing event was associated with ca. 40% improvement in the conductivity. The improvement appeared to diminish upon the following reductions. However, no difference within the uncertainty was observed in the oxidation effect between the samples. Sample c experienced a combined re-oxidation and temperature cycle after the first reducing period, which appeared to restrain the improvement (cf. Table 5.2).

Porosity

The reproducibility study showed that a significant scatter in some of the electrical characteristics ($t_{r,i}$, $\sigma_{r,i}$, $\Delta\sigma_{24,i}$) will be present due to slight microstructural variation between otherwise identically prepared samples. The structural variations were not visible with microscopy. However, the porosity of the as-sintered samples differed, and appeared to reflect the microstructural differences. The porosity of the samples tested at 1000°C as measured by geometrical gauging (ε_{geom}) is summarized in Table 5.3. The uncertainty on the measurements was estimated to be maximum ± 0.5%.

Table 5.3. As-sintered, geometrically gauged porosity (ε_{geom}) of the samples tested at 1000°C.

Sample	State	ε_{geom} [%]
3Y-bar-1000-a	As-sintered	8.5 ± 0.5
3Y-bar-1000-b	As-sintered	6.7 ± 0.5
3Y-bar-1000-c	As-sintered	4.6 ± 0.5
3Y-strip-1000	As-sintered	17.0 ± 0.5
8Y-bar-1000	As-sintered	3.4 ± 0.5
8Y-strip-1000	As-sintered	8.4 ± 0.5

The electrical properties of the first reducing period as a function of the measured as-sintered porosity are illustrated in Figure 5.4. The data not included in Table 5.2 can be seen in Appendix D, Table D1. The figure includes samples with the composition 3Y (red symbols) and 8Y (green symbols) that were tested at 1000°C. Error bars indicate the uncertainty on the electrical measurements. The uncertainty on the porosity corresponds to the size of the measurement points.

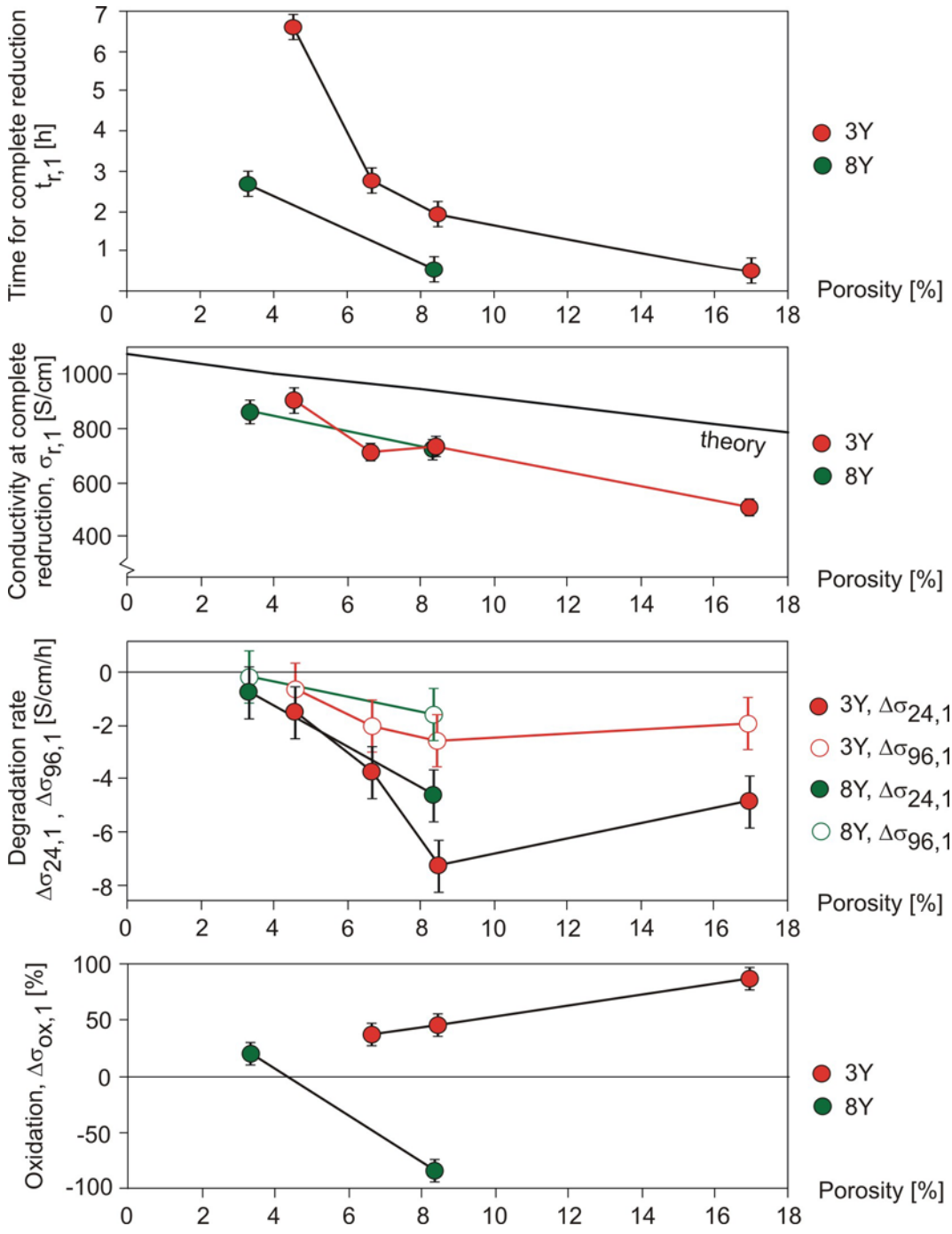

Figure 5.4. The electrical properties at 1000°C of the first reducing period as a function of the as-sintered porosity. Red symbols represent samples of composition 3Y, and green symbols represent 8Y. The relationship between porosity and conductivity described in [67] and [68] is illustrated in the diagram of the complete reduced conductivity ($\sigma_{r,1}$), and the curve denoted "theory".

A relationship between porosity and the electrical parameters appeared evident. The time for complete reduction decreased markedly when the porosity increased. A difference between the

two compositions was also observed. Longer times were required for complete reduction of 3Y compared to 8Y (cf. Figure 5.4).
The conductivity after complete reduction also decreased with porosity (cf. Figure 5.4). The decrease was generally in accordance with the trend of the relationship described in the literature (cf. Section 5.4.2).
A similar degradation pattern was seen for the two compositions. If the porosity was below ca. 8.5%, increase in porosity was associated with increased degradation. However, above 8.5% porosity, the degradation appeared unaffected by further increases in porosity (cf. Figure 5.4).
The relationship between porosity and the effect of the first oxidation differed between the two compositions. For the 3Y composition, higher porosity seemed to generate better conductivity upon the first oxidation. For the 8Y composition, higher porosity was observed to have the opposite effect (cf. Figure 5.4).

Composition of the ceramic component

From Figure 5.4 an effect of the yttria content in the ceramic component on the electrical parameters was indicated. The samples of the composition 3Y were more reluctant to reduction, and displayed slightly faster degradation rates, which were particularly evident on the 24 hour scale (cf. Figure 5.4). Also, the effect of the first oxidation was different for the two ceramic compositions. For samples with the composition 3Y, the oxidation was associated with a positive effect on the conductivity, whereas the oxidation generally appeared detrimental to samples with the composition 8Y (cf. Figure 5.4).

Temperature

To investigate the effect of the temperature on the electrical parameters, some of the cermets were reduced and redox cycled isothermally at temperatures between 800°C and 1200°C. The characteristics of the samples are listed in Table 5.4. The as-sintered geometrically based porosity of the samples is included in the table.

Table 5.4. Characteristics of the samples that were reduced and redox cycled isothermally at 800-1200°C. ε_{geom} denotes the as-sintered geometrically based porosity.

	3Y-bar-800		3Y-bar-850		3Y-bar-1000-b		3Y-bar-1200	
ε_{geom} [%]	6.7	± 0.5	8.5	± 0.5	6.7	± 0.5	6.4	± 0.5
$t_{r,1}$ [h]	5.49	± 0.25	9.03	± 0.25	2.74	± 0.25	3.72	± 0.25
$\sigma_{r,1}$ [S/cm]	781	± 39	775	± 39	706	± 35	769	± 38
$\Delta\sigma_{24,1}$ [S/cm/h]	-1	± 1	-3	± 1	-4	± 1	1	± 1
$\Delta\sigma_{96,1}$ [S/cm/h]	0	± 1	-		-1	± 1	0	± 1
$\Delta\sigma_{ox,1}$ [%]	-25	± 10	-		37	± 10	0	± 10

The time for complete reduction varied between 3-9 hours. The relationship to the temperature appeared complex, but generally longer times were required for the two low-temperature tests at 800°C and 850°C (cf. Table 5.4).
The conductivity after complete reduction is shown as a function of the temperature in the Arrhenius plot in Figure 5.5. Excluding the test at 1200°C, the conductivity increased with decreasing temperature as expected for an electronic conductor. The contribution from the YSZ phase to the conductivity was negligible (< 1 S/cm) in the investigated temperature range. For the test point at 850°C the conductivity was slightly above the linear trend defined by the points at 800°C and 1000°C. The porosity of this sample was also ca. 2% higher (cf. Table 5.4). Based on the theoretical curve shown in Figure 5.4, the 2% extra porosity was estimated to decrease the conductivity by ca. 30 S/cm. Thus, further deviation from the linear trend appeared when taking the difference in porosity into account.
A tendency to higher degradation rates at higher temperatures was observed. However again, the test at 1200°C displayed diverging behavior (cf. Table 5.4). Regarding the effect of the first

oxidizing event, improved conductivity was only observed for the sample tested at 1000°C (cf. Table 5.4).

The temperature of reduction is a possible parameter on the conductivity upon complete reduction. To investigate this, the measurements were compared with the Arrhenius plot of a model cermet, and a cermet that was reduced at 1000°C. The Arrhenius plots are included in Figure 5.5.
The applied model was the simulated Ni-YSZ cermet described by Sunde [69]. The cermet consisted of uni-sized particles with a radius of 1 μm organized in a cubic lattice, and where the Ni particle fraction was 0.5. The cermet reduced at 1000°C was of the same type as the samples in Table 5.4 (i.e. 3Y-bar-1000), however the porosity was slightly lower (4.6 ± 0.5%). After reduction the conductivity was measured with 50-100°C intervals from the 1000°C to 700°C. For each measurement the temperature was kept constant for 3 hours, and the average conductivity was used for the Arrhenius plot.

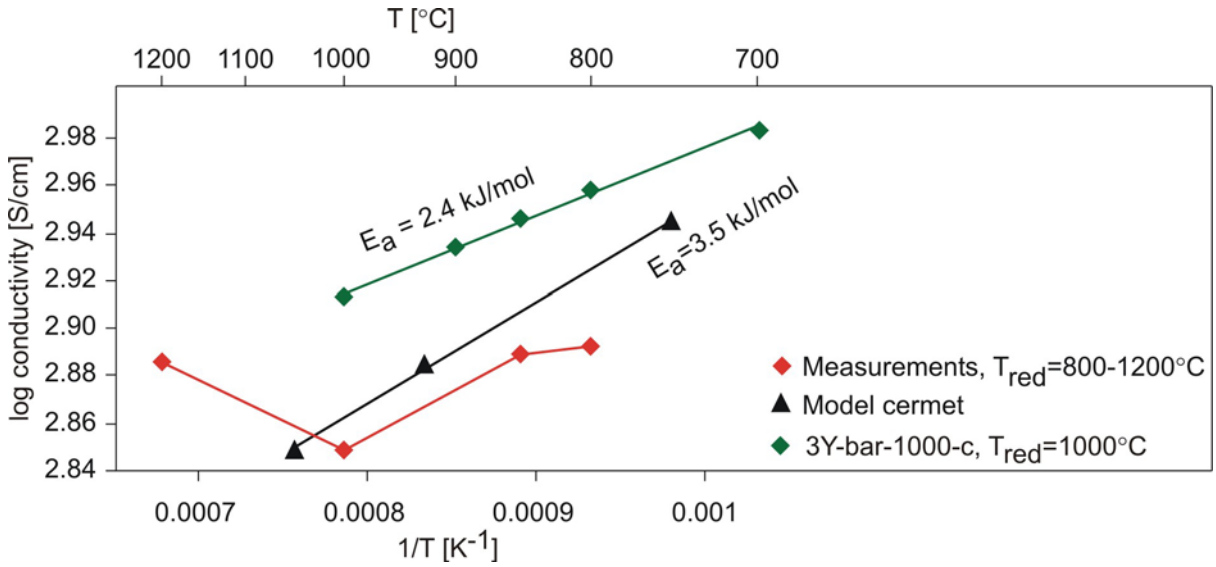

Figure 5.5. Arrhenius plots for samples reduced and tested at different temperatures (T_{red}) (shown with red), for a model cermet (black), and for a cermet reduced at 1000°C (green). The activation energy (E_a) based on the slope of the linear curves is included.

For the model cermet, and the cermet reduced at 1000°C, the conductivity increased linearly with decreasing temperature. However, the model cermet displayed lower conductivity values and higher activation energy for the investigated temperature range (cf. Figure 5.5).
When comparing the samples reduced at different temperatures to the model cermet and the cermet reduced at 1000°C, an effect of the temperature of reduction was indicated. Markedly different temperature dependence was observed for the samples reduced at different temperatures. For reductions carried out above 1000°C, the conductivity was observed to increase with the temperature, and for reductions below 850°C the temperature dependence was much weaker compared to the two linear trends (cf. Figure 5.5).
Below 1000°C the conductivity of the samples reduced at different temperatures was lower than the conductivity of the sample reduced at 1000°C. The difference was in the order of 100 S/cm (cf. Figure 5.5). However, the porosity also differed between the samples. The porosity of the sample reduced at 1000°C was ca. 2-4% below the porosity of the other samples (4.6% compared to 6.7 and 8.5%, cf. Table 5.4). Based on the linear relationship between porosity and conductivity shown in Figure 5.4 this corresponded to ca. 30-60 S/cm higher conductivity values. When considering the uncertainty on the measurements (cf. Table 5.4), the difference in the conductivity ranges between the samples was minor.

5.3.2 Measurements on porous YSZ

Microstructure

The porous YSZ structures were produced by dissolving the nickel phase with acid. Complete removal of the nickel upon the acid treatment was indicated by the associated weight changes, and SEM investigations. Backscatter electron micrographs (BSE) of the resulting structures are shown in the Figures 5.6a, b, and c.

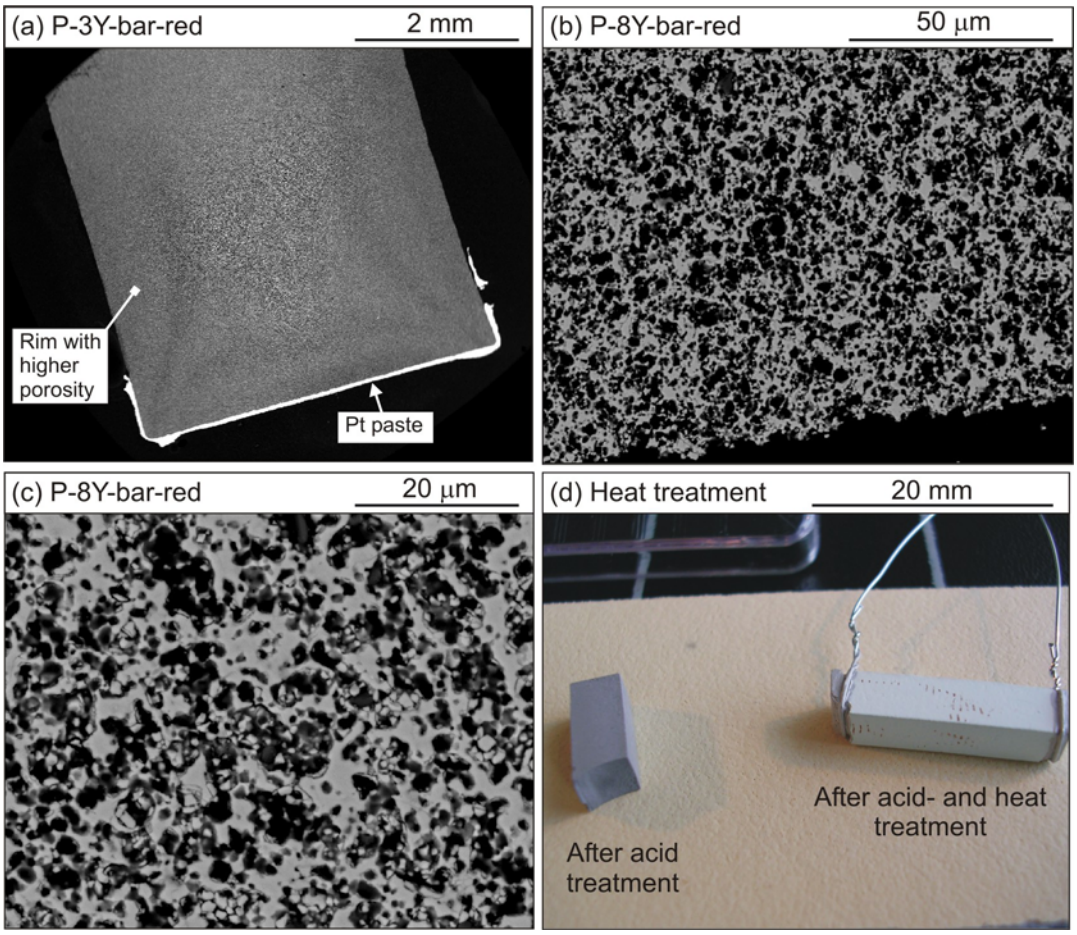

Figure 5.6. (a-c) SEM-BSE micrographs of samples subjected to acid treatment. (d) Photo of acid treated sample before and after heat treatment at 1100°C.

A gradient in porosity was suggested in the samples at lower magnification. The core of the samples appeared to contain lower porosity. Figure 5.6a illustrates this for the sample P-3Y-bar-red. The gradient was not related to the nickel content. Nickel was not detected in any of the zones by qualitative chemical analyses with EDS (energy dispersive spectroscopy).

Despite that complete Ni removal was verified by weight changes and EDS, the samples preserved a grayish color after acid treatment. The color vanished after heat treatment at 1100°C as illustrated in Figure 5.6d. This indicated that some of the Ni remained in the structure after the exposure to acid (causing the gray color), and then dissolved into YSZ upon heating (causing the gray color to disappear). However, the amounts of Ni causing the colors must be small, as the solubility of Ni in YSZ is significantly below 2.5 m/o [3].
The treatment with acid was observed to affect the ceramic phase as well. ICP-OES analyses (inductively coupled plasma optical emission spectroscopy) of the acids used, showed significant

traces of yttrium on the ppm-level [70]. Thus, to some degree, yttria was extracted and dissolved from the structures simultaneously with the dissolution of nickel.

The porosity of the samples was measured with mercury porosimetry after acid treatment. The pore size distributions and total porosity (ε_{Hg}) are shown in Figure 5.7.

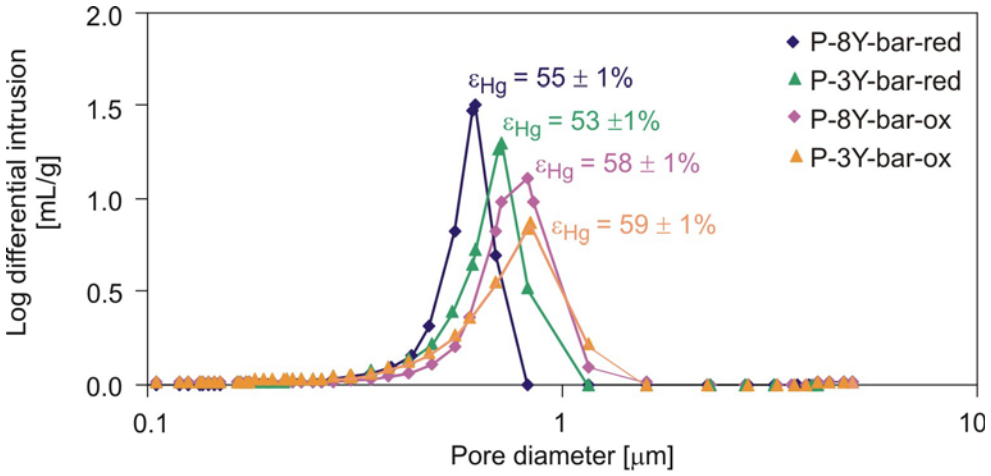

Figure 5.7. Pore size distribution and porosity (ε_{Hg}) of the porous YSZ samples after acid treatment as measured by mercury porosimetry.

The total porosity of the YSZ samples representing the YSZ structure in the reduced state was similar, cf. the blue (P-8Y-bar-red) and green (P-3Y-bar-red) curves in Figure 5.7. The pore size distribution appeared slightly coarser for the P-3Y-bar-red.
For both compositions, the total porosity was higher for the YSZ samples representing the YSZ structures of the re-oxidized cermets (i.e. P-8Y-bar-ox and P-3Y-bar-ox in Figure 5.7). The pore size distribution also appeared coarser in both cases.

Conductivity

The conductivity of the porous bar shaped samples were tested with the set-up illustrated in Figure 5.1. However in this case, infiltration of the Pt paste into the highly porous samples was a possible source of error on the measurements. The SEM micrograph in Figure 5.6a shows some of the applied Pt paste on the sample edge. The paste was seen to stay on the surface of the samples, and thus not believed to be a source of error.
The conductivity of the samples was measured in the temperature range 500-1000°C with 100°C intervals. Each temperature was held for 5-10 hours, and the average conductivity of the period determined. Arrhenius plots for the samples are shown in Figure 5.8. The Arrhenius plot for dense 8YSZ is included in the figure for comparison [71].
The conductivity of the porous samples was approximately an order of magnitude below the dense sample. However, the trend of the curves was similar with activation energy (E_a) of 84 kJ/mol (cf. Figure 5.8). When comparing the two compositions, the samples of 3Y composition displayed lower conductivity than 8Y (cf. Figure 5.8). This was in accordance with the general knowledge [1].
When comparing the samples representing the YSZ network in the reduced state with the samples representing the YSZ network of a re-oxidized cermet (i.e. comparison of P-8Y-bar-red with P-8Y-bar-ox, and P-3Y-bar-red with P-3Y-bar-ox), the conductivity was lower for the re-oxidized network. The relative decrease was more pronounced for the samples of composition 8Y (ca. 38%), compared to the 3Y composition (ca. 25%) (cf. Figure 5.8).

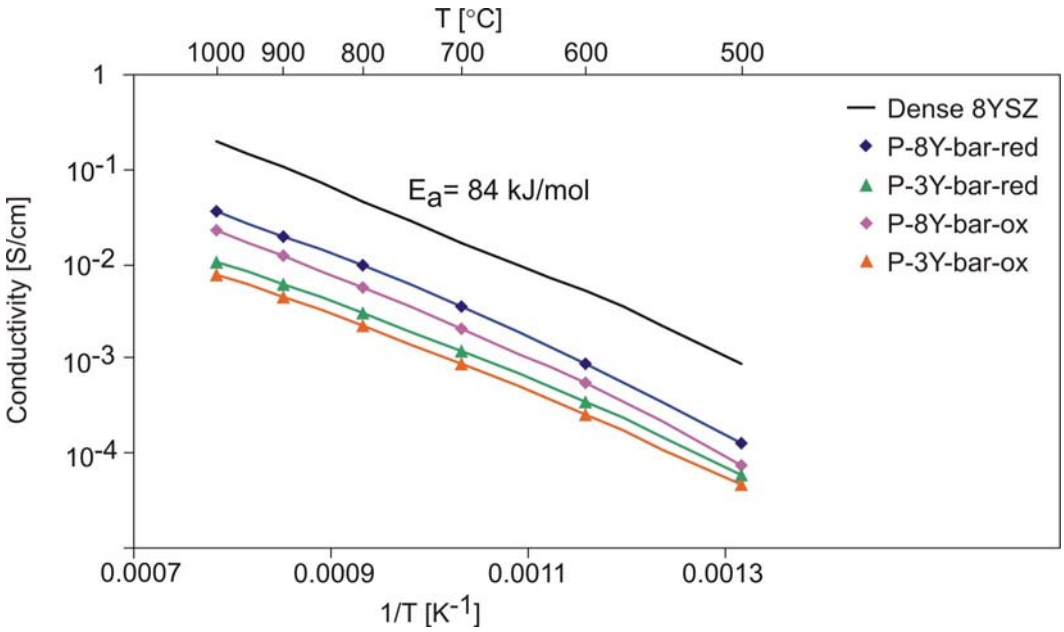

Figure 5.8. Arrhenius plots for dense YSZ, and the porous acid treated samples. The activation energy (E_a) based on the slope of the linear curve is included.

5.3.3 EIS on symmetrical cells

Impedance spectroscopy was performed on symmetrical cells before and after a redox cycle. Figure 5.9 shows the impedance spectra for the two types of cells before oxidation, tested in wet H_2 at 850°C and 1000°C. After the oxidizing event, spectra applicable for analyses were not obtained.

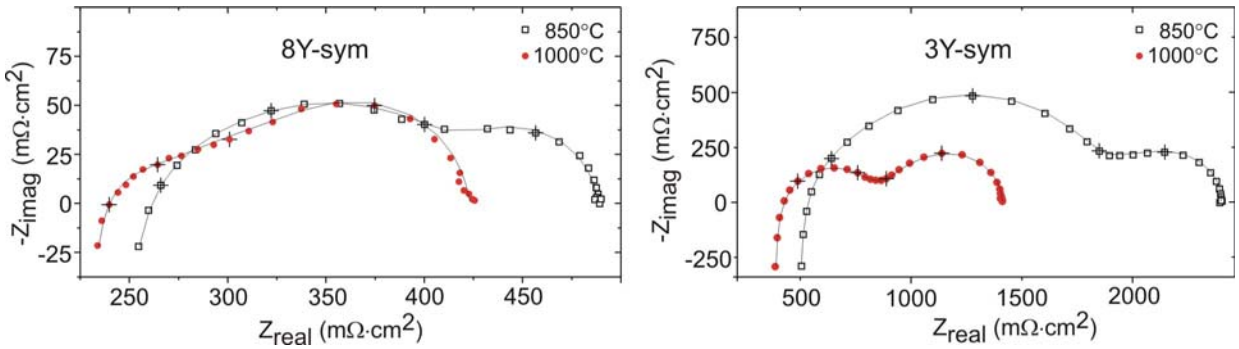

Figure 5.9. Impedance spectra for symmetrical cells of the type 8Y-sym and 3Y-sym obtained at 850°C and 1000°C in H_2 + 3 vol% H_2O. Crosses indicate the frequencies 25 kHz, 2.5 kHz, 0.25 kHz, 0.025 kHz. Black lines are fitted curves for 8Y-sym, and represent connection of data points for 3Y-sym.

Qualitatively, the resistance of 3Y-sym was observed to be much higher than the resistance of 8Y-sym. Both the series (R_s) and polarization (R_p) resistance was higher in the case of 3Y-sym. In addition, the electrolyte of 3Y-sym was half as thick as the electrolyte of 8Y-sym (cf. section 5.2.1), which further stresses the relation.

The conductivity is known to be lower for 3YSZ than 8YSZ (cf. Section 5.3.2 and [1]). Thus, a lower performance of 3Y-sym was expected. However, a part of the much worse performance is likely to be related to the microstructure. In fact, widespread delamination was observed in the as-prepared samples of 3Y-sym (cf. Figure 5.10a). Due to the delamination, current constriction was likely to contribute to the resistance in the 3Y-sym.

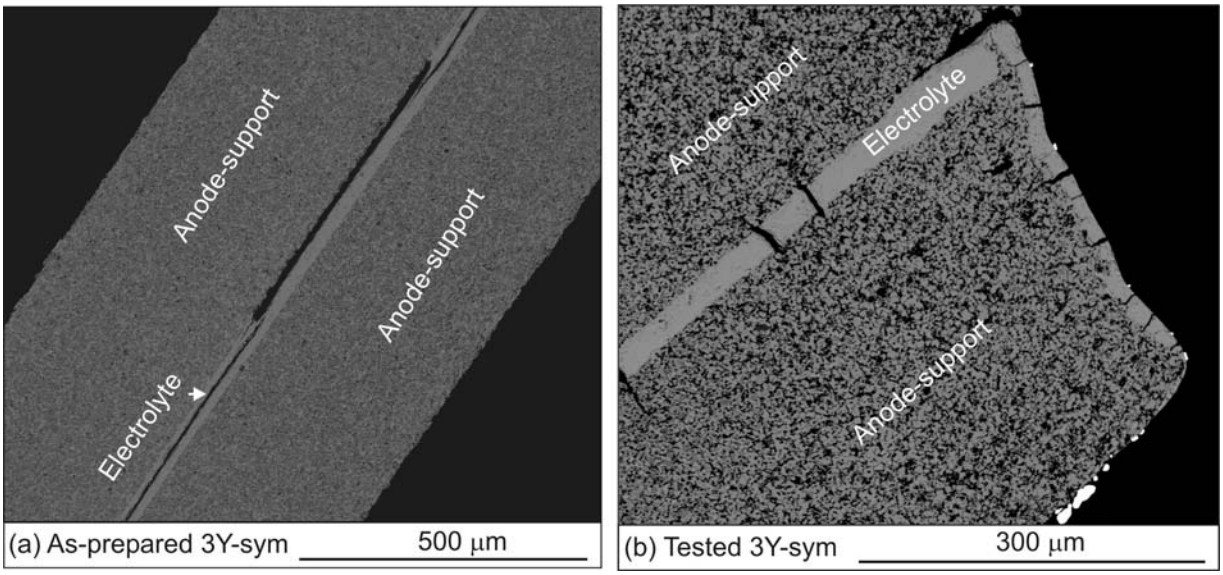

Figure 5.10. SEM-BSE micrographs. (a) As-prepared 3Y-sym before testing. (b) 3Y-sym sample after test and re-oxidation.

The polarization values of 8Y-sym were qualitatively observed to be in the range of 200 $m\Omega \cdot cm^2$ (cf. Figure 5.9). This was ca. a factor of 2 higher than for previously measurements [3], where values below 100 $m\Omega \cdot cm^2$ were reported for electrolyte-supported symmetrical cells with similar electrode composition.
The test set-up used for the previous measurements was designed for minimizing gas diffusion limitations. The set-up was not used in the present study. Diffusion resistance may constitute a considerable part of the polarization, if this is not taken into account in the test set-up [65]. Thus, the low frequency arc in Figure 5.9 is believed to represent diffusion limitations. When excluding the diffusion contribution in Figure 5.9, the polarization resistance of 8Y-sym at 850°C was estimated to 60-100 $m\Omega \cdot cm^2$ [72], which was in agreement with the values previously obtained.
Cracks in the electrolyte were observed in cells subjected to a re-oxidizing event (cf. Figure 5.10b). The cracks formed perpendicular to the electrolyte layer, and were seen in both types of symmetrical cells.

5.4 Discussion

5.4.1 Ni sintering

Degradation of the cermet conductivity generally followed immediately upon complete reduction (cf. Section 5.3.1.). The decrease in the electronic conductivity is believed to reflect Ni coarsening and agglomeration. Grain growth and particle coalescence will imply loss of nickel particle contacts. When the number of contact points decreases, so does the number of electrical pathways. The decrease in percolation degree causes the observed decrease in bulk conductivity. Similar observations have been reported in the literature [10, 36, 41, 44, 45, 73]. The driving force for the nickel sintering has been ascribed to the poor wettability between Ni and YSZ [11, 74, 75].

The degradation in conductivity decreased with time. The degradation was particularly strong during the first 24 hours, and diminished subsequently. The bulk conductivity reflected the decrease in Ni sintering with time, as predicted by thermodynamics. The difference in surface

energies that drives the sintering process varies inversely with particle size, and the sintering will slow down as it proceeds with an asymptotic trend [76].
The conductivity profiles were fitted to estimate the restriction on the lifetimes due to sintering. The degradations were fitted to either power or exponential decays. Fitting the data to the same type of decay did not give convincing results. This indicated that different sintering mechanisms were dominant for the investigated samples depending on the sample composition and microstructure. The fits for the two strip shaped samples, and for the sample displaying the lowest degradation after 96 h, which was 8Y-bar-1000, are illustrated in Figure 5.10. The equations for the fits describing the conductivity (σ) as a function of time (t) are shown in Equations 5.6-5.8.

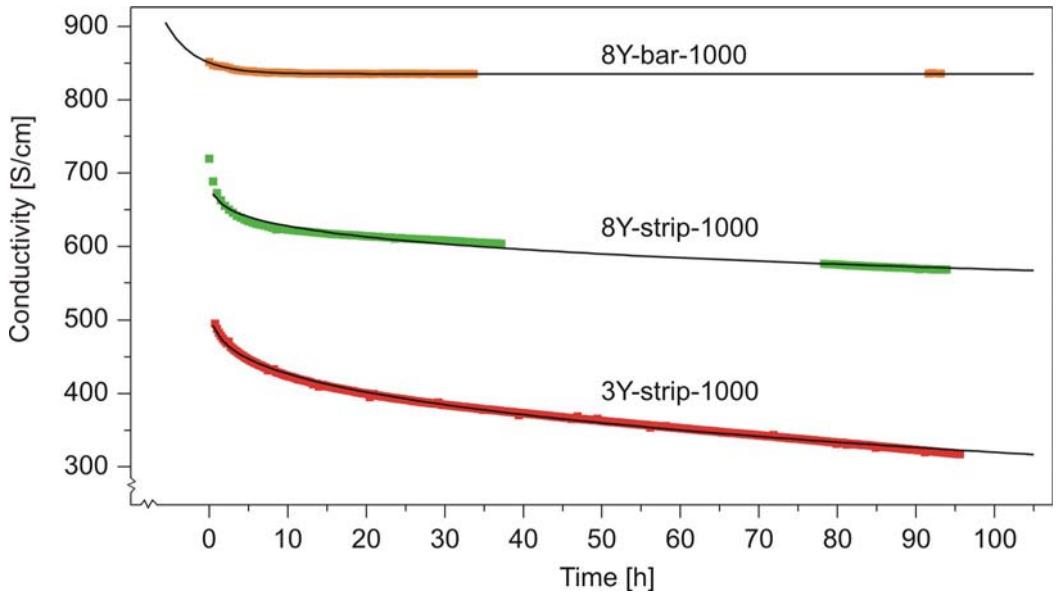

Figure 5.10. Fits of the conductivity degradation profiles during the first reducing period.

Eq. 5.6 8Y-bar-1000: $\sigma(t) = 15.14 \cdot \exp\left(\frac{-t}{3.65}\right) + 835.30$

Eq. 5.7 8Y-strip-1000: $\sigma(t) = 716.80 - 53.60 \cdot t^{0.22}$

Eq. 5.8 3Y-strip-1000: $\sigma(t) = 536.67 - 55.67 \cdot t^{0.29}$

The commercial required lifetime for an anode structure is 40,000 hours, within which enough conductivity (> 100 S/cm) must be maintained [10]. The fits indicated that the conductivity will not drop below 100 S/cm for the samples 8Y-bar-1000 and 8Y-strip-1000 within this time frame. For the sample 3Y-strip-1000 the limit of 100 S/cm will be reach after 1215 hours of operation at 1000°C.
The 3Y-strip-1000 represent the technological anode-support structure, and the fit indicates that the present degradation rate is not commercial tolerable. However, long-term tests on full cells have indicated that the conductivity of the anode is not the main restriction on the lifetime of operation [77, 64]. Thus, long-term conductivity experiments are believed to be required for more precise estimates of the lifetimes.

The degradation was observed to be influenced by the sample porosity, composition of the ceramic component, and the test temperature (cf. Section 5.3.1). The porosity did not appear as a relevant parameter for improvement of the anode. An effect on the degradation rate was only

indicated for sample porosity below 8.5%. Higher yttria content of the ceramic component reduced the degradation significantly. Thus, the composition of the ceramic component appeared as a parameter of technological relevance. Also the temperature appeared as a significant parameter. Lowering the test temperature generated lower degradation.
In the literature, the composition of the ceramic component has also been pointed out as an important parameter [44, 45, 73, 78, 79]. Further, an effect of the presence and content of water [36, 78], and an effect of the local porosity environment has been reported [75, 80, 81].

For more precise estimates of the cermet lifetime, and the influencing parameters, long-term experiments, or knowledge of the sintering mechanism, and detailed descriptions of the sintering kinetics, are needed. Analytical descriptions of the nickel sintering are difficult to obtain due to the numerous influencing parameters, which in some cases also are difficult to quantify. In addition, the sintering process includes a stochastic nature.
However, the sintering of Ni catalysts has been described extensively in the literature [76, 82]. For the Ni catalysts, two sintering models have been proposed, and described analytically. The models are atom migration (Ostwald ripening) and crystallite migration (coalescence). The Ostwald ripening process describes migration of metal atoms from one particle to another. The migration takes either place on the surface of the solid, or in the gas phase, depending on the temperature. The coalescence process involves migration of the metal crystallites themselves on the support. Bigger particles are then formed when particles collide. Surface atom mobility is believed to enable the migration of the crystallites [76].
Although the anode structure has similarities to the nickel catalysts, major differences are the nickel loading and the operation temperature. The required electrical percolation of the anode involves higher nickel contents, and direct contact between most of the nickel particles. This is believed to alter the sintering mechanisms and kinetics markedly. At elevated temperatures, the surface self-diffusion coefficient for Ni is high, and the Ni surface described as mobile Ni atoms behaving as a two-dimensional reactive gas [3]. Even though the sintering mechanism in the anode corresponds to the coalescence model of the catalyst, the microstructural different anode system is likely to generate different sintering kinetics.

5.4.2 Porosity

The porosity appeared as a significant parameter on the electrical properties (cf. Section 5.3.1). Generally, the relationship between porosity (P) and the conductivity of the Ni-YSZ cermets has been described with a power as shown in Equation 5.9 [63, 67, 68]. k is a constant for a specific material system.

Eq. 5.9 $$\sigma(P) = k \cdot (1 - P)^{1.5}$$

The trend predicted by Equation 5.9 was in general accordance with the observations. Thus, the equation was considered viable for correction, when comparing samples with different porosity.

5.4.3 Temperature of reduction

The sample reduced at 1000°C displayed higher conductivity and a weaker temperature dependence, than predicted from a simulated model cermet (cf. Section 5.3.1). The difference may be explained by the structure in the model being an approximation, and by the temperature dependence assumed in the model. In the literature, twice as high activation energies have been reported for similar structures [67].

The temperature of reduction appeared to influence on the formation of the Ni network. Better percolation was indicated for reduction temperatures above 1000°C, and worse percolation was indicated to form when reduction was carried out below 850°C. Similar observations were reported by Grahl-Madsen et al. [40].

5.4.4 Re-oxidation

The conductivity improved upon the first oxidation at 1000°C (cf. Section 5.3.1). The improvement was believed to reflect the reorganization of the re-oxidized NiO phase as described in Chapter 3. If the oxidation proceeds fast, the nickel particles were seen to divide into several particles, which then grew into the surrounding voids. Thus, upon re-reduction, a better percolating Ni network will form.
For the low-porosity samples, the conductivity degraded faster upon the second reduction (cf. Section 5.3.1). The increased degradation was believed to reflect the damage, and the associated increased porosity, formed upon the oxidation, as described by the model in Chapter 2.

The change in conductivity related to the oxidations, was seen to depend on temperature. This was in accordance with the observations that the oxide growth depended on the temperature (cf. Chapter 3). However, no improvement in conductivity was associated with the oxidations carried out at 800°C and 1200°C (cf. Section 5.3.1). For temperatures above 800°C, split up of the growing NiO particles was expected (cf. Chapter 3).
However, the damage on the cermet associated with the oxidation is also believed to be influenced by the temperature. Less damage was indicated at lower temperatures (cf. Chapter 2). Thus, the lack of improvement observed at 800°C is ascribed to restrictions on the voids for the NiO growth. For the experiment at 1200°C, the damage upon oxidation was severe, which prevented the formation of a better percolating Ni network.

The change in conductivity upon oxidation also depended on the order of the oxidation (cf. Section 5.3.1). The oxidizing events were initially seen to have a positive effect on the conductivity. However, upon successive cycles the effect diminished, and in some cases became negative. The development is believed to reflect the increasingly damaged structure as described in Chapter 2, where the formation of a well-percolating Ni-network becomes increasingly difficult.
The positive effect of the oxidation diminished faster for the more porous samples, and samples with the composition 8Y. In accordance with the model described in Chapter 2, the indicated faster damaging of these structures is ascribed to their lower mechanical strength.

5.4.5 Conductivity of porous YSZ

The acid treatment for removal of nickel was indicated to leave traces of nickel in the structure, and to extract yttria from the ceramic component (cf. Section 5.3.2). Still, the conductivity measurements of the resulting samples appeared to be an appropriate measure for the porous YSZ structure. In accordance with expectations, the conductivity of porous 3YSZ was lower than that of 8YSZ with similar porosity.
Re-oxidation of nominally identical cermet samples resulted in YSZ networks with higher porosity, slightly coarser pores, and lower conductivity (cf. Section 5.3.2). The observations were in agreement with the model described in Chapter 2, where the oxidation was suggested to imply damage on the YSZ network. Further in agreement with the model, less damage on the mechanically stronger 3YSZ network was indicated by the conductivity measurements. The

changes in porosity appeared to be too subtle, to reflect any differences between the tow ceramic compositions.

5.4.6 Method

Short-term (< 24 h) reorganization of the Ni-phase is in the literature reported from electrical measurements [36, 40, 41]. However, for microscopic verification of the coarsening, and quantitative correlation, long-term experiments (typically > 1000 h) are needed [10, 11, 73, 83]. Despite the high sensitivity of the method, in principle inter-particle changes in the range of few angstroms will affect the electrical contacts, the electrical measurements appeared to be a useful quantitative measure of the cermet microstructure, and the microstructural changes on both the short-term and long-term scale. For comparison, microscopy provides much lower resolutions (of the order of 0.1 μm for scanning electron microscopy [3]), and only two-dimensional observations of the structure. Thus, electrical measurements are believed to be a useable tool for the anode development.

5.5 Conclusions

The changes in the nickel-YSZ anode microstructure upon redox cycling were characterized with DC conductivity and EIS measurements. The conclusions are:

- The slight microstructural variations between identically prepared samples generated a significant scatter in some of the electrical properties. The influenced parameters were: the time for complete reduction, the conductivity upon complete reduction, and the 24 hours degradation rate.

- The as-sintered porosity was observed to reflect the scatter in the electrical parameters of the identically prepared samples. Thus, the porosity was a sensitive indicator of the microstructure as measured by conductivity.

- Samples with higher porosity displayed shorter times for complete reduction, and lower conductivity upon complete reduction. For the samples with porosity below 8.5%, the degradation rate increased with increasing porosity. For sample porosity above 8.5%, the degradation rate appeared unaffected by increased porosity.

- The observed relationship between sample porosity and conductivity was consistent with descriptions in the literature, where the conductivity was related to the porosity (P) by the power: $(1\text{-}P)^{1.5}$.

- The yttria content of the ceramic component was observed to influence on the electrical properties. Lower stability of the Ni-3YSZ system, compared to the Ni-8YSZ system, was suggested by higher degradation rates, and longer times for complete reduction.

- The conductivity degradation was related to sintering of the nickel phase. The lifetime of the samples was estimated by fitting to power or exponential decay. The degradation rates were not believed to be the main limitation on the lifetime of operation. However, long-term experiments are needed for better evaluations of the lifetime.

- The temperature influenced on the electrical properties. In accordance with general knowledge, lower temperatures were associated with longer times for complete reduction, and lower degradation rates. The temperature at which the reduction was carried out was indicated to influence on the formed Ni network. Better percolation was suggested to form at higher temperatures, where the Ni mobility was higher.

- The electrical observations were in accordance with the model of the redox mechanism proposed in Chapters 2 and 3.

  • Damage of the ceramic network upon re-oxidation was supported by increased porosity, and lower conductivity of the YSZ structures of cermets subjected to a redox cycle.

  • Reorganization of the NiO phase upon re-oxidation was indicated by the increased conductivity following oxidations at 1000°C. Further, in accordance with the observations in Chapters 2 and 3, the change in conductivity upon oxidation was temperature dependent.

  • The mechanically stronger 3Y composition appeared more redox resilient. Less damage on the YSZ network was indicated from the conductivity measurements on the porous YSZ network and on the cermets.

- DC conductivity measurements appeared as a sensitive measure of the anode microstructure. Thus, electrical characterization is a viable method for evaluating microstructures and microstructural changes.

- A method for measuring the electrochemical performance of the technological anode by application of symmetrical cells was developed. However, further verification is needed before the method can be applied as a development tool.

Acknowledgement

N. Bonanos is acknowledged for help in designing and performing the DC conductivity measurements. R. Barfod (Risø National Laboratory) is acknowledged for fitting the impedance spectrum of 8Y-sym. K. V. Hansen (Risø National Laboratory) is acknowledged for providing the ICP-OES analyses.

6 Optimal shape of thin tensile test specimen

6.1 Introduction

The prevalent solid oxide fuel cell (SOFC) design consists of ceramic laminates with thickness far below 1 mm. The mechanical properties of the ceramic layers are a key factor on the reliability and stability of the technology [19, 31, 54]. The strength of the anode support was indicated to be an important parameter on the redox performance [84].
A suitable test method for mechanical characterization of thin samples is lacking. Flexural tests are problematic due to elastic flexibility. The flexibility leads to large sample deflections and resultant frictional forces in the set-up [25, 29]. Tensile testing on anode materials has been limited to samples of rectangular shape, where stress concentrations in the specimen fixation area were critical [25]. However, the method may be improved by design of the specimen shape. Reduced stress concentration is intuitively achieved when introducing a transition zone between fixation and gauge section.
For tensile test specimen, the transition zone has traditionally been defined with a circular boundary [85]. However, further optimization is possible with finite element (FEM) analyses [85, 86, 87]. For an axisymmetrical sample, a reduction in the stress concentration from 28.8% to 9.9% was reported by modifying the circular transition zone using FEM [85].
In this chapter improved designs for a thin sample in tensile load was developed using FEM analyses. The technological applicability of the designs was tested on the technologically relevant SOFC anode supports.

6.2 Method for shape optimization

The problem to be solved concerns a planar specimen with a straight-sided gauge section, and with wider ends, so that higher stresses are generated in the gauge section. The zone between the wide end and the gauge section is the transition zone. By optimizing the shape of the transition zone, the stress concentrations can be minimized. The optimizations were performed using the gradient based structural design optimization system ODESSY (Optimum DESign SYstem), developed at the Institute of Mechanical Engineering, Aalborg University [88, 89].
On grounds of symmetry, the design problem was approached based on the geometry of one quarter of a specimen. The geometry was defined by a set of points and curves as illustrated in Figure 6.1. Points were numbered and prefixed "p", curves were prefixed "c". For definition of the curve c6, a quadratic B-spline was used. B-splines define a smooth curve constructed from a number of control points. For quadratic B-spline curves the smoothing is accomplished by piecewise second-degree polynomial curves. Curve c6 is defined as the quadratic B-spline of the points: p6, pc6_0, pc6_1, pc6_2, pc6_3, pc6_4, pc6_5, and p7 (cf. Figure 6.1).
The dimensional geometry of the test specimen as defined on Figure 6.1 was investigated using finite element analysis, and gradient based shape optimization in order to find the design with the lowest stress concentration possible, i.e. with the minimum maximum principal stress.
The design optimization problem is solved in an iterative loop based on finite element analysis, analytical design sensitivity analysis, and mathematical programming. In this case SLP (Sequential Linear Programming) is used for solving the mathematical programming problem.
It is noted that the boundary conditions are prescribed stresses at the external boundaries. Thus, according to the Michell theorem (1899) the stress field of the two-dimensional body is independent of the elastic properties.
Optimizations were performed with two gauge section lengths (cf. Figure 6.1): $L_1 = 2B$ (denoted design 1), and $L_1 = 14B$ (denoted design 2). The length of the transition zone (ΔL), and the length of the end zone (L_0) were fixed at respectively $\Delta L = 4B$ and $L_0 = B_0$. The width of the end

zone (B_0) was tentatively varied between $B_0 = 1.5B$, $B_0 = 2B$, and $B_0 = 3B$. $B_0 = 3B$ was chosen for the optimizations of the shape of c6.

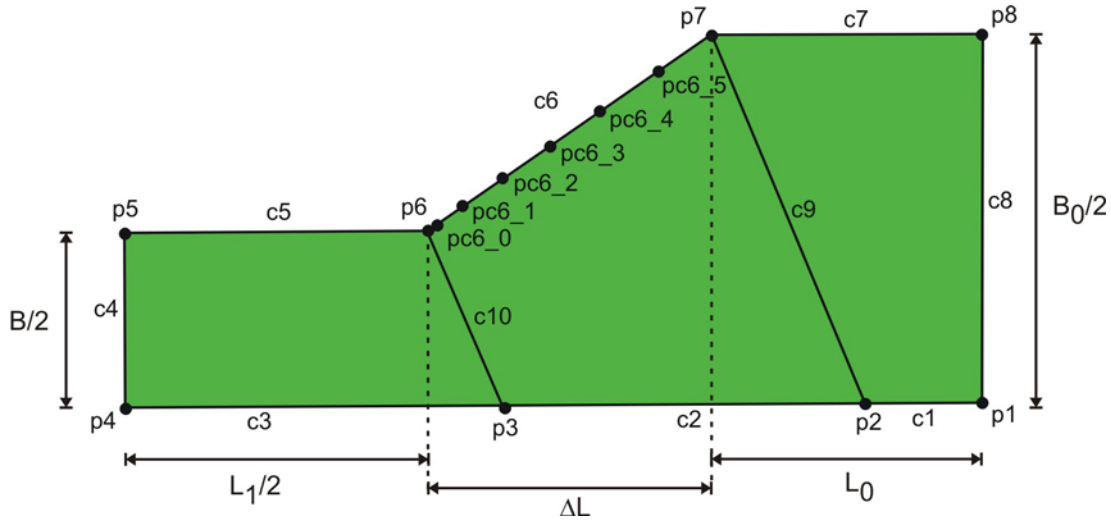

Figure 6.1. The start geometry of one quarter of a specimen. The geometrical dimensions were defined by the numbered points (prefixed "p"), and curves (prefixed "c"). The shape of the curve c6 is defined as the quadratic B-spline of the points on the curve. The dimensional parameters are indicated: B_0 denotes the width of the end zone, B is the width of the gauge section, L_1 is the length of the straight-sided gauge section, ΔL is the length of the transition zone, and L_0 is the length of the end zone.

6.3 Experimental

6.3.1 Sample preparation

Anode supports with dimensions and compositions corresponding to the technological material were prepared. The samples were produced from powders of NiO (purity 99% from Alfa Aesar), 3 mol% Y_2O_3-stabilised ZrO_2 (3YSZ) (TZ-3YB from Tosoh Co.), and Al_2O_3 (Catapal® from Sasol). The powders were mixed in weight fractions of 55.7%, 43.7%, 0.6%, respectively, and processed into a slurry. Thin foils were subsequently made by tape casting, and the foils were sintered at 1300°C to a thickness of ca. 300 µm.
The sintered foils were cut by laser into the defined optimized shape. Data on the shape was transmitted to the laser control system as a high-density number of (x,y)-points.
Tabs for fixation of the sample in the test set-up were mounted onto the samples. The tabs were made of 1 mm aluminum plates, and equipped with an axial-centered hole at which the specimen was fixed in the set-up (cf. Figure 6.6). The hole for fixation was placed at considerable distance from the sample. The width of the tabs was B_0, and they were attached to the last 4 mm of the end zone of the sample. At each end, the sample was sandwiched in-between two tabs. Irregularities from the laser along the cut edge were removed before the tabs were mounted. For mounting, cyanoacrylate glue was used.

6.3.2 Experimental procedure

Uniaxial tensile load was achieved using an Instron model TT-CM no. A-0050. The load was applied vertically through the tabs mounted on the samples. A displacement rate of 0.5 mm/min was used, and data logged every 0.33 seconds.
The samples were examined with scanning electron microscopy (SEM). A Fei Quanta 600 equipped with an EDAX® thin window detector and EDAX® Genesis software was used.

6.4 Results from shape optimization

6.4.1 Design 1 (L_1 = 2B)

The distribution of the normalized stress levels for the optimized design 1 with a short gauge section is shown in Figure 6.2. The normalized stress levels correspond to the stress concentration factors.

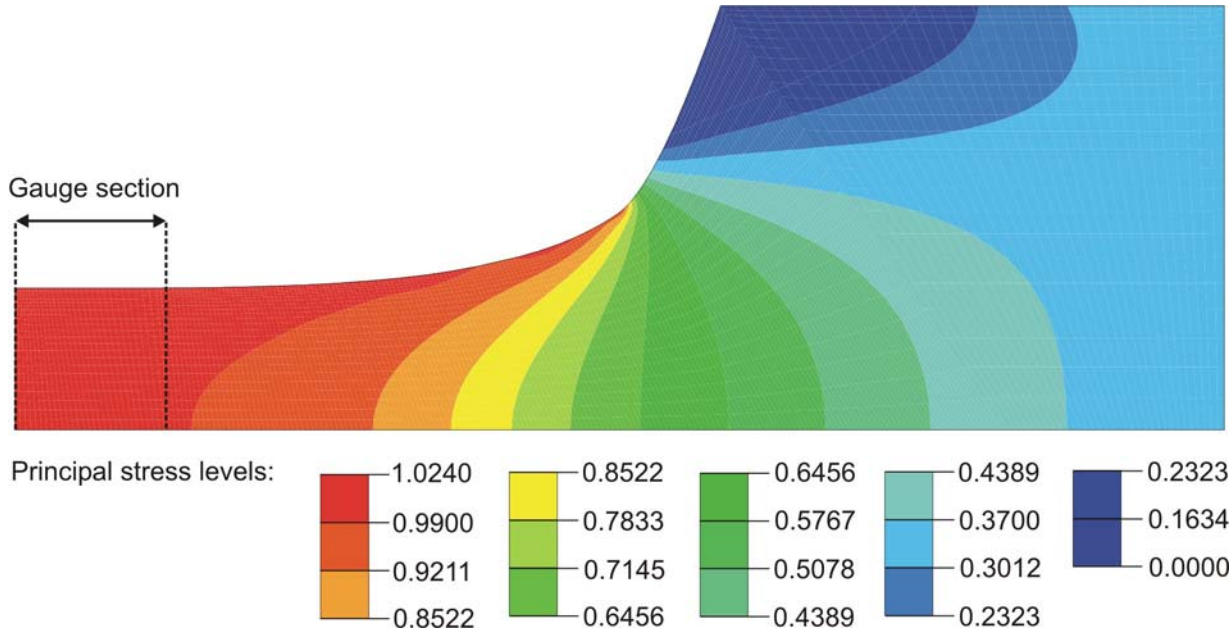

Figure 6.2. Distribution of the normalized stress levels in the optimized design 1 with short gauge section, and the geometrical constraints: L_1=2B, ΔL=4B, L_0=B_0, and B_0=3B.

The maximum principal stress for the design was 1.02, which occurred in the gauge section and along the edge of the transition zone. In the central part of the transition zone and the fixation area, stress concentration factors far below 1 occurred (cf. Figure 6.2).
The gauge section was defined as the part of the straight-sided section, where the stress concentration variation was ± 1%. The gauge section is indicated in Figure 6.2.
With this design, B_0 was tentatively reduced from 3B to 2B and 1.5B. However, changing the geometric constraint did not improve the optimized stress state significantly. Thus, B_0 = 3B was chosen for further use.

6.4.2 Design 2 (L_1 = 14B)

The distribution of the normalized stress levels (or stress concentration factors) for the optimized design 2 with a long gauge section is shown in Figure 6.3.
The maximum principal stress for the design was 1.004, which occurred in the gauge section and along the edge of the transition zone (cf. Figure 6.3). The gauge section was defined as the part of the straight-sided section, where the stress concentration was below ± 1%, as indicated in Figure 6.3.

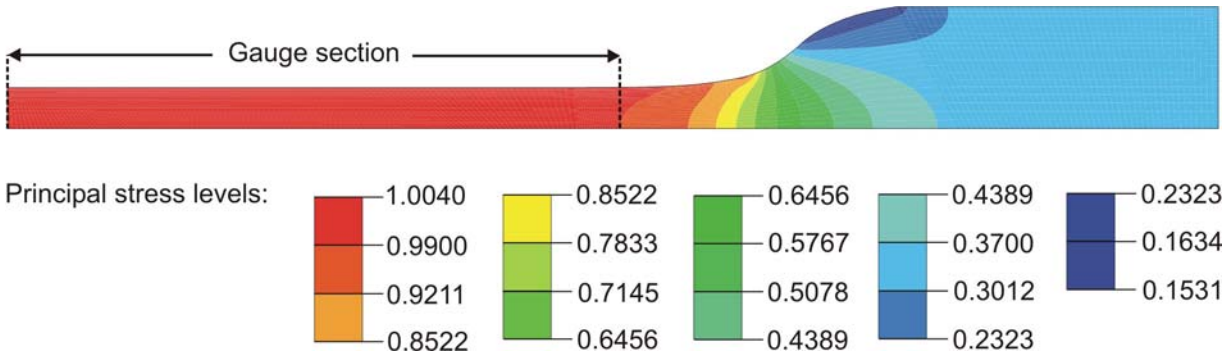

Figure 6.3. Distribution of the normalized stress levels in the optimized design 2 with a long gauge section, and the geometrical constraints: L_1=14B, ΔL=4B, L_0=B_0, and B_0=3B.

6.5 Results

6.5.1 Microstructure before testing

Figure 6.4a-c shows SEM-SEI micrographs (secondary electron images) of the laser cut surfaces.

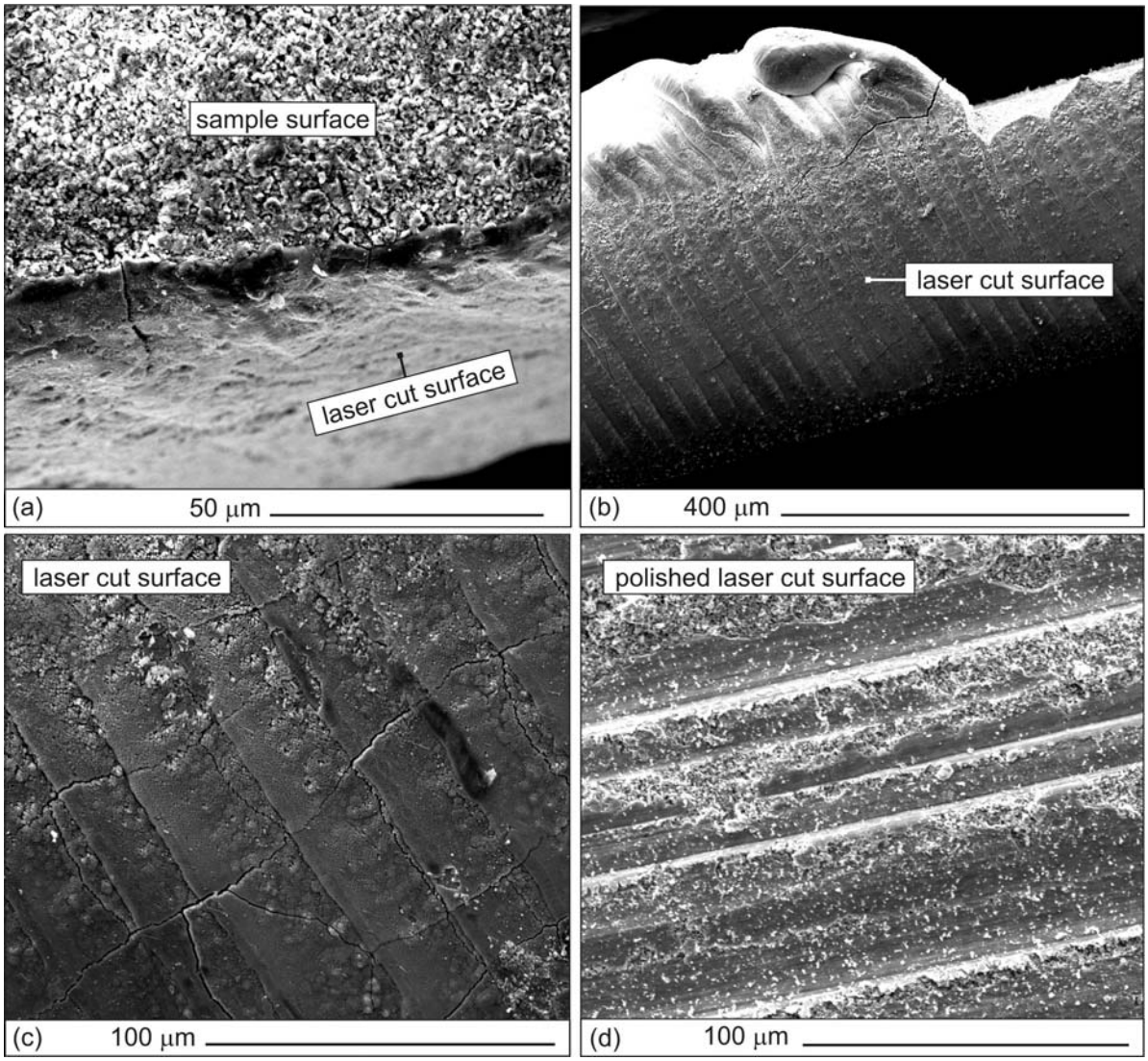

Figure 6.4. SEM-SEI micrographs. (a) Profile of the laser cut surface. (b,c) Laser cut surface. (d) Laser cut surface after mechanical polishing.

In accordance with previous investigations [90, 91] laser cutting affected the investigated samples surfaces significantly. The surface appeared denser compared to the granular appearance of the as-sintered sample surface (cf. Figure 6.4a), marks from the laser pulses were evident (cf. Figure 6.4b), and associated with substantial cracking (cf. Figure 6.4c). Further, a ridge of material from the cutting process formed along the cut edge. In some places, the ridge was torn off during handling. However, this did not appear to affect the surface (cf. Figure 6.4b).
The marks from the laser were believed to be shallow, as they were not visible in profile (cf. Figure 6.4a). However, the surface condition of a tensile specimen is known to influence on the strength measurements [29]. Thus, the defects introduced during cutting were attempted to be removed by mechanical polishing with a CNC (computer numerical control) controlled diamond cutting instrument. A SEM-SEI micrograph of a laser cut surface after polishing is shown in Figure 6.4d. However, the polishing appeared just as detrimental as the laser cutting to the surface, and was not further used.

6.5.2 Microstructure of tested samples

SEM-SEI micrographs of the fractured surfaces of the tested samples are shown in Figure 6.5.

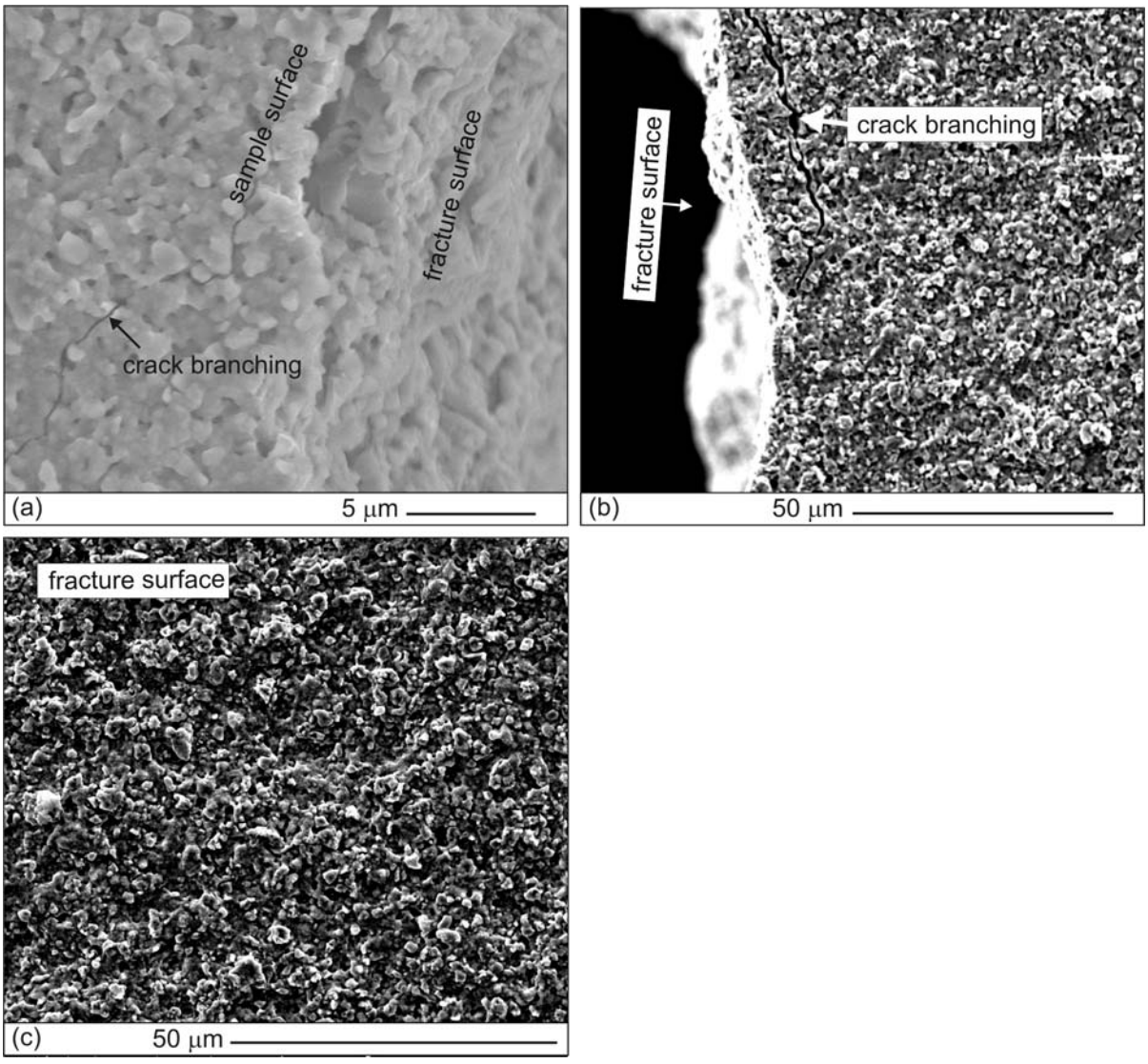

Figure 6.5. SEM-SEI micrographs. (a) Profile of fracture surface in a sample of design 1. (b) Profile of fracture surface in a sample of design 2. (c) Fracture surface in a sample of design 2.

For both designs, the fractures appeared to be inter-granular (cf. Figures 6.5a, b, c). Branching of the propagating crack was observed (cf. Figures 6.5a and b).

6.5.3 Tensile test

The samples were positioned in the self-aligning set-up shown in Figure 6.6a, and put under tensile load. The figure illustrates a tested sample with a short gauge section. An example of a measured stress-strain curve is shown in Figure 6.6b.
During testing, the origin of the failures was not possible to register with the eye, as the fracture appeared instantaneously. The samples with the short gauge section typically fractured in a wedge-shaped pattern. Samples with a long gauge section generally displayed simple single fractures (cf. Figure 6.7).

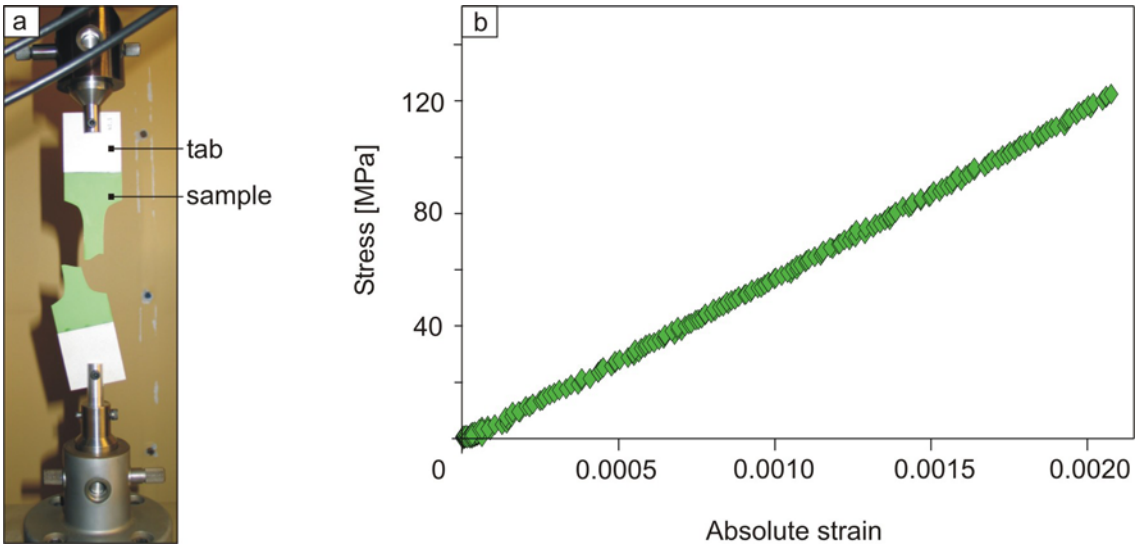

Figure 6.6. (a) The tensile test set-up with a sample of design 1. (b) Stress-strain curve for a tested sample of design 2.

Position of failure

The position of the fracture along the left (LP) and right (RP) edge of the sample was measured as the distance between the fracture and the tab on the top fragment. The measured fracture positions for the two designs are illustrated in Figure 6.7 as red lines.
The gauge sections as defined in Sections 6.4.1 and 6.4.2 are indicated in Figure 6.7. The failures appeared to be stochastically distributed between the gauge section and the transition sections.

Weibull statistics

The data from the tensile tests were treated with Weibull statistics. The Weibull equation describes the probability of failure (P_f) for an elastic body under the tensile stress τ. The relationship is shown in Equation 6.1.

Eq. 6.1
$$\ln\left[\ln\left(\frac{1}{1-P_f}\right)\right] = m\cdot\ln(\tau) - m\cdot\ln(\tau_0)$$

The equation describes a linear relationship with the slope m, and the intercept $-m\cdot\ln(\sigma_0)$. The slope is also denoted the Weibull modulus, and is an expression of the dispersion in the fracture strength of the brittle material [92].

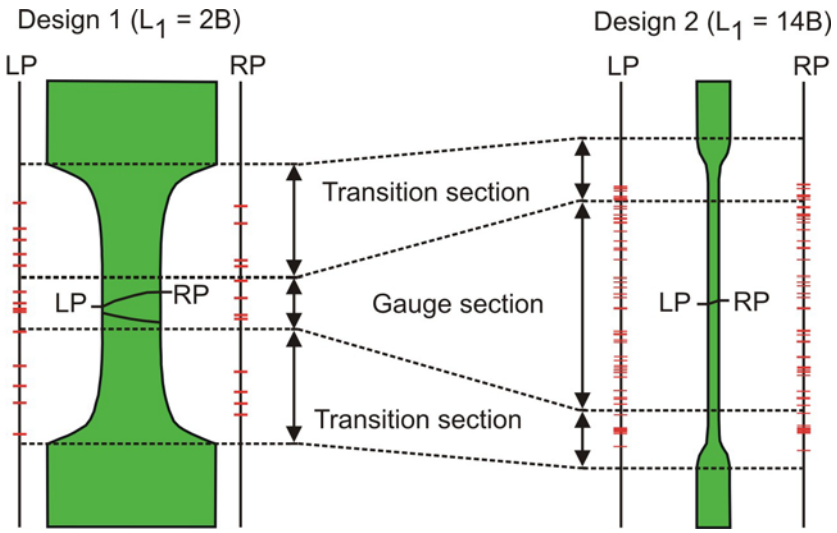

Figure 6.7. The position of failures along the left (LP) and right (RP) edge of the samples. The fracture positions are marked with red lines.

For Weibull characterization, a probability of failure is assigned to each experimentally determined fracture stress. Based on Monte Carlo simulations, the method of linear regression was recommended by Khalili et al. [92]. Here the probability of failure for the n'th lowest fracture strength out of a total of N samples was defined as shown in Equation 6.2.

Eq. 6.2 $$P_f = \frac{n - 0.5}{N}$$

In addition to the Weibull modulus, Weibull characterization includes the median strength (τ_{50}). The median strength is defined as the stress where the probability of failure is 50% [29].

The analytical application of the Weibull statistics as described above, implies data that refer to a uniformly stressed test volume [29, 92]. Thus, for correct statistics, data where the fracture initiated outside the uniformly stressed area must be discarded, or the stress state distribution must be taken into account.

The Weibull statistics are specific for the tested sample size. Thus, for comparison of Weibull data, correction to equivalent sizes must be made. The mean strength may be correlated to equivalent test volumes or equivalent surface area. The formulas for correction are shown in Equations 6.3 and 6.4. The mean strength $\tau_{50,1}$ refers to the volume V_1 or the surface area A_1. Analogous, the mean strength $\tau_{50,2}$ refers to the volume V_2 or the surface area A_2.

Eq. 6.3 $$\frac{\tau_{50,1}}{\tau_{50,2}} = \left(\frac{V_1}{V_2}\right)^{\frac{-1}{m}}$$

Eq. 6.4 $$\frac{\tau_{50,1}}{\tau_{50,2}} = \left(\frac{A_1}{A_2}\right)^{\frac{-1}{m}}$$

Weibull data for the samples analyzed in the present study are summarized in Table 6.1. For both designs, statistical data for the case where tests failed in the gauge section are only included, and for the case where all tests are included, are shown. For the gauge section case, with gauge

sections as defined in Section 6.4, the stress state is uniform within 1%, and the size of the gauge section is easily calculated as the section is straight-sided (cf. Section 6.4). When all tests are included the stress state is not uniform, and the test size of the sample (also denoted the effective volume) difficult to calculate. No values are included in Table 6.1.

Table 6.1. Weibull data for the tensile tests. N is the number of samples, m is the Weibull modulus, τ_{50} is the median strength, $\tau_{50,range}$ is the uncertainty range on the median strength resulting from the standard deviation on m, $\tau_{50,Vref}$ and $\tau_{50,Aref}$ are respectively the volume and surface area corrected median strength, V_{gauge} is the volume of the gauge section, V_{ref} is the reference volume, A_{gauge} is the surface area of the gauge section, and A_{ref} is the reference surface area.

	Tests failed in gauge section		All tests	
	Design 1 (L_1=2B)	Design 2 (L_1=14B)	Design 1 (L_1=2B)	Design 2 (L_1=14B)
N	4	39	15	52
m	5 ± 3	9 ± 1	4 ± 1	10 ± 1
τ_{50} [MPa]	169 ± 2	150 ± 2	162 ± 2	151 ± 2
$\tau_{50,range}$ [MPa]	[20;119·10^6]	[86;308]	[66;769]	[92;280]
$\tau_{50,Vref}$ [MPa]	163 ± 2	150 ± 2	-	-
$\tau_{50,Aref}$ [MPa]	115 ± 1	150 ± 2	-	-
V_{gauge} [mm^3]	50.96	58.24	-	-
V_{ref} [mm^3]	58.24	58.24	-	-
A_{gauge} [mm^2]	7.28	35.50	-	-
A_{ref} [mm^2]	35.50	35.50	-	-

The uncertainty on the median strength was assumed to be 1%. The strength did not differ significantly between the case where all tests were included and the statistically correct case where only samples fractured in the gauge section were included.
The uncertainty on the Weibull modulus was believed to be significant. Precise characterization of brittle materials is known to require a minimum of 20 samples, and preferably more than 30 samples. If the sample population is smaller, a significant uncertainty on the data must be expected [92, 93]. The standard deviation on the Weibull modulus on account of the number of tested samples were evaluated in [92]. Based on this reference, the standard deviation on m, and the resulting uncertainty range on the median strength ($\tau_{50,range}$) were calculated and included in Table 6.1. The number of tested samples was seen to be a big influence on the uncertainty of the Weibull parameters.

For comparison of the two designs, the median strength was corrected to a reference test size (V_{ref} and A_{ref}), corresponding to the gauge volume (V_{gauge}) and the gauge surface area (A_{gauge}) of design 2. The volume corrected median strength ($\tau_{50,Vref}$) was observed to be slightly higher for design 1, whereas the surface area corrected strength ($\tau_{50,Aref}$) of design 1 was below that of design 2 (cf. Table 6.1).

6.6 Discussion

Shaping of the samples into the designed shape appeared as the main limitation of the test method. The laser cutting was seen to introduce marks that were not eliminated by subsequent mechanical polishing (cf. Section 6.5.1). Deviations from the ideal shape will occur due to cutting and machining precision. The laser cutting was carried out based on a high-density number of (x,y)-points, whereas the optimized shape was defined by a B-spline curve. In addition, the laser pulses were seen to give rise to an uneven cut profile (cf. Section 6.5.1).
The observed similarity in median strength for the two designs indicates that the developed method is viable for strength test of materials. However, the similarity may also reflect the cutting procedure. For further verification of the method, experiments on materials with variable strength are a possibility.

Despite the similarity in Weibull parameters between the case including all tests, and the case including tests with fractures in the gauge section (cf. Section 6.5.3), distinction between fractures in the gauge section and outside the gauge section is necessary for correct Weibull statistics.

The measured median strength may be corrected to a reference volume or a reference surface area. Which is more appropriate depends on the origin of the failures [54]. For both designs the failures appeared to be stochastically positioned along the perimeter of the gauge and the transition section (cf. Section 6.5.3). From this it was indicated that the failures initiated along the edge. Further, the failures are likely to initiate at the edge, since the maximum stress concentrations were calculated to occur here (cf. Section 6.4), and due to the laser cutting making surface flaws more likely to dominate as failure initiators compared to bulk flaws. Thus, correction to a reference surface area is believed more appropriate.
When comparing the surface area corrected median strengths, the strength of design 1 was significantly lower than that of design 2. However, the statistical population of design 1 was very low. Thus, the difference was believed to be statistically based, and not related to the material properties.

Better experimental statistics were obtained for design 2. A successful test was defined as a measurement, where the failure occurred within the gauge section. The success rate for design 2 was 75% (39 out of a total of 52 tests). For design 1, the success rate was only 26% (4 out of 15 tests) (cf. Section 6.5.3).

6.7 Conclusions

Improved shapes for thin tensile test specimen were defined, and the technological applicability of the designs tested on the anode support for SOFC. The conclusions are:

- Shape optimization of the samples appeared as viable possibility when performing tensile strength tests on thin specimen. However, the practical shaping of the samples appeared as a main limitation of the method. Laser cutting of the as-sintered samples was observed to alter the appearance of the sample surface. The failures were indicated to initiate along the cut edge. Further experiments are needed for verification of the method.

- Better experimental statistics were obtained with the design containing a longer gauge section. Thus, from a practical view, this design is to be preferred for future testing.

- The tensile strength of the laser cut technological anode-support material was determined to be 150 MPa.

Acknowledgment

E. Lund (Aalborg University) is acknowledged for performing the shape optimization. B. F. Sørensen (Risø National Laboratory) is acknowledged for help and guidance in designing the experiments. J. O. Olsson, E. G. Hansen, and E. Vogeley (Risø National Laboratory) are acknowledged for technical support on the experiments.

7 Strength of nickel-YSZ cermets

7.1 Introduction

Commercialization of the solid oxide fuel cell (SOFC) technology involves improvement of the robustness and stability of the system. The parameters are related to the mechanical properties of the system components [19, 31, 54]. For the anode, the strength of the nickel-YSZ cermet is believed to be a key parameter on the redox stability [84] and cf. Chapters 4 and 5. Better redox resistance was observed for cermets containing the mechanically stronger 3 mol% yttria stabilized zirconia (3YSZ) as the ceramic component, compared to cermets containing 8 mol% yttria stabilized zirconia (8YSZ).
The effect of the anode cermet strength on the redox performance has not been quantified. So far, knowledge of the technological cermet strength has been limited. A suitable method for test of the thin technological cermets has been lacking (cf. Chapter 6). Further, the mechanical characterization of nickel-YSZ cermets has been focused on pressed samples with the ceramic component 8YSZ. In contrast, the structurally supporting cermet of the technologically cell is porous, and contains 3YSZ. Mechanical data on nickel-YSZ cermets reported in the literature are listed in Table 7.1.

Table 7.1. Mechanical data on nickel-YSZ cermets at room temperature. For references where more values were reported, the range in the values is shown.

Sample type	Shape	Porosity [%]	Method	Strength [MPa]	Reference
As-sintered anode-supported half-cell	Planar	-	Tensile	≥150	[25]
As-sintered anode-supported cell	Planar	-	Ring-on-ring	270 ± 20	[94]
As-sintered 75 mol% NiO-8YSZ	Laminated layers	23	Ring-on-ring	91-111	[95]
As-sintered 75 mol% NiO-8YSZ	Laminated layers	7-23	Ring-on-ring	86-125	[96]
Reduced 75 mol% Ni-8YSZ	Laminated layers	40	Ring-on-ring	50-71	[96]
As-sintered 56 wt% NiO-8YSZ	Pressed plates	34	4-point bend	110	[9]
Reduced 56 wt% Ni-8YSZ	Pressed plates	-	4-point bend	77.5	[9]
As-sintered 40 vol% NiO- 8YSZ	Pressed plates	30-45	3-point bend	13-33	[97]
As-sintered 56 wt% NiO-YSZ	Pressed plates	20-38	Bending	70-190	[47]
As-sintered 75 mol% NiO-8YSZ	-	31	4-point bend	56	[98]
Reduced 40 vol% Ni-8YSZ	Bar	-	3-point bend	80-120	[98]
As-sintered NiO-8YSZ	-	-	4-point bend	80-120	[98]
Reduced Ni-8YSZ	-	-	4-point bend	60-80	[98]
Reduced 37-58 vol% Ni-8YSZ	Pressed discs	21-29	4-point bend	30-74	[99]
Reduced 37-58 vol% Ni-3YSZ	Pressed discs	21-29	4-point bend	136-409	[99]

The samples previously investigated varied widely in composition, shape, porosity, and test volume. The strength values were seen to be correspondingly scattered (cf. Table 7.1). However, the strength of cermets containing 3YSZ as the ceramic component was observed to be approximately a factor of five higher than that of the corresponding cermets containing 8YSZ

(cf. Table 7.1, reference [99]). Further, measurements on anode-supported cells and half-cells [25, 94], i.e. samples where a nickel-3YSZ cermet constituted the structural supporting member, also indicated significantly higher strength of cermets containing 3YSZ.
In this chapter the strength of pressed cermets, and technologically relevant cermets, containing either 3YSZ or 8YSZ as the ceramic component was measured. The strength was measured for cermets in the as-sintered, reduced and re-oxidized state. Conventional flexural 4-point bending, and the tensile test method described in Chapter 6 were applied for the measurements. The mechanical properties of the cermets were correlated to the redox performance of the materials.

7.2 Experimental

7.2.1 Sample preparation

Samples were prepared from NiO powder (purity 99% from Alfa Aesar), Al_2O_3 powder (Catapal® from Sasol), 3YSZ (TZ-3YB from Tosoh Co.), and 8YSZ (TZ-8Y from Tosoh Co.). Two compositions with similar NiO contents, and containing either 8YSZ, or 3YSZ and a minor amount of Al_2O_3, were prepared. The two compositions were denoted 8Y and 3Y, respectively. The solid material contents were 56.8 wt% NiO and 43.2 wt% 8YSZ for 8Y, and 55.7 wt% NiO, 43.7 wt% 3YSZ, and 0.6 wt% Al_2O_3 for 3Y.
Samples corresponding to the technological anode cermet were produced by processing the powders into slurries. The slurries were tape cast into thin foils, and the foils sintered at 1300°C to a thickness of ca. 0.3 mm. The sintered foils were cut by laser into strip shaped samples of dimensions 9 mm x 50 mm for flexural tests, and into bone shaped samples of design 1 (as described in Chapter 6) for tensile tests.
Pressed cermets were produced by heat treating some of the green tape cast foil into powder. The resulting powder was pressed into bar shaped samples of dimensions 5 mm x 5 mm x 50 mm. The pressing was done by uniaxial followed by isostatic pressing at 80 MPa. The bars were subsequently sintered at 1300°C.
A part of the as-sintered strip and bar shaped samples was subsequently completely reduced at 1000°C for 96 h in 9 vol% H_2-N_2. A part of the reduced samples were further re-oxidized at 1000°C for 24 h in air. To avoid warping of the strips during the re-oxidation, the samples were sandwiched between two porous plates during the treatment.
The samples were named after the state (s = sintered, r = reduced, ro = re-oxidized), composition (3Y or 8Y), and sample shape (strip, bone, or bone). Thus, a sintered bar shaped sample of the composition 3Y is denoted s-3Y-bar.

7.2.2 Experimental procedure

The bone shaped samples were tested in the tensile set-up described in Chapter 6. For some of the samples, the elastic modulus was measured in combination with measuring the tensile strength. The elastic modulus was measured by attaching mechanical extensometers to the samples, or by applying a Mintron non-contact video extensometer. For detection of the displacements with the Mintron, the samples were equipped with black labels spaced 20 mm apart.
The bar and strip shaped samples were tested in flexural 4-point bend load. The span ratio was 10:20 mm, and a crosshead speed of 0.22 mm/min was used. The bars were positioned in the set-up by use of spacers. Scotch® double-sided tape was used for positioning of the strips. Flexural test was performed on intact samples only. Some of the bars and strips failed or warped upon the re-oxidation. None of these were tested.

The porosity of the samples was quantified by Archimedes' method, and by weighing and geometrical gauging. The procedures were as described in Chapter 2, Section 2.2.2.

7.3 Results

7.3.1 Porosity

The weight and geometrical dimensions of all the prepared samples were measured, and the geometrical porosity (ε_{geom}) calculated. The open porosity was measured on two specimen of each type by the Archimedes' method (ε_{arch}). The average porosity of the different states are listed in Table 7.2. Data for the bone shaped samples are not included specifically, as they correspond to the strips. For the geometrically based porosity, the standard deviation from the number of N samples is included. An uncertainty of 1.0% was estimated on the Archimedes' based porosity.

Table 7.2. Porosity of the samples in the different states based on geometrical gauging (ε_{geom}) and Archimedes' method (ε_{arch}). N denotes the number, or the range in the number of measured samples.

State	Method	N	Porosity [%]			
			3Y-bar	3Y-strip	8Y-bar	8Y-strip
As-sintered	ε_{geom}	40-72	7.5 ± 1.0	17.0 ± 4.2	1.5 ± 2.3	12.3 ± 6.0
	ε_{arch}	2	0.5 ± 1.0	15.6 ± 1.0	0.5 ± 1.0	4.4 ± 1.0
Reduced	ε_{geom}	10-15	27.8 ± 0.8	35.5 ± 1.2	23.8 ± 1.5	28.3 ± 1.3
	ε_{arch}	2	25.6 ± 1.0	33.0 ± 1.0	17.1 ± 1.0	27.3 ± 1.0
Re-oxidized	ε_{geom}	5-12	18.0 ± 0.9	28.6 ± 3.3	12.7 ± 0.7	-
	ε_{arch}	2	11.8 ± 1.0	12.4 ± 1.0	3.7 ± 1.0	19.9 ± 1.0

The sample type 8Y-strip warped into irregular shapes upon re-oxidation. Thus, no geometrically based porosity data were obtained for the re-oxidized 8Y-strip (cf. Table 7.2).
The as-sintered porosity differed markedly between the two sample shapes: bar and strip. Lower porosity was observed for the bars, and the open porosity was insignificant. The lower porosity of the bars compared to the corresponding strip was maintained upon reduction and re-oxidation (cf. Table 7.2).
For all sample types, the open porosity constituted an increasing part of the porosity upon reduction and re-oxidation. Compared to the as-sintered state, the porosity was generally higher for the re-oxidized state (cf. Table 7.2).
Both the open and the closed porosity will influence on the mechanical properties of the material. Thus, for strength evaluations the geometrical porosity is the more relevant value.

7.3.2 Weibull statistics

The strength values were calculated based on the maximum load (F_{max}) before sample failure. For tensile and flexural 4-point bend tests, the strength is calculated as shown in Equations 7.1 and 7.2, respectively.

Eq. 7.1 $$\tau_{tensile} = \frac{F_{max}}{A}$$

Eq. 7.2 $$\tau_{4pb} = MOR = \frac{3 \cdot S \cdot F_{max}}{4 \cdot w \cdot h^2}$$

A is the cross section area perpendicular to the load, w is the width of the sample in the set-up, h is the height of the sample, and S is the distance between the outer span in the 4-point set-up. The flexural strength is also denoted the modulus of rupture (MOR).

The strength data were treated with Weibull statistics. The method of linear regression described in Chapter 6, Section 6.5.3 was applied. For the tensile tests, only data where the fracture occurred within the uniformly stressed gauge section were included (cf. Chapter 6, Section 6.4.1). For flexural test of bar shaped samples, only data where the fracture occurred within the loaded volume (i.e. the trapezoid defined by the inner and outer span) were included. For the strips it was not possible to identify the position of the critical cracks during testing. Thus, all measurements on strips were included for the statistics.

For comparison of the different sample shapes and methods, the median strength was corrected to a reference volume ($\tau_{50,Vref}$), and a reference surface area ($\tau_{50,Aref}$). Reference values corresponding to the reference in Chapter 6 (Section 6.5.3) was chosen.
For the tensile test samples, the gauge volume and gauge surface area were as defined in Chapter 6, Section 6.5.3. However, for the flexural test samples, the gauge volume usable for comparisons, corresponds to the effective volume (V_E). The effective volume is defined as the volume subjected to uniform tension that would have the same probability of failure as the 4-point bend test [100]. For a flexural set-up with an outer-to-inner span ratio of 2, the effective volume is calculated as shown in Equation 7.3 [101]. V is the volume of the rectangular parallelepiped within the outer span, and m is the Weibull modulus.

Eq. 7.3 $$V_{gauge} = V_E = \frac{m+2}{4\cdot(m+1)^2}\cdot V$$

The gauge surface area of samples tested in 4-point bend mode was taken as the sample surface area between the outer spans, where maximum and uniform tensile stress occurs.

The Weibull data are summarized in Table 7.3. By analogy with Chapter 6 (Section 6.5.3) the uncertainty on the median strength (τ_{50}) was assumed to be 1%. The standard deviation on the Weibull modulus (m) was estimated from the sample population size as described in [92], and the resulting uncertainty range on the median strength ($\tau_{50,range}$) is included in the table.
Precise Weibull characterization is known to require at least 20 samples. For smaller sample populations a significant uncertainty on the data is expected [92, 93]. The sample population sizes for the tests summarized in Table 7.3 were seen to result in a significant uncertainty on the Weibull modulus, and on the range of the calculated median strength. Despite the large uncertainties, the calculated median strength (τ_{50}) was applied for the comparison of the samples in the following sections. However, based on the relative small sample populations, the results must be taken tentatively.

Table 7.3. Weibull data. N is the number of samples, m is the Weibull modulus, τ_{50} is the median strength, $\tau_{50,range}$ is the range on the median strength resulting from the standard deviation on m, $\tau_{50,Vref}$ and $\tau_{50,Aref}$ are respectively the volume and surface area corrected median strength, V_{gauge} is the volume of the gauge section, V_{ref} is the reference volume, A_{gauge} is the surface area of the gauge section, and A_{ref} is the reference surface area.

State	Parameter	3Y-bar	3Y-strip	3Y-bone	8Y-bar	8Y-strip	8Y-bone
As-sintered	N	20	20	4	20	20	4
	m	5 ± 1	2 ± 1	4 ± 3	9 ± 2	6 ± 1	25 ± 3
	τ_{50} [MPa]	292 ± 3	304 ± 3	169 ± 2	163 ± 2	329 ± 3	107 ± 1
	$\tau_{50,range}$ [MPa]	[125;983]	[114;1361]	[20;119·10^6]	[71;547]	[127;1374]	[69;185]
	$\tau_{50,Vref}$ [MPa]	430 ± 4	296 ± 3	163 ± 2	198 ± 2	318 ± 3	107 ± 1
	$\tau_{50,Aref}$ [MPa]	353 ± 4	598 ± 6	109 ± 1	179 ± 2	429 ± 4	100 ± 1
	V_{gauge} [mm^3]	332.83	54.72	50.96	317.34	47.70	50.96
	V_{ref} [mm^3]	58.24	58.24	58.24	58.24	58.24	58.24
	A_{gauge} [mm^2]	83.00	180.00	7.28	82.00	180.00	6.83
	A_{ref} [mm^2]	35.50	35.50	35.50	35.50	35.50	35.50
Reduced	N	20	22	-	20	21	-
	m	12 ± 2	3 ± 1	-	13 ± 3	3 ± 1	-
	τ_{50} [MPa]	257 ± 3	462 ± 5	-	186 ± 2	333 ± 3	-
	$\tau_{50,range}$ [MPa]	[105;958]	[183;1753]	-	[81;631]	[135;1237]	-
	$\tau_{50,Vref}$ [MPa]	297 ± 3	449 ± 4	-	212 ± 2	304 ± 3	-
	$\tau_{50,Aref}$ [MPa]	276 ± 3	825 ± 8	-	198 ± 2	545 ± 5	-
	V_{gauge} [mm^3]	331.14	53.64	-	220.66	43.20	-
	A_{gauge} [mm^2]	83.20	180.00	-	81.80	180.00	-
Re-oxidized	N	18	23	-	10	-	-
	m	10 ± 2	6 ± 1	-	6 ± 2	-	-
	τ_{50} [MPa]	205 ± 2	206 ± 2	-	146 ± 1	-	-
	$\tau_{50,range}$ [MPa]	[86;744]	[100;560]	-	[47;1201]	-	-
	$\tau_{50,Vref}$ [MPa]	246 ± 2	194 ± 2	-	193 ± 2	-	-
	$\tau_{50,Aref}$ [MPa]	224 ± 2	267 ± 3	-	168 ± 2	-	-
	V_{gauge} [mm^3]	367.16	52.74	-	351.65	-	-
	A_{gauge} [mm^2]	86.80	180.00	-	86.40		-

7.3.3 Composition of the ceramic component

The effect of the composition of the ceramic component on the mechanical properties was examined. The Weibull parameters for the as-sintered samples of composition 3Y and 8Y are illustrated in Figure 7.1 as a function of the as-sintered porosity. Samples of the composition 3Y are shown with red, and the composition 8Y is shown with green. The shape of the measurement points indicates the sample shape. Squares represent bars, rectangles represent strips, and circles symbolize the bone shaped samples. The empirical relationship for a porous NiO-8YSZ cermet reported by Radovic and Lara-Curzio [102] is included in the figure.

The porosity of the as-sintered samples differed significantly (cf. Figure 7.1), and the sample porosity is known to influence on the median strength. The measurement points for 8Y-bar and 8Y-bone were in good agreement with the empirical relationship between the porosity and the median strength reported in the literature. However, 8Y-strip deviated strongly from the trend, both in the case of the volume, and the surface area corrected strength values (cf. Figure 7.1).

When ignoring the strip shaped samples, higher median strength for samples of 3Y composition was indicated. This was particularly evident for samples with low porosity. For sample porosity above 17% a limited effect was indicated (cf. Figure 7.1).

Lower Weibull moduli for samples of 3Y composition were generally observed (cf. Figure 7.1). The Weibull modulus has not been related empirically to the porosity, similarly to the median strength.

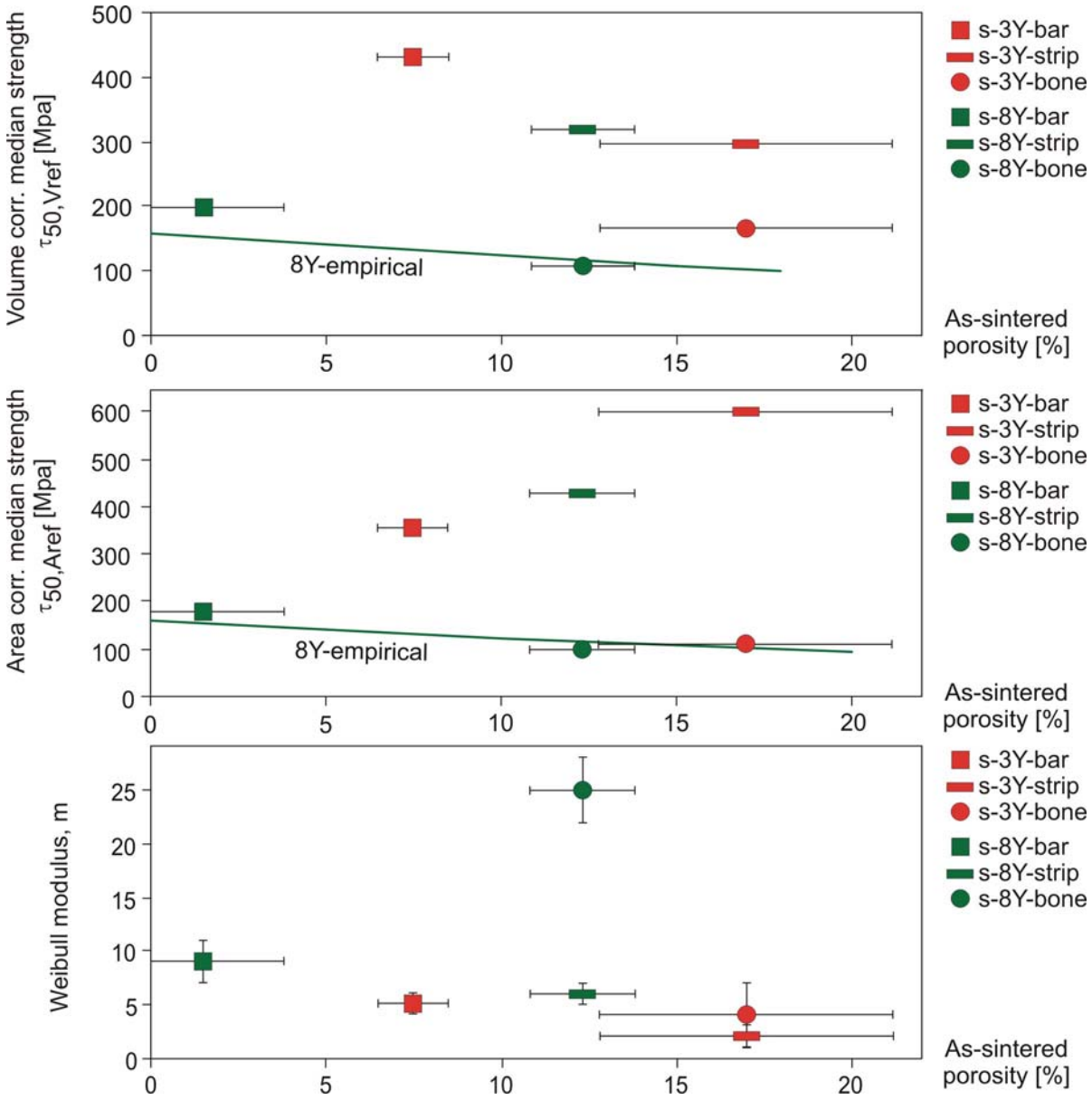

Figure 7.1. Weibull parameters for the as-sintered samples of composition 3Y (red), and 8Y (green) as a function of the as-sintered porosity. The shape of the measurement points indicate the sample shape: squares represent bars, rectangles represent strips, and circles represent bone shaped samples. The curve "8Y-empirical" illustrates an empirical relationship for a composition corresponding to 8Y reported in [102]. Error bars indicate the standard deviation.

7.3.4 Oxidation state

The effect of redox cycling on the mechanical properties was examined. The changes in the Weibull parameters from the as-sintered, to the reduced and re-oxidized state, are illustrated in Figure 7.2 for four different samples, as a function of the associated changed porosity. From the top it is the volume corrected median strength, the area corrected median strength, and the Weibull modulus. The state of the sample is indicated next to the measurement point: "s" denotes as-sintered, "r" is reduced, and "ro" is re-oxidized. Analogous to Figure 7.1, the color and shape of the measurement points indicate the sample composition and shape, respectively. The composition 3Y is shown with red, and 8Y with green. Squares represent bars, rectangles represent strips, and circles represent the bone shaped samples. The empirical relationship for a porous NiO-8YSZ cermet is also shown [102].

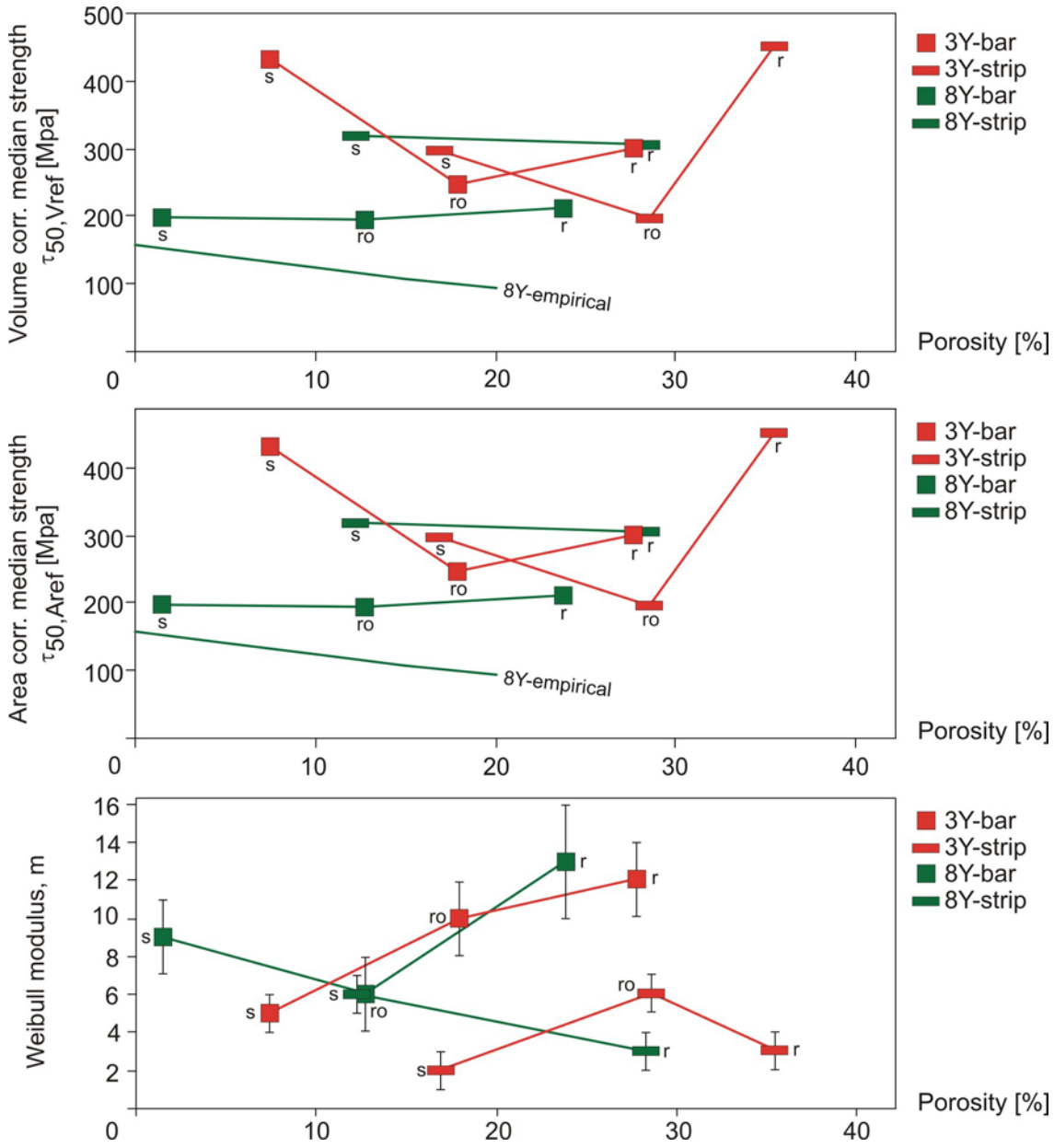

Figure 7.2. Changes in the Weibull parameters from the as-sintered (s), to the reduced (r) and re-oxidized (ro) state, for four different samples, as a function of the associated changed porosity. The oxidation state of the sample is indicated next to the measurement point. The color of the measurement points indicate the composition: 3Y is shown with red, and 8Y shown with green. The shape of the measurement point indicates the sample shape: squares represent bars, rectangles represent strips, and circles represent bone shaped samples. The curve "8Y-empirical" illustrates an empirical relationship for a composition corresponding to 8Y reported in [102]. Error bars indicate the standard deviation.

For all samples the porosity increased from the as-sintered to the re-oxidized state. When the samples were in the reduced state, even higher porosity was observed (cf. Figure 7.2).

When observing the median strength of 8Y samples in the oxidized states (s and ro), they did not follow the empirical relationship (8Y-empirical). Higher median strengths were observed, and the strength appeared less porosity dependent. However, for samples of the composition 3Y, a strong median strength dependence on porosity was observed, and significantly lower strengths were observed for the re-oxidized states (cf. Figure 7.2).

The effect of reduction on the median strength appeared complex. Considering the large increase in porosity associated with the nickel reduction, decreased median strength would be expected.

However, if the volume corrected data were observed, only 3Y-bar displayed a significant decrease, and the strength was only decreased compared to the as-sintered state. The same pattern was seen for the area corrected values (cf. Figure 7.2). For 3Y-strip, the median strength was highest for the reduced state, and for samples of the composition 8Y, no significant change in the median strength was observed upon reduction (cf. Figure 7.2).
The influence of the porosity on the Weibull modulus was ambiguous. Both increase and decrease of the modulus with increasing porosity was observed (cf. Figure 7.2).

7.3.5 Test method

Better experimental statistics was obtained for flexural test on bar shaped samples compared to tensile test on the bones. For the bars, all the samples failed within the gauge volume. For the bones, only 4 out of 20 samples failed in the test section, and could be included in the Weibull calculations. The success rate for the strip shaped samples was not possible to evaluate as the position of the failures could not be recognized.
In addition to determine the success rate, the test method appeared to influence on the measured mechanical properties. From Figure 7.1, samples of identical porosity, but tested in respectively flexural set-up (i.e. strips), and tensile set-up (i.e. bone shaped samples), was compared. Lower median strengths and higher Weibull moduli were indicated to be obtained with the tensile set-up.

7.3.6 Elastic modulus

The slope of the straight-line portion of a stress-strain curve represents the elastic modulus, also denoted Young's modulus. Stress-strain curves measured by applying strain gauge and video extensometer on samples of the type s-3Y-bone are shown in Figure 7.3.

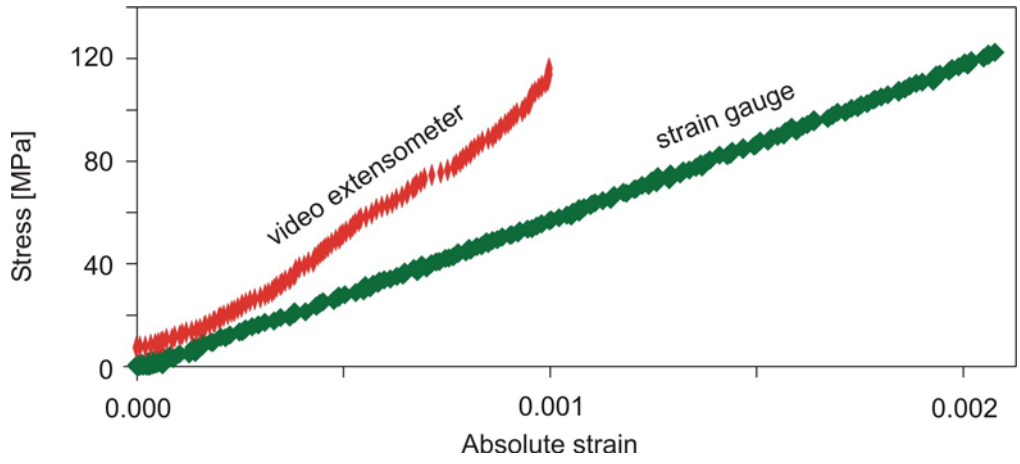

Figure 7.3. Stress-strain curves measured with video extensometer and strain gauge.

For both methods the elastic modulus was defined based on the strain interval 0-0.1%. The averages and the standard deviations on the measured samples are listed in Table 7.5. N denotes the number of tests. In contrast to the strength, the elastic modulus is not sensitive to the flaw distribution. Thus, the value was determined using relatively few measurements.
The test method appeared to influence on the elastic modulus. Lower values were obtained when strain gauges were applied. From the video extensometer measurements, the values for the as-sintered 3Y-bone were observed to be approximately half the size of the as-sintered 8Y-bone.

Table 7.5. Elastic moduli (E) of the as-sintered samples measured with video extensometer and strain gauge. N is the number of tested samples. The standard deviation on the measurements is included.

	As-sintered 3Y-bone		As-sintered 8Y-bone	
	N	E [GPa]	N	E [GPa]
Video extensometer	2	114 ± 5	4	226 ± 31
Strain gauge	10	60 ± 4	-	-

7.4 Discussion

7.4.1 Test method

Flexural 4-point bend test on strip shaped samples resulted in a high uncertainty on the data. For the statistic treatment, it was not possible to reject measurements where the fracture occurred outside the test volume. Further, during testing the strips bended considerably before failure, and the flexibility of the samples introduced friction into the set-up. The mechanisms may result in artificial higher fracture loads [29]. The strength data obtained for the strips were indeed observed to deviate significantly, and to have higher values compared to corresponding measurements (cf. Figures 7.1 and 7.2). Thus, flexural 4-point bend test did not appear to be an appropriate method for strength testing the technological relevant anode materials.
The sample population was a critical parameter on the quality of the data. Much better experimental statistics were obtained for the pressed cermets (100%) compared to the tensile test on the bone shaped samples (20%) (cf. Section 7.3.5). However, the bone shaped samples were of the first developed design. A significant improvement in the success rate was achieved with a modified design (75%) (cf. Chapter 6). If the improved design is applied, tensile tests are believed to be an opportunity for testing the technologically relevant anode cermet materials.

7.4.2 Composition of the ceramic component

Due to the high uncertainty believed to be associated with the measurements on the strip shaped samples, they were not included in the evaluation of the effect of the sample composition. Samples of the composition 3Y generally displayed higher median strength compared to 8Y. The difference was more pronounced for samples with low porosity (cf. Section 7.3.3).
The relationship is explained by the difference in yttria content of the ceramic phase. With yttria dopant levels below 8 mol%, partially stabilized zirconia is obtained [26]. Partially stabilized zirconia is a two-phase material of tetragonal or monoclinic particles dispersed in a cubic matrix, and the material has enhanced mechanical properties. The mechanical improvement are due to crack deflection and transformation toughening, however the exact effect depends on the particle sizes and volume fractions [27, 29].
The pronounced effect observed in the low-porosity samples may be explained by more efficient toughening mechanisms when the porosity is low. However, the lack of difference between the two compositions for the high-porosity samples may also be explained by the sample preparation. The high-porosity samples were bone shaped, and the shape produced by laser cutting for both compositions (cf. Chapter 6). Thus, the similarity may reflect the shaping method. In addition, the statistical foundation is weak as the number of high-porosity samples included in the analyses was low (cf. Section 7.3.2).

The presence of transformation toughening is apart from higher median strengths, also characterized by higher Weibull moduli. According to Kendall et al. the Weibull modulus is expected to increase with a factor of 1.67 if transformation toughening is introduced into a material with a defined flaw distribution [103].

In the present study, the opposite trend was observed (cf. Section 7.3.3). The Weibull moduli for the 3Y samples were observed to be at least 50% lower than for the corresponding 8Y samples. This indicated that transformation toughening was not the working toughening mechanism. However, differences in porosity were also indicated to be present between corresponding 3Y and 8Y samples (cf. Section 7.3.3). The type, size, and distribution of the critical defects are likely to be related to the porosity [102]. Thus, transformation toughening is still believed to occur in the samples.
The low Weibull moduli observed for the 3Y samples may also be related to the higher median strengths. The Weibull parameters are known to be mutual interacting, and materials with higher fracture stress will display higher dispersions [92].

7.4.3 Oxidation state

Re-oxidation of the anode cermet is believed to be associated with damage on the ceramic network [84] and cf. Chapters 2 and 4. In accordance with the model of the redox mechanism, increased porosity and reduced strength were generally observed when comparing the as-sintered and re-oxidized samples (cf. Section 7.3.4).
Increased porosity is associated with a smaller minimum solid load bearing area. Thus, the strength is expected to decrease with increasing porosity. The decrease is commonly described to follow an exponential trend [102, 104, 105]. Radovic and Lara-Curzio [102] reported the relationship shown in Equation 7.4, obtained by fitting experimental data for a NiO-8YSZ cermet.

Eq. 7.4 $$\tau = 157.7 \cdot \exp(-2.58 \cdot \varepsilon)$$

The relationship was illustrated in the Figures 7.1 and 7.2. The as-sintered 8Y samples appeared to be in accordance with the relationship (cf. Figure 7.1). However, when the re-oxidized 8Y samples were included, the porosity dependence appeared to be minor (cf. Figure 7.2). The 3Y samples showed a much stronger decrease in strength with increasing porosity (cf. Figures 7.1 and 7.2).
The deviations from the empirical relationship indicate that the increase in porosity upon re-oxidation does not account for all of the degradation in strength. For the 3Y samples displaying more severe decrease in strength with porosity, a contributing mechanism may be damage on the ceramic network. The minor porosity dependence observed for the 8Y samples may be statistical, as the number of samples were relatively low (cf. Table 7.3). Furthermore, the exponential relationship is not universally applicable. The simple expression does not consider stress concentrations and other pore shape effects. For instance porosity may influence on the strength ambiguously. Pores can possibly absorb or dissipate the energy of a propagating crack, by deflecting, branching, or bridging of the crack, and the mechanisms will counteract the effect of the reduced load bearing area [27].

The porosity of the cermets increased markedly upon reduction. For the bar shaped samples a decrease in strength compared to the as-sintered state was also observed upon reduction. The decrease in strength was more severe for the 3Y-bar (cf. Figure 7.2). Significant decrease in strength upon reduction has also been reported on the half-cell scale [91].
For samples in the reduced state metallic nickel will be present. The strength of nickel is reported to be in-between that of 8YSZ and 3YSZ [99]. Thus, the nickel network may account for the difference in strength degradation observed for the compositions 3Y and 8Y upon reduction.

7.4.4 Elastic modulus

The elastic moduli measured with video extensometer and strain gauge was seen to differ (cf. Section 7.3.6). The inconsistency may be explained by the different limitations of the two methods. The strain gauge is a metallic patterned foil, whose electrical resistance varies in proportion to the amount of strain in the device. The foil needs to be bonded to the specimen, and the weight and mounting possibly influence on the results. However, the influence of the mounted foil is believed to be minor for brittle materials.
Non-contacting methods like video extensometers depend on mechanically driven optical followers, and are ultimately restricted by the wavelength of visible light (0.4-0.7 μm). However, for the present measurements, focus of the instrument was difficult to attain, and the resolution limit believed to be in the range of the measured strains. Thus, for the set-up applied in this study, better E values were believed to be obtained with strain gauges.
The video extensometer measurements indicated that the elastic moduli of the 8Y-bone were twice as high as for 3Y-bone. The difference may be related to the compositions, however the sample porosity is likely to be a part of the explanation. Higher porosity of 3Y-bone was indicated in Section 7.3.1, and the elastic modulus is known to decrease with increasing porosity. The exact relationship between the porosity and the E modulus will depend on the size and distribution of the pores. Exponential and parabolic relationships have been reported [29, 105]. The observed difference between the two sample materials indicated that sufficient resolution was achieved with the video extensometer.

7.4.5 Relationship between strength and redox performance

The obtained median strengths can be correlated to the redox performance. In Chapter 2 the redox performance was evaluated as the bulk expansion upon a re-oxidizing event measured by dilatometry. Figure 7.4 illustrates the bulk expansion measured at 1000°C in dilatometry (cf. Chapter 2) as a function of the median strength. The median strength corresponds to the strength of the oxidized structure existing before the re-oxidation that caused the expansion quantified by dilatometry. Volume corrected median strengths are represented with closed symbols, and surface area corrected strengths represented with open symbols.

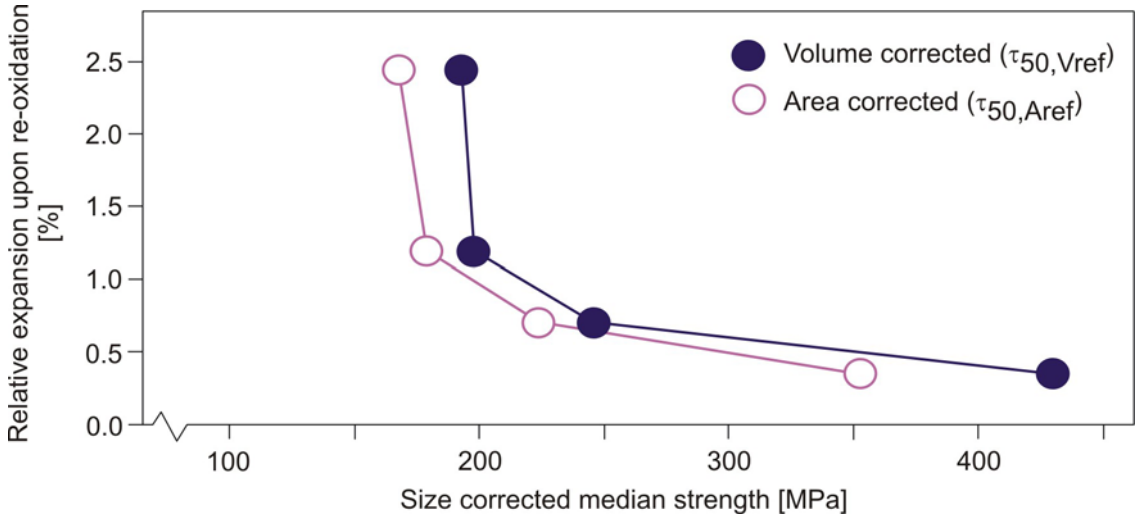

Figure 7.4. The relative bulk expansion upon a re-oxidizing event at 1000°C as function of the median strength. The median strength corresponds to the strength of the oxidized structure existing before the re-oxidation. Closed symbols represent volume corrected median strengths, and open symbols represent surface area corrected values.

The volume and area corrected median strengths were similarly correlated to the relative expansion upon re-oxidation. The relationship appeared to be inverse proportional, and from approximately 500 MPa an asymptotic course was suggested (cf. Figure 7.4). Thus, higher cermet strength is believed to improve the redox performance. However, for cermets displaying median strengths above ca. 500 MPa redox performance improvement requires significant strengthening.

7.5 Conclusions

The strength of nickel-YSZ cermets in the as-sintered, reduced, and re-oxidized was measured. The cermets contained either 3YSZ or 8YSZ as the ceramic part. The measurements were carried out by flexural 4-point bending, and uniaxial tensile tests. Due to sample populations below 30 the conclusions are only tentative. The measurements showed:

- Flexural 4-point bend test on strips of the technological cermet resulted in data associated with high uncertainties. The method is not recommended for further work.

- The strength of cermets containing 3YSZ as the ceramic component appeared to be higher compared to cermets containing 8YSZ. The difference was ascribed to transformation toughening occurring in the 3YSZ ceramic phase. The toughening mechanism was suggested to be more effective for low-porosity samples.

- Tensile tests on bone shaped samples may be influenced, and even determined by the sample preparation. Further experiments are needed to verify this.

- The strength observations were in accordance with the model of the redox mechanism proposed in Chapter 2. Damage on the YSZ network upon re-oxidation was indicated by increased porosity, and the reduction in strength of the cermets in the re-oxidized state compared to the as-sintered state.

- Also in accordance with the model proposed in Chapter 2, higher cermet strength was indicated to improve the redox performance. However, for cermets with median strengths above ca. 500 MPa, improvement of the redox performance was indicated to require a significant strengthening as the relationship appeared to become asymptotic.

- Different elastic modulus was obtained when applying strain gauge and video extensometer. The strain gauges were believed to give more precise results, however both methods appeared sufficient for detecting relative differences in E moduli.

Acknowledgement

B. F. Sørensen (Risø National Laboratory) is acknowledged for help in designing the experiments. J. O. Olsson and E. Vogeley (Risø National Laboratory) are acknowledged for technical support on the tensile tests.

8 Mechanical requirements to a redox stable nickel-YSZ cermet

8.1 Introduction

Redox stability of the anode is considered to be a commercial requirement for many applications of the solid oxide fuel cell (SOFC) technology [19, 21]. However, oxidation of the anode in the state-of-the-art nickel-YSZ (yttria stabilized zirconia) anode-supported design, is detrimental to the cell performance [8, 23, 58]. The degradation is related to a bulk expansion of the anode structure upon the re-oxidation, which generates cracks in the electrolyte [8, 9, 84].
The mechanical strength of the ceramic cermet component influences on the bulk expansion. Less bulk expansion was indicated for cermets with higher strength [84] and cf. Chapter 7. However, the tolerated anode bulk expansion where cracking of the electrolyte is avoided, has not been quantified. Nor has the equivalent demanded strengthening of the cermet been evaluated.
In this chapter the mechanical requirements for a redox stable anode were quantified. The solid oxide fuel cell was modeled as simple layered systems. Models involving respectively two and three layers were proposed, and both uniaxial and biaxial stresses, and the energy relations were considered. The models were applied to evaluate the stress state of the state-of-the-art electrolyte during redox cycling, and to identify possible parameters for improving the redox stability. The models were related to synchrotron measurements, where the stress state in the anode layer of a cell was analyzed in-situ during redox cycling [106].

8.2 Experimental

Synchrotron analyses were performed at beamline ID15 at the European Synchrotron Radiation Facility (ESRF). An x-ray beam with a wavelength of 0.173 angstrom was applied. The experiments were carried out by a group from Risø National Laboratory, and the data treatment performed by R. Martins. Further details are given in [62] and [106].
Two samples of the technologically relevant SOFC were investigated: a half-cell (i.e. a cell without the cathode layer), and a full cell. The samples were heated to ca. 850°C, and subjected to two redox cycles. 4 vol% H_2-3 vol% H_2O-He was used as reducing gas, and air as oxidizing medium. The diffraction data was acquired after each process step (reduction or re-oxidation) was completed.
The data analyses were limited to the nickel phase (NiO or Ni). However, the stress state of the ceramic phase (YSZ) can be deduced indirectly, as the stresses must outbalance the stresses in the nickel phase. For the calculations, the lattice parameter of NiO was assumed to be strain free after the initial heating in air to 850°C. The lattice parameter of Ni was assumed to be strain free just before the second re-oxidation. At this point the sample had been under reducing conditions at high temperature for several hours, and was believed to be structurally relaxed.

8.3 Models

The models were layered systems, where the single layers represented the electrolyte, anode, and anode support. The cathode was not included as its contribution to the cell strength was believed to be insignificant.
All the layers were assumed to be stress and strain free before the model anode was subjected to the re-oxidation. Thus, residual stresses, for instance accumulated during sintering and reduction,

were neglected in the models. However, residual stresses are likely to be present in the actual cell [107, 108]. The effect of the residual stresses was discussed separately in the discussion.
The layers were assumed to remain planar during all the processes. This was believed to be a reasonable assumption, as the cells are fixed to planarity when mounted in the stack. Curvature upon for instance re-oxidation is therefore not likely to occur.
The layers were assumed not to be restricted by other components in the stack. The dimensional change of the layers was assumed to be determined by the mutual restrictions between the layers in the system.

8.3.1 Uniaxial 2-layered system

A sketch of the bi-layered system is shown in Figure 8.1. The sketch illustrates the as-sintered state, and the re-oxidized state for the case where the anode is free to expand, and for the case where the layers are coherent.

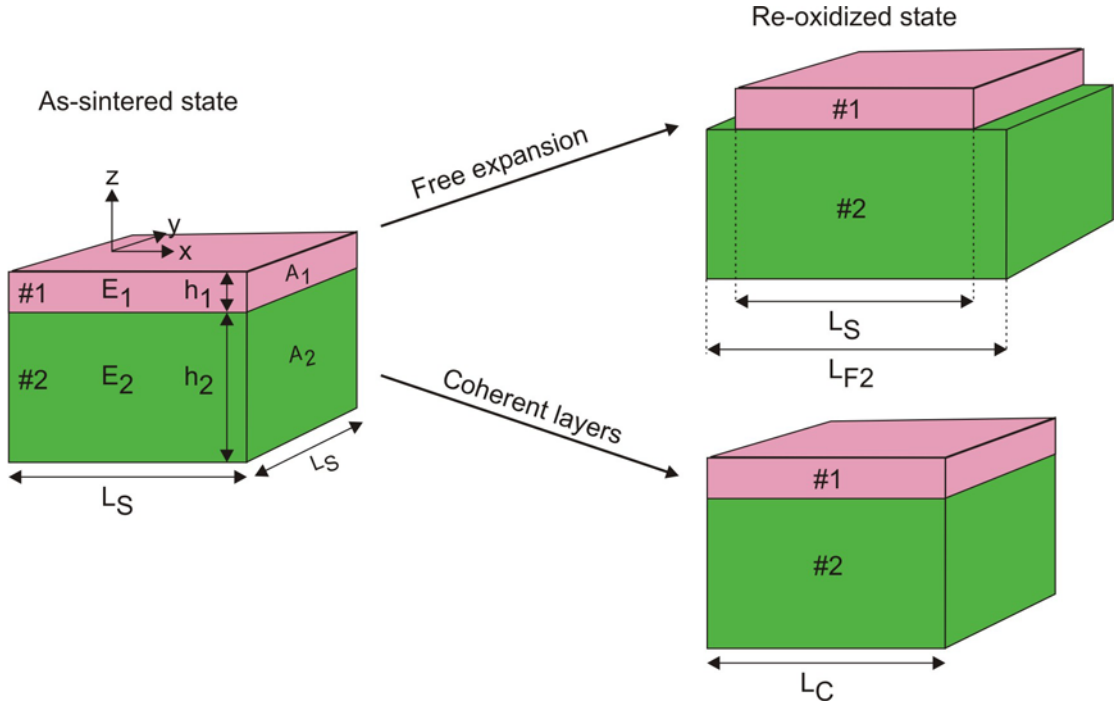

Figure 8.1. Sketch of the 2-layer system in the as-sintered state, and in the re-oxidized state for the case of free anode expansion, and for the case of coherent layers. Layer 1 represents the electrolyte, and layer 2 represents the anode support. Each layer is assigned an elastic modulus (E_i), a thickness (h_i), a lateral dimension (L_i), and a cross-section area (A_i).

Layer 1 represents the electrolyte, and layer 2 represents the anode support (cf. Figure 8.1). The actual cell design also contains a thin functional anode layer between the electrolyte and the anode-support (cf. Chapter 1, Section 1.2.1.2). The layer was omitted in this model. Each layer is characterized by an elastic modulus (E_i), a thickness (h_i), a lateral dimension (L_i), and a cross-section area (A_i).
The dimensions of the layers are indicated in Figure 8.1. The model only considers the changes in the x-direction. The as-sintered state was defined as stress free, and the lateral dimension of the layers was L_S.
Upon re-oxidation, the anode-support will expand to L_{F2} if it was allowed to expand freely. The dimension of the electrolyte layer on the other hand, will remain constant (cf. Figure 8.1). However, if the layers were coherent, the dimension of both layers will be L_C upon re-oxidation,

where $L_S < L_C < L_{F2}$ (cf. Figure 8.1). The expansion of the anode is then restricted by the electrolyte, and the anode layer will be in compression, while the electrolyte will be in tension.

For the coherent case, the stress in the electrolyte (τ_1) is given by Hooke's law, which applies to materials with elastic behavior (cf. Equation 8.1). E_1 is the elastic modulus of the electrolyte, and ε_1 is the strain. As the lateral dimensions of the layers are much bigger than the layer thickness (above a factor of 400 for the actual cell design), the stresses are assumed to be constant, and independent of the z-position in each layer.

Eq. 8.1 $$\tau_1 = E_1 \cdot \varepsilon_1$$

From Figure 8.1 it is seen that the strain in the layers can be expressed as shown in Equations 8.2 and 8.3.

Eq. 8.2 $$\varepsilon_1 = \frac{L_C - L_S}{L_S} = \frac{L_C}{L_S} - 1$$

Eq. 8.3 $$\varepsilon_2 = \frac{L_C - L_F}{L_{F2}} = \frac{L_C}{L_{F2}} - 1$$

When inserting Equation 8.2 into Equation 8.1, Equation 8.4 describes the stress in the electrolyte.

Eq. 8.4 $$\tau_1 = E_1 \cdot \left(\frac{L_C}{L_S} - 1 \right)$$

The layers were assumed to remain planar during the process and unrestricted by the surroundings. Thus, the forces in the layers will outbalance each other as shown in Equation 8.5.

Eq. 8.5 $$F_1 + F_2 = 0$$

The force is the product of the stress and the perpendicular cross section area. When this is inserted into Equation 8.5, and combined with Hooke's law, Equation 8.6 is obtained. By further rearrangements Equations 8.7 and 8.8 are obtained.

Eq. 8.6 $$E_1 \cdot \varepsilon_1 \cdot A_1 + E_2 \cdot \varepsilon_2 \cdot A_2 = 0$$

Eq. 8.7 $$E_1 \cdot \varepsilon_1 \cdot L_S \cdot h_1 + E_2 \cdot \varepsilon_2 \cdot L_S \cdot h_2 = 0$$

Eq. 8.8 $$E_1 \cdot \varepsilon_1 \cdot h_1 + E_2 \cdot \varepsilon_2 \cdot h_2 = 0$$

Equations 8.2 and 8.3 are substituted into Equation 8.8, resulting in Equation 8.9.

Eq. 8.9 $$E_1 \cdot \left(\frac{L_C}{L_S} - 1 \right) \cdot h_1 + E_2 \cdot \left(\frac{L_C}{L_{F2}} - 1 \right) \cdot h_2 = 0$$

By rearranging Equation 8.9, an expression of the ratio L_C/L_{F2} is obtained (cf. Equation 8.10-8.14).

Eq. 8.10 $$E_1 \cdot h_1 \cdot \frac{L_C}{L_S} - E_1 \cdot h_1 + E_2 \cdot h_2 \cdot \frac{L_C}{L_{F2}} - E_2 \cdot h_2 = 0$$

Eq. 8.11 $$L_C \cdot \left(\frac{E_1 \cdot h_1}{L_S} + \frac{E_2 \cdot h_2}{L_{F2}} \right) = E_1 \cdot h_1 + E_2 \cdot h_2$$

Eq. 8.12 $$L_C = \frac{E_1 \cdot h_1 + E_2 \cdot h_2}{\frac{E_1 \cdot h_1}{L_S} + \frac{E_2 \cdot h_2}{L_{F2}}}$$

Eq. 8.13 $$L_C = \frac{L_S \cdot L_{F2} \cdot (E_1 \cdot h_1 + E_2 \cdot h_2)}{L_{F2} \cdot E_1 \cdot h_1 + L_S \cdot E_2 \cdot h_2}$$

Eq. 8.14 $$\frac{L_C}{L_S} = \frac{L_F \cdot (E_1 \cdot h_1 + E_2 \cdot h_2)}{L_F \cdot E_1 \cdot h_1 + L_S \cdot E_2 \cdot h_2}$$

Finally, when Equation 8.14 is substituted into Equation 8.4, an expression of the stress in the electrolyte for the coherent case is obtained, as a function of the elastic moduli, layer thickness, and free expansion (cf. Equation 8.15).

Eq. 8.15 $$\tau_1 = E_1 \cdot \left(\frac{L_{F2} \cdot (E_1 \cdot h_1 + E_2 \cdot h_2)}{L_{F2} \cdot E_1 \cdot h_1 + L_S \cdot E_2 \cdot h_2} - 1 \right)$$

8.3.2 Uniaxial 3-layered system

If a third layer, corresponding to the functional anode layer is added to the model, the system is modified to the sketch shown in Figure 8.2. Layer 1 is still the electrolyte, layer 2 is the anode support, and layer 3 represents the functional anode. Again, the model only considers the changes in the x-direction.
The as-sintered state was defined to be stress free, and the lateral dimension of the layers is L_S. Upon re-oxidation with free expansion, the anode layers (layers 2 and 3) will expand to L_{F2} and L_{F3} respectively. The lateral dimension of the electrolyte will remain constant (L_S). Re-oxidation when the layers are coherent will result in a common dimensional change of the layers to L_C, where $L_S < L_C < L_{F2} < L_{F3}$ (cf. Figure 8.2). Accordingly, tensile stress is generated in the electrolyte, and compressive stresses occur in the anode layers. The stresses are assumed constant and independent of the z-position in each layer. For the coherent case, the strains occurring in the three layers can be described as shown in Equations 8.16-8.18.

Eq. 8.16 $$\varepsilon_1 = \frac{L_C - L_S}{L_S} = \frac{L_C}{L_S} - 1$$

Eq. 8.17 $$\varepsilon_2 = \frac{L_C - L_{F2}}{L_{F2}} = \frac{L_C}{L_{F2}} - 1$$

Eq. 8.18 $$\varepsilon_3 = \frac{L_C - L_{F3}}{L_{F3}} = \frac{L_C}{L_{F3}} - 1$$

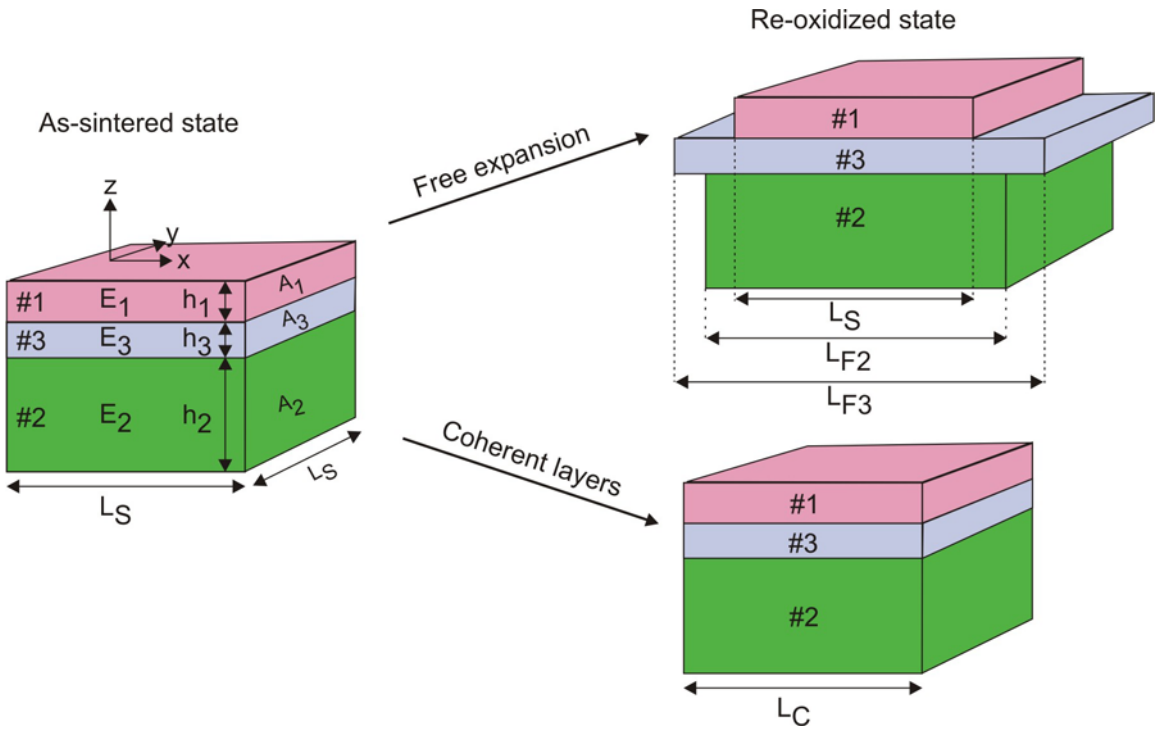

Figure 8.2. Sketch of the 3-layer system in the as-sintered state, and in the re-oxidized state for the case of free anode expansion, and for the case of coherent layers. Layer 1 represents the electrolyte, layer 2 represents the anode support, and layer 3 represents the functional anode. Each layer is assigned an elastic modulus (E_i), a thickness (h_i), a lateral dimension (L_i), and a cross-section area (A_i).

By application of Hooke's law and Equation 8.16, the stress in the electrolyte (τ_1) is expressed in Equation 8.19.

Eq. 8.19 $$\tau_1 = E_1 \cdot \varepsilon_1 = E_1 \cdot \left(\frac{L_C}{L_S} - 1 \right)$$

The layered system was assumed to remain planar and unrestricted by the surroundings. Thus, the sum of the forces in the layers is zero (cf. Equation 8.20).

Eq. 8.20 $$F_1 + F_2 + F_3 = 0$$

Equation 8.20 is modified by expressing the forces as the product of the stress and the cross section area, and by applying Hooke's law (cf. Equations 8.21-8.23).

Eq. 8.21 $$E_1 \cdot \varepsilon_1 \cdot A_1 + E_2 \cdot \varepsilon_2 \cdot A_2 + E_3 \cdot \varepsilon_3 \cdot A_3 = 0$$

Eq. 8.22 $$E_1 \cdot \varepsilon_1 \cdot L_S \cdot h_1 + E_2 \cdot \varepsilon_2 \cdot L_S \cdot h_2 + E_3 \cdot \varepsilon_3 \cdot L_S \cdot h_3 = 0$$

Eq. 8.23 $$E_1 \cdot \varepsilon_1 \cdot h_1 + E_2 \cdot \varepsilon_2 \cdot h_2 + E_3 \cdot \varepsilon_3 \cdot h_3 = 0$$

Equations 8.16-8.18 are substituted into Equation 8.23, from which Equation 8.24 is obtained.

Eq. 8.24 $$E_1 \cdot \left(\frac{L_C}{L_S} - 1 \right) \cdot h_1 + E_2 \cdot \left(\frac{L_C}{L_{F2}} - 1 \right) \cdot h_2 + E_3 \cdot \left(\frac{L_C}{L_{F3}} - 1 \right) \cdot h_3 = 0$$

By rearranging Equation 8.24, an expression of the ratio L_C/L_S is obtained (cf. Equation 8.25-8.30), that can be substituted into Equation 8.19 (cf. Equation 8.31). In consistence with the 2-layer model, the stress in the electrolyte is then expressed as a function of the elastic moduli, layer thickness, and free expansion of the layers comprised in the model.

Eq. 8.25 $$E_1 \cdot h_1 \cdot \frac{L_C}{L_S} - E_1 \cdot h_1 + E_2 \cdot h_2 \cdot \frac{L_C}{L_{F2}} - E_2 \cdot h_2 + E_3 \cdot h_3 \cdot \frac{L_C}{L_{F3}} - E_3 \cdot h_3 = 0$$

Eq. 8.26 $$L_C \cdot \left(\frac{E_1 \cdot h_1}{L_S} + \frac{E_2 \cdot h_2}{L_{F2}} + \frac{E_3 \cdot h_3}{L_{F3}} \right) = E_1 \cdot h_1 + E_2 \cdot h_2 + E_3 \cdot h_3$$

Eq. 8.27 $$L_C = \frac{E_1 \cdot h_1 + E_2 \cdot h_2 + E_3 \cdot h_3}{\frac{E_1 \cdot h_1}{L_S} + \frac{E_2 \cdot h_2}{L_{F2}} + \frac{E_3 \cdot h_3}{L_{F3}}}$$

Eq. 8.28 $$L_C = \frac{E_1 \cdot h_1 + E_2 \cdot h_2 + E_3 \cdot h_3}{\frac{(E_1 \cdot h_1 \cdot L_{F2} + E_2 \cdot h_2 \cdot L_S) \cdot L_{F3} + L_S \cdot L_{F2} \cdot E_3 \cdot h_3}{L_S \cdot L_{F2} \cdot L_{F3}}}$$

Eq. 8.29 $$L_C = \frac{L_S \cdot L_{F2} \cdot L_{F3} \cdot (E_1 \cdot h_1 + E_2 \cdot h_2 + E_3 \cdot h_3)}{(E_1 \cdot h_1 \cdot L_{F2} + E_2 \cdot h_2 \cdot L_S) \cdot L_{F3} + L_S \cdot L_{F2} \cdot E_3 \cdot h_3}$$

Eq. 8.30 $$\frac{L_C}{L_S} = \frac{L_{F2} \cdot L_{F3} \cdot (E_1 \cdot h_1 + E_2 \cdot h_2 + E_3 \cdot h_3)}{(E_1 \cdot h_1 \cdot L_{F2} + E_2 \cdot h_2 \cdot L_S) \cdot L_{F3} + L_S \cdot L_{F2} \cdot E_3 \cdot h_3}$$

Eq. 8.31 $$\tau_1 = E_1 \cdot \left(\frac{L_{F2} \cdot L_{F3} \cdot (E_1 \cdot h_1 + E_2 \cdot h_2 + E_3 \cdot h_3)}{(E_1 \cdot h_1 \cdot L_{F2} + E_2 \cdot h_2 \cdot L_S) \cdot L_{F3} + L_S \cdot L_{F2} \cdot E_3 \cdot h_3} - 1 \right)$$

8.3.3 Biaxial 3-layered system

The biaxial stress state for the 3-layer system illustrated in Figure 8.2 was examined. The description was obtained by similar manners as for the uniaxial case. The layers were assumed to be isotropic and plane. Thus biaxial stress occurred away from the boundaries. The biaxial stress state is defined by the equations shown in Eq. 8.32. τ denotes stress, and ε denotes strain.

Eq. 8.32 $$\tau_{xx}(z) = \tau_{yy}(z) \quad , \quad \varepsilon_{xx} = \varepsilon_{yy}$$

Hooke's law modifies to Equation 8.33 for the biaxial stress state. P represents the strain under free expansion. The other terms represent strain related to the stresses due to layer coherence. ν is the Poisson's ratio (i.e. the ratio between the normal strain in width and length for a tensile loaded sample). The Poisson's ratio and the elastic modulus describe the elastic properties of a material.

Eq. 8.33 $$\varepsilon_{xx} = \frac{\tau_{xx}}{E} - \frac{\upsilon \cdot \tau_{yy}}{E} + P$$

The stresses were assumed constant and independent of the z-position in each layer. Thus, for each layer Hooke's law can be expressed as shown in Equations 8.34-8.36.

Eq. 8.34 $$\varepsilon_1 = \frac{\tau_1}{E_1} \cdot (1 - \upsilon_1) + P_1$$

Eq. 8.35 $$\varepsilon_2 = \frac{\tau_2}{E_2} \cdot (1 - \upsilon_2) + P_2$$

Eq. 8.36 $$\varepsilon_3 = \frac{\tau_3}{E_3} \cdot (1 - \upsilon_3) + P_3$$

For the case where the three layers are coherent, the strain must be identical for each layer. The common resultant strain is denoted ε_0 as shown in Equation 8.37.

Eq. 8.37 $$\varepsilon_1 = \varepsilon_2 = \varepsilon_3 = \varepsilon_0$$

Equations 8.34-8.36 are then modified into Equations 8.38-8.40.

Eq. 8.38 $$\varepsilon_0 = \frac{\tau_1}{E_1} \cdot (1 - \upsilon_1) + P_1$$

Eq. 8.39 $$\varepsilon_0 = \frac{\tau_2}{E_2} \cdot (1 - \upsilon_2) + P_2$$

Eq. 8.40 $$\varepsilon_0 = \frac{\tau_3}{E_3} \cdot (1 - \upsilon_3) + P_3$$

By rearranging Equations 8.38-8.40 an expression for the stress in each layer is obtained (cf. Equations 8.42-8.44). For convenience, and since ν_i is not equal to 1, the abbreviation E_i^* as defined in Equation 8.41, is used.

Eq. 8.41 $$E_i^* = \frac{E_i}{1 - \upsilon_i}$$

Eq. 8.42 $$\tau_1 = \varepsilon_0 \cdot \frac{E_1}{1 - \upsilon_1} - \frac{E_1}{1 - \upsilon_1} \cdot P_1 = \varepsilon_0 \cdot E_1^* - E_1^* \cdot P_1$$

Eq. 8.43 $$\tau_2 = \varepsilon_0 \cdot \frac{E_2}{1 - \upsilon_2} - \frac{E_2}{1 - \upsilon_2} \cdot P_2 = \varepsilon_0 \cdot E_2^* - E_2^* \cdot P_2$$

Eq. 8.44 $$\tau_3 = \varepsilon_0 \cdot \frac{E_3}{1 - \upsilon_3} - \frac{E_3}{1 - \upsilon_3} \cdot P_3 = \varepsilon_0 \cdot E_3^* - E_3^* \cdot P_3$$

Planarity and no restrictions from the surroundings are assumed during the re-oxidation process. Thus by analogy with Equations 8.21-8.23, the forces in the layers outbalance each other, and Equation 8.45 is valid.

Eq. 8.45 $$\tau_1 \cdot h_1 + \tau_2 \cdot h_2 + \tau_3 \cdot h_3 = 0$$

By substitution of Equations 8.42-8.44 into 8.45, Equation 8.46 is obtained. The equation is rearranged (Equation 8.47), and an expression of ε_0 is achieved (cf. Equation 8.48).

Eq. 8.46 $$\left(\varepsilon_0 \cdot E_1^* - E_1^* \cdot P_1\right) \cdot h_1 + \left(\varepsilon_0 \cdot E_2^* - E_2^* \cdot P_2\right) \cdot h_2 + \left(\varepsilon_0 \cdot E_3^* - E_3^* \cdot P_3\right) \cdot h_3 = 0$$

Eq. 8.47 $$\varepsilon_0 \cdot \left(E_1^* \cdot h_1 + E_2^* \cdot h_2 + E_3^* \cdot h_3\right) - \left(E_1^* \cdot P_1 \cdot h_1 + E_2^* \cdot P_2 \cdot h_2 + E_3^* \cdot P_3 \cdot h_3\right) = 0$$

Eq. 8.48 $$\varepsilon_0 = \frac{E_1^* \cdot P_1 \cdot h_1 + E_2^* \cdot P_2 \cdot h_2 + E_3^* \cdot P_3 \cdot h_3}{E_1^* \cdot h_1 + E_2^* \cdot h_2 + E_3^* \cdot h_3}$$

Equation 8.48 is substituted into Equation 8.42. From this, the stress of layer 1 can be expressed as a function of the free expansion, layer thickness, and elastic properties of the layers (cf. Equations 8.49-8.50).

Eq. 8.49 $$\tau_1 = \frac{\left(E_1^* \cdot P_1 \cdot h_1 + E_2^* \cdot P_2 \cdot h_2 + E_3^* \cdot P_3 \cdot h_3\right)}{E_1^* \cdot h_1 + E_2^* \cdot h_2 + E_3^* \cdot h_3} \cdot E_1^* - E_1^* \cdot P_1$$

Eq. 8.50 $$\tau_1 = \frac{E_1^* \cdot E_2^* \cdot h_2 \cdot \left(P_2 - P_1\right) + E_1^* \cdot E_3^* \cdot h_3 \cdot \left(P_3 - P_1\right)}{E_1^* \cdot h_1 + E_2^* \cdot h_2 + E_3^* \cdot h_3}$$

From Figure 8.2 follows that the free expansion of the electrolyte is zero ($P_1 = 0$). Thus, the equation further simplifies to Equation 8.51.

Eq. 8.51 $$\tau_1 = \frac{E_1^* \cdot E_2^* \cdot h_2 \cdot P_2 + E_1^* \cdot E_3^* \cdot h_3 \cdot P_3}{E_1^* \cdot h_1 + E_2^* \cdot h_2 + E_3^* \cdot h_3}$$

8.3.4 Energy balance considerations

The resistance to crack growth can be used to evaluate whether the electrolyte will fracture. In fracture mechanics this is done by considering the energy balance. The elastic energy released upon cracking is compared to the energy expended to create the crack. The criterion for propagation of a crack is then, that the decrease in potential energy is equal to or bigger, than the energy consumed.
The potential energy released is called the energy release rate ($\mathcal{G}$). Generally $\mathcal{G}$ depends on the stress level as well as the sample geometry and crack size.
The energy expended to create cracking is a material property. The property is described by the critical energy release rate ($\mathcal{G}_{IC}$) that is the energy used per crack area formed, and has the unit J/m^2. For ceramics, the energy is primarily consumed to form new surface. For metals, plastic deformation also takes up a significant part of the energy. Depending on the material, $\mathcal{G}_{IC}$ can be constant or increase with the size of the crack. The last mentioned behavior is characteristic for materials with toughening mechanisms (e.g. transformation toughening, fiber pullout, or micro crack toughening) [29, 93].

The criterion for fracture is illustrated in Figure 8.3. In the Figure, the $\mathcal{G}_{IC}$-curve for a material with and without toughening is shown as a function of the crack size, a. The energy release rates for three different stress levels ($\tau_1<\tau_2<\tau_3$) are also shown.

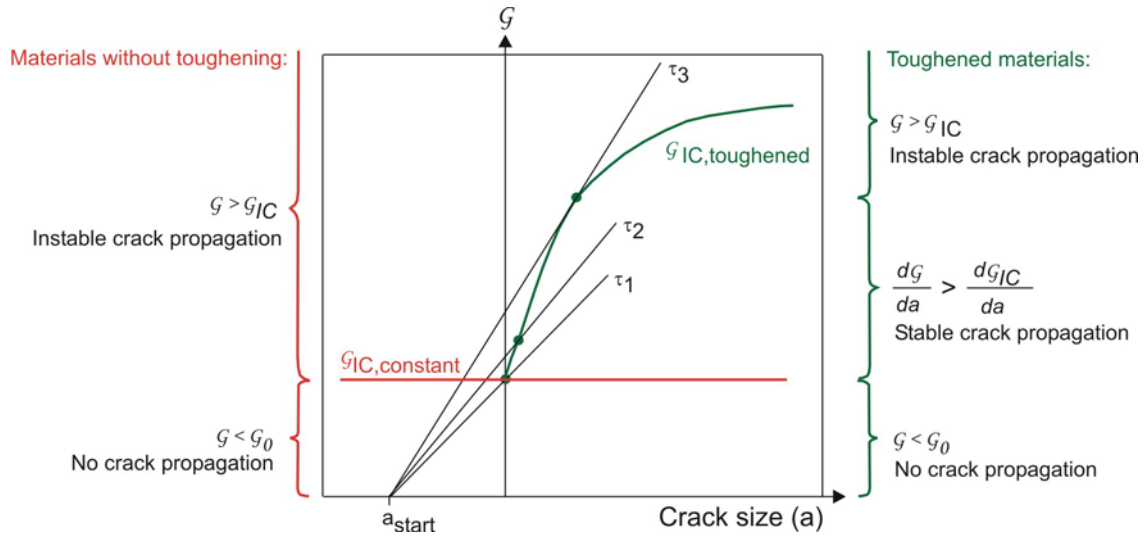

Figure 8.3. The critical energy release rate for a material with ($\mathcal{G}_{IC,toughened}$), and without toughening mechanisms ($\mathcal{G}_{IC,constant}$) as a function of the crack size, a. The energy release rates for three different stress levels ($\tau_1<\tau_2<\tau_3$) are shown. (Modified after [93]).

Instable, or steady state cracking will occur independent of the crack size when $\mathcal{G} \geq \mathcal{G}_{IC}$. Generally, for identical load (e.g. τ_2 and τ_3, cf. Figure 8.3), the critical energy release rate is reached at a later stage for materials with toughening mechanisms (cf. Figure 8.3). Further, for loads below τ_3 a stable crack growth range exists for the toughened materials, where crack growth will be stopped (cf. Figure 8.3).

A simple 2-layer system is illustrated in Figure 8.4. The system consists of a thin film of thickness, h, on a semi-infinite substrate. The film (layer 1) may represent the electrolyte, and the substrate may represent the anode support.

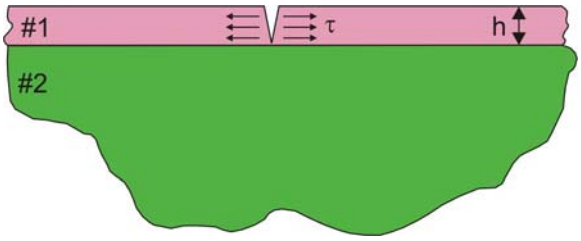

Figure 8.4. Two-layer model consisting of a thin film (layer 1) on a semi-infinite substrate (layer 2). τ denotes the tensile stress prior to the introduction of the crack.

For this system, the steady state energy release rate of the crack in the film follows Equation 8.52 [109]. τ denotes the tensile stress prior to the introduction of the crack. Lined E_1 is defined in Equation 8.53, and $g(\alpha,\beta)$ is tabulated by Beuth [109]. The variables to the function (α and β) are defined in Equations 8.54 and 8.55, respectively.

Eq. 8.52 $$\mathcal{G} = \frac{1}{2} \cdot \frac{\tau^2 \cdot h}{\overline{E_1}} \cdot \pi \cdot g(\alpha,\beta)$$

Eq. 8.53 $$\overline{E}_1 = \frac{E_1}{1-\upsilon^2}$$

Eq. 8.54 $$\alpha = \frac{\overline{E}_1 - \overline{E}_2}{\overline{E}_1 + \overline{E}_2}$$

Eq. 8.55 $$\beta = \frac{\mu_1 \cdot (1-2\cdot\upsilon_2) - \mu_2 \cdot (1-2\cdot\upsilon_1)}{2\cdot\mu_1 \cdot (1-\upsilon_2) + 2\cdot\mu_2 \cdot (1-\upsilon_1)}$$

8.4 Application of the models

8.4.1 Material properties

The layer models were applied to calculate the stress state of the state-of-the-art electrolyte upon the first re-oxidation. The material properties for the state-of-the-art layers found in the literature, and reported earlier in this thesis, were used. The values are summarized in Table 8.1.

Table 8.1. State-of-the-art material properties for the layers in the models. $\tau_{1,fracture}$ is the fracture strength of the electrolyte, E is Young's modulus, ν is Poisson's ratio, h is layer thickness. The subscripts refer to the layer number in the models. L_S is the as-sintered lateral dimension, P_2 and P_3 are respectively the relative expansion of layer 2 and 3 upon the first re-oxidation. RT signifies room temperature.

Parameter	Value	Material	Test conditions	Reference
$\tau_{1,fracture}$	265 MPa	8YSZ, dense	900°C, ring-on-ring	[110]
E_1	155 GPa	8YSZ, dense	900°C, impulse excitation technique	[110]
E_2	60 GPa	NiO-3YSZ, 17% porous	RT, strain gauge	Chapter 7
E_3	120 GPa	NiO-8YSZ, 12% porous	RT, estimated	Chapter 7
ν_1	0.315	8YSZ, dense	-	[110]
ν_2	0.17	NiO-8YSZ, 31% porous	-	[98]
ν_3	0.317	NiO-8YSZ, 11% porous	-	[98]
h_1	10 μm	-	-	[111]
h_2	300 μm	-	-	[111]
h_3	10 μm	-	-	[111]
L_S	120 mm	-	-	[111]
P_2	0.35 %	NiO-3YSZ, 8% porous	1000°C, dilatometry	Chapter 2
P_3	1.19 %	NiO-8YSZ, 2% porous	1000°C, dilatometry	Chapter 2

The fracture strength of the electrolyte decreases with increasing temperature [110]. For the models, a value valid for the realistic operational temperature of the SOFC was applied (cf. Table 8.1).

The elastic moduli of the anode support (E_2) and the functional anode (E_3) were based on Chapter 7. A quantitative value of E_2 was believed obtained with strain gauge. With video extensometer E_3 was qualitatively determined to twice the size of E_2 (cf. Chapter 7, Section 7.3.6). Thus, for the present calculations E_2 was assumed to be 60 GPa, and E_3 to be 120 GPa.

The Poisson's ratios of the anode support (ν_2), and the functional anode layer (ν_3) were estimated from [98]. However, no data for the actual anode support composition (NiO-3YSZ) was found. The Poisson's ratio was seen to depend on the porosity. As the anode support layer is more porous than the functional anode (cf. Chapter 7, Section 7.3), the reported high-porosity value was assigned to the anode support, and the low-porosity value to the functional anode.

The dimensions of the anode support and the functional anode layer after free expansion during the re-oxidation, are in the models denoted L_{F2} and L_{F3} respectively (cf. Figure 8.2). The

dimensions can be expressed by the relative expansion (P_i) of the layer, and the as-sintered lateral dimension (L_S) as shown in Equations 8.56 and 8.57.

Eq. 8.56 $$L_{F2} = L_S \cdot (1 + P_2)$$

Eq. 8.57 $$L_{F3} = L_S \cdot (1 + P_3)$$

In Chapter 2, relative expansions of the anode support material, and the functional anode material, were measured on pressed bar shaped samples. The values were used as respectively P_2 and P_3 (cf. Table 8.1).

8.4.2 Uniaxial 2-layered model

The stress in the electrolyte (τ_1) predicted from the uniaxial 2-layer model was shown in Equation 8.15. Substitution of Equation 8.56 results in Equation 8.58.

Eq. 8.58 $$\tau_1 = E_1 \cdot \left(\frac{L_S \cdot (1+P_2) \cdot (E_1 \cdot h_1 + E_2 \cdot h_2)}{L_S \cdot (1+P_2) \cdot E_1 \cdot h_1 + L_S \cdot E_2 \cdot h_2} - 1 \right)$$

With the state-of-the-art values from Table 8.1, the model predicts a tensile stress of 500 MPa in the electrolyte. This is far above the fracture strength of the electrolyte of 265 MPa (cf. Table 8.1). However, the thickness of the support (h_2), and the relative expansion of the anode support (P_2) are technological adjustable parameters. The stress in the electrolyte as a function of h_2 and P_2 is illustrated in Figure 8.5. Apart from the variables, the values from Table 8.1 are used as fixed values.

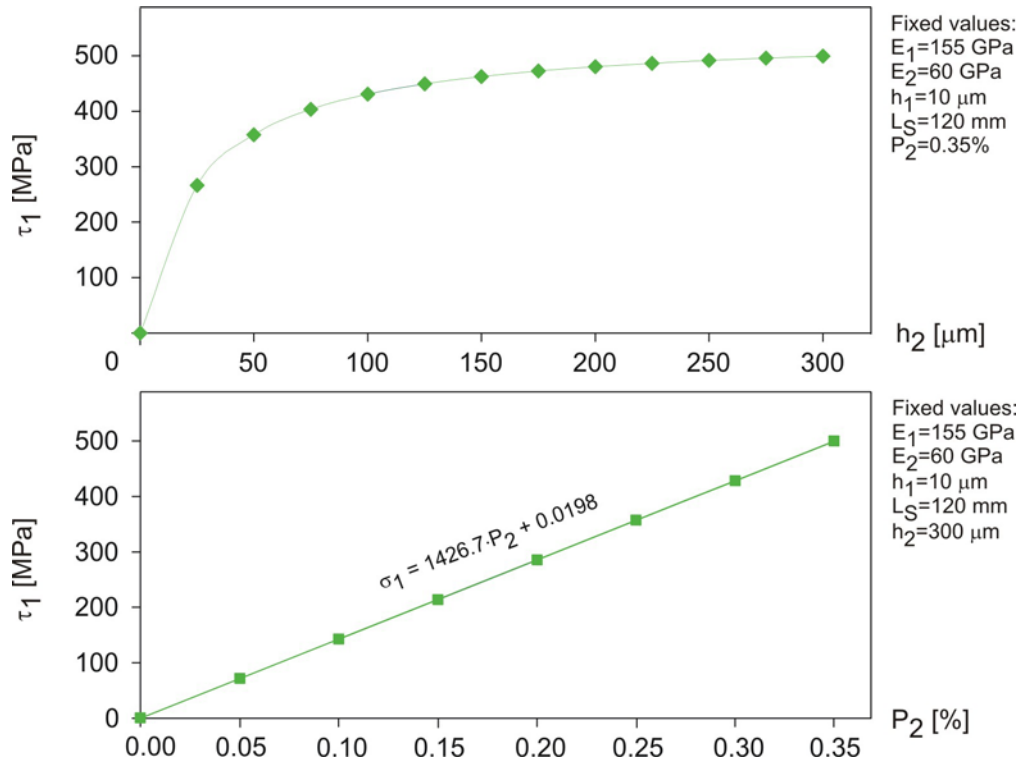

Figure 8.5. The stress in the electrolyte (τ_1) as a function of the anode support thickness (h_2), and the relative expansion of the anode-support (P_2), as predicted with the uniaxial 2-layered model.

If the state-of-the-art thickness of the anode support (h_2 = 300 µm, cf. Table 8.1) is decreased, the stress in the electrolyte decreases. For the stress to be below 265 MPa, the thickness must be reduced to approximately 25 µm (cf. Figure 8.5).
If instead the relative expansion of the anode support is decreased from the state-of-the-art value P_2 = 0.35% (cf. Table 8.1), the stress in the electrolyte was observed to decrease linearly. For the electrolyte stress to be reduced to below 265 MPa, the expansion must be limited to 0.19% (cf. Figure 8.5).

8.4.3 Uniaxial 3-layered model

The stress in the electrolyte (τ_1) predicted from the uniaxial 3-layer model was shown in Equation 8.31. Substitution of Equations 8.56 and 8.57 results in Equation 8.59.

Eq. 8.59
$$\tau_1 = E_1 \cdot \left(\frac{L_S^{\,2} \cdot (1+P_2) \cdot (1+P_3) \cdot (E_1 \cdot h_1 + E_2 \cdot h_2 + E_3 \cdot h_3)}{(E_1 \cdot h_1 \cdot L_S \cdot (1+P_2) + E_2 \cdot h_2 \cdot L_S) \cdot L_S \cdot (1+P_3) + L_S^{\,2} \cdot (1+P_2) \cdot E_3 \cdot h_3} - 1 \right)$$

With the state-of-the-art values from Table 8.1, the model predicts a tensile stress of 580 MPa in the electrolyte, which is far above the fracture strength of the electrolyte of 265 MPa (cf. Table 8.1).
The thickness of the anode support (h_2) and the functional anode (h_3), as well as the relative expansions (P_2, P_3), are technological adjustable parameters. The stress in the electrolyte as a function of the four parameters is illustrated in Figure 8.6. Apart from the variables, the values from Table 8.1 are used as fixed values.

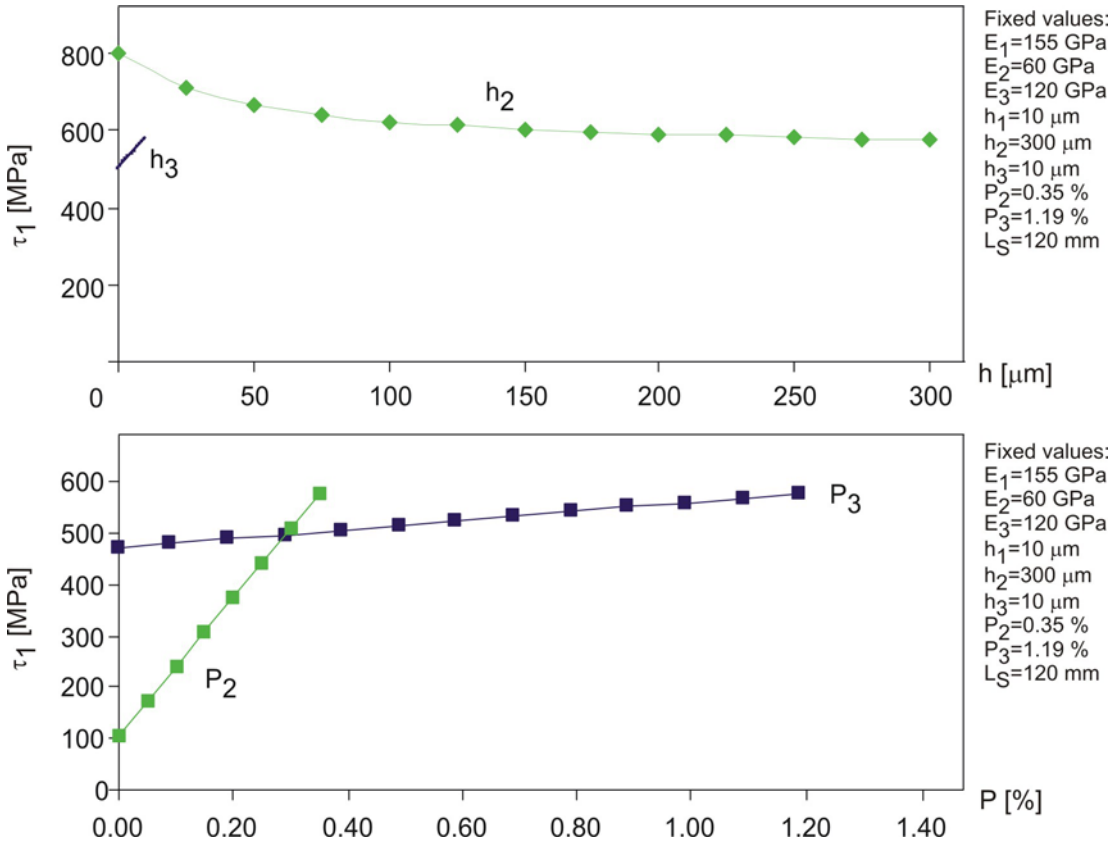

Figure 8.6. The stress in the electrolyte (τ_1) as a function of the anode support thickness (h_2), the functional anode thickness (h_3), the relative expansion of the anode support (P_2), or the relative expansion of the functional anode (P_3), as predicted with the uniaxial 3-layered model.

From Figure 8.6 it is seen that it is not possible to reduce the stress in the electrolyte to below 265 MPa by reducing the thickness of either the anode support (h_2) or the functional anode (h_3). Also, sufficient reduction of the electrolyte stress by reducing the relative expansion of the functional anode (P_3) is predicted impossible. The relative expansion of the anode support (P_2) appears as the only efficient parameter. If the expansion is reduced to 0.12% the stress level will be below the fracture strength of the electrolyte.

8.4.4 Biaxial 3-layered model

The stress in the electrolyte (τ_1) predicted from the biaxial 3-layer model was shown in Equation 8.51. With the state-of-the-art values from Table 8.1, the model predicts a tensile stress of 850 MPa in the electrolyte, which is far above the fracture strength of the electrolyte of 265 MPa (cf. Table 8.1).
The thickness of the anode support (h_2) and the functional anode (h_3), as well as the relative expansions (P_2, P_3), are technological adjustable parameters. The stress in the electrolyte as a function of the four parameters is illustrated in Figure 8.7. Apart from the variables, the values from Table 8.1 are used as fixed values.

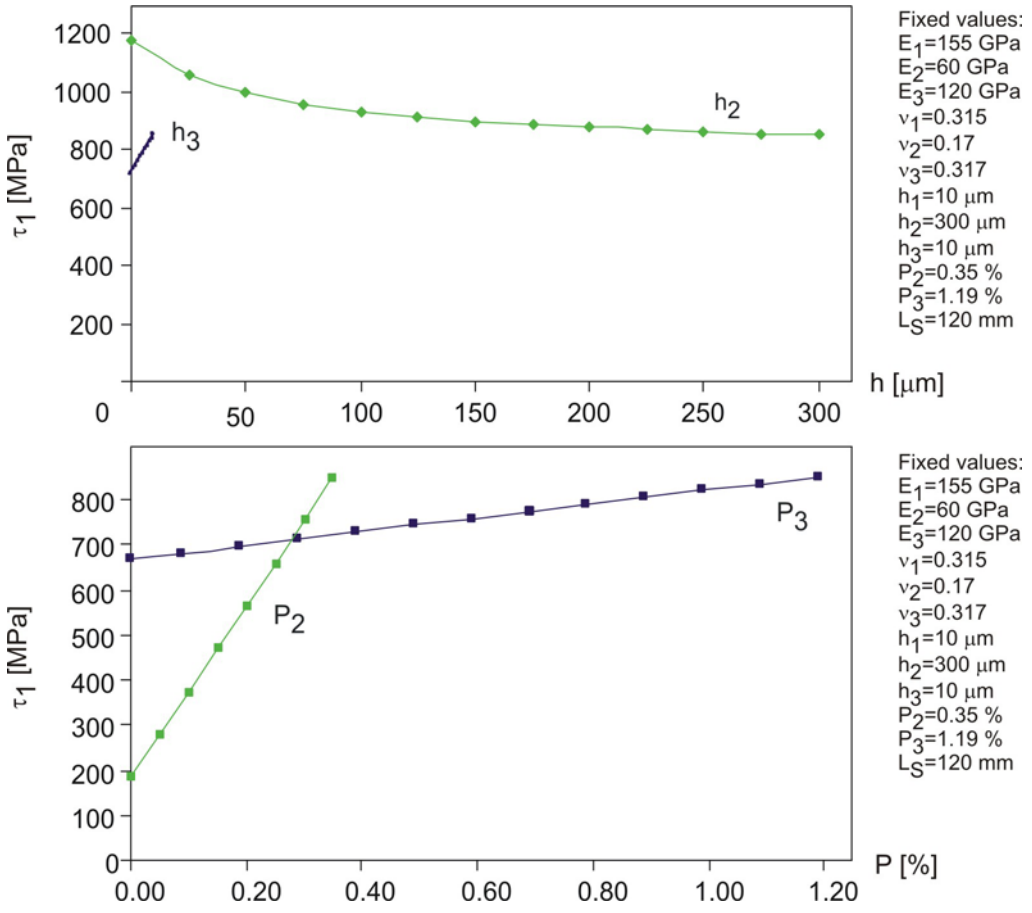

Figure 8.7. The stress in the electrolyte (τ_1) as a function of the anode support thickness (h_2), the functional anode thickness (h_3), the relative expansion of the anode support (P_2), or the relative expansion of the functional anode (P_3), as predicted with the biaxial 3-layered model.

In analogy with the uniaxial 3-layer model, Figure 8.7 predicts the relative expansion of the anode support (P_2) to be the only efficient parameter. The stress in the electrolyte will become below the fracture strength if the expansion is reduced to 0.04% (cf. Figure 8.7).

8.4.5 Model based on fracture energy considerations

The energy release rate was described as a function of the tensile stress, and the thickness of the film layer in Equation 8.52. Based on the fracture criterion ($\mathcal{G} \geq \mathcal{G}_{IC}$), it is possible to calculate a critical thickness ($h_{c,1}$) for a given stress state, or a critical stress ($\tau_{c,1}$) for a given film thickness, below which, fracture of the electrolyte-film cannot occur.
For calculations, the critical energy release rate for the electrolyte is reported to be $\mathcal{G}_{IC} = 2.8$ J/m^2 [112]. The parameters α and β were calculated to respectively 0.4716 and 0.2212 from Equations 8.54 and 8.55, and based on the values in Table 8.1. The function $g(\alpha,\beta)$ was approximated to 1.949 with the table in [109], where the closest tabulated values to the calculated α and β values (0.50 and 0, respectively) were used.
The tensile stresses in the electrolyte (τ_1) predicted by the layer models with the state-of-the-art parameter values, are shown in Table 8.2. For each stress state, the corresponding critical thickness ($h_{1,c}$) was calculated from Equation 8.52. The results are shown in Table 8.2. Also, for the state-of-the-art electrolyte thickness (h_1 = 10 μm), the critical stress in the electrolyte ($\tau_{1,c}$) was calculated with Equation 8.52 for the three models (cf. Table 8.2).

Table 8.2. Critical thickness and stress predicted from Equation 8.52. τ_1 is the tensile stress in the electrolyte as observed with the three different layer models and the state-of-the-art parameter values. $h_{c,1}$ is the corresponding critical electrolyte thickness. h_1 denotes the electrolyte thickness, and $\tau_{1,c}$ is the corresponding critical stress.

Model	Critical thickness		Critical stress	
	τ_1 [MPa]	$h_{1,c}$ [μm]	h_1 [μm]	$\tau_{1,c}$ [MPa]
Uniaxial, 2-layer	499	$6.31 \cdot 10^{-10}$	10	0.004
Uniaxial, 3-layer	576	$4.74 \cdot 10^{-10}$	10	0.004
Biaxial, 3-layer	852	$2.17 \cdot 10^{-10}$	10	0.004

With the stresses predicted by the layer models, the thickness of the electrolyte must be reduced several orders of magnitude below the state-of-the-art 10 μm, before fracture of the electrolyte upon re-oxidation is prevented (cf. Table 8.2). Also, the critical stress obtained with a 10 μm thick electrolyte is several orders of magnitude below the stresses predicted present by the layer models (cf. Table 8.2).

8.5 Synchrotron data

The stress state of the Ni and NiO phase was analyzed with synchrotron upon redox cycling. The shear components were observed to be negligible. The in-plane principal stress components are shown for subsequent oxidation states in Figure 8.8. A full cell and a half-cell were analyzed. The samples were nominally identical, apart from the full cell containing the cathode layer as well.
The two samples showed similar behavior (cf. Figure 8.8). The cathode layer of the full cell did not appear to influence significantly on the stress state.
At room temperature compressive stress was observed. However, upon heating the residual stress was assumed to become close to zero. The following reduced nickel states displayed tensile residual stresses, and the re-oxidized states displayed compressive stresses (cf. Figure 8.8).
At room temperature tensile stresses in the nickel phase were expected as the TEC of NiO is higher than the TEC of YSZ (cf. Chapter 2, Section 2.3.1). However, tension upon reduction is in accordance with shrinkage of the nickel phase when reduced, and compression upon re-

oxidation in accordance with expansion of the phase that is restricted by the YSZ phase. For the first re-oxidation, the compressive stress was around -200 MPa. The stress increased to up to -700 MPa upon the second re-oxidation (cf. Figure 8.8). The compressive stress in the nickel phase is outbalanced by equivalent tensile stress in the YSZ phase. Thus, the measured stresses were observed to be in the same order of magnitude as the tensile stresses predicted by the layer models (cf. Table 8.2).

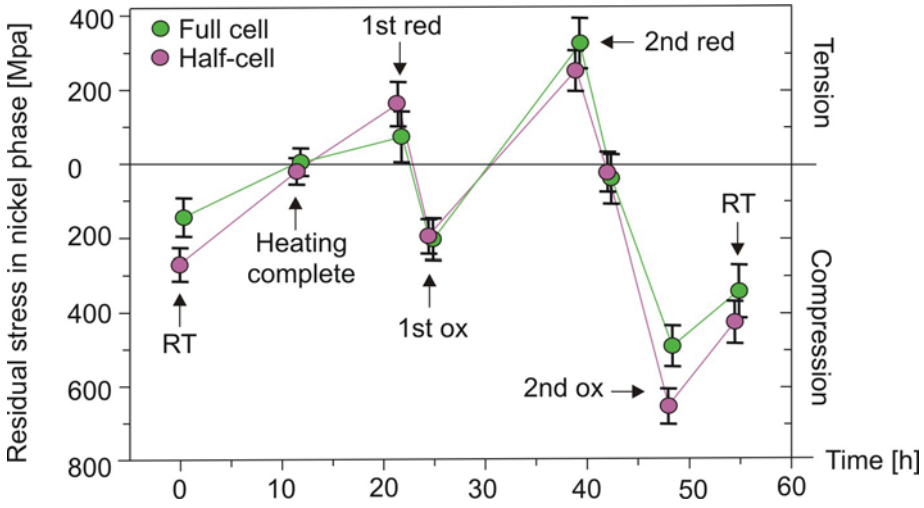

Figure 8.8. Residual in-plane stress in the Ni and NiO phase of an anode cermet in different states. The measurements were based on synchrotron analyses of a full cell and a half-cell. (Figure modified after [106]).

8.6 Discussion

8.6.1 Model predictions

The more detailed models predicted a more severe stress state of the electrolyte upon re-oxidation. Correspondingly, the demands for redox stability became tougher for the more advanced models. The relative expansion of the anode support (P_2) required to keep the tensile stress of the electrolyte below the fracture strength of 265 MPa is considered. In the uniaxial 2-layer model the requirement was 0.19%. For the uniaxial 3-layered model, and the biaxial 3-layered system the requirement further intensified to respectively 0.12% and 0.04% (cf. Sections 8.4.2-8.4.4).

The uniaxial 2-layer model also predicted the anode support thickness (h_2) as a possible parameter. However, the thickness needs to be reduced to below 25 μm before redox stability was obtained (cf. Section 8.4.2). This is not a possibility with the current production techniques and design. For the 3-layered systems, the opposite correlation with h_2 was observed. When h_2 was reduced, the stress in the electrolyte increased, as the expansion of the functional anode (layer 3) became increasingly influential (cf. Sections 8.4.3 and 8.4.4).

The uniaxial, 2-layer model appeared to be too simple, and to produce results that were significantly different from the results of the more advanced models. Thus, the biaxial, 3-layer model is believed to represent the actual conditions during a redox cycle most precisely. The biaxial model predicted a significant improvement in P_2 before redox stability was achieved. An improvement of ca. a factor of 10 (from 0.35% to 0.04%, cf. Section 8.4.4) was estimated to be necessary.

The models were in general agreement with synchrotron analyses of the in-situ stress state of the electrolyte. The measured stresses were in the same order of magnitude as the values predicted by the models. However, the synchrotron analyses were not fully understood, and was only taken

as qualitative data. The measured stresses were observed to increase upon the second redox cycle. This was in agreement with the model of the redox mechanism proposed in Chapter 2, where the cermet structure was shown to become increasingly strained upon the second redox cycle.

8.6.2 Residual stresses

The models did not consider residual stresses present before the re-oxidation. The actual requirements to obtain redox stability will be influenced by the stresses present. The residual stresses depend on the history of the cell. Stresses are introduced during co-sintering, mounting of the cell in the stack, and reduction of the functional anode and anode support.
The anode support, functional anode, and electrolyte are typically co-sintered at temperatures above 1300°C. The operational temperature is lower, around 800°C. Thus, due to TEC mismatch ($TEC_{anode}>TEC_{electrolyte}$ cf. Chapter 2, Section 2.3.1), compressive stress is introduced into the electrolyte.
The TEC mismatch results in curvature of the cell. When mounting the cells into a stack, the cells are flattened by a mechanical load. The process generates additional compressive stress into the electrolyte provided relaxation processes do not eliminate the effect [113].
Furthermore, restrictions inflicted by the other stack components may add compressive stress into the electrolyte. Also, the reduction of the nickel network, which involves shrinkage of metallic part of the cermet structure, may add to the compressive stresses in the electrolyte.

Fisher et al. [108] measured the residual stress in the electrolyte after co-sintering, mechanical flattening, and reduction of a cell design comparable to the 3-layered model in Figure 8.2. The measurements were done by x-ray diffraction at room temperature. Following the three steps, a resulting compressive stress of -520 MPa ± 30 MPa was measured in the electrolyte at room temperature. At 800°C the stress was estimated to be reduced to -240 MPa.
The prime source to the created compressive stress was the TEC mismatch. The intermediate flattening step did not alter the stress from the as-co-sintered state. However, the flattening was done at elevated temperature (1360°C), and plastic deformation of the anode and electrolyte was suggested to accommodate the initial compressive stress formed.
The reduction process was reported to reduce the compressive stress of the electrolyte slightly. However, in a similar study [107], no change in the stress distribution upon reduction was observed.
Thus, a residual compressive stress of at least -240 MPa may be assumed to be present in the electrolyte prior to the first re-oxidation. This is believed to be a minimum value, since the flattening is likely to be carried out at lower temperatures. In addition, compressive stresses from the surrounding stack set-up have not been included.
A residual compressive stress will counteract the tensile stress generated upon the re-oxidation. The tensile stress predicted by the biaxial model was 852 MPa (cf. Table 8.2). When taking the residual stress into account, the electrolyte is believed to fracture when the tensile stress from the re-oxidation (τ_1) exceeds 505 MPa (= 265 MPa +240 MPa). From Figure 8.7 the allowed expansion of the anode support (P_2) is then estimated to be 0.17%.

8.7 Conclusions

The mechanical requirements to a redox stable anode were quantified by use of simple layered models. The conclusions are:

- The layer models were seen to be a possible development tool for evaluating the redox stability. However, the 2-layer model where uniaxial stresses were considered, appeared too simple to represent the actual system sufficiently.

- The requirements for obtaining redox stability intensified with the more detailed models.

- The 3-layer model where biaxial stresses were considered, predicted the system to be redox stable if the anode support expansion was reduced by an order of magnitude, i.e. from 0.35% to 0.04%.

- If the residual stresses in the electrolyte introduced before the re-oxidation were taken into account, the system was estimated to be redox stable for anode support expansions below 0.17%.

- A model based on the fracture energy balances indicated that the critical electrolyte thickness, or the critical stress in the electrolyte, were not realistic technological aims.

- Synchrotron measurements are a possible method of evaluating the stress states in the layers. The data appeared only to be qualitative. However, the measurements indicated that the cathode layer did not influence on the stress state in the other layers, as assumed in the models. Further, in accordance with the model of the redox mechanism proposed in Chapter 2, the synchrotron analyses indicated increased strain upon the second redox cycle.

Acknowledgements

M. V. Berthelsen (Danish Technical University and Risø National Laboratory) is acknowledged for the development of the uniaxial, 2-layered model. B. F. Sørensen (Risø National Laboratory) is acknowledged for support on the theory, and the development of the biaxial, 3-layered model. A. Hagen (Risø National Laboratory), R. V. Martins (Risø National Laboratory and GKSS), H. F. Poulsen (Risø National Laboratory), V. Honkimäki (European Synchrotron Radiation Facility), T. Buslaps (European Synchrotron Radiation Facility), and R. Feidenshans'l (Risø National Laboratory) are acknowledged for the synchrotron experiments and associated data treatment.

9 Modification of nickel-YSZ cermets with additives

9.1 Introduction

For commercial applications of the solid oxide fuel cell (SOFC) technology, redox stability of the anode is required in many cases [19, 21]. However, the state-of-the-art nickel-YSZ anode-supported SOFC is not redox stable. Redox cycling of the cermet structure is associated with microstructural changes. The nickel phase will reorganize, and damage on the ceramic network is introduced upon oxidation [84] and cf. Chapters 2-5. The microstructural changes are permanent, and detrimental to the cell performance [8, 23, 58].
The microstructural changes are reflected in the bulk properties, as for example the dimensional changes, and the conductivity of the structure. From bulk measurements, the microstructural changes were seen to depend on the cermet structure, composition, and temperature. Less change was observed for cermets with a stronger ceramic component (cf. Chapters 2-4, 7), cermets with a higher yttria content (cf. Chapter 5), and for cermets tested at lower temperatures (cf. Chapters 2 and 5). Models of the system indicated that the cermet will be redox stable if the bulk expansion upon re-oxidation is limited to 0.17%. This corresponds to a reduction by a factor of 2 from the state-of-the-art value (cf. Chapter 8).
In this chapter the anode support composition was modified with additives, and the effect on the microstructural stability was examined by bulk measurements. The additives were Al_2O_3, CeO_2, and TiO_2, and both the types of additive and the volume percent of the additive, were varied. The microstructural changes were quantified with dilatometry and DC conductivity measurements, and compared to reference samples of standard composition without additives.

9.2 Theory

9.2.1 Strengthening mechanisms

The ceramic component may be strengthened in different ways. One way is to improve the grain contacts. This is obtained with harsher sintering, introduced by for instance higher sintering temperature, or finer particle sizes. Decreasing the porosity will also increase the strength. However, significant changes in sintering procedure or sample porosity are not likely to be technological relevant solutions.
Another possible way to strengthen the ceramic component is to apply additives. The additives may result in second phase particles, incorporated into the ceramic structure. The particles can act as crack impediments, or generate internal stress fields that will alter the crack path. The required energy for crack propagation will then increase, resulting in a toughened structure [27].
If additions of whiskers or fibers are not considered, the additive promoted toughening mechanisms may be divided into five main groups,. The mechanisms are sketched in Figure 9.1, and the illustrations show (a) transformation toughening, (b) bridging, (c) deflection, (d) micro cracking, and (e) bowing [27, 29].

Transformation toughening

Transformation toughening is known from partially stabilized zirconia (PSZ). PSZ is two-phase zirconia of cubic, and tetragonal or monoclinic, zirconia. The mixture is produced in doped zirconia, for instance yttria doped zirconia, when the yttria content is below ca. 8 mol% [26].
For the composition 3 mol% Y_2O_3-ZrO_2, the monoclinic symmetry (m-YSZ) is stable at temperatures below 1200°C. However, metastable tetragonal YSZ particles (t-YSZ) will be

retained at temperatures below 1200°C, if the particles are sufficiently fine, or sufficiently constrained by the matrix [26].
The metastable t-YSZ particles will transform to the stable monoclinic symmetry in the vicinity of a propagating crack, as tensile stress prevails here. The phase transformation involves a volume expansion (3-5%), and shear strain (1-7%). Thus, a compressive stress is generated in the matrix, and further propagation of the crack becomes increasingly difficult. The transformation zone results in increased toughness and strength [27].
The mechanism is illustrated in Figure 9.1a. The volume expansion of the transformed m-YSZ particles is illustrated by a dark pink border. The transformation zone in the vicinity of the crack is shown with yellow, and the arrows indicate the generated compressive stresses.

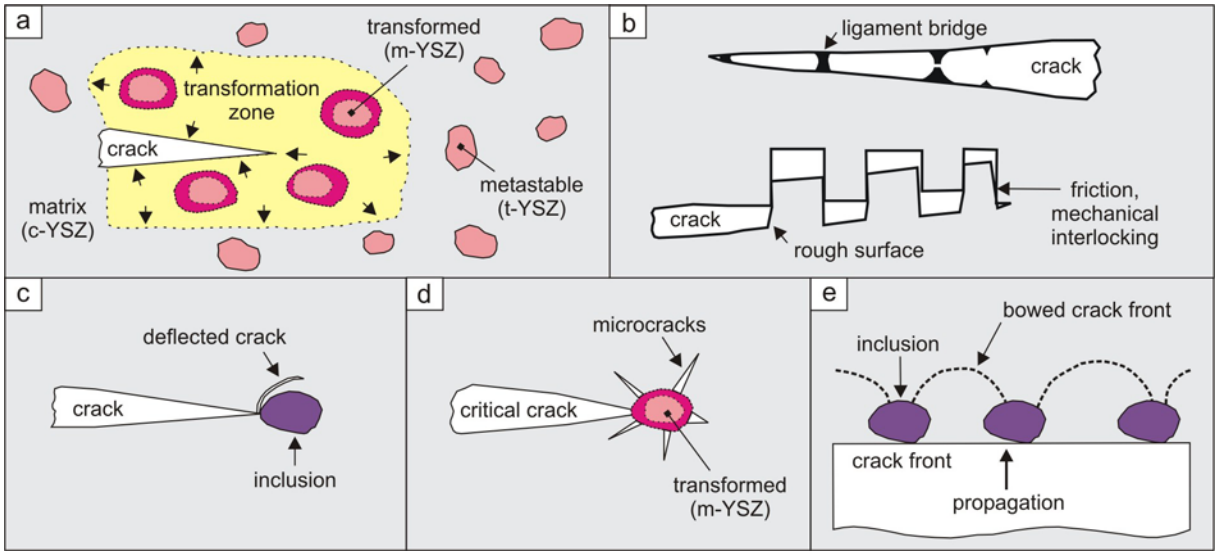

Figure 9.1. Additive promoted toughening mechanisms. The matrix is shown with gray color. (a) Transformation toughening. Particles with a dark pink border illustrates phase transformed and volume expanded particles. The yellow zone is the transformation zone where compressive stresses, indicated by arrows, are generated. (b) Bridging. The lower sketch illustrates frictional or mechanical interlocking. The upper sketch illustrates ligamentary bridges. (c) Deflection. The particle represents a second phase inclusion. (d) Micro cracking. A phase transformation, involving expansion of the particle has generated micro cracks around the particle. (e) Bowing. The particles indicate second phase inclusions with higher resistance to fracture than the matrix. (Modified after [27, 29]).

Bridging

Bridging is also called crack-interface traction, and involves restraining forces that hold the surfaces together. The two principal mechanisms are shown in Figure 9.1b. The lower sketch shows toughening due to frictional forces, or mechanical interlocking of the opposing fracture surfaces. These may be generated by a rough surface. The rough fracture surfaces may be formed due to large second phase particles. The upper sketch illustrates formation of ligamentary bridges behind the crack front. The ligaments make further crack propagation increasingly difficult [27].

Deflection

The interaction between an advancing crack and a second phase inclusion may result in the crack deviating from planarity. The process is illustrated in Figure 9.1c. The deflection results in a reduced stress state at the crack tip, i.e. reduction of the stress-intensity factor. The mechanical properties are therefore improved when deflection occurs [27].

Micro cracking

Micro crack toughening involves a matrix where micro cracks prevail. The micro cracks may be produced from thermal or elastic mismatch between the matrix and the inclusions, or during phase transformation of the inclusions. As an example, Figure 9.1d illustrates the transformation

of a metastable t-YSZ particle to m-YSZ, which involves a volume expansion, and the generation of micro cracks. When a critical propagating crack impinges with the particle, the micro cracks will absorb or dissipate the crack energy. In addition, the reduced elastic modulus of the micro cracked material has a toughening effect [27, 29].

Bowing

Crack bowing occurs due to interaction between a moving crack front, and dispersed second phase particles with higher resistance to fracture. The mechanism is illustrated in Figure 9.1e. Particles in the path of the propagating crack will pin the crack front. Further propagation will involve bowing of the crack front, and an enhanced crack front length. As a result, further movement of the crack will be increasingly difficult [27].

9.2.2 Additives

The effect of an additive is complex related to the mechanical properties. The effect will depend on the type, volume percent, dispersion, and particle size of the second phase. The particle size distribution of the matrix, and the porosity of the structure, will be influences as well. The additives may influence on properties that are indirectly related to the mechanical properties, e.g. the sintering process [114], and the thermal expansion coefficient (TEC) [34].
Strengthening of dense zirconia, or porous nickel-zirconia cermets, with additives has been investigated previously [27, 115, 116, 117, 118, 119]. The data from the literature are summarized in Table 9.1. Where information on the test conditions were found, these are included in the table.

Table 9.1. Literature studies on strengthening of zirconia with additives. Where information on the test conditions were found, they are shown.

Material to be strengthened	Additive	Strength [MPa]	Test conditions	Reference
Dense ZrO_2	2-3 mol% Y_2O_3 or CeO_2	900	Flexural	[27]
Dense ZrO_2	3 wt% MgO	290	Tensile, 25°C	[27]
Dense ZrO_2	3.3 wt% CaO	650	Flexural	[27]
Dense ZrO_2	2 mol% Y_2O_3 + 20 wt% Al_2O_3	1050	-	[27]
Porous NiO-YSZ	1.2% Al_2O_3	119	950°C	[120]
Porous NiO-YSZ	8 mol% Y_2O_3	32	-	[97]
Porous NiO-YSZ	10 mol% Y_2O_3	50	-	[97]
Single crystal ZrO_2	0.3 mol% Tb_2O_3	1100	Flexural	[115]
Single crystal ZrO_2	0.3 mol% CeO_2	1900	Flexural	[115]
Porous ZrO_2	10-15 mol% Ti	485	Compressive	[116]
Porous ZrO_2	12 mol% CeO_2 + 0.3 mol% CuO	350	Flexural, 25°C	[117]
Porous ZrO_2	12 mol% CeO_2 + 0.3 mol% MnO_2	450	Flexural, 25°C	[117]
Dense ZrO_2	6-16 mol% CeO_2	730	Flexural	[118]
Dense ZrO_2	6-16 mol% CeO_2 + 20 wt% Al_2O_3	1200	Flexural	[118]
Dense ZrO_2	10 mol% Y_2O_3 + 0-30 mol% Al_2O_3	400	Flexural	[119]

Direct comparison of the references is not possible due to the varying test conditions (cf. Table 9.1). However, addition of alumina was seen to improve the mechanical properties [27]. Further, ceria and titania appeared as additives with potential for strengthening of the structure (cf. Table 9.1).

The additives may influence on other performance parameters. For nickel cermets, application of additives has been observed to reduce the Ni sintering [44, 73, 78, 82, 121, 122], to improve the electrochemical performance [44, 45, 73, 123, 124, 125, 126, 127, 128], and to influence on the carbon deposition and sulfur tolerance [78, 129]. Data from the literature related to nickel sintering are summarized in Table 9.2.

Table 9.2. Literature studies on the effect of additives on nickel sintering.

Material	Additive	Effect of additive	Reference
Dense Ni-8YSZ	Ti	Improved Ni-8YSZ wettability	[121]
Porous Ni-YSZ	Co	Reduced Ni sintering	[122]
Porous Ni-YSZ	MgO, TiO_2, Mn_3O_4, Cr_2O_3	Cermet sintering aid Improve Ni-YSZ wettability	[78]
Porous Ni-8YSZ	5 mol% TiO_2	Reduced Ni sintering	[73]
Porous Ni-YSZ	TiO_2	Improve Ni-YSZ wettability	[44]
Porous Ni-8YSZ	5-10 mol% TiO_2	Improve Ni-YSZ wettability Reduced Ni sintering	[130]

The addition of titania was in several studies observed to provide better wettability of the nickel phase towards the ceramic. This was believed to account for reduced Ni sintering.
Based on the literature studies, Al_2O_3, CeO_2, and TiO_2 were chosen as additives to the SOFC anode support. The additives appeared to have potential for strengthening the cermet structure, and in some cases, also to reduce the nickel sintering.

9.3 Experimental

9.3.1 Sample preparation

The samples containing additives were prepared from NiO powder (99% from Alfa Aesar), 3 mol% yttria stabilized zirconia (3YSZ) (TZ3YB from Tosoh Co.), 3YSZ added 20 wt% Al_2O_3 (TZ3Y20AB from Tosoh Co.), alumina (Catapal® from Sasol), ceria (from Aldrich), and titania powder (from Merck).
The NiO content was similar for all compositions, and only the ceramic part was varied. Three compositions containing alumina were prepared. The alumina constituted respectively 15, 28, and 41 vol% of the ceramic phase, and the three compositions were denoted A15, A28, and A41. The solid material contents are shown in Table 9.3. For A28, the as-delivered mixed powder (TZ3Y20AB) was applied. For the other compositions, the alumina was added separately.
For compositions with ceria and titania, the additive constituted 41 vol% of the ceramic phase. The two compositions were denoted C41 and T41, respectively. The solid material contents are shown in Table 9.3.

Table 9.3. Compositions of the materials containing additives, when the nickel component is in the oxidized and reduced state.

Material	Components	Oxidized state		Reduced state	
		Wt%	Vol%	Wt%	Vol%
A15	NiO / Ni	54.8	50.9	48.8	41.2
	3YSZ	40.5	41.7	45.9	50.0
	Al_2O_3	4.7	7.4	5.3	8.8
A28	NiO / Ni	56.0	50.9	50.0	41.2
	3YSZ	35.2	35.6	40.0	42.6
	Al_2O_3	8.8	13.5	10.0	16.2
A41	NiO / Ni	57.3	50.9	51.3	41.2
	3YSZ	29.3	29.0	33.4	34.7
	Al_2O_3	13.4	20.1	15.3	24.1
C41	NiO / Ni	55.7	54.9	49.7	45.1
	3YSZ	24.3	26.6	27.6	32.3
	CeO_2	20.0	18.6	22.7	22.6
T41	NiO / Ni	56.7	50.9	50.7	41.2
	3YSZ	29.1	29.0	33.1	34.7
	TiO_2	14.2	20.1	16.2	24.1

The powders were processed into ethanol-based slurries containing polyvinylpyrrolidone (PVP) as dispersant, and the slurries were ball milled. The liquid was subsequently evaporated while stirring and the resultant powder crushed in mortar and ball mill.
The resultant powders were pressed into bar shaped samples using uniaxial, followed by isostatic pressing at 80 MPa. The bars were sintered at 1300°C. Some of the samples were subsequently reduced in pure H_2 at 850°C for 3 hours.
The samples were pressed in two turns, with two slightly different pressing tools. As this may have introduced differences between the samples, the batch number (b1 or b2) was included in the sample name.
Nominally identical bar shaped samples without additives were prepared. However, the powder for pressing was produced from tape cast slurries, instead of evaporated slurries. The composition and preparation procedure were as described in Chapter 2, Section 2.2.1, for the composition denoted 3Y.

9.3.2 Experimental procedure

Dilatometer measurements were carried out with a Netzsch Dil 402E instrument. Baselines were achieved using polycrystalline alpha-alumina. The tested samples were ca. 20 mm in length, and loaded horizontally in the set-up. The uncertainty of the instrument was 1 μm. This corresponds to an uncertainty of 0.01% on the measured relative expansions.
The samples were heated to 700°C or 1000°C at 2°C/min in air. Redox cycling was subsequently carried out. 9 vol% H_2/N_2 with a flow of 25 ml/min was used as reducing gas, and air was used as oxidizing medium. In between gas shifts, the chamber was flushed with N_2 for 15 minutes.

DC conductivity measurements were made with a 4-electrode set-up. Platinum current electrodes were wrapped around both ends of the bar. The wires were guided by mechanically cut grooves at the edges. Pt paste was applied around the wire, and at the ends to ensure contact. Potential probes of platinum were fixed in the set-up, and brought into contact with the sample by a spring load (cf. Chapter 5, Figure 5.1).
The resistance was measured using a Keithley 850 micro-ohmmeter. A current pulse defined by the hardware was enforced in both directions, and the potential between the probes measured. The resolution of the instrument in the measurement range of 200 mΩ was reported to be 10 μΩ. For reliability reasons, a measurement was rejected if the resistance for opposite current directions differed by more than 5%. Otherwise the average resistance was used.
The samples were heated to 850°C or 1000°C at 100°C/h in air, and redox cycling subsequently carried out. The reducing gas was 4.5 vol% H_2/N_2, and air was used as the oxidizing gas. The gas flow was in both cases 100 ml/min. N_2 was used as flushing gas for ca. 15 min in between gas shifts.

The particle size distributions of the slurries and powders were measured using light scattering particle sizing. A Beckman Coulter LS 13 320 instrument was applied.
The microstructure of the samples was examined with scanning electron microscopy (SEM). A Fei Quanta 600 equipped with an EDAX® thin window detector, and EDAX® Genesis software was used. The samples were coated with ca. 10 nm silver to minimize the charging effect.
The sample porosity was quantified by weighing and geometrical gauging. The procedures were as described in Chapter 2, Section 2.2.2. The open porosity was measured with mercury porosimetry (Autopore IV 9500 V1.05 from Micromeritics Instrument Corporation).
Phases were identified with x-ray powder diffraction (XRD) in a Stoe Bragg-Brentano diffractometer. Cu K_α x-ray was applied as radiation source. The analyses were performed on solids.

9.4 Results

9.4.1 Particle size distribution

The particle size distributions of the slurries, and the powders just before pressing, were measured with light scattering particle sizing. The 50% quantiles (D_{50}) are listed in Table 9.4. The D_{50} is the particle diameter under which 50 vol% of the particles are found. 3Y denotes the composition without additives (cf. Chapter 3, Section 3.3.1).

Table 9.4. D_{50} of the slurries and powders for pressing.

	3Y	A15	A28	A41	C41	T41
Slurry, D_{50} [μm]	2.4 ± 0.3	1.4 ± 0.3	1.8 ± 0.3	1.7 ± 0.3	2.6 ± 0.3	1.0 ± 0.3
Pressing powder, D_{50} [μm]	1.8 ± 0.3	9.2 ± 0.3	5.7 ± 0.3	8.2 ± 0.3	3.9 ± 0.3	5.9 ± 0.3

All slurries displayed a D_{50} of approximately 2.0 μm, considering the uncertainty. For the pressing powders, much higher D_{50} was indicated for the compositions containing additives, than for the standard 3Y without additives. The evaporation of the slurries with additives are believed to procedure the larger agglomerates in the powders (cf. Section 9.3.1). The measurements on the compositions with additives may also be vitiated by errors. The light scattering technique relies on the refractive index (RI) of the particles. Mixtures of NiO and YSZ are possible to measure, as the RI of the two components are similar, respectively 2.1818 and 2.19-2.20. However, the RI of the additives differs significantly from NiO and YSZ. The refractive index of alumina is much lower (1.768 or 1.760 depending on symmetry), and much higher for titania (2.583, 2.586, or 2.741). No RI for ceria was found [56].

9.4.2 Scanning electron microscopy

SEM-BSE (backscatter electron) micrographs of the samples 3Y, A28 and C41 in the as-sintered and reduced state are shown in Figure 9.2.
The phases present in the as-sintered samples were qualitatively separated by energy dispersive spectrometry (EDS) analyses. In the as-sintered 3Y sample the darker phase was NiO, and the lighter phase was YSZ (cf. Figure 9.2a). For the as-sintered A28 the lighter phase was NiO, and the darker phase was seen to contain Al, Zr, and Ni (cf. Figure 9.2c). For the as-sintered C41 the darker phase was identified as NiO, and the lighter phase contained Ce and Zr (cf. Figure 9.2e). When comparing the as-sintered structures, the ceramic phases of A28 and C41 appeared to be more fine-grained and less coherent than that of 3Y.
For samples in the reduced state, the metallic nickel was believed to be the particles containing grinding marks (cf. Figures 9.2d and f). No grinding marks were seen in 3Y, and the low contrast made it impossible to separate the phases. However, when the images of the reduced structures were compared, the samples containing additives appeared more porous.

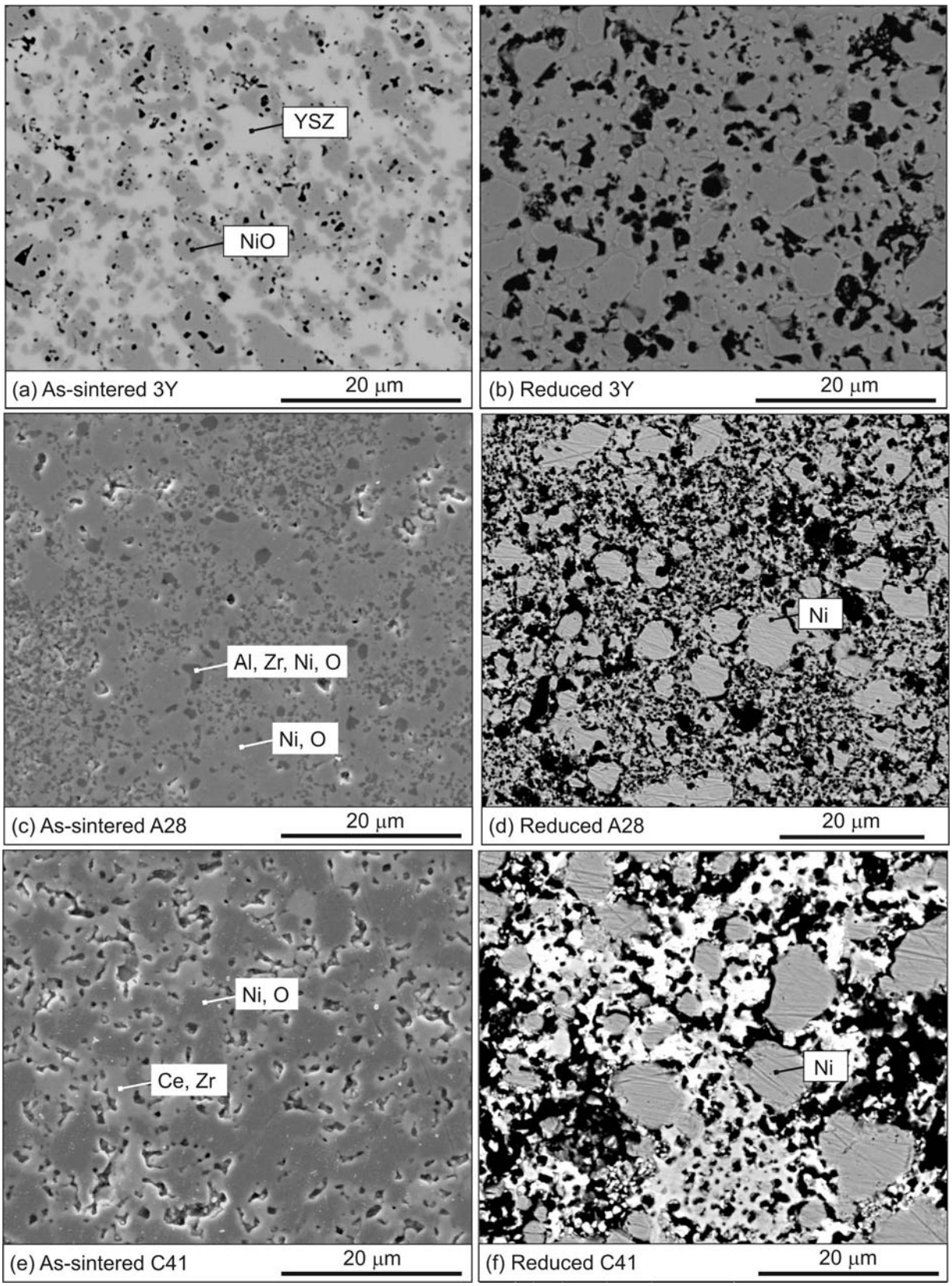

Figure 9.2. SEM-BSE micrographs. (a) As-sintered 3Y. (b) Reduced 3Y. (c) As-sintered A28. (d) Reduced A28. (e) As-sintered C41. (f) Reduced C41.

9.4.3 Porosity

The porosity of the as-sintered samples was measured based on geometrical gauging (ε_{geom}), and by applying mercury porosimetry (ε_{Hg}). All of the produced samples were geometrically measured, and the average and standard deviations are shown in Table 9.5. Mercury porosimetry was only applied to one sample of the measured type. The geometrical based density was included in the table. N denotes the number of samples, and in the sample names b1 and b2 refer to the pressing batch.

Table 9.5. Geometrically based porosity (ε_{geom}), and porosity measured by mercury porosimetry (ε_{Hg}). The geometrically based density is included. N denotes the number of samples.

Sample	N	As-sintered porosity [%]		As-sintered density [g/cm^3]
		ε_{geom}	ε_{Hg}	
3Y	39	7.5 ± 0.9	0.0 ± 1.0	5.9 ± 0.1
A15-b1	6	14.9 ± 0.9	7.6 ± 1.0	5.3 ± 0.1
A15-b2	3	19.2 ± 1.3	-	5.0 ± 0.1
A28-b1	3	10.7 ± 0.6	-	5.5 ± 0.0
A28-b2	3	13.7 ± 1.2	-	5.3 ± 0.1
A41-b1	6	19.9 ± 1.0	15.1 ± 1.0	4.8 ± 0.1
A41-b2	3	22.3 ± 3.3	-	4.6 ± 0.2
C41-b1	3	15.0 ± 1.4	-	5.6 ± 0.1
T41-b1	6	8.7 ± 0.6	-	5.5 ± 0.0
T41-b2	3	10.9 ± 1.4	-	5.4 ± 0.1

The scatter observed on the density of the samples was minor (cf. Table 9.5). However, the density of 3Y was seen to be slightly higher.
Differences between the samples were reflected more distinctly in the geometrical porosity. The porosity of 3Y was generally lower than that of the samples containing additives, as indicated from the SEM micrographs (cf. Section 9.4.2). Further, the open porosity was indicated to constitute at least 50% of the porosity for samples containing additives, whereas the fraction was insignificant for 3Y (cf. Table 9.5). For the samples containing additives, higher porosity was indicated for the samples pressed in the second batch (b2).

9.4.4 Phases

Samples of A28 and C41 in the as-sintered and reduced state were examined with x-ray powder diffraction. The identified phases are summarized in Table 9.6.

Table 9.6. Phases identified with x-ray powder diffraction in as-sintered and reduced A28 and C41.

As-sintered A28	Reduced A28	As-sintered C41	Reduced C41
NiO	Ni	NiO	Ni
Tetragonal YSZ	Tetragonal YSZ	Cubic $(Ce,Zr)O_2$, a_1=5.3356 Å	Cubic $(Ce,Zr)O_2$, a_1=5.3531 Å
Al_2NiO_4		Cubic $(Ce,Zr)O_2$, a_2=5.1783 Å	Cubic $(Ce,Zr)O_2$, a_2=5.2018 Å

In the as-sintered A28 the alumina appeared to be in the form of a spinel phase (Al_2NiO_4). Upon reduction, alumina was no longer traced by XRD. However, the spinel was believed to reduce into Ni and Al_2O_3. The disappearance of the alumina phase was ascribed to the relative low atomic number of Al, and small grain sizes (cf. Chapter 2).
In the C41 samples two cubic ceria-zirconia phases were identified. The lattice parameters of the two cubic phases (a_1 and a_2) were determined by refinement. For both ceria-zirconia mixtures, the cubic lattice parameter was observed to expand upon reduction (cf. Table 9.6).

9.4.5 Dilatometry

The results from the dilatometry measurements are summarized in Table 9.7. The geometrically based porosity of the sample in the as-sintered state, and the temperature of the experiment were included in the table. b1 and b2 in the sample name refer to the pressing batch. Samples of identical composition and pressing batch were differentiated by a serial letter in the last part of the sample name.

Some of the samples experienced a temperature cycle during the measurements from 1000°C to room temperature and back, due to failure of the instrument software. Thus, the following measurements were not directly comparable to the other experiments. The affected values are indicated with # in Table 9.7.

For the experiments carried out at temperatures below 1000°C, the dimensional change proceeded slowly. Despite more than 4 times longer exposure time compared to the corresponding experiments at 1000°C, equilibrium was difficult to achieve. In cases where equilibrium was not obtained, the measured maximum value is shown in brackets in Table 9.7.

Table 9.7. Relative linear changes upon successive redox steps as measured with dilatometry. The uncertainty on the data is ± 0.01%. # indicates measurements affected by a preceding temperature cycle. For measurements where equilibrium was not obtained, the measured maximum value is shown in brackets.

Sample	As-sintered porosity [%]	Temperature [°C]	Relative linear change [%] 1st red	1st ox	2nd red	2nd ox
3Y	8.0	1000	0.00	0.35	-0.08	0.70
A15-b1	14.9	1000	-0.17	4.83#	-0.49#	7.02#
A15-b2	18.1	1000	-0.14	2.32	-0.31	3.20
A28-b1-a	10.9	1000	0.01	0.28	-0.83	2.28
A28-b1-b	10.9	700	0.03	(>0.64)	-	-
A28-b2-a	14.8	850	-0.35	(>2.28)	-	-
A28-b2-b	12.5	1000	-0.69	3.43	-1.46	-
A41-b1	20.3	1000	-0.20	7.20	-0.70	6.89
A41-b2	19.0	1000	-0.57	1.61	-0.60	2.02
C41-b1-a	14.1	1000	0.75	0.35	0.71	0.91
C41-b1-b	14.1	700	(>0.62)	0.51#	-	-
T41-b1	8.5	1000	-0.61	2.20	-0.75	2.11
T41-b2	9.5	1000	-0.13	8.05	-0.45	(>1.80)

Pressing batch

An effect of the pressing batch the sample originated from was observed, when comparing identical tested samples from the two batches, b1 and b2. When comparing A28-b1-a and A28-b2, significantly worse dimensional changes were observed for batch 2 (A28-b2-a and b, cf. Table 9.7). When comparing A41-b1 and A41-b2, the change was only worse for batch 2 (A41-b2) upon the first reduction. Upon the following redox steps, the changes were more severe for batch 1 (A41-b1, cf. Table 9.7). For the samples T41-b1 and T41-b2, only the expansion upon oxidation was worse for the sample from batch 2 (i.e. T41-b2, cf. Table 9.7). For the samples A15-b1 and A15-b2 no significant difference upon the first reduction was observed between the two batches.

The as-sintered porosity differed between samples from different batches. However, a relationship between the parameters was not evident (cf. Table 9.7).

Since the batch number appeared to influence qualitatively on the data, further comparisons were only made between samples from the same batch.

Type of additive

The effect of the type of additive was examined by comparing samples with different additives, but pressed in the same batch, and containing identical amounts of additive (i.e. 41 vol% of the ceramic phase).

When comparing the samples from batch 1 (i.e. A41-b1, C41-b1-a, and T41-b1) an effect of the additive type was seen. The sample containing ceria (C41-b1-a) expanded upon both reductions and re-oxidations. The other samples displayed shrinkage upon reduction (cf. Table 9.7). The expansion of the ceria sample was in consistence with the XRD measurements (cf. Section 9.4.4), where expansion of the lattice parameter was observed upon reduction.
The dimensional changes upon oxidation were more severe for the alumina containing sample, A41-b1. Less expansion was observed for the titania containing sample (T41-b1), and even less for C41-b1-a. However, the as-sintered porosity also differed markedly between the samples, from 8.5% in T41-b1 to 20.3% in A41-b1. The difference in porosity may influence on the measurements (cf. Chapter 2).
When comparing the samples from batch 2 (i.e. A41-b2 and T41-b2), the opposite trend was observed. Less expansion upon oxidation was seen for A41-b2 compared to T41-b2. However, the difference in porosity was similar to the case of batch 1 (9.5% for T41-b2 to 19.0% for A41-b2) (cf. Table 9.7). Thus, when including batch 2, the as-sintered porosity did not appear as a key factor for the investigated range.
When comparing the samples to the composition without additives (3Y, cf. Table 9.7), none of the modified compositions displayed as good a performance. In contrast to the samples containing 41 vol% additives, no dimensional change was associated with the first reduction of 3Y, and the expansion upon the first re-oxidation was limited to 0.35%. Only C41-b1-a was in the same range; the other samples displayed values above 1%.

Amount of alumina

An effect of the amount of alumina added to the cermet was seen. When comparing the samples from batch 1 (i.e. A15-b1, A28-b1-a, and A41-b1), the sample A28-b1-a displayed better performance, i.e. less dimensional changes (cf. Table 9.7). However, when comparing the samples from batch 2 (i.e. A15-b2, A28-b2-b, and A41-b2), A28-b2-b performed the worst, and the least dimensional changes were seen for A41-b1.
The as-sintered porosity differed between the investigated samples. However, a clear relationship to the dilatometry measurements was not observed (cf. Table 9.7).
When the samples were compared to the sample without additive (3Y, cf. Table 9.7), only A28-b1-a displayed similar performance upon the first redox cycle. In all other cases, the dimensional change was significantly worse for the samples containing additives.

Temperature

An effect of the temperature was difficult to see, as equilibrium was often not achieved in the experiments performed below 1000°C. No comparable data was achieved for the samples C41-b1-a and C41-b1-b (cf. Table 9.7). When comparing A28-b2-a and A28-b2-b (respectively 850°C and 1000°C), the dimensional change was indicated to be worse for the high-temperature sample. However, when comparing A28-b1-a and A28-b1-b (respectively 1000°C and 700°C), more severe dimensional changes were suggested at the lower temperature (cf. Table 9.7).

9.4.6 DC conductivity

The parameters used to characterize the electrical behavior were the same as defined in Chapter 5, Section 5.3.1. The parameters were: $\sigma_{r,i}$, $t_{r,i}$, $\Delta\sigma_{24,i}$, $\Delta\sigma_{96,i}$, and $\Delta\sigma_{ox,i}$, where i refers to the number of the reducing period. For a reduction, the time is set to zero when the reducing gas flow is started. $\sigma_{r,i}$ and $t_{r,i}$ denote respectively the conductivity and time at complete reduction. $\Delta\sigma_{24,i}$ and $\Delta\sigma_{96,i}$ describe the degradation in the conductivity by the slope of the straight line between the initial complete reduction, and the measurement points after 24 and 96 hours of reducing conditions. $\Delta\sigma_{ox,i}$ is the relative change in conductivity between before and after an oxidizing event. The parameters are illustrated in Chapter 5, Figure 5.2.

The results from the conductivity measurements are summarized in Table 9.8. The same uncertainties assumed in Chapter 5 were assigned to the electrical parameters in the present chapter, i.e. 5% uncertainty on conductivity values, 0.25 h on times, 1 S/cm/h on degradation values, and 10% on conductivity ratios.

Table 9.8. Electrical characteristics for the first and second reducing periods. The porosity refers to the as-sintered state. # indicates measurements affected by a preceding temperature cycle. * indicates measurements affected by strongly fluctuating conductivity curves.

Sample	Porosity	T	1st reducing period				
	[%]	[°C]	$t_{r,1}$ [h]	$\sigma_{r,1}$ [S/cm]	$\Delta\sigma_{24,1}$ [S/cm/h]	$\Delta\sigma_{96,1}$ [S/cm/h]	$\Delta\sigma_{ox,1}$ [%]
3Y	8.5	1000	1.92±0.25	731 ±37	-7 ± 1	-3 ± 1	45 ± 10
A15-b1	14.5	1000	*1.04±0.25	*877 ±44	*2 ± 1	*2 ± 1	-57 ± 10
A15-b2	18.8	1000	6.30±0.25	189 ± 9	-2 ± 1	-1 ± 1	657 ± 10
A28-b1-a	11.2	1000	13.44±0.25	300 ±15	-1 ± 1	0 ± 1	147 ± 10
A28-b1-b	11.2	850	11.14±0.25	175 ± 9	-1 ± 1	0 ± 1	8 ± 10
A28-b2	13.8	1000	10.70±0.25	323 ±16	0 ± 1	0 ± 1	-
A41-b1	19.4	1000	4.81±0.25	168 ± 8	-1 ± 1	0 ± 1	128 ± 10
A41-b2	22.3	1000	7.45±0.25	104 ± 5	-1 ± 1	0 ± 1	291 ± 10
C41-b1-a	14.3	1000	5.33±0.25	538 ±27	-2 ± 1	-1 ± 1	184 ± 10
C41-b1-b	14.3	850	6.61±0.25	549 ±27	#-4 ± 1	#-2 ± 1	#42 ± 10
T41-b1	8.0	1000	9.74±0.25	76 ± 4	-2 ± 1	-1 ± 1	1275 ± 10
T41-b2	10.9	1000	-	-	-	-	233 ± 10

Sample	2nd reducing period			
	$t_{r,2}$ [h]	$\sigma_{r,2}$ [S/cm]	$\Delta\sigma_{24,2}$ [S/cm/h]	$\Delta\sigma_{96,2}$ [S/cm/h]
3Y	1.46±0.25	699 ±35	-11 ± 1	-
A15-b1	3.58±0.25	556 ±28	-7 ± 1	-1 ± 1
A15-b2	*11.45±0.25	*1004 ±50	*4 ± 1	*-4 ± 1
A28-b1-a	*5.77±0.25	*704 ±35	*-5 ± 1	-
A28-b1-b	4.30±0.25	172 ± 9	0 ± 1	-
A28-b2	-	-	-	-
A41-b1	4.23±0.25	330 ±17	-1 ± 1	-1 ± 1
A41-b2	9.78±0.25	321 ±16	-2 ± 1	-1 ± 1
C41-b1-a	5.04±0.25	727 ±36	-5 ± 1	-
C41-b1-b	#6.01±0.25	#521 ±26	#-3 ± 1	#-1 ± 1
T41-b1	5.08±0.25	285 ±14	-7 ± 1	-2 ± 1
T41-b2	6.62±0.25	301 ±15	-8 ± 1	-2 ± 1

For comparison, data for a corresponding bar shaped sample without additives are included in the table. In consistency with the present chapter, the sample is denoted 3Y. However, the sample corresponds to the sample 3Y-bar-1000-a in Chapter 5, Section 5.3.1.

Samples of identical composition and pressing batch were differentiated by a serial letter in the last part of the sample name (cf. Table 9.8).

One of the samples (C41-b1-b) experienced a temperature cycle during the measurements from 1000°C to room temperature and back, due to an electrode failure. Thus, the following data were not directly comparable to the other experiments. The affected values are indicated with # in Table 9.8.

Some of the alumina containing samples displayed severe conductivity fluctuations over short time scales. The fluctuations are illustrated in Figure 9.3, where the periods of oxidizing conditions are indicated. The fluctuations influence on the meaning of the electrical parameters. Values determined from strongly fluctuating curves are marked with asterisk in Table 9.8.

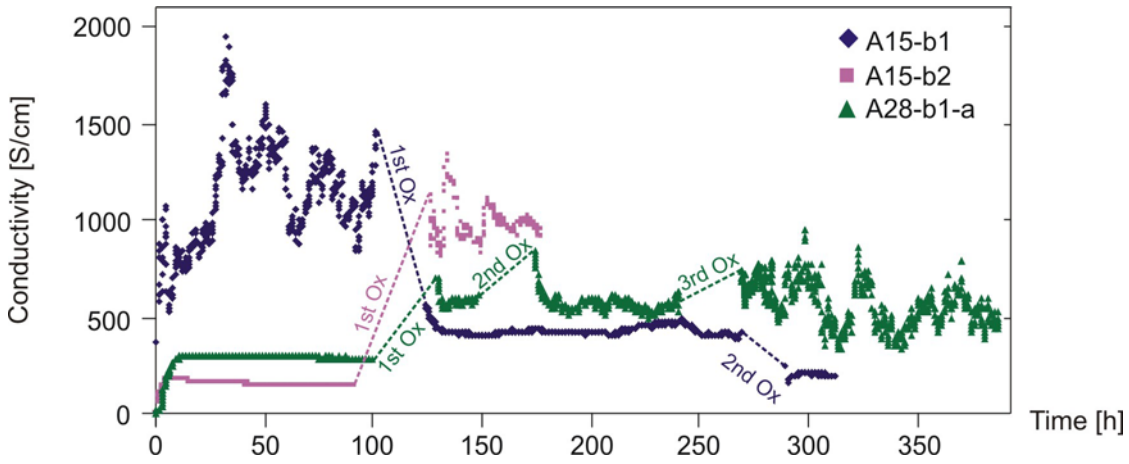

Figure 9.3. DC conductivity profiles of A15-b1, A15-b2, and A28-b1-a. Periods of oxidizing conditions are indicated.

Pressing batch

When comparing identically tested samples of the same composition, but from different pressing batches, an effect of the batch was observed. For the samples A41-b1 and A41-b2, the sample from batch 2 displayed significantly longer times for reduction. Further, for the first reducing period the sample from batch 2 also displayed lower conductivity, and a larger oxidation effect. Upon the second reducing period, no significant difference was observed between the two batches (cf. Table 9.8). When comparing T41-b1 and T41-b2, a larger oxidation effect was seen for the sample from batch 1 (T41-b1). For the samples A28-b1-a and A28-b2, only the time for complete reduction differed between the batches (cf. Table 9.8).
The as-sintered porosity differed slightly between the corresponding samples from the two batches. However, an evident relationship between the porosity and the variations in the electrical parameters were not seen.

Type of additive

The effect of the type of additive was examined by comparing the samples with 41 vol% additive, and pressed within the same batch.
When the samples from batch 1 were compared, the conductivity differed significantly between samples with different additives. The conductivity of the ceria containing sample (C41-b1-a) was much higher than that of the alumina sample (A41-b1), and even higher than the titania containing sample (T41-b1). The same pattern between the conductivity was observed for the corresponding samples from the second batch (cf. Table 9.8).
When comparing the oxidation effect of the samples from batch 1, a considerable pronounced effect was observed for T41-b1. The effect was around an order of magnitude above that for the alumina (A41-b1) and ceria (C41-b1-a) sample. However, the titania sample from the second batch (T41-b2) displayed an oxidation effect in the same range as the others (cf. Table 9.8).
No significant differences in the conductivity degradation were measured between the samples during the first reducing period. However, worse degradation following a temperature cycle was indicated (cf. Table 9.8). For the second reducing period worse degradation was observed for the samples containing ceria (C41-b1-a and b) and titania (T41-b1 and b2). The alumina samples (A41-b1 and b2) displayed the same degradation rates as during the first reducing period (cf. Table 9.8).
Compared to the sample without additives (3Y), the degradation rates of the samples containing additives were in all cases lower, and the oxidation effect considerably higher. However, the conductivity of the additive samples was generally also much lower (cf. Table 9.8).

The as-sintered porosity of the samples that were compared was observed to differ markedly. However, an evident relationship between the porosity and the variations in the electrical parameters were not seen.

Amount of alumina

An effect of the added amount of alumina was seen. However, the effect appeared to be complex related to the electrical parameters.
When comparing the samples from batch 1, the conductivity decreased with the amount of alumina, and the sample with the smallest amount of alumina (A15-b1) displayed conductivity values in the same range as the sample without additives (3Y), when ignoring the scatter (cf. Table 9.8). Regarding the oxidation effect, then alumina additions above 15 vol% appeared to have a positive effect. Compared to the sample without additives, the oxidation effect was about a factor of 3 higher. For the second reducing period, the high alumina content resulted in smaller degradation rates (cf. Table 9.8).
In contrast to batch 1, all samples from the second batch displayed conductivity values significantly below the reference sample 3Y. The oxidation effect for the samples was markedly higher, especially for the low-alumina sample (A15-b2) (cf. Table 9.8).
Differences in the as-sintered porosity between the samples were seen. The lower conductivity for the first reducing period of samples containing additives was associated with a higher as-sintered porosity compared to 3Y. However, the titania sample T41-b1 was an exception. A simple relationship between the as-sintered porosity and the oxidation effect was not observed (cf. Table 9.8).

Temperature

Samples of the types A28-b1 and C41-b1 were tested at both 850°C and 1000°C. When comparing A28-b1-a and A28-b1-b, a higher conductivity and an improved oxidation effect was observed for the high-temperature sample (A28-b1-a, cf. Table 9.8). When comparing C41-b1-a and C41-b1-b, similar conductivity was observed at the two temperatures, however an improved oxidation effect for the high-temperature sample was also suggested in this case (cf. Table 9.8).

9.5 Discussion

Modification of the anode support composition with additives was observed to affect the redox behavior of the cermet significantly. For quantitative evaluation of the effect of the additives, the microstructure of the samples with different compositions needs to be comparable. However, the microstructures of the produced samples were observed to be complexly related to the chemical composition and the processing.
The samples containing additives displayed coarser particle size distributions of the pressing powder (cf. Section 9.4.1), higher as-sintered porosity (cf. Section 9.4.3), and a ceramic phase that appeared more fine-grained and less coherent (cf. Section 9.4.2). Furthermore, differences in the microstructure of samples pressed in different batches were indicated from the measurements (cf. Sections 9.4.3, 9.4.5, and 9.4.6).
The reproducibility of pressed samples adds another complexity to the deduction of the effect of the additives. For dilatometry measurements, identically prepared samples displayed a variation of 5% on the expansion upon the first oxidation, and differed up to a factor of 2 for the second oxidation (cf. Chapter 2, Section 2.3.1). Similarly, conductivity measurements on identically prepared samples were seen to result in variations on the electrical parameters (cf. Chapter 5, Section 5.3.1). Differences up to 4 hours on times, 100 S/cm on conductivity, and 5 S/cm/h on the degradation rate after 24 hours, were observed. However, for the 96 hours degradation rates, and the oxidation effect, the differences were within the uncertainty.

Despite the variations in microstructure, qualitative effects related to the additives were believed possible to deduce, if the variations were considered.

9.5.1 Effect of the additives

The redox behavior, as measured with dilatometry, was significantly different for the samples containing additives, compared to the unmodified sample. Unmodified samples generally displayed no dimensional changes upon the first reduction, and then respectively expansion and shrinkage upon the following oxidations and reductions (cf. Chapter 2). However, the samples containing ceria expanded upon both reductions and re-oxidations, and for the samples containing alumina or titania, shrinkage was observed from the first reduction. Further, the expansions upon the re-oxidations were generally significantly larger, than for the unmodified sample. Only one of the samples containing additive (A28-b1-a) displayed significantly, i.e. more than 5%, lower expansions than the unmodified sample (cf. Section 9.4.5).

The expansion upon reduction for the ceria samples was explained by the bigger ion size of Ce^{3+} compared to Ce^{4+}. Further, the cerium was observed to form solid solutions with the zirconia, and the lattice parameters were seen to increase upon reduction (cf. Section 9.4.4).
The shrinkage observed upon the first reduction for samples containing alumina or titania, was believed to reflect phases containing the additives that dissociated upon reduction. For the alumina samples, traces of a Ni-Al-spinel phase were seen in the as-sintered state. The spinel phase was believed to be a part of the ceramic network, and to reduce into Ni and fine-grained Al_2O_3. The phase change then accounts for the observed shrinkage (cf. Section 9.4.5 and Chapter 2). Similar dimensional changes were observed for the samples containing titania. Thus, corresponding phase changes are believed to occur.
The enhanced expansions, generally observed for the samples containing additives, may be due to the differences in microstructure, and not directly related to the additive. The additives containing samples generally appeared more porous, and with less coherent ceramic networks (cf. Sections 9.4.2 and 9.4.3). The microstructure may account for a part of the significantly worse expansions upon the first and second oxidations. However, the low-porosity titania samples also displayed severe expansions, indicating a direct effect of the additive (cf. Section 9.4.5).
The sample A28-b1-a displayed the best redox performance regarding the bulk expansion upon oxidation. However, the obtained value of $0.28 \pm 0.01\%$ was still too large, according to the models in Chapter 8, where expansions below 0.17% were predicted to be required.

The electrical properties of samples containing additives differed significantly from the unmodified sample. The conductivity was generally lower for the additive samples, in the order of several hundreds of S/cm, despite identical nickel content (cf. Sections 9.3.1 and 2.2.1). However, improved oxidation effects, and decreased degradation rates, both on the 24 hours and 96 hours scale, were observed for the samples containing additives.
The decreased conductivity was partly ascribed to the higher as-sintered porosity of the samples containing additives. However, the low-porosity samples containing titania also displayed much lower conductivity (cf. Section 9.4.6). Thus, the lower conductivity either reflects the different processing of the additive samples, or indicates the presence of a direct effect of the additives on the percolation degree. The different oxidation effect and degradation rate indicated that the additives influenced on the mobility of the nickel phase.

The lower degradation rates for the samples with additives included potentially longer lifetimes of the cermet structure. By analogy with Chapter 5, Section 5.4.1, the lifetime was estimated from fitting the degradation profile. The degradation of the best performing additive containing

sample (A28-b1-a), and a corresponding sample without additive was fitted to exponential decays. The fits and equations are shown in Figure 9.4.

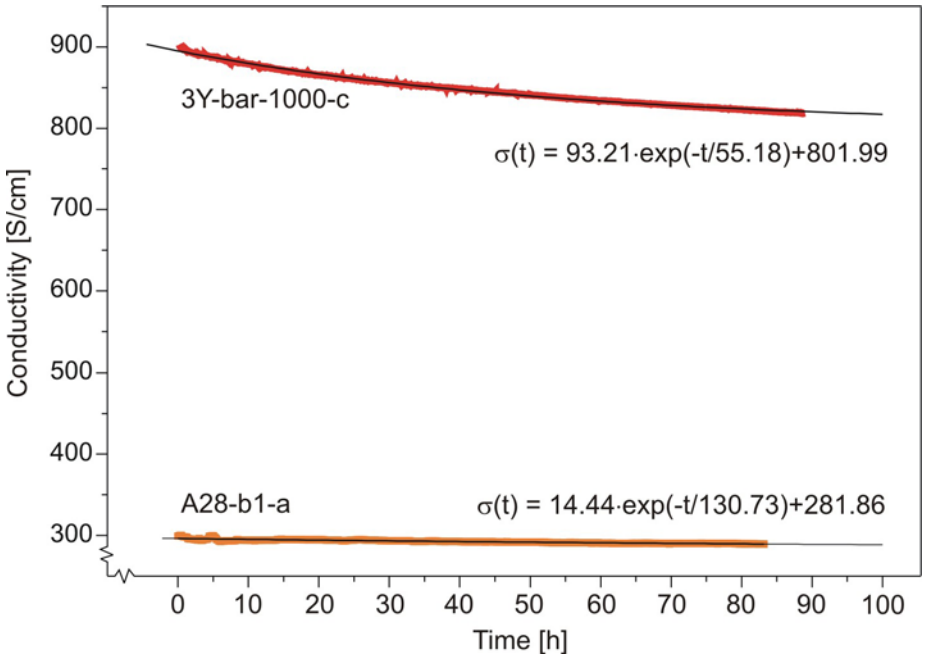

Figure 9.4. Fits of the conductivity degradation profiles.

Despite the difference in the conductivity level, both samples were estimated to have commercial lifetimes (40,000 hours with conductivity > 100 S/cm). Thus, the application of additives do not influence significantly on the restriction on the lifetime due to sintering.

9.5.2 Effect of the amount of additive and temperature

Regarding the expansion upon oxidation, 28 vol% of alumina was indicated as the composition closest to the optimum. However, large variations between the different pressing batches were seen, indicating that the optimum was sensitive to the microstructure (cf. Section 9.4.5).
The conductivity was suggested to decrease when the amount of added alumina increased. However, the oxidation effect was seen to improve with the amount of additive (cf. Section 9.4.6). This further indicated an effect of the additive on the mobility of the nickel phase.
The temperature was ambiguously related to the bulk expansions (cf. Section 9.4.5). The electrical oxidation effect was indicated to be enhanced for higher temperatures. The observation was believed to reflect the higher mobility of the nickel phase at the higher temperature.
Determination of the optimum amount of additive and temperature in relation to the redox behavior, may result in significant redox performance improvements. However, extensive experimental work is believed to be required.

9.5.3 The redox mechanism

The redox mechanism proposed in Chapters 2, 3 and 5 predicted that the bulk expansion upon oxidation would increase if the ceramic component was weakened. Thus, higher porosity, temperature cycling, and increased nickel redistribution promote increased expansion.
Based on the model, the additives did not seem to provide the expected strengthening of structure. However, an increase in porosity was associated with the additive samples, and may account for the apparent absence of improved mechanical properties.

The redox mechanism predicted reorganization of the nickel phase upon reduction, when in the reduced state, and upon re-oxidation. The reorganization depended on the nickel mobility, and was seen to vary with the porosity and temperature. According to the model, re-oxidations involved damage on the ceramic network, and increased porosity. A critical porosity was believed to exist, above which, the formation of a well percolating nickel network becomes more difficult (cf. Chapters 2, 3 and 5).
The additives appeared to have an ambiguous effect on the nickel reorganization. Diminished mobility was suggested by lower conductivity degradation rates, and lower percolation degrees upon the first reduction. However, an improved oxidation effect was also observed for the additive samples, suggesting increased mobility promoted by the additives.
The low percolation upon the first reduction was believed to be an effect of the processing of the samples containing additives, resulting in for instance differences in the pressing powders. The conductivity fluctuations observed for A15-b1 during the first reducing period was believed to reflect the low percolation degree.
The oxidations were associated with increased porosity, which provided for better percolation to be formed. The improved oxidation effect for samples containing additives was therefore ascribed to the microstructure and not the additives directly. Upon the first oxidation, the fluctuations for the A15-b1 sample disappeared, indicating better and more stable percolation. However, for some of the other samples fluctuations were introduced upon an oxidizing event and in some cases the fluctuations became enhanced with the number of cycles. The fluctuations were believed to reflect that the critical porosity is approached.

9.6 Conclusions

The state-of-the-art nickel-YSZ anode support composition was modified with oxide additives (Al_2O_3, CeO_2, and TiO_2), and the effect on the structural ageing of the cermet, and the redox behavior was examined. The conclusions are:

- The additives were observed to influence on the ageing and the redox behavior of the cermet. Thus, improving the anode support through the use of additives appeared as a potential concept.

- The examination of the effect of the additives was complicated by microstructural differences introduced partly due the chemical differences. Thus, quantification of the effects of the additives will require further processing studies.

- A strengthening effect of the additives was not possible to be evaluated from the measurements. Further experimental work, involving either strength measurements, or samples with comparable microstructures, will be required for this.

- The additives promoted lower conductivity degradation rates.

- Ceria was excluded as a potential additive, as the samples displayed bulk expansion upon both reduction and re-oxidation.

- A sample containing 28 vol% of alumina displayed significantly lower bulk expansion upon the first oxidation compared to the unmodified sample. However, the reduction was not estimated to be sufficient for providing a redox stable cell.

- Determination of the optimum amount of additive, temperature, and processing in relation to the redox behavior and ageing, may result in significant improvements. However, this will require extensive experimental work.

- In accordance with the redox model from Chapter 2, a critical porosity above which, the formation of a well percolating nickel network becomes more difficult, was indicated.

Acknowledgement

H. Z. Stummann (Haldor Topsøe A/S) is acknowledged for technical support on the dilatometry measurements. K. Mortensen (Risø National Laboratory) is acknowledged for technical support on the sample preparation.

10 Overall summary and discussion

10.1 Introduction

The nickel-YSZ cermet of the state-of-the-art anode-supported solid oxide fuel cell (SOFC) degrades when operated, and upon redox cycling. The degradation is believed to be critical for the commercialization of the SOFC technology [19, 21].
The degradation in performance has been related to microstructural changes occurring in the nickel-YSZ cermet. However, knowledge of the relationship between the microstructure and performance has been limited. Characterization of the complex cermet microstructure is known to be difficult, and characterization of the microstructural changes have been equally scarce [10, 49, 50, 51].
In the present thesis the microstructure and the performance of nickel-YSZ cermets were characterized both directly and indirectly, by application of various techniques. The purpose was to get a better understanding of the degradation mechanisms, to identify some of the key structural parameters and tools for improving the cermet, and to apply the knowledge to produce an improved cermet.
The results from the applied techniques were discussed individually in the Chapters 2-9. In this chapter an overall summary and discussions of the findings regarding the redox mechanism, nickel sintering, structural parameters, development tools, and cermet improvement, are presented.

10.2 The redox mechanism

A model of the redox mechanism on the microstructural level was proposed based on the investigations. The model was illustrated by the simple cartoon in Chapter 2 (cf. Figure 2.6). To include the observations from the later chapters, a modified cartoon is illustrated in Figure 10.1. Green particles represent NiO, gray particles represent Ni, and the pink matrix is the YSZ component of the cermet. Pores and fractures are shown in white. The electrolyte and current collector placed adjacent to the nickel-YSZ cermet is shown with a darker pink and gray color. The microstructural evolution in the steps shown in Figure 10.1 is described below.

(a) The as-sintered structure consists of pores, and percolating networks of NiO and YSZ.
(b) Upon reduction the nickel phase reorganizes due to the volume reduction of the phase, and the wetting properties. The nickel particles become rounded, and particle sintering occurs.
(c) Upon re-oxidation the microstructure does not revert to the as-sintered state. Reversion is prevented by the nickel redistribution that occurred in the reduced state, and the oxide growth.
    The oxide growth is guided by the oxidation kinetics, and the local pore morphology. Slow kinetics results in the growth of an external peel, uniformly into the void around the individual particles. When the oxidation kinetics is fast, the Ni/NiO particles divide into 2-4 particles that grow into the surrounding voids. The situation with fast kinetics, corresponding to high temperatures, is illustrated.
    Where the growth of the particles cannot be accommodated within the structure, stresses are generated in the YSZ matrix. At weak points, or where the stresses are higher, the YSZ network fractures. This permits bulk expansion of the cermet which generates cracks in the electrolyte.
(d) When the structure is re-reduced, an improved percolating nickel network is formed compared to the first reduced state. This is facilitated by the partial disintegrated YSZ network, and the possible NiO redistribution that occurred during the oxide growth. The disintegration also promotes faster Ni particle rounding and sintering.

(e) The steps described in (c-d) are repeated upon succeeding redox cycling. Re-oxidations are associated with fractures in the YSZ matrix, bulk expansion, and cracks in the electrolyte as long as Ni/NiO redistribution occurs.

(f) Reductions are associated with improved nickel percolation as long as the structure is not too fragmented. At a critical porosity the ability to form a well percolating nickel network is lost.

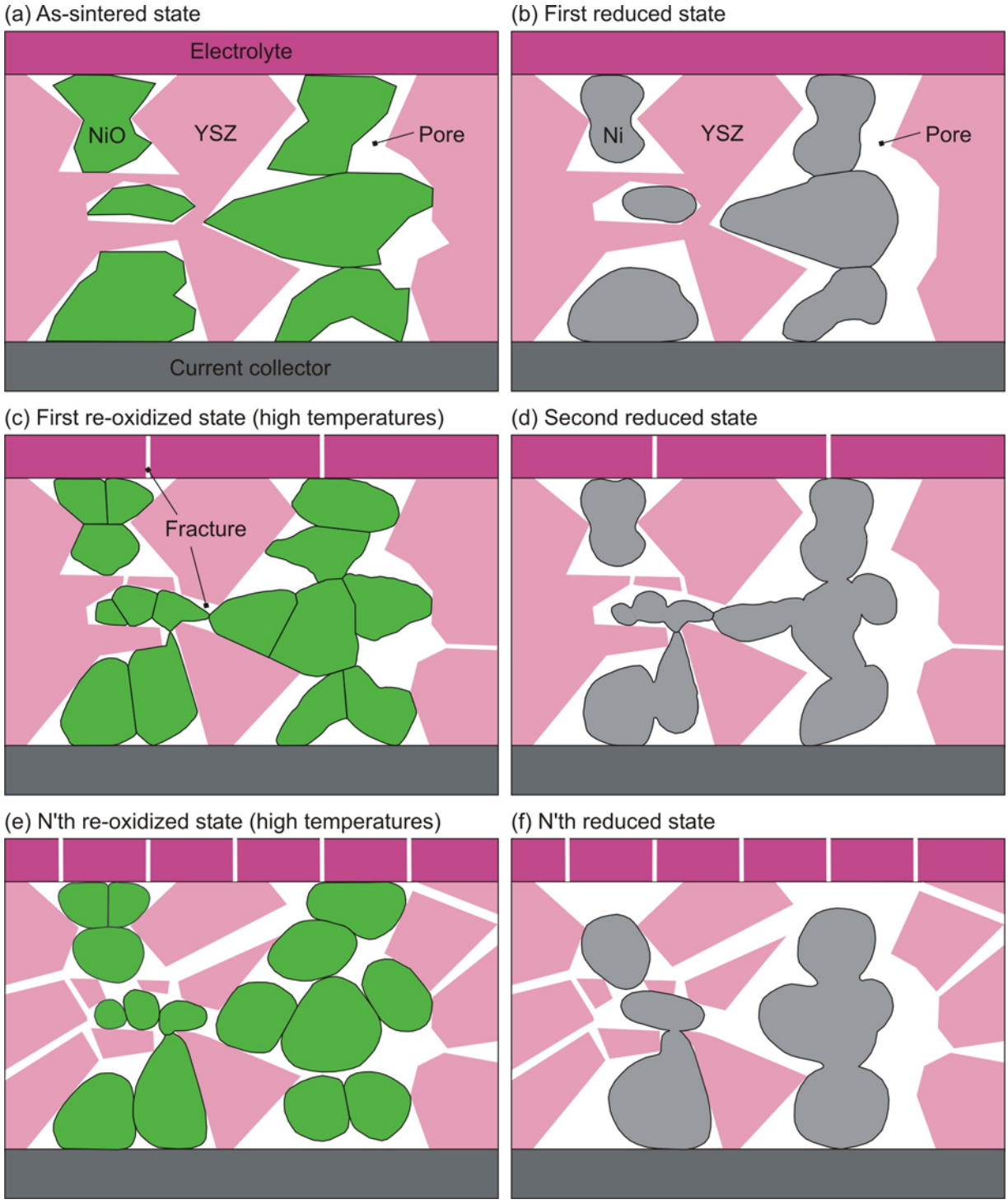

Figure 10.1. Cartoon illustrating the microstructural changes in the Ni/NiO-YSZ cermet upon successive redox steps. Green and gray particles represent respectively NiO and Ni. The pink matrix is the cermet YSZ. The electrolyte and current collector are shown with a darker pink and gray color. Pores and fractures are shown with white. (a) As-sintered state. (b) First reduced state. (c) First re-oxidized state, when oxidized at high temperature. (d) Second reduced state. (e) N'th re-oxidized state. (f) N'th reduced state.

The descriptions of the redox mechanism were previously limited to the observation of a bulk expansion of the cermet structure, inflicting mechanical damage onto the cell, and degraded performance. The bulk expansion was without details, explained by the volume difference between Ni and NiO [8, 9, 19, 58]. This model suggests that the dynamic reorganization of the Ni/NiO phase, when reduced and upon re-oxidations, is responsible for the bulk expansion.

Observations

The model was developed based on a mixture of direct and indirect observations of the microstructure. For the reduced states, rounding of the Ni particles was observed in-situ with environmental scanning electron microscope, ESEM (cf. Chapter 3). However, the sintering of the Ni particles was only observed indirectly from conductivity measurements (cf. Chapter 5). The applied microscopy techniques did not provide appropriate resolution, or phase contrast for the sintering to be evident (cf. Chapter 3).

For the re-oxidation process, the oxide growth and the temperature dependence of the oxide growth were seen in-situ with ESEM (cf. Chapter 3). Furthermore, conductivity measurements indicated redistribution of the NiO phase during oxidation. When the reduced cermet conductivity was compared before and after an oxidizing event, the conductivity had changed. The change in conductivity was seen to depend on the temperature. For oxidizing events carried out at 1000°C, the oxidation was associated with an improvement in the conductivity. For tests performed at lower temperatures (800°C-850°C), or higher temperature (1200°C), the relative improvement was either negligible or absent (cf. Chapter 5).

The temperature dependence of the conductivity change can be explained by the oxide growth being determined by both the growth kinetics, and the sample porosity. For lower temperatures the slow oxide growth prevents split-up of the NiO particles, or the process is less severe. This prevents the formation of a better percolating Ni network upon reduction. For the higher temperatures the fast oxide growth generates severe disintegration and increased porosity upon oxidation, corresponding to the scenario sketched in Figure 10.1e. Thus, upon re-reduction, the critical porosity for obtaining a well percolating network is close to be reached.

Mechanical disintegration of the cermet YSZ matrix upon oxidation was not observed in-situ. However, the indications were many. The re-oxidized structures appeared mechanically weakened (cf. Chapter 7), displayed increased porosity (cf. Chapters 2-4), bulk expansion (cf. Chapters 2 and 5), and decreased ionic conductivity of the YSZ matrix (cf. Chapter 5). Obvious micro cracks in the YSZ matrix were rare (cf. Chapter 3). The apparent lack of micro cracks was explained by the fractures predominantly occurred where the YSZ network was weak, e.g. where the solid volume was small.

Upon successive redox cycles the first redox steps were indicated to be repeated. The succeeding redox cycles were associated with further increased porosity (cf. Chapter 3), bulk expansion (cf. Chapter 2), and microstructural strain (cf. Chapter 8). The presence of a critical porosity was indicated by decreased conductivity (cf. Chapter 5), and suggestions of diminished bulk expansions (cf. Chapter 2) upon repeated redox cycling.

Temperature cycling was indicated to result in similar disintegration of the YSZ matrix. Preceding temperature cycles were indicated to be followed by enhanced bulk expansion, and nickel redistribution.

Quantification

Quantification of the microstructural changes was difficult. The ESEM technique was combined with image analysis, but statistical data was not achieved. The necessary high resolution limited the image analyses to approximately 10 grains per experiment. Further, the in-situ experiments were restricted to short periods of time, and to sample surfaces. Thus, ageing and microstructural changes within the bulk were not observed.

Light microscopy (LM) or scanning electron microscopy (SEM) was combined with image analysis. Representative sample areas were easily analyzed with the techniques. However, with the low resolution of LM it was not possible to detect microstructural changes on the investigated time scales. The SEM images provided sufficient resolution, and may be usable for quantifying the oxidized microstructures. However, extensive manual sorting is required for statistical values due to relative poor phase contrasts. Thus, in the present work SEM was only applied as a qualitative measure.
The microstructures and the microstructural changes were indirectly quantified with bulk techniques: dilatometry, conductivity, porosity, mechanical strength, and redox kinetics. Dilatometry, conductivity, and porosity appeared as sensitive measures of the microstructure. However, the microstructural variations for identically prepared samples were reflected in the measurements. Thus, when microstructural relationships were evaluated, the natural scatter had to be considered.
The redox kinetics did not appear as a sensitive measure of the microstructure. Mechanical strength tests appeared as a potential measure. However, the tests required large sample populations, and the test methods need further optimization for test of the technologically relevant cermet.

10.3 Nickel sintering

Sintering of the nickel particles was observed to initiate immediately upon reduction. The sintering appeared to be strong during the first ca. 24 hours. From 24-100 hours the sintering diminished, and was estimated to approach a steady state was (cf. Chapter 5).
The sintering rates were influenced by the porosity, the composition of the ceramic component, and the temperature. However, the porosity appeared only as a factor if the porosity was below 8.5%, i.e. below the technologically relevant cermet. For the low porosity-samples, the sintering rate increased with increasing porosity (cf. Chapter 5).
Nickel self-diffusion was believed to be the main sintering mechanism. The observations suggested the process to be faster at surfaces where sufficient porosity existed, and to proceed slower at Ni-Ni grain boundaries, at Ni-YSZ boundaries, and at surfaces where the local porosity was low. The nickel surface atom mobility in the cermet structure is illustrated in Figure 10.2. The length of the arrows indicates the mobility.

Quantification

The nickel sintering was monitored indirectly by conductivity measurements. However, minor microstructural variations due to processing, and the stochastic nature of the sintering process implied scatter in the electrical parameters.
The restriction on the lifetime of the cermets due to Ni sintering was estimated from the conductivity measurements. The degradations were fitted to power or exponential decay. The lifetime of the technological anode support was estimated to be below the commercial requirement of 40,000 hours with conductivity above 100 S/cm (cf. Section 5.4.1). However, based on the literature, the anode degradation in conductivity is not believed to be the main restriction on the lifetime. Better lifetime estimates are believed to be achievable with long-term conductivity tests.
Quantification of the sintering by electrochemical characterization was indicated as a possibility. A way to produce symmetrical cells appropriate for the measurements, and based on the technologically relevant cermet, was identified.

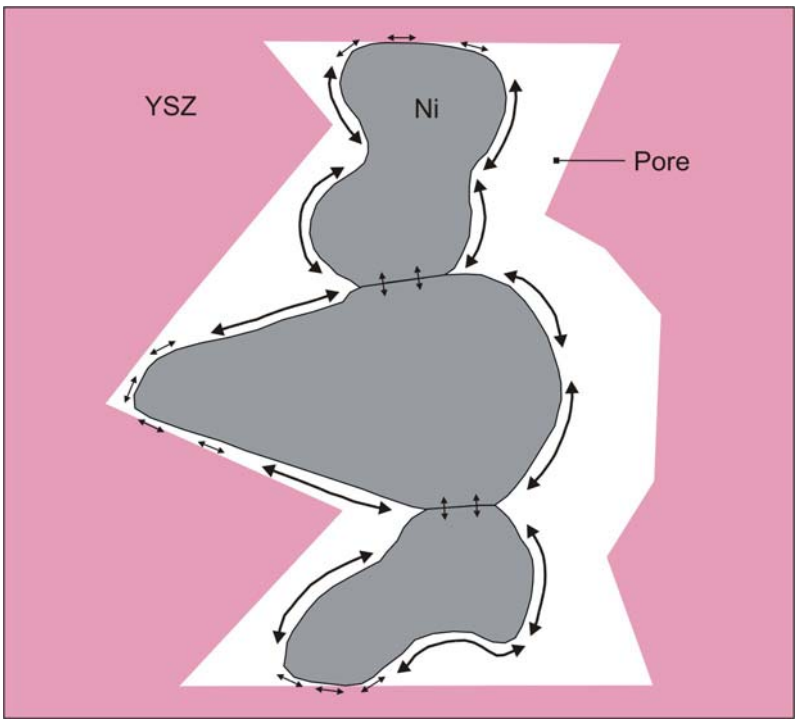

Figure 10.2. Nickel surface atom mobility in the cermet structure. The length of the arrows indicates the mobility.

10.4 Microstructural key parameters

The redox behavior and the nickel sintering were from the literature known to be influenced by microstructural parameters. Particle size distribution, porosity, and porosity distribution were seen to influence on the redox behavior [8, 19, 58]. The local porosity, and chemical composition of the ceramic component were observed as influences on the nickel sintering [38, 73, 122, 130].
The present work showed that the mechanical strength of the ceramic network, and the degree of nickel redistribution were also potential key parameters on the redox behavior. The cermet bulk expansion upon re-oxidation decreased, when the ceramic matrix was strengthened (cf. Chapter 2). Less expansion was indicated for samples with lower porosity, and samples tested at lower temperatures, where less redistribution of the nickel phase occurs (cf. Chapters 2, 3, and 5).
Based on the studied range of porosity, the total porosity did not appear as a direct technologically relevant parameter. For as-sintered sample porosity above 8.5%, no significant relationship between porosity and the conductivity degradation was observed (cf. Chapter 5). For as-sintered porosity above 15%, the gas diffusion into the samples did not limit the rates of the reduction or re-oxidation (cf. Chapter 4). However, the porosity is an indirect parameter on the strength. Thus, an optimum porosity interval, with sufficient gas diffusion and strength, is believed to exist.

Quantification

An empirical relationship between the cermet strength and the cermet bulk expansion was established. The parameters were inversely related, and the relationship approached an asymptotic trend for strengths above approximately 500 MPa (cf. Chapter 7).
The allowable bulk expansion of a redox stable cermet was quantified from layer models. The models predicted a reduction of the present expansion values with at least a factor of two (cf. Chapter 8). This corresponded to a significant improvement in the strength, which was not believed to be possible to achieve by modifications of the processing, e.g. sintering route.

10.5 Development of the anode support

Strengthening of the cermet structure was attempted by modifying the anode support cermet composition. Significant strengthening is believed possible to achieve, when second phase particles are incorporated into a ceramic matrix. In addition, nickel sintering may be diminished when the composition of the ceramic component is modified.
Al_2O_3, TiO_2, and CeO_2 was chosen as additives, and the effect observed indirectly with dilatometry and conductivity measurements. The additives influenced on the ageing and redox behavior of the cermet, and lower degradation rates and bulk expansions were achieved in some cases. However, the investigated combinations of additive type, amount, and processing did not result in cermets that displayed sufficient strength or redox stability. Determination of the optimum combination may result in significant improvements.

10.6 Tools for development of the cermet

Further development is required before a redox stable cermet for the anode-supported cell is obtained. A combination of the bulk techniques: dilatometry, strength, layer models, and conductivity, appeared to be the best way of characterization the cermet microstructure, the microstructural changes, and the ageing and redox performance. However, the sensitivity of the methods, combined with the stochastic nature of some of the processes, resulted in large scatter in some of the quantified values, that must be taken into account.
Relationships between the bulk measurements and microstructural parameters were not established. Direct observations of the microstructure and the microstructural changes were possible with ESEM and SEM. However, for statistical quantification of the microstructure, extensive work will be required.
To promote systematic cermet development, the relationships between the bulk properties and microstructural parameters must be obtained. This will require extensive and systematic experimental work. In addition to the laborious characterization of the microstructures, the complex matter of controlling the microstructure will be included. Simulation models may provide a supplement to the experiments. The relationships are illustrated in Figure 10.3.

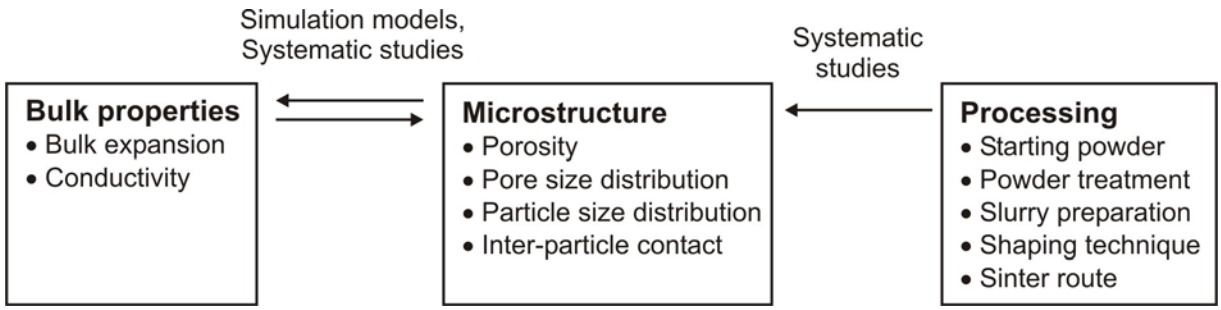

Figure 10.3. Relationship between bulk properties, microstructure, and processing. The ways of getting quantitative information on the relationships are indicated above the arrows.

Microstructural simulation models

Simulation models may provide a shortcut to explain the relationship between microstructure and bulk performance. In a microstructural simulation model a simplified cermet structure is generated, and the electrical conductivity and polarization resistance is calculated based on the current balances.
The cermet structure may be generated based on different microstructural variables, such as nickel particle fraction, pore fraction, and particle sizes. However, the structures rely on

spherical particles of variable diameter. The structures are generally produced by random deposition of the discrete Ni and YSZ particles. Pores may be represented as discrete particles, or present as the interstices. The method is also referred to as Monte Carlo simulation [131].
Simulation models have previously only been applied to a limited extend. The relationship between nickel agglomeration and the conductivity or electrochemical performance was investigated in [10, 37, 38, 42, 69, 132, 133, 134]. The model by Sunde was used in assisting the understanding the temperature dependence on the conductivity (cf. Chapter 5, Figure 5.5). However, the models only provided knowledge of the basic phenomena, and is difficult to correlate with experimental data.
The limitation of the simulation models is related to representing a complex microstructures with the simplified structures. The present models do not contain sufficient details. As an example, the software developed by Sunde [69, 135], includes the following microstructural parameters: the nickel particle fraction, the contact area between particles, the diameter of the spherical particles, and the bulk dimensions of structure. Complex structural parameters as particle size distributions, irregular particle shape, local porosity, and network fragmentation, were indicated to be required for precise description of the ageing and the redox processes. However, including the parameters will require extensive development of the software.

11 Overall conclusions

- The redox instability of the state-of-the-art nickel-YSZ cermet of the anode-supported SOFC can be ascribed to a dynamic reorganization of the Ni/NiO phase, when in the reduced state and upon re-oxidation. The redistribution generates fractures in the YSZ matrix, and bulk expansion of the cermet structure upon re-oxidations. The bulk expansion promotes cracks in the electrolyte.

- The redistribution of the reduced nickel phase occurs as rounding of the particles and sintering. The degree of sintering depends on the temperature, the composition of the ceramic component, and possibly on the local porosity.

- The redistribution of the Ni/NiO phase upon oxidation depends on the kinetics and the local porosity. At higher temperatures the oxide growth involves fragmentation of the particles. At lower temperatures the growth occurs in the form of an external oxide peel.

- The mechanical strength of the ceramic component was indicated as a technological potential parameter for improving the redox stability. However, considerable strengthening will be required. Strengthening that will result in a reduction of the bulk expansion upon re-oxidation with a factor of two was estimated.

- Structural strengthening can be achieved by modifying the cermet composition with additives. The additives can also promote reduced nickel sintering. Thus, application of additives is a possibility for improving the redox stability.

- Development of the nickel-YSZ cermet is complicated by difficulties in characterizing the cermet microstructure. Direct observations usually only provide qualitative results. Future development will be empirically based, or involve detailed descriptions of the relationships between microstructural parameters and cermet bulk properties.

12 Outlook

Further development is required before the nickel-YSZ cermet of the anode-supported cell is redox stable. The development can be approached in two ways: (i) development based on empirical experimental work; (ii) development based on microstructural characterization. Systematic experimental work will be required for both approaches.

It would be interesting to examine the full potential of the application of additives regarding strengthening of the ceramic component, and minimization of the nickel sintering. Areas of interest are:

- Alumina was indicated as a potential additive for improving the strength and the nickel sintering properties. Thus, experiments to discover the optimum impact of the alumina additive would be interesting. The experiments will involve determination of the optimum alumina content, and processing route.
- Other additives, or combinations of additives, may be of equal interest, and investigated in a similar manner.
- The mechanical strength will be a quality measure of the impact of the additive, and the redox behavior. Further verification and optimization of the tensile strength test are therefore of interest.
- To investigate the nickel sintering degradation pattern, and to obtain precise lifetime estimates, long-term conductivity experiments are of interest.

The fundamental approach involves quantitative microstructural characterization. Based on this, the critical microstructural parameters for the nickel sintering, and the oxidation process, are to be identified. Regarding this approach, the areas of interest involve:

- Systematic image analyses of cermet structures based on light microscopy, SEM, and ESEM.
- Development and application of complex simulation models, where microstructural parameters as particle size distribution, irregular particle shape, local porosity, and matrix fractures are implemented.
- Experiments to deduce analytical descriptions of the nickel sintering in the cermet structure.
- Experiments to include the relationship between microstructure and electrochemical performance. Electrochemical tests on symmetrical cells upon ageing and redox cycling are of interest.

The temperature and the local porosity were indicated to be significant factors on the microstructure, and on the degree of redistribution of the Ni/NiO phase. The following areas are therefore of interest:

- Experiments to describe the temperature dependence of the microstructural evolution.
- Manufacture of structures where the redistribution of the nickel phase is suppressed by steric hindrances.

References

1. N. Q. Minh, T. Takahashi, Science and technology of ceramic fuel cells, Elsevier Science B.V., Amsterdam, The Netherlands (1995).

2. M. Mogensen, P. H. Larsen, P. V. Hendriksen, B. Kindl, C. Bagger, S. Linderoth, Solid oxide fuel cell testing: Results and interpretation, in SOFC VI proc. vol. 99-19, S. C. Singhal, M. Dokiya (eds.), The Electrochemical Society, Inc., Pennington, NJ, USA, 904-915 (1999).

3. S. Primdahl, Ph.D. thesis, Nickel/yttria-stabilised zirconia cermet anodes for solid oxide fuel cells, University of Twente, The Netherlands (1999).

4. M. Mogensen, S. Skaarup, Kinetic and geometric aspects of solid oxide fuel cell electrodes, Solid State Ionics, 86-88, 1151-1160 (1996).

5. M. Brown, S. Primdahl, M. Mogensen, Structure/performance relations for Ni/Yttria-stabilized zirconia anodes for solid oxide fuel cells, Journal of The Electrochemical Society, 147, 475-485 (2000).

6. K. V. Jensen, Ph.D. thesis, The nickel-YSZ interface. Structure, composition and electrochemical properties at 1000 C, The Technical University of Denmark, Risø National Laboratory and Nordic Energy Research programme (2002).

7. M. Lang, T. Franco, M. Johnson, G. Schiller, P. Szabo, Characterisation of vacuum plasma sprayed planar solid oxide fuel cells during reduction-oxidation cycling, in 6th European SOFC Forum proc. vol. 2, M. Mogensen (ed.), European Fuel Cell Forum, Oberrohrdorf, Switzerland, 877-886 (2004).

8. D. Fouquet, A. C. Müller, A. Weber, E. Ivers-Tiffée, Kinetics of oxidation and reduction of Ni/YSZ cermets, Ionics, 9, 103-108 (2003).

9. G. Stathis, D. Simwonis, F. Tietz, A. Moropoulou, A. Naoumides, Oxidation and resulting mechanical properties of Ni/8Y2O3-stabilized zirconia anode substrate for solid-oxide fuel cells, Journal of Materials Research, 17, 951-958 (2002).

10. D. Simwonis, F. Tietz, D. Stöver, Nickel coarsening in annealed Ni/8YSZ anode substrates for solid oxide fuel cells, Solid State Ionics, 132, 241-251 (2000).

11. S. P. Jiang, Sintering behaviour of Ni/Y2O3-ZrO2 cermet electrodes of solid oxide fuel cells, Journal of Materials Science, 38, 3775-3782 (2003).

12. B. C. H. Steele, Solid oxide fuel cell anode composition, Patent, GB 2 394 114 A (2004).

13. S. Tao, J. T. S. Irvine, Discovery and characterization of novel oxide anodes for solid oxide fuel cells, The Chemical Record, 4, 83-95 (2004).

14. P. H. Larsen, Ph.D. thesis, Sealing materials for solid oxide fuel cells, Sheffield University, UK (1999).

15. M. Magyarova, M. Winiarczyk, Haldor Topsøe A/S: The solid oxide fuel cell strategy, Copenhagen Business School Case Competition (2004).

16. G. Robert, A. Kaiser, E. Batawi, Structured body for an anode used in fuel cells, Patent, US 2003/0165726 A1 (2003).

17. K. J. Haltiner, S. Mukerjee, D. M. England, M. T. Faville, S. M. Kelly, B. Edlinger, J. Tachtler, Oxygen isolation and collection for anode protection in a solid-oxide fuel cell stack, Patent, US 2003/0235747 A1 (2003).

18. A. C. Müller, A. Krügel, A. Weber, E. Ivers-Tiffée, Characterization of multilayer anodes for SOFC, in Materials Research Society Symposium Proceedings volume 756, P. Knauth, J. M. Tarascon, E. Traversa, H. L. Tuller (eds.), Materials Research Society, Pittsburgh, PA, USA, 533-538 (2003).

19. G. Robert, A. Kaiser, E. Batawi, Anode substrate design for RedOx-stable ASE cells, in 6th European SOFC Forum proc. vol. 1, M. Mogensen (ed.), European Fuel Cell Forum, Oberrohrdorf, Switzerland, 193-200 (2004).

20. P. Sarkar, H. Rho, Crack-resistant anode-supported fuel cell, Patent, US 2004/0121222 A1 (2004).

21. S. Tao, J. T. S. Irvine, A redox-stable efficient anode for solid-oxide fuel cells, Nature Materials, 2, 320-323 (2003).

22. G. Robert, A. Kaiser, K. Honegger, E. Batawi, Anode supported solid oxide fuel cells with a thick anode substrate, in 5th European SOFC Forum proc. vol. 1, J. Huijsmans (ed.), European Fuel Cell Forum, Oberrohrdorf, Switzerland, 116-122 (2002).

23. M. Cassidy, G. Lindsay, K. Kendall, The reduction of nickel-zirconia cermet anodes and the effects on supported thin electrolytes, Journal of Power Sources, 61, 189-192 (1996).

24. C. Bagger, Improved production methods for YSZ electrolyte and Ni-YSZ anode for SOFC, in 1992 Fuel Cell Seminar, 241-244 (1992).

25. S. Primdahl, M. J. Jørgensen, C. Bagger, B. Kindl, Thin anode supported SOFC, in SOFC VI proc. vol. 99-19, S. C. Singhal, M. Dokiya (eds.), The Electrochemical Society, Inc., Pennington, NJ, USA, 793-802 (1999).

26. C. C. Appel, N. Bonanos, A. Horsewell, S. Linderoth, Ageing behaviour of zirconia stabilised by yttria and manganese oxide, Journal of Materials Science, 36, 4493-4501 (2001).

27. R. Stevens, Engineering properties of zirconia, in Engineered materials handbook. Ceramic and glasses, vol. 4, S. J. Schneider (ed.), ASM International, The Materials Information Society, 775-785 (1991).

28. G. A. Carter, R. D. Hart, N. M. Kirby, D. Milosevic, Chemically-mixed powders for solid oxide fuel cells, Journal of the Australian Ceramic Society, 39, 149-153 (2003).

29. M. Bengisu, Engineering ceramics, Springer-Verlag Berlin Heidelberg, Germany (2001).

30. H. Yakabe, Y. Baba, I. Yasuda, X-ray stress measurements for anode-supported planar SOFC, in SOFC VII proc. vol. 2001-16, H. Yokokawa, S. C. Singhal (eds.), The Electrochemical Society, Inc., Pennington, NJ, USA, 303-310 (2001).

31. J. Malzbender, R. W. Steinbrech, L. Singheiser, Determination of the interfacial fracture energies of cathodes and glass ceramic sealants in a planar solid-oxide fuel cell design, Journal of Materials Research, 18, 929-934 (2003).

32. R. M. C. Clemmer, S. F. Corbin, Influence of porous composite microstructure on the processing and properties of solid oxide fuel cell anodes, Solid State Ionics, 166, 251-259 (2004).

33. M. Mori, T. Yamamoto, H. Itoh, H. Inaba, H. Tagawa, Thermal expansion of nickel-zirconia anodes in solid oxide fuel cells during fabrication and operation, Journal of The Electrochemical Society, 145, 1374-1381 (1998).

34. O. Kesler, R. L. Landingham, Improvements in mechanical behaviour of SOFC anodes, in Material Research Society Symposium Proceedings vol. 756, P. Knauth, J. M. Tarascon, E. Traversa, H. L. Tuller (eds.), Materials Research Society, Pittsburgh, PA, USA, 539-544 (2003).

35. R. Barfod, P. V. Hendriksen, P. H. Larsen, Status on test of cells with high alumina content in the anode support, Internal report, Risø National Laboratory, BC-note 730 (2005).

36. R. J. Aaberg, R. Tunold, F. W. Poulsen, N. Bonanos, Short term structural changes in NiO/YSZ electrodes upon reduction, in 2nd European SOFC Forum proc. vol. 1, B. Thorstensen (ed.), European Fuel Cell Forum, Oberrohrdorf, Switzerland, 363-372 (1996).

37. A. Ioselevich, A. A. Kornyshev, W. Lehnert, Statistical geometry of reaction space in porous cermet anodes based on ion-conducting electrolytes. Patterns of degradation, Solid State Ionics, 124, 221-237 (1999).

38. A. Ioselevich, A. A. Kornyshev, W. Lehnert, Degradation of solid oxide fuel cell anodes due to sintering of metal particles. Correlated percolation model, Journal of The Electrochemical Society, 144, 3010-3019 (1997).

39. R. Ihringer, S. Rambert, J. van Herle, Performance and characterisation of anode-supported cells co-cast with thin 8YSZ, in 4th European SOFC Forum, A. J. McEvoy (ed.), European Fuel Cell Forum, Oberrohrdorf, Switzerland, 241-249 (2000).

40. L. Grahl-Madsen, P. H. Larsen, N. Bonanos, J. Engell, S. Linderoth, Manufacture and properties of NiO-YSZ anode supports and current collectors, in 5th European SOFC Forum proc., J. Huijsmans (ed.), European Fuel Cell Forum, Oberrohrdorf, Switzerland, 82-89 (2002).

41. L. Kindermann, F. W. Poulsen, C. Bagger, In plane conductivity of improved Ni-cermet anodes, in 3rd European SOFC Forum proc. vol. 2, P. Stevens (ed.), European Fuel Cell Forum, Oberrohrdorf, Switzerland, 133-143 (1998).

42. R. Vassen, D. Simwonis, D. Stöver, Modelling of the agglomeration of Ni-particles in anodes of solid oxide fuel cells, Journal of Materials Science, 36, 147-151 (2001).

43. D. Waldbillig, A. Wood, D. G. Ivey, Enhancing the redox tolerance of anode supported solid oxide fuel cells by microstructural modification, in SOFC IX proc. vol. 2005-07, S. C. Singhal, J. Mizusaki (eds.), The Electrochemical Society, Inc., Pennington, NJ, USA, 1244-1256 (2005).

44. D. Skarmoutsos, P. Nikolopoulos, F. Tietz, I. C. Vinke, Physical characterization of Y0.25Zr0.60Ti0.15O2-x and its performance as a Ni/Y0.25Zr0.60Ti0.15O2-x anode cermet in an SOFC, Solid State Ionics, 170, 153-158 (2004).

45. A. Tsoga, P. Nikolopoulos, A. Kontogeorgakos, F. Tietz, A. Naoumides, Additives for improved long-term behaviour of the SOFC anode cermet, in SOFC V proc. vol. 97-40, U. Stimming, S. C. Singhal, H. Tagawa, W. Lehnert (eds.), The Electrochemical Society, Inc., Pennington, NJ, USA, 823-832 (1997).

46. E. E. Underwood, The mathematical foundations of quantitative stereology, in Stereology and quantitative metallography. ASTM Special Technical Publication STP 504, G. E. Pellissier, S. M. Purdy (eds.), American Society for Testing and Materials, Philadelphia, PA, USA, 3-38 (1972).

47. D.-S. Lee, J.-W. Heo, J.-H. Lee, J. K. H. W. Lee, S.-W. Kim, G.-H. Kim, H. S. Song, Electrical and microstructural characterization of Ni/YSZ cermet anode for anode-supported type SOFC, in Solid State Ionics: Trends in the new millennium, B. V. R. Chowdari et al. (eds.), World Scientific Publishing Co., 477-482 (2002).

48. N. M. Tikekar, T. J. Armstrong, A. V. Virkar, Low temperature reduction kinetics of solid oxide fuel cell (SOFC) anodes, in Electrochemical Society Proceedings vol. 2002-26, E. D. Wachsman, K. Swider-Lyons, M. F. Carolan, F. H. Garzon, M. Liu, J. R. Stetter (eds.), The Electrochemical Society, Inc., Pennington, NJ, USA, 81-90 (2002).

49. J.-H. Lee, H. Moon, H.-W. Lee, J. Kim, J.-D. Kim, K.-H. Yoon, Quantitative analysis of microstructure and its related electrical property of SOFC anode, Ni-YSZ cermet, Solid State Ionics, 148, 15-26 (2002).

50. J.-H. Lee, J.-W. Heo, D.-S. Lee, J. Kim, G.-H. Kim, H.-W. Lee, H. S. Song, J.-H. Moon, The impact of anode microstructure on the power generating characteristics of SOFC, Solid State Ionics, 158, 225-232 (2002).

51. K.-R. Lee, S. H. Choi, J. Kim, H.-W. Lee, J.-H. Lee, Viable image analyzing method to characterize the microstructure and the properties of the Ni/YSZ cermet anode of SOFC, Journal of Power Sources, 140, 226-234 (2005).

52. T. Werber, Joining of nickel powder grains by thermal-oxidation, Solid State Ionics, 42, 205-211 (1990).

53. N. M. Tikekar, T. J. Armstrong, A. V. Virkar, Reduction and re-oxidation kinetics of nickel-based solid oxide fuel cell anodes, in SOFC VIII proc. vol. 2003-07, S. C. Singhal, M. Dokiya (eds.), The Electrochemical Society, Inc., Pennington, NJ, USA, 670-679 (2003).

54. J. Malzbender, R. W. Steinbrech, L. Singheiser, Strength of planar cells for SOFC application, in SOFC VIII proc. vol. 2003-07, S. C. Singhal, M. Dokiya (eds.), The Electrochemical Society, Inc., Pennington, NJ, USA, 1463-1472 (2003).

55. Introduction manual to the Beckman Coulter LS 13 320 instrument (2009).

56. CRC handbook of chemistry and physics, 68th edition, CRC Press, Inc., Boca Raton, FL, USA (1988).

57. D. Waldbillig, A. Wood, D. G. Ivey, Thermal analysis of the cyclic reduction and oxidation behaviour of SOFC anodes, Solid State Ionics, 176, 847-859 (2005).

58. D. Waldbillig, A. Wood, D. G. Ivey, Electrochemical and microstructural characterization of the redox tolerance of solid oxide fuel cell anodes, Journal of Power Sources, 145, 206-215 (2005).

59. A. Wood, M. Pastula, D. Waldbillig, D. G. Ivey, Initial testing of solutions to redox problems with anode-supported solid oxide fuel cells, in SOFC IX proc. vol. 2005-07, S. C. Singhal, J. Mizusaki (eds.), The Electrochemical Society, Inc., Pennington, NJ, USA, 571-583 (2005).

60. H. Mori, C. J. Wen, J. Otomo, K. Eguchi, H. Takahashi, Investigation of the interaction between NiO and yttria-stabilized zirconia (YSZ) in the NiO/YSZ composite by temperature-programmed reduction technique, Applied Catalysis A-General, 245, 79-85 (2003).

61. A. R. Rojas, H. E. Esparza-Ponce, L. Fuentes, A. Lópes-Ortiz, A. Keer, J. Reyes-Gasga, In situ x-ray Rietveld analysis of Ni-YSZ solid oxide fuel cell anodes during NiO reduction in H2, Journal of Physics D: Applied physics, 38, 2276-2282 (2005).

62. A. Hagen, R. V. Martins, H. F. Poulsen, V. Honkimäki, T. Buslaps, R. Feidenhans'l, A depth-resolved in situ study of the reduction and oxidation kinetics in solid oxide fuel cells, Internal report, Risø National Laboratory (2005).

63. H. Song, J.-H. Lee, J. Kim, H.-W. Lee, Improved multi-functionality of Ni/YSZ cermet anode by optimizing fabrication processes, in International conference on fuel cell science, engineering and technology, R. K. Shah, S. G. Kandlikar (eds.), American Society of Mechanical Engineers, New York, USA, 511-516 (2004).

64. R. Barfod, M. Mogensen, T. Klemensoe, A. Hagen, Y.-L. Liu, P. V. Hendriksen, Detailed characterization of anode supported SOFCs by impedance spectroscopy, in SOFC IX proc. vol. 2005-07, S. C. Singhal, J. Mizusaki (eds.), The Electrochemical Society, Inc., Pennington, NJ, USZ, 524-533 (2005).

65. C. A. H. Chung, K. V. Hansen, M. Mogensen, Effect of impurities on anode performance, in Cocoa Beach Conference (2004).

66. D. Johnson, ZView2, Screibner Associates, Inc. (2003).

67. D. W. Dees, T. D. Claar, T. E. Easler, D. C. Fee, F. C. Mrazek, Conductivity of porous Ni/ZrO2-Y2O3 cermets, Electrochemical Storage, 134, 2141-2146 (1987).

68. W. Hu, H. Guan, X. Sun, S. Li, M. Fukumoto, I. Okane, Electrical and thermal conductivities of nickel-zirconia cermets, Journal of the Australian Ceramic Society, 81, 2209-2212 (1998).

69. S. Sunde, Ph.D. thesis, Computer simulations of composite electrodes in solid oxide fuel cells, Norwegian University of Science and Technology, Trondheim, Norway (1999).

70. K. V. Hansen, Personal communication (2005).

71. M. Mogensen, 8YSZ calculated conductivity, Internal report, Risø National Laboratory (2005).

72. R. Barfod, T. Klemensø, Evaluation of symmetric anodes, Internal report BC-693, Risø National Laboratory (2004).

73. D. Skarmoutsos, A. Tsoga, A. Naoumides, P. Nikolopoulos, 5 mol% TiO2-doped Ni-YSZ anode cermets for solid oxide fuel cells, Solid State Ionics, 135, 439-444 (2000).

74. D.-S. Lee, J.-H. Lee, J. Kim, H.-W. Lee, H. S. Song, Tuning of the microstructure and electrical properties of SOFC anode via compaction pressure control during forming, Solid State Ionics, 166, 13-17 (2004).

75. A. C. Khandkar, S. Elangovan, M. Liu, M. Timper, Thermal cycle fatigue behaviour of high temperature electrodes, in Proceedings of the symposium on high temperature electrode materials and characterization vol. 91-6, D. D. Macdonald, A. C. Khandkar (eds.), The Electrochemical Society, Inc., Pennington, NJ, USA, 175-190 (1991).

76. J. R. Rostrup-Nielsen, J. Sehested, J. K. Nørskov, Hydrogen and syngas by steam reforming, Advances in Catalysis, 47, 65-139 (2002).

77. A. Hagen, R. Barfod, P. V. Hendriksen, Y.-L. Liu, S. Ramousse, Effect of operational conditions on long-term stability of SOFCs, in SOFC IX proc. vol. 2005-07, S. C. Singhal, J. Mizusaki (eds.), The Electrochemical Society, Inc., Pennington, NJ, USA, 503-513 (2005).

78. W. Z. Zhu, S. C. Deevi, A review on the status of anode materials for solid oxide fuel cells, Materials Science and Engineering, A362, 228-239 (2003).

79. H. Itoh, Y. Hiei, T. Yamamoto, M. Mori, T. Watanabe, Optimized mixture ratio in YSZ-supported Ni-YSZ anode material for SOFC, in SOFC VII proc. vol. 2001-16, H. Yokokawa, S. C. Singhal (eds.), The Electrochemical Society, Inc., Pennington, NJ, USA, 750-758 (2001).

80. P. Mardilovich, G. S. Herman, D. Champion, C. Beatty, J. O'Neill, Fuel cell and passive support, Patent, EP 1467421 A2 (2004).

81. S. Elangovan, A. Khandkar, Analysis of the morphological instability of two phase mixed conducting electrodes, in Proceedings of the first international symposium on ionic and mixed conducting ceramics vol. 91-12, T. A. Ramanarayanan, H. L. Tuller (eds.), The Electrochemical Society, Inc., Pennington, NJ, USA, 122-132 (1991).

82. J. Sehested, A. Carlsson, T. V. W. Janssens, P. L. Hansen, A. K. Datye, Sintering of nickel steam-reforming catalysts on MgAl2O4 spinel supports, Journal of Catalysis, 197, 200-209 (2001).

83. S. P. Jiang, S. H. Chan, Development of Ni/Y2O3-ZrO2 cermet anodes for solid oxide fuel cells, Materials Science and Technology, 20, 1109-1118 (2004).

84. T. Klemensø, C. Chung, P. H. Larsen, M. Mogensen, The mechanism behind redox instability of SOFC anodes, Journal of the Electrochemical Society, 152, in press (2005).

85. P. Pedersen, C. L. Laursen, Design for minimum stress concentration by finite elements and linear programming, Journal of Structural Mechanics, 10, 375-391 (1983).

86. J. P. Queau, PH. Trompette, Two-dimensional shape optimal design by the finite element method, International Journal for numerical methods in engineering, 15, 1603-1612 (1980).

87. E. S. Kristensen, N. F. Madsen, On the optimum shape of fillets in plates subjected to multiple in-plane loading cases, International Journal for numerical methods in engineering, 10, 1007-1019 (1976).

88. ODESSY, Report, Institute of Mechanical Engineering, Aalborg University, Denmark, www.ime.aau.dk (2005).

89. E. Lund, Ph.D. thesis, Finite element based design sensitivity analysis and optimization, Institute of Mechanical Engingeering, Aalborg University, Denmark (2005).

90. N. Christiansen, S. Kristensen, H. Holm-Larsen, P. H. Larsen, M. Mogensen, P. V. Hendriksen, S. Linderoth, Status of SOFC development at Haldor Topsøe / Risø, in 5th European SOFC Forum, J. Huijsmans (ed.), European Fuel Cell Forum, Oberrohrdorf, Switzerland, 34-41 (2002).

91. H. Toftegaard, F. Wang, Tensile tests on SOFC materials - unreduced and reduced anode support and anode-electrolyte half-cell, Internal report Risø-I-2359, Risø National Laboratory (2005).

92. A. Khalili, K. Kromp, Statistical properties of Weibull estimators, Journal of Materials Science, 26, 6741-6752 (1991).

93. B. F. Sørensen, M. H. Jørgensen, J. H. Andreasen, C. P. Debel, N. Christiansen, J. T. Rheinlander, N. Langvad, Mekaniske egenskaber og design, Forskningscenter Risø, Roskilde (1995).

94. Component reliability in solid oxide fuel cell systems for commercial operation, Status report from the CORE-SOFC project (2004).

95. M. Radovic, E. Lara-Curzio, B. Armstrong, C. Walls, Effect of thickness and porosity on the mechanical properties of planar components for solid oxide fuel cells at ambient and elevated temperatures, in Ceramic Engineering and Science Proceedings, 24, 3, American Ceramic Society, 329-334 (2003).

96. E. Lara-Curzio, M. Radovic, B. Armstrong, C. Walls, M. Lance, P. Tortorelli, S. Waters, L. Walker, A. Murphy, Reliability and durability of materials and components for solid oxide fuel cells, Report, http://www.ornl.gov/sci/fossil/Publications/ANNUAL-2003/feaa066.pdf (2003).

97. K. S. Lee, I. S. Han, D. W. Seo, S. K. Woo, Improvement of strength in porous ceramics by control of additives, in Materials Science Forum vol. 439, Trans Tech Publications, Switzerland, 68-73 (2003).

98. N. M. Sammes, Y. Du, The mechanical properties of tubular solid oxide fuel cells, Journal of Materials Science, 38, 4811-4816 (2003).

99. K.-Z. Fung, J. Chen, C. Tanner, A. V. Virkar, Low temperature solid oxide fuel cells with dip-coated YSZ electrolytes, in SOFC IV proc. vol. 95-1, M. Dokiya, O. Yamamoto, H. Tagawa, S. C. Singhal (eds.), The Electrochemical Society, Inc., Pennington, NJ, USA, 1018-1027 (1995).

100. J. H. Andreasen, Reliability-based design of ceramics, Materials & Design, 15, 3-13 (1994).

101. T. Hoshide, J. Abe, A statistical approach to strength evaluation incorporating porosity effect for porous ceramics, Fatigue & Fracture of Engineering Materials & Structures, 26, 383-389 (2003).

102. M. Radovic, E. Lara-Curzio, Mechanical properties of tape cast nickel-based anode materials for solid oxide fuel cells before and after reduction in hydrogen, Acta Materialia, 52, 5747-5756 (2004).

103. K. Kendall, N. M. Alford, S. R. Tan, J. D. Birchall, Influence of toughness on Weibull modulus of ceramic bending strength, Journal of Material Research, 1, 120-123 (1986).

104. J. H. She, T. Ohji, Fabrication and characterization of highly porous mullite ceramics, Materials Chemistry and Physics, 80, 610-614 (2003).

105. J. F. Yang, T. Ohji, S. Kanzaki, A. Diaz, S. Hampshire, Microstructure and mechanical properties of silicon nitride ceramics with controlled porosity, Journal of the American Ceramic Society, 85, 1512-1516 (2002).

106. R. Martins, Results from the in-situ residual strain measurements in SOFC at the ESRF, Internal report, Risø National Laboratory (2005).

107. H. Yakabe, Y. Baba, T. Sakurai, M. Satoh, I. Hirosawa, Y. Yoda, Evaluation of residual stresses in a SOFC stack, Journal of Power Sources, 131, 278-284 (2004).

108. W. Fischer, J. Malzbender, G. Blass, R. W. Steinbrech, Residual stresses in planar solid oxide fuel cells, Journal of Power Sources, 150, 73-77 (2005).

109. J. L. Beuth Jr., Cracking of thin bonded films in residual tension, International Journal of Solids Structures, 29, 1657-1675 (1992).

110. A. Selcuk, A. Atkinson, Strength and toughness of tape-cast yttria-stabilized zirconia, Journal of the American Ceramic Society, 83, 2029-2035 (2000).

111. N. Christiansen, S. Kristensen, H. Holm-Larsen, P. H. Larsen, M. Mogensen, P. V. Hendriksen, S. Linderoth, Status of the SOFC development at Haldor Topsøe/Risø, in SOFC VIII proc. vol. 2003-07, S. C. Singhal, M. Dokiya (eds.), The Electrochemical Society, Inc., Pennington, NJ, USA, 105-112 (2003).

112. A. N. Kumar, B. F. Sørensen, Fracture energy and crack growth in surface treated yttria stabilized zirconia for SOFC applications, Materials Science and Engineering, A333, 380-389 (2002).

113. T. Ye, Z. Suo, A. G. Evans, Thin film cracking and the roles of substrate and interface, International Journal of Solids Structures, 29, 2639-2648 (1992).

114. R. Chaim, G. Basat, A. Kats-Demyanets, Effect of oxide additives on grain growth during sintering of nanocrystalline zirconia alloys, Materials Letters, 35, 245-250 (1998).

115. G. A. Gogotsi, D. Y. Ostrovoy, Mechanical behaviour of partially stabilized zirconia crystals with terbia and ceria additives, Journal of the European Ceramic Society, 15, 1177-1184 (1995).

116. A. G. Karaulov, T. G. Gal'chenko, N. M. Chudnova, E. B. Loenko, Metal-modified zirconia refractories, Refractories and Industrial Ceramics, 38, 161-163 (1997).

117. S. Maschio, O. Sbaizero, S. Meriani, E. Bischoff, Sintering aids for ceria-zirconia alloys, Journal of Materials Science, 27, 2734-2738 (1992).

118. S. C. Sharma, N. M. Gokhale, R. Dayal, R. Lal, Synthesis, microstructure and mechanical properties of ceria stabilized tetragonal zirconia prepared by spray drying technique, Bulletin of Material Science, 25, 15-20 (2002).

119. S. R. Choi, N. P. Bansal, Mechanical behaviour of zirconia/alumina composites, Ceramics International, 31, 39-46 (2005).

120. F. L. Lowrie, R. D. Rawlings, B. C. H. Steele, Comparison of strength and microstructure of thin fully stabilised zirconia at room temperature and 950 C, in SOFC IV proc. vol. 95-1, M. Dokiya, O. Yamamoto, H. Tagawa, S. C. Singhal (eds.), The Electrochemical Society, Inc., Pennington, NJ, USA, 318-325 (1995).

121. A. Tsoga, A. Naoumidis, P. Nikolopoulos, Wettability and interfacial reactions in the systems Ni/YSZ and Ni/Ti-TiO2/YSZ, Acta Materialia, 9, 3679-3692 (1996).

122. A. Ringuede, D. Bronine, J. R. Frade, Ni1-xCox/YSZ cermet anodes for solid oxide fuel cells, Electrochimica Acta, 48, 437-442 (2002).

123. W.-H. Su, X.-Q. Huang, C.-X. Zhang, Z. Lu, T.-Q. Lu, T.-M. He, L. Pei, Z.-G. Liu, Study on the composite materials used for solid oxide electrolyte fuel cell, in SOFC VII proc. vol. 2001-16, H. Yokokawa, S. C. Singhal (eds.), The Electrochemical Society, Inc., Pennington, NJ, USA, 746-749 (2001).

124. M. Ozawa, T. Itoh, E. Suda, Mechanical loss of Zr0.8-xCexY0.2O1.9 (x=0-0.4), Journal of Alloys and Compounds, 374, 12-123 (2004).

125. J.-H. Lee, J. Kim, S.-W. Kim, H.-W. Lee, H. S. Song, Characterization of the electrical properties of Y2O3-doped CeO2-rich CeO2-ZrO2 solid solutions, Solid State Ionics, 166, 45-52 (2004).

126. J. van Herle, R. Vasquez, Conductivity of Mn and Ni-doped stabilized zirconia electrolyte, Journal of the European Ceramic Society, 24, 1177-1180 (2004).

127. X. Guo, Roles of alumina in zirconia for functional applications, Journal of the American Ceramic Society, 86, 1867-1873 (2003).

128. S.-I. Lee, J. M. Vohs, R. J. Gorte, A study of SOFC anodes based on Cu-Ni and Cu-Co bimetallics in CeO2-YSZ, Journal of The Electrochemical Society, 151, A1319-A1323 (2004).

129. E. Batawi, C. Voisard, U. Weissen, J. Hoffmann, Y. Sikora, J. Frei, Materials development at Sulzer Hexis for the provision of a combined heat and power SOFC system, in 6th European SOFC Forum proc. vol. 2, M. Mogensen (ed.), European Fuel Cell Forum, Oberrohrdorf, Switzerland, 767-773 (2004).

130. X. Mantzouris, N. Zouvelou, D. Skarmoutsos, P. Nikolopoulos, F. Tietz, Interfacial properties and structure stability of Ni/Y2O3-ZrO2-TiO2 cermet anodes for solid oxide fuel cells, Journal of Materials Science, 40, 2471-2475 (2005).

131. S. Sunde, Simulations of composite electrodes in fuel cells, Journal of Electroceramics, 5, 153-182 (2000).

132. S. H. Chan, Z. T. Xia, Anode micro model of solid oxide fuel cell, Journal of The Electrochemical Society, 148, A388-A394 (2001).

133. J. Abel, A. A. Kornyshev, W. Lehnert, Correlated resistor network study of porous solid oxide fuel cell anodes, Journal of The Electrochemical Society, 144, 4253-4259 (1997).

134. A. S. Ioselevich, A. A. Kornyshev, Approximate symmetry laws for percolation in complex systems: Percolation in polydisperse composites, Physical Review E, 65, 021301-1-021301-11 (2002).

135. S. Sunde, Software documentation for Monte Carlo simulations of composite SOFC electrodes and modelling of internal reforming at SOFC anodes, Internal report BC-311, Risø National Laboratory (1996).

Appendices

Appendix A List of publications

1. T. Klemensø, C. Chung, P. H. Larsen, M. Mogensen, "The mechanism behind redox instability of SOFC anodes", in SOFC-IX proc. vol. 2005-07, S. C. Singhal, J. Mizusaki, (eds.), p. 1226, The Electrochemical Society Proceedings Series, Pennington, NJ, USA (2005).

2. R. Barfod, M. Mogensen, T. Klemensø, A. Hagen, Y.-L. Liu, P.V. Hendriksen, "Detailed characterization of anode supported SOFCs by impedance spectroscopy", in SOFC-IX proc. vol. 2005-07, S. C. Singhal, J. Mizusaki, Editors, p. 1226, The Electrochemical Society Proceedings Series, Pennington, NJ, USA (2005).

3. T. Klemensø, C. Chung, P.H. Larsen, M. Mogensen, "The mechanism behind redox instability of anodes in high-temperature solid oxide fuel cells", Journal of the Electrochemical Society, 152, 11 (*in print*). (Improved version of publication 1 for the journal).

Appendix B Additional data to Chapter 3

Table B1. Average Ni grain diameter, area, and roundness after respectively 1 hour and 96 hours of reducing conditions. The values are based on image analysis of light microscope micrographs. Between 1435-2530 grains were analyzed. The standard deviations on the values are included.

Parameter	State	r-8Y-bar	r-8Y-strip	r-3Y-bar	r-3Y-strip
Ni grain diameter [μm]	1 h reduction	1.65 ± 0.14	1.83 ± 0.11	1.61 ± 0.16	1.52 ± 0.08
	96 h reduction	1.31 ± 0.12	1.63 ± 0.15	1.62 ± 0.12	1.53 ± 0.08
Ni grain area [μm^2]	1 h reduction	0.23 ± 0.02	0.23 ± 0.01	0.20 ± 0.04	0.21 ± 0.02
	96 h reduction	0.15 ± 0.03	0.17 ± 0.03	0.20 ± 0.02	0.17 ± 0.02
Ni grain roundness	1 h reduction	1.88 ± 0.13	1.84 ± 0.08	1.75 ± 0.20	1.69 ± 0.06
	96 h reduction	1.78 ± 0.12	1.94 ± 0.19	1.87 ± 0.08	1.73 ± 0.06

Table B2. Range in phase fractions as observed with SEM-BSE micrographs and image analyses.

State	Phase	8Y-bar	8Y-strip	3Y-bar	3Y-strip
As-sintered	Pore [%]	2-8	1-8	3-7	5-23
	NiO [%]	44-66	50-60	45-54	43-57
	YSZ [%]	26-52	32-49	40-51	28-43
1st reduced	Pore [%]	1-12	16-22	4-32	23-38
	Solid [%]	88-99	78-84	68-96	62-77
1st re-oxidized	Pore [%]	1-10	14-24	1-16	7-13
	NiO [%]	49-58	42-50	43-55	42-55
	YSZ [%]	39-45	31-40	37-47	33-46
4th re-oxidized	Pore [%]	24-45	27-36	8-37	23-38
	NiO [%]	16-26	37-49	39-60	40-54
	YSZ [%]	36-52	18-28	20-43	20-27

Table B3. Maximum in-plane linear dimension (length), area, and roundness of the nickel particles A, B, C observed with ESEM (cf. Figures 3.5 and 3.6) during successive redox steps. The uncertainty on the length is qualitatively estimated to ± 0.05 μm.

State	Parameter	A	B	C
As-sintered	Length [μm]	0.91	1.01	1.61
	Area [μm^2]	0.49	1.41	1.92
	Roundness	1.48	1.14	1.22
1st reduction	Length [μm]	0.78	1.50	1.33
(2 h up to 800°C)	Area [μm^2]	0.35	1.37	1.10
	Roundness	0.92	1.03	0.97
1st re-oxidation	Length [μm]	0.75	1.47	1.40
(1 h at 800°C)	Area [μm^2]	0.46	1.69	1.42
	Roundness	1.37	1.10	1.03
2nd reduction	Length [μm]	0.65	1.33	1.14
(2 h at 800°C)	Area [μm^2]	0.36	1.28	0.99
	Roundness	0.90	1.03	0.96
2nd re-oxidation	Length [μm]	0.94	1.47	1.36
(2h at 800°C)	Area [μm^2]	0.49	1.79	1.20
	Roundness	1.17	1.04	1.18

Appendix C Additional data to Chapter 4

Table C1. Time for complete reduction at 1000°C as measured with TGA.

Sample	1st reduction [min]	2nd reduction [min]	3rd reduction [min]
3Y-powder-1000	36 ± 2	28 ± 2	-
3Y-layer-1000	31 ± 2	31 ± 2	31 ± 2
3Y-bar-1000	72 ± 2	52 ± 2	44 ± 2
8Y-powder-1000	28 ± 2	26 ± 2	-
8Y-bar-1000	50 ± 2	30 ± 2	27 ± 2

Table C2. Times for complete re-oxidation at 1000°C as measured with TGA.

Sample	1st re-oxidation [min]	2nd re-oxidation [min]	3rd re-oxidation [min]
3Y-powder-1000	22 ± 2	21 ± 2	-
3Y-layer-1000	27 ± 2	23 ± 2	22 ± 2
3Y-bar-1000	252 ± 2	50 ± 2	-
8Y-powder-1000	26 ± 2	30 ± 2	-
8Y-bar-1000	147 ± 2	34 ± 2	30 ± 2

Appendix D Additional data to Chapter 5

Table D1. Electrical characteristics of samples tested at 1000°C with variable yttria content in the ceramic component.

	8Y-bar-1000	3Y-bar-1000-c	8Y-strip-1000	3Y-strip-1000
ε_{geom} [%]	3.36	4.56	8.39	16.97
$t_{r,1}$ [h]	2.68	6.63	0.50	0.50
$\sigma_{r,1}$ [S/cm]	851.40	904.57	719.72	506.20
$\Delta\sigma_{24,1}$ [S/cm/h]	-0.77	-2.07	-4.63	-4.83
$\Delta\sigma_{96,1}$ [S/cm/h]	-0.16	-0.69	-1.60	-1.99
$\Delta\sigma_{ox,1}$ [%]	19.70	-	-84.32	87.31
$t_{r,2}$ [h]	2.55	-	0	0.38
$\sigma_{r,2}$ [S/cm]	1001.19	-	88.85	591.94
$\Delta\sigma_{24,2}$ [S/cm/h]	-1.08	-	-0.61	-1.51
$\Delta\sigma_{ox,2}$ [%]	4.70	-	-	-